DOCTOR OF PHILOSOPHY

Bio-optical properties and its application for ocean colour algorithm in east coast of peninsular Malaysia water

Idris, Md

Award date:
2012

Awarding institution:
Bangor University

BIO-OPTICAL PROPERTIES AND ITS APPLICATION FOR OCEAN COLOUR ALGORITHM IN EAST COAST OF PENINSULAR MALAYSIA WATER

MD. SUFFIAN B. IDRIS

A thesis submitted in accordance with the requirements of the Bangor University
for the degree of

DOCTOR OF PHILOSOPHY

School of Ocean Sciences
Bangor University
Wales

Supervised By:

Dr. Dave Bowers
Dr. Gay Mitchelson-Jacob

JANUARY 2012

This thesis is dedicated to

the memory of my loving mother, **ALLAHYARHAMAH JAUYAH HASAN**, who left us much too soon and to whom I owe everything. May **ALLAH** bless her soul and grant her **JANNAH**.

Declaration

This work has not previously been accepted in substance for any other degree and is not currently being submitted in candidature for any other degree.

Signed (Candidate)

Date

Statement 1

This is to certify that the work here submitted was carried out by the candidate himself. Due acknowledgement has been made of any assistance received.

Signed (Candidate)

Date

Statement 2

I hereby give consent for my thesis, if accepted, to be available for photocopying and for inter-library loan, and for the title to be made available outside organisations.

Signed (Candidate)

Date

Abstract

The core subject of this thesis is to assess the applicability of ocean colour algorithms for deriving chlorophyll and CDOM concentrations in east coast of Peninsular Malaysia waters. A series of bio-optical observations were conducted in the study area during the 2009 seasons. These included in-water constituents (chlorophyll, suspended sediment and CDOM), absorption properties and reflectance. The analysis of the data reveals a clear seasonal signal with high values of all constituents and absorption properties during the northeast monsoon and low values during the southwest and inter-monsoon seasons. The timing, magnitude and spatial extent of these changes are associated with seasonal changes in hydrographic conditions (wind forcing, sea surface temperature and freshwater input). Contrary to the trend during the monsoon seasons, inter-monsoon chlorophyll concentrations were higher offshore with some evidence of the pigment packaging effect. In the blue part of the spectrum, non-phytoplankton material (CDOM and detritus) is a dominant absorber (>70% of non-water absorption) regardless of the season and this does not always covary with chlorophyll concentration.

The performance of standard empirical and semi-analytical ocean colour algorithms at retrieving chlorophyll concentration was evaluated and validated using the bio-optical data in the study area. The results of our analysis showed that both types of algorithm often perform poorly in the study area, either due to a wide range of variation in in-water constituents or uncertainties in the spectral shape and magnitude of inherent optical properties. Using a series of in-situ bio-optical data, the algorithm best-suited for the study area was developed and evaluated. The results of this study indicate that a regionally-tuned chlorophyll algorithm can provide more accurate estimate of chlorophyll concentration provided that there exist a mean relationship between chlorophyll and CDOM, and the spectral shape of absorption does not change with varying environmental conditions. The most consistent result of this study was that absorptions by phytoplankton and CDOM can be well estimated by a simple blue-green band ratio, offering a great opportunity to discriminate chlorophyll from CDOM.

Time-series of remote sensed distributions of chlorophyll, CDOM, sea surface temperature and wind speed were examined to evaluate variability of physical forcing and environmental conditions on seasonal and inter-annual variations in ocean colour in the study region. The results of this study confirm that the strong seasonal and inter-annual cycles of chlorophyll and CDOM concentrations are related to climatically driven cycles of monsoon and physical forcing (wind speed and SST). It is also shown that the annual cycle for both chlorophyll and CDOM concentrations is often overshadowed by inter-annual climate variability.

ACKNOWLEDGEMENTS

I am truly grateful to my supervisor Dr. Dave Bowers for everything from my heart. His patience, encouragement and guidance throughout my study period lead me to this wonderful research area. His is not only a great scientist with innovative ideas but also a kind person. Also, I deeply appreciate my really nice co-supervisor, Dr. Gay Mitchelson-Jacob for her thoughtful advice and comments on my research. I have been fortunate to work with two such fine people. I am also thankful my thesis committee members, Prof. David Thomas, Dr. Jaco-Baas and Dr. Andrew Davies for their helpful discussion and suggestion on this project.

I owe my loving thanks to my wife, Shaharul Suhaila and my two lovely kids, Aleesha Safiyya and Amir Hazeem for all of their love, patience and understanding. Lastly, I would like to thank my father, Idris Ahmad; parents in-law and families for all their loving support during my stay abroad.

Financial support for this study was provided, in part, by the Institute of Oceanography, Universiti Malaysia Terengganu and the Malaysian Ministry of Science, Technology & Innovation (MOSTI) through the E-Science Research grant 52020.

TABLE OF CONTENTS

CHAPTER 4: REMOTE SENSING REFLECTANCE: IN-SITU OBSERVATIONS AND MODELS

CHAPTER 5: SEASONAL AND INTER-ANNUAL VARIABILITY OF MODIS-DERIVED OCEAN COLOUR

CHAPTER 6: DISCUSSION AND CONCLUSIONS

LIST OF FIGURES

LIST OF TABLES

CHAPTER 1

BACKGROUND

1.1 Introduction to ocean colour remote sensing

The colour of the ocean depends upon the interaction of incident light with the various substances present in the water. The amount and type of substance controls the quantity and colour of the incoming light energy that can penetrate through the water column and scatter out of the water. The two key optical processes involved during the interactions of incident light with substances in the water column are absorption and scattering. Preisendorfer (1961) defines the absorption and scattering coefficients of seawater as inherent optical properties (IOPs) since their magnitude is characterized only by the behaviour of electromagnetic radiation in the medium but not by the intensity or angular distribution of ambient light. In contrast, the part of the incoming light that is returned back toward its source, depends both on the medium (IOPs) and on the geometry of ambient light within the water column. The "remote sensing reflectance, R_{rs}", is classified by Preisendorfer (1961) as apparent optical properties (AOP). Generally, the optically active constituents of the water can be represented by broadly defined substances such as phytoplankton, dissolved organic matter and suspended inorganic sediments. The relative amount of these substances in the water is used to classify the types of water, either as case-1 or case-2 (Morel and Prieur, 1977).

Since the water leaving radiance depends on the medium, there exists a clear relationship between ocean colour and in-water constituents. Investigating the spectral signals associated with the interactions of light with various underwater substances constitutes basic research in oceanic remote sensing. Knowledge of the variability of bio-optical properties of the water constituents and the radiative transfer through the water column and atmosphere as a function of the water constituents enables their derivation through remote sensing. In ocean remote sensing, there are 2 approaches to formulate this derivation from measured R_{rs}, one is empirical, and the other is analytical.

The empirical approach uses strong absorption (principally in the blue bands) and low absorption (in the green) of chlorophyll contained in phytoplankton. This difference in absorption is the basis for the empirical approach in estimating chlorophyll concentration from the early periods of ocean colour remote sensing i.e. Coastal Zone Colour Scanner (Gordon et al., 1983) until the current satellite sensor of MODIS (O'Reilly et al., 2000). Whilst the empirical approach for the retrieval of chlorophyll in case 1-water (open ocean) has proven successful (Gitelson et al., 2007; Darecki and Stramski, 2004; Carder et al., 1999), interpretation of ocean colour data in optically complex case-2 waters (coastal water) is more difficult and has been shown to have poor predictability (Dall'Olmo et al., 2005; Gons, 1999; Schalles, 2006). The analytical approach based on the radiative transfer theory tackles this problem by deriving the magnitude of each IOP component from the spectral observations of ocean colour. The performance of this approach, however, relies on accurate parameterization in the spectral models for absorption coefficients of each constituent present in the water. The analytical approach has evolved considerably in the last 25 years, since the work by Gordon et al., (1988) and Morel (1988). Since then, there have many applications of a semi-analytical algorithm for the retrieval of constituents concentration as well as optical properties of water (e.g., Garver and Siegel, 1997; Carder et al., 1999, 2004; Lee et al., 2002; Chomko et al., 2003). However, significant difficulties remain, mainly because it is not easy to accurately express the change of each optical property of constituent in a wide range of water types.

In general, operational ocean colour algorithms either empirical or semi-analytical, show relatively variable performance depending on the region, season and type of water (e.g., O’Reilly et al., 1998; Darecki and Stramski, 2004; Carder et al., 2004). Since the interpretation of ocean colour data relates the optical properties to a single phytoplankton pigment index (chlorophyll) as indicator of primary production, any changes to the chlorophyll specific absorption coefficients of phytoplankton could result in errors in the chlorophyll estimation from remote sensing observation. As the chlorophyll specific absorption coefficient varies temporally and spatially as a consequence of differences in the composition, cell size and concentration of pigments (Morel and Bricaud, 1986; Sathyendranath et al., 1987; Bricaud et al., 2004), the success of remotely sensed estimates of chlorophyll concentration requires prior knowledge of this absorption property. Empirical and semi-analytical algorithms must be adjusted to account for the specific bio-optical properties of the local environment.

In this study, we seek to understand the spatial variability of the bio-optical properties of east coast Peninsular Malaysia waters over different seasons. While such studies have been relatively well documented in other South China Sea regions (e.g., Tang et al., 2004, Liu et al., 2002) no information regarding bio-optical properties is available in east coast of Peninsular Malaysia waters. Further, the study area is influenced strongly by seasonal atmospheric conditions (the monsoon) and thus, the optical properties of the waters are expected to vary with seasons. If this is the case, we would also expect that the current global chlorophyll algorithms would not work well when applying them to the study area. Therefore, the performance of these algorithms needs to be evaluated and assessed, and alternative or regionally tuned algorithms may need to develop for estimating chlorophyll concentration in east coast of Peninsular Malaysia waters

1.2 Case-1 and Case-2 waters

The optical properties of ocean waters can vary significantly amongst different aquatic environments and is greatly influenced by a variety of physical, biological and chemical processes in the ocean. In optical oceanography and for modeling purposes, water bodies that have similar optical behaviour are often described by similar bio-optical models. The dependence of optical properties on water constituents is generally simplified into case-1 and case-2 waters.

Case-1 waters are those waters whose optical properties are determined primarily by phytoplankton and its related co-varying decay products of biological origins such as detritus and coloured dissolved organic matter (Gordon and Morel, 1983). Several studies (Morel and Ahn, 1990, 1991; Stramski and Kiefer, 1991) have shown that a number of heterotrophic organisms like flagellates, bacteria and viruses that co-exist with phytoplankton can also influence the optical properties of case-1 waters. In these waters, the contribution of other substances is relatively small and can be modeled as a function of phytoplankton concentration (Sathyendranath, 2000). Although it does not always hold as a good assumption, open ocean waters are generally considered as case-1 type. In case-2 waters, other substances which do not always covary with the phytoplankton pigment, significantly contribute to the optical properties of water body. Such substances include coloured dissolved organic matter (CDOM) contained in land runoff and suspended organic particles, are not related to the phytoplankton decay products. In these waters, absorption due to pigments may be a less important factor in determining variations in the optical properties of the water. Case-2 waters are typically coastal or near-shore.

1.3 Marine Optics: Concept and theory

Marine optics is the quantitative study of light propagation through seawater and its interactions with molecules and particles present in water. The geometrical and spectral distributions of this incoming and outgoing light are governed by the radiative transfer equation and depend on the optical properties of water, its constituents, processes at the air-sea interface and incident radiance distribution. Two basic radiometric parameters that are commonly used to describe the spectral distribution of the light field are radiance and irradiance. Further explanations and definitions of these radiometric parameters can be found in Mueller et al (2003), Mobley (1994) and Preisendorfer (1976).

In general, radiance L (μW cm^{-2} sr^{-1}) is defined as the radiant flux per unit solid angle from direction (θ, ϕ), per unit area normal to the direction of the flux.

$$L(\theta, \phi) = \frac{d^2\Phi}{d\varpi dA \cos\theta} \qquad 1.1$$

where $d\varpi$ in steradians is an element of solid angle in the specified direction and θ is the angle between this direction and normal to a specified point on a flat surface. Radiance is thus, a function of both position and direction (Figure 1.1).

Irradiance E (μW cm^{-2}) can be defined as the radiant flux (ϕ) per unit area (A) through any point on a horizontal surface in the hemisphere above the surface (Mueller et al, 2003).

$$E\ (\mu W\ cm^{-1}) = \frac{d\Phi}{dA} \qquad 1.2$$

where $d\Phi$ is the element of radiant flux and dA is the element of area at the surface. Thus, irradiance can be regarded as a function of position on a specified surface (Figure 1.1).

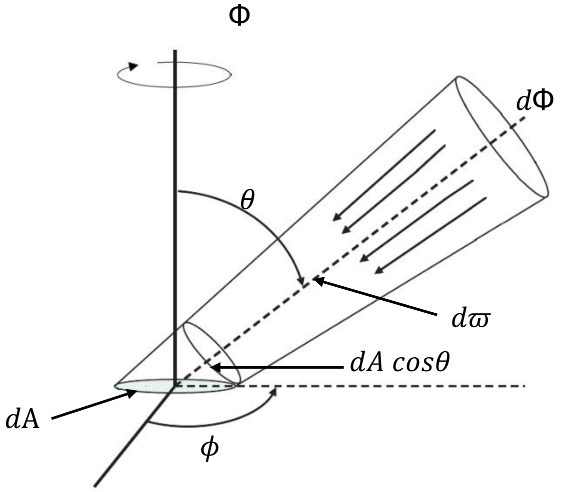

Figure 1.1: The radiance concept

In ocean optics, irradiance can be further divided into a vector and scalar quantity. Vector irradiance describes the total radiant intensity incident on a plane surface (from all directions either above or below it) whilst, scalar irradiance is the total radiant intensity impinging on a spherical surface. Both irradiances can be a measure of either an upward or a downward flux of light. These two measures are the values on the upper (i.e. facing zenith) and lower (i.e. facing nadir) faces (Figure 1.2), respectively, on a horizontal surface. The vector irradiances, downwelling E_d and upwelling E_u components can be defined as an integral of the radiance (L) in a spherical coordinated system by:

$$E_d = \int_{2\pi} L(\theta, \varphi)\cos(\theta)\, d\omega$$

$$E_u = -\int_{-2\pi} L(\theta, \varphi)\cos(\theta)\, d\omega \qquad 1.3$$

where the negative sign before the second integral is used to force E_u to be positive. Similarly, the scalar irradiances, downwelling E_{od} and upwelling E_{ou} components, are described as integral of radiance distribution over the upper or lower hemisphere, respectively.

$$\begin{aligned} E_{od} &= \int_{2\pi} L(\theta,\varphi)d\omega \\ E_{ou} &= \int_{-2\pi} L(\theta,\varphi)d\omega \end{aligned} \qquad 1.4$$

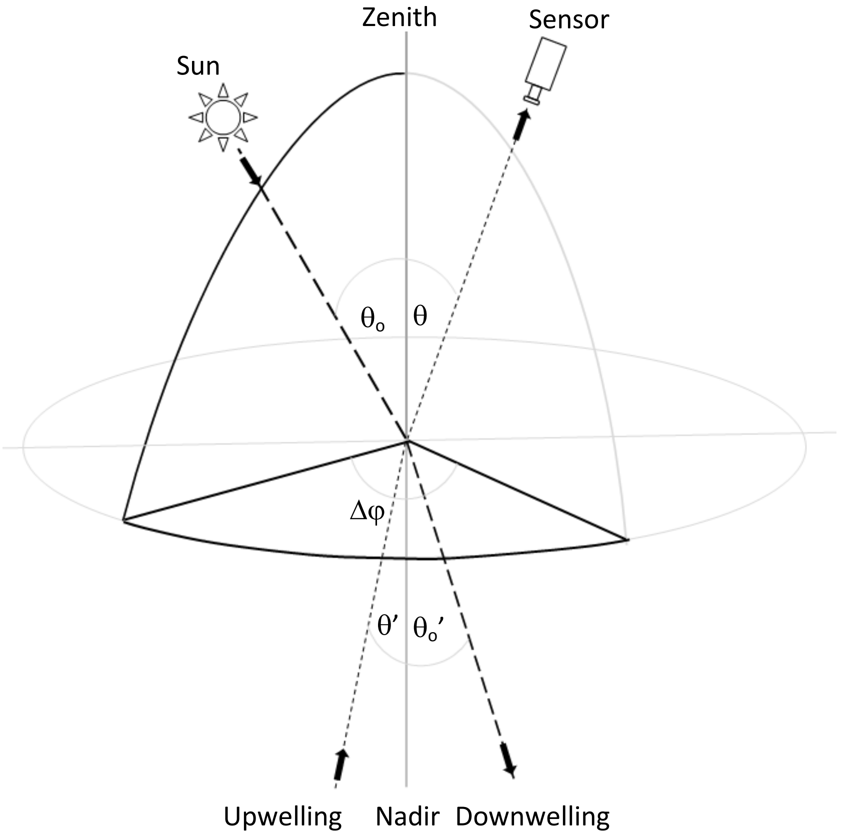

Figure 1.2: Angles used to define the radiation light field.

1.3.1 Apparent Optical Properties (AOPs)

As mentioned earlier, AOPs are the optical properties dependent upon the spatial distribution of the incident radiation and they are commonly used to represent the intrinsic colour of the ocean. Commonly used and measured AOPs in ocean colour studies are reflectance (irradiance and remote sensing reflectance), water leaving radiance and diffuse attenuation coefficient. The irradiance reflectance or spectral hemispherical reflectance $R(z,\lambda)$ is the dimensionless quantity measured at depth z, denoting the ratio of upward and downward irradiance and is given by.

$$R(z,\lambda) = \frac{E_u(z,\lambda)}{E_d(z,\lambda)} \qquad 1.5$$

The $R(z,\lambda)$ value just below the water surface (z=0), $R(0^-,\lambda)$ is determined using the extrapolation of the log-transformed $E_u(0^-,\lambda)$ and $E_d(0^-,\lambda)$ measured at various depths to z=0.

The remote sensing reflectance, $R_{rs}(\lambda)$ in sr^{-1} is defined as the ratio of water leaving radiance to the downward irradiance just above the water surface ($z=0^+$) and is given by:

$$R_{rs}(\lambda) = \frac{L_w(\lambda)}{E_d(0^+,\lambda)} \qquad 1.6$$

where the water leaving radiance $L_w(\lambda)$ in μW cm^{-2} sr^{-1} nm^{-1} is the radiance leaving the water and quantified just above the water surface; $E_d(0^+,\lambda)$ in μW cm^{-2} nm^{-1} is the downward irradiance just above the water surface. $L_w(\lambda)$ can be calculated by:

$$L_w(\lambda) = L_u(0^+,\lambda) = L_u(0^-,\lambda) \text{ x } \left(\frac{1-\rho}{\eta_w{}^2}\right) \qquad 1.7$$

where $L_w(0^+,\lambda)$ is the upwelling radiance just above the surface; $L_u(0^-,\lambda)$ is the upwelling radiance just below the surface extrapolated from $L_u(z,\lambda)$ at multiple depths z; ρ is the Fresnel reflectance of the air-sea interface (0.021); η_w is the refractive index of seawater. For η_w equal to 1.345 and the incident angle θ less than 30°, the reflectance is practically constant and the transmittance (1-ρ) is equal to 0.98 (Mobley, 1994). According to Mobley (1994), for angles greater than 30°, the reflectance increases rapidly with ρ approaching 1 when θ for water-incident rays exceeds the critical angle of 48°. In our study, the zenith angle of water leaving radiance is less than 30° (16 to 30° of sun zenith angle) and thus, the transmittance, (1-ρ) has been set to 0.98.

The normalized water leaving radiance which was first introduced by Gordon and Clark (1981) is the variable of most interest in the remote sensing of ocean colour. The normalization process removes the effects of illumination conditions dependent of the sun zenith angle and the atmospheric transmittance (Mueller and Austin, 1995). The normalized water leaving radiance $L_{wn}(\lambda)$ is then given by:

$$L_{wn}(\lambda) = L_w(\lambda) \text{ x } \frac{F_o(\lambda)}{E_d(0^+,\lambda)} = R_{rs}(\lambda) \text{ x } F_o(\lambda) \qquad 1.8$$

where $F_o(\lambda)$ is the mean extraterrestrial solar irradiance. Another parameter that depends on solar zenith angle θ_o is the angular distribution factor of spectral radiance, Q (Austin, 1974; Morel and Gentili, 1996). Its precise determination is of important in ocean colour studies especially when comparing different ocean colour sensors at different times and under different view angles. The Q factor (unit sr) relates upwelled spectral radiance to upwelled spectral irradiance at $z=0^-$ (see Figure 1.2 for the angle terms).

$$Q(\theta_o, \theta', \Delta\varphi) = \frac{E_u(\theta_o)}{L_w(\theta_o, \theta', \Delta\varphi)} \qquad 1.9$$

Considering the optical properties of case I waters and solar and viewing angles typical of those involved in satellite ocean colour observation, Q may vary between 3 and 5 (Morel et al., 1995). However, for most case-2 waters, it may vary between 2.4 and 5.6 (Bukata, 2005).

1.3.2 Inherent Optical Properties (IOPs)

Specifically, the IOPs characterize how a light field propagates through a given point in the medium and quantify the net loss of light by absorption and scattering. The most important IOPs of natural waters are the absorption coefficient a, and the scattering coefficient b. The sum of these two coefficients is the beam attenuation coefficient c, given as.

$$\mathrm{c} = \mathrm{a} + \mathrm{b} \qquad 1.10$$

All these coefficients are measured as fraction of light (either absorbed or scattered) per unit distance in a participating medium and expressed in units of m^{-1}. As schematically illustrated in Figure 1.3, absorption and scattering occur when a narrow collimated monochromatic beam of light with spectral radiant flux, $\Phi_i(\lambda)$, propagates in a volume of water, ΔV, with thickness, Δr. During this process, some incident light is absorbed $[\Phi_a(\lambda)]$, some $\Phi_i(\lambda)$ is scattered out of the direction of the beam at an angle, Ψ, $[\Phi_s(\lambda)]$, and the remaining fraction propagate in the same direction as the beam and is transmitted $[\Phi_t(\lambda)]$ through the volume. For the scattering process, only an elastic scattering is assumed to occur. Theoretical explanations of absorption and scattering can be found in Mobley (1994) and Wozniak and Dera (2007).

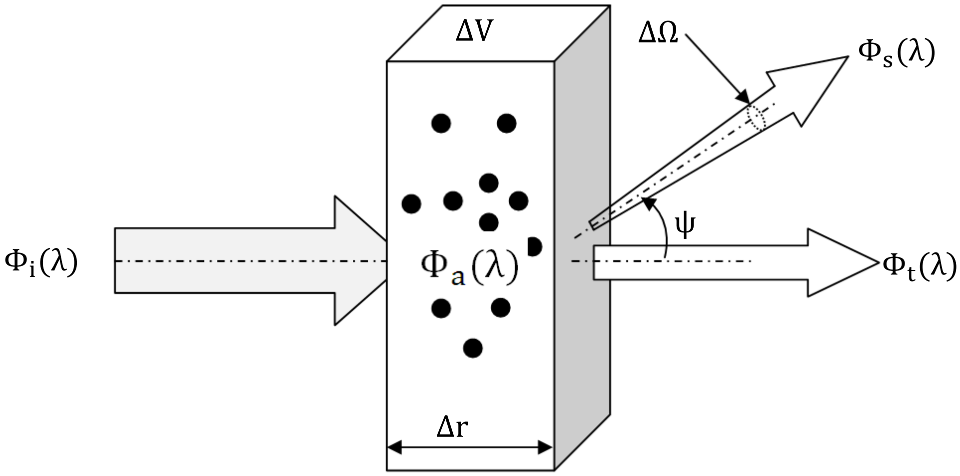

Figure 1.3: Geometry used to define IOPs. After Mobley (1994)

The fraction of incident light that is absorbed per unit distance Δr within the volume is absorption coefficient $a(\lambda)$ and is given by:

$$a(\lambda) = \frac{\Phi_a(\lambda)/\Phi_i(\lambda)}{\Delta r} = \frac{A(\lambda)}{\Delta r} \qquad 1.11$$

The fraction of incident light that is scattered out of the beam is known as scattering coefficient and is given by:

$$b(\lambda) = \frac{\Phi_s(\lambda)/\Phi_i(\lambda)}{\Delta r} = \frac{B(\lambda)}{\Delta r} \qquad 1.12$$

The beam attenuation coefficient is a sum of $a(\lambda)$ and $b(\lambda)$ and is calculated as:

$$c(\lambda) = \frac{\Phi_t(\lambda) - \Phi_i(\lambda)}{\Phi_i(\lambda)\Delta r} = \frac{A(\lambda) + B(\lambda)}{\Delta r} \qquad 1.13$$

where $A(\lambda)$, $B(\lambda)$ and $T(\lambda)$ are the spectral absorptance, scatterance and transmittance, respectively. Their standard unit is percent or a factor between 0 and 1.

a) Absorption

The absorption coefficient of natural waters depends on the amount and types of individual particles in the water as well as the wavelength of light incident upon them. Because of the optical independence of the individual particles, absorption of natural water is the sum of the contributions of phytoplankton, non-pigmented particulate or detritus, dissolved organic matter and the pure water itself. The absorption of natural waters or so-called total absorption coefficient, a can be written as:

$$a = a_w + a_{ph} + a_d + a_g \qquad 1.14$$

where a_w, a_{ph}, a_d and a_g are denoted to absorption by pure water, phytoplankton, non-pigmented particulate or detritus and CDOM, respectively. Figure 1.4 presents example of the the shapes of absorption spectra of pure water etc. In general, pure water absorbs light very weakly in the blue and green regions of the spectrum, but absorption increases markedly towards both red and UV parts of the spectrum. The most widely used a_w datasets are by Smith and Baker (1981) and Pope and Fry (1997) with the latter absorption values is regarded as one of the most reliable set in the visible wavelengths (Zhao et al., 2002). In this study, we will use the a_w values from Pope and Fry (1997) as their work is more recent.

Phytoplankton pigments which, are the basis of oceanic photosynthesis, are strong absorbers of visible light. The absorption spectrum of phytoplankton typically has two distinct absorption peaks, one near 440 nm and another around 675 nm both of which are produced by chlorophyll-a. Other pigments such as chlorophyll-b, chlorophyll-c and carotenoids usually show some smaller absorption maxima at wavelength between 460 and 650 nm (Kirk, 1994). Detritus and CDOM are strong absorbers in the blue and absorption exponentially decreases with wavelength. Since detritus and CDOM exhibit similar spectral shapes, they are typically modeled together (Roesler, 1998). In coastal waters, CDOM absorption can be significant at all wavelengths and may reduce the light availability to phytoplankton.

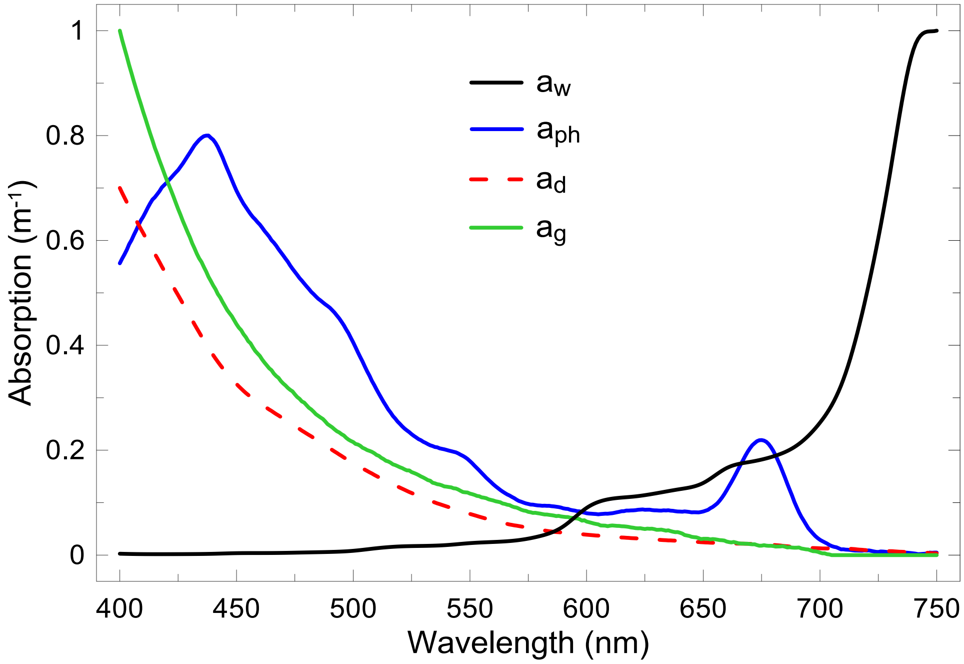

Figure 1.4: Qualitative comparison of the shapes of absorption spectra of pure water (a_w), phytoplankton (a_{ph}), detritus (a_d) and CDOM (a_g).

b) Scattering

The scattering coefficient, b is divided into two parts; forward, b_f and backward scattering, b_b.

$$b = b_f + b_b \qquad 1.15$$

Forward and backscattering coefficients can be derived by the angular ranges $0 \le \theta \le \pi$ (0° to 180°) and $\pi/2 \le \theta \le \pi$ (90° to 180°) at a given zenith angle θ, respectively. Mathematically, they can be expressed as:

$$b_f = 2\pi \int_0^{\frac{\pi}{2}} \beta(\theta)\, sin(\theta)\, d(\theta) \qquad 1.16$$

$$b_b = 2\pi \int_{\frac{\pi}{2}}^{\pi} \beta(\theta)\, sin(\theta)\, d(\theta) \qquad 1.17$$

where β is the volume scattering function that describes the directional dependence of this scattering. The backscattering coefficient is important in remote sensing but it is very difficult to measure. It is often assumed to be constant proportional to total scattering ($b_b \approx 0.019b$) based on a study of Petzold (1972), although it can vary considerably depending on the water type. The backscattering coefficient of natural water can be separated into contributions from pure water, b_{bw} and particles, b_{bp}.

$$b_b = b_{bw} + b_{bp} \qquad 1.18$$

The particle backscattering, b_{bp} can be due to living (phytoplankton) and non-living (mineral) particulates suspended in the water. The scattering by CDOM is neglected in most applications (Pozdnyakov and Grassl, 2003) due to the small size of CDOM molecules relative to the wavelength of visible light and is set to zero. In general, the spectral shape and magnitude of b_{bp} is primarily determined by the concentration of particles, their shape, index of refraction and the particle size distribution. Accurate b_{bp} determinations are importance for the interpretation of remotely sensed signals since the upwelling radiance exiting the ocean is directly proportional to this parameter and inversely proportional to the absorption coefficient.

1.3.3 Relating AOPs and IOPs

Determination of the relationships between AOPs and IOPs is essential for developing quantitative radiative transfer models of spectral irradiance in the ocean (Kirk 1994; Mobley 1994). Radiative transfer models describe the propagation of light within the ocean and thus provide a mathematical solution for linking the known IOPs and spectral radiance distribution to the AOPs of the water column. In ocean colour studies, the conversion of remotely sensed data in terms of water leaving radiance into geophysical data products requires the accurate relationships between these data products and AOPs through in-situ measurements of IOPs.

The most commonly used expression relating irradiance reflectance, R to IOPs was introduced by Gordon et al. (1975).

$$R = f\frac{b_b}{a} \quad for\ b_b \ll a \qquad 1.19$$

where f is a dimensionless factor which varies between 0.3 and 0.5, depending on the sun zenith angle (Kirk, 1984; Gordon, 1989) and the inherent optical properties (Morel and Ahn, 1991; Morel and Gentili, 1996). The condition $b_b << a$ usually holds for most oceanic waters where the water itself contributes more to backscattering than the suspended particles. However, this condition may not hold in coastal waters where backscattering by particles are the major contributor to total backscattering. In this case, equation 1.19 is replaced by (Gordon et al., 1975)

$$\mathrm{R} = \mathrm{f}\frac{\mathrm{b_b}}{\mathrm{b_b} + \mathrm{a}} \qquad 1.20$$

By combining equations 1.9 and 1.2, Gordon et al., 1988 also show that the remote sensing reflectance, R_{rs} are related to IOPs:

$$\mathrm{R_{rs}} = \frac{\mathrm{L_w}(\theta_0, \theta', \Delta\varphi)}{\mathrm{E_d}(\theta_0)} = \frac{\mathrm{f}(\theta_0)}{\mathrm{Q}(\theta_0, \theta', \Delta\varphi)}\left(\frac{\mathrm{b_b}}{\mathrm{b_b} + \mathrm{a}}\right) \qquad 1.21$$

The ratio f/Q has been shown to less dependent than either f or Q alone and its values range between 0.09 and 0.12 sr^{-1} for homogenous case-1 waters (Morel and Gentili, 1993).

1.3.4 Bio-optical models

Retrievals of in-water constituents from satellite measurements of water leaving radiance has been studied extensively since the launch of the first ocean colour satellite, the coastal zone colour scanner (CZCS) in the late 1970's (O'Reilly et al., 1998). Since then, many studies have focused on developing techniques for estimating in-water constituents especially phytoplankton chlorophyll concentration from ocean colour imagery. In the estimation of chlorophyll and other bio-optical properties, empirical (Clark, 1981, 1994; Gordon and Morel, 1983; Aiken et al., 1995; O'Reilly et al., 1998; Kahru, 1998) and semi-analytical approaches (Gordon et al., 1988; Morel, 1988; Garver and Siegel, 1997; Carder et al., 1999; Lee et al., 2002) have been used extensively over the past decades. Although most of these algorithms are applied globally, it is recognized that there is no universal bio-optical algorithm applicable to all water types and ocean areas. This is due to the inherent variability of many bio-optical constituents that vary with region and season.

a) Band ratio algorithms

The most common empirical ocean colour algorithms are based on assumption that the ratio of the spectral reflectances at two wavelengths is a known function of the chlorophyll concentration. Using the ratio of the reflectance in the blue and green parts of the spectrum, a simple log-linear equation can be used to estimate the phytoplankton pigment concentration. The functional form of the band ratio algorithms is given by:

$$\log_{10}[\mathrm{Chl}] = \sum_{i=0}^{M} a_i R^i \qquad 1.22$$

where R is the $\log_{10}$ ratio of reflectances at specific wavelengths, a is determined empirically from a regression between the radiance ratio and chlorophyll concentration, [Chl] and M varying 1 (first order) to 4 (fourth order). In general, the band ratio algorithms provide a good estimation of chlorophyll concentration in case-1 water, where their efficacy relies on the assumption that other non-pigmented materials (dissolved organic matter and detritus) are highly correlated with chlorophyll. Typically, these algorithms are valid only for data having the same optical properties to those datasets used for the determinations of the coefficients (Sathyendranath, 2000). Therefore, they are particularly sensitive to changes in composition of water constituents that vary accordingly to region and season.

In case-2 water, where radiance at a given wavelength includes contributions by materials other than chlorophyll, the band ratio algorithms are no longer appropriate. In this water, reflectance in the blue spectral range is almost insensitive to changes in chlorophyll due to the strong absorption by dissolved organic matter and detritus (Ruddick et al., 2001). Even though, some attempts have been made for the estimation of chlorophyll in case-2 waters using the absorption wavelength of phytoplankton in the red and near-infrared spectral regions (e.g., Gitelson and Kondratyev 1991; Gitelson 1992; Dekker 1993; Ruddick et al. 2001), the band ratio algorithms do not always work well for this category of waters (Darecki and Stramski, 2004).

The operational band ratio algorithms, SeaWIFS OC4-v6 and MODIS OCM3-v6 that are used in this study, have been developed from the most spatially extensive set of bio-optical measurements of NASA SIMBIOSIS project (Fargion and McClain, 2001) and comprises of some 2,853 sets of measurements, with chlorophyll values between 0.01 and 90 mg m^{-3} (O"Reilly et al., 2000). The OC4 model is a modified cubic polynomial that relates a band ratio to chlorophyll concentration based on whichever reflectance ratio, R_{rs}(443/547), R_{rs}(488/547) or R_{rs}(510/547) is the most dominant (O'Reilly et al., 2000). The MODIS OCM3 (Carder et al., 1999) is a SeaWIFS analogue and takes the same form as the OC4 model. However, as MODIS lacks a 510 nm band used in the OC4 algorithm, it utilizes only the maximum of two band ratios [R_{rs}(443/547) and R_{rs}(488/547)].

b) Semi-analytical algorithms

Semi-analytical algorithms are based on theoretical relationships between reflectance measured by the satellite and inherent optical properties (absorption and scattering coefficients) of the water. The algorithms utilize an analytical approach by relating water reflectance and IOPs through radiative transfer theory and the approximation of R_{rs} as in equation 1.21. The spectral reflectance model is inverted to derive chlorophyll and IOPs (absorption or backscattering coefficients) of other optically active substances (non-pigmented particulate matter and CDOM) that do not covary with chlorophyll. However, several terms used in the radiative transfer model such as backscattering, chlorophyll-a specific absorption coefficient or spectral shapes of detrital absorption are parameterized using empirical relationships (O`Reilly et al, 1998). In that sense, the algorithm is termed as semi-analytic. Because these algorithms separately retrieve chlorophyll and CDOM, they have been proposed for use in case-2 waters.

Although these models and their inversion account for all optically active substances and primarily target case-2 waters, they are more sensitive to errors in water leaving radiance than band ratio algorithms that do not have forward and inverse components (IOCCG, 2000). In coastal waters, where bio-optical properties are complex, the relationship between water reflectance and IOPs behaves as a non-linear function of the concentration of the relevant substance. Any incorrect assumptions or inaccurate parameters will introduce significant errors in the forward model and thus will cause significant variation in the predicted substance concentration. The theoretical approach of the semi-analytical model was first introduced by

Gordon et al (1988) and Morel (1988) for case-1 waters. In their work, the functional dependency of the diffuse attenuation coefficient and chlorophyll concentration was used as a base to invert the reflectance model. Since then, numerous semi-analytical solutions have been proposed for the retrieval of constituent concentrations as well as optical properties of water (Garver and Siegel, 1997; Carder et al, 1999; Lee et al, 2002).

The semi-analytical MODIS algorithm by Carder et al., (1999) was purposely developed to derive chlorophyll concentrations by separating the effects of the major absorption components, phytoplankton pigment and non-pigmented materials. One of the main characteristics of this algorithm is the adjustment of both chlorophyll-specific absorption coefficients and CDOM-detrital absorption coefficients for regional and temporal changes, hence reducing the typical errors of remote estimation of chlorophyll-a concentration in case-2 waters. The success of their algorithm however, depends on the classification of the bio-optical domains that is based on the relationship between sea surface temperature (SST) and nitrate depletion temperature (NDT). The NDT is the surface temperature for a given oceanic location above which the nitrate concentration becomes negligible (Kamykowski, 1987). This is based on the inverse relationship between nutrients (nitrate, phosphate and silicate) and temperature which ultimately affects phytoplankton growth, biomass and species composition. This relationship occurs seasonally in surface water to varying degrees depending on geographic location and can be used to show a place where a major transition in the types of phytoplankton is occurring. In general, a large size class of phytoplankton coincides with a supply of nitrate while a small size class predominates in nitrate-depleted waters (Carder et al., 1999).

The bio-optical domains with different values for the empirical parameters are classified into (1) unpackaged – high ratios of photoprotective pigments to chlorophyll and low self-shading, (2) packaged – low ratio and self-shading and (3) transitional or global average type. In the semi-analytical equations, the model is inverted to solve for two unknown variables, phytoplankton absorption at 675 nm and coloured detrital matter (detritus and CDOM) at 400 nm as a function of ratios of observed remote sensing reflectances. Chlorophyll concentration is then derived from an empirical relationship with $a_{ph}(676)$. However, this semi-analytical model is only valid for oligotrophic waters where chlorophyll concentration does not exceed 2.0 mg m^{-3}. For larger values of chlorophyll concentration, an empirical algorithm of Aiken et al., (1995) is used to derive chlorophyll concentration. Carder et al., (1999) claim that the performance of their semi-analytical algorithm is comparable with the empirical approach for all water types (case-1 and case-2) and the accuracy of the algorithm can be further increased if the data is adjusted into appropriate bio-optical domains. However, they also found that the algorithm tended to overestimate the chlorophyll by a factor of two in upwelling and high-latitude regions.

Lee et al., (2002) developed a multiband quasi-analytical algorithm (QAA) based on the Carder model. As is the case for many other inversion algorithms, the QAA is purposely developed to separate the contribution of phytoplankton and CDOM absorption coefficients from the total absorption coefficient for deriving chlorophyll and CDOM concentrations. However, unlike the conventional semi-analytical algorithm, QAA does not need a priori knowledge of the spectral shape of phytoplankton absorption. One of the advantages of this algorithm is that it is easy to model with relatively simple mathematics and its stepwise derivation concept allows the effect of uncertainties of each variable to be evaluated at each level. Briefly, the QAA employs a series of analytical, semi-analytical and empirical equations to convert R_{rs} to total absorption and backscattering coefficients in two analytical steps. The first step involves a derivation of total absorption and particulate backscattering coefficients at a specific reference wavelength from remote sensing reflectance. Lee et al., (2002) proposed two reference wavelengths, 555 nm for oceanic water (case-1) and 640 nm for high-absorbing coastal waters (case-2). A combination of results at 555 nm and 640 nm is also proposed for both case-1 and case-2 waters. In the second step, phytoplankton and CDOM absorption coefficients are spectrally decomposed from the derived total absorption coefficient by relating them to their spectral ratios at 412 and 443 nm. Therefore, the accuracy of both absorption coefficients depends not only on the accuracy of derived $a(\lambda)$, but also on their spectral dependencies. The equations of the semi-analytical and QAA can be found in Appendices A and B, respectively.

1.4 Thesis aims and structure

This research is motivated by interest in understanding the marine optical environment in east coast of Peninsular Malaysia. The study is not only important in many aspects of oceanography but also can be used to characterize the ecologically and economically important marine resources at large temporal and spatial scales. In this context, satellite ocean color offers enormous potential for fisheries applications and other environmental problems associated with fisheries such as harmful algal bloom and coastal pollution. Because the satellite is the only biological measurement and fish production and stock depend greatly on production of plankton, there is a large scale relationship either directly or indirectly between the satellite chlorophyll and fish feeding locations. The fishery sector in Malaysia has for decades been playing a significant role in national economy and contributes nearly 1.5% to the national Gross Domestic Product (GDP) (Department of Fisheries Malaysia, 2010). This sector is also a source of employment, foreign exchange and a major supplier (60% - 70%) of animal protein to the Malaysian population. With continued growth in population, intensive exploitation of the coastal resource and under-exploited deep-sea fishing (Mohd Mazlan, 1998), demand for fish in this country is expected to increase beyond its current supply. Under the Third National Agricultural Policy 1998-2010 (NAP3), the government is putting up effort to increase fish production by promoting exploration of offshore marine resources by means of modern technology. The use of satellite ocean colour could facilitate this effort to further explore potential fishing zone in Malaysia Exclusive Economic Zone (EEZ) by reducing search time for locating fish sites and operating costs for fishing vessels, thereby increases catch per unit effort. Although other oceanic conditions such as sea surface temperature (SST), salinity, ocean currents and wind speed are also important to identify the potential fishing grounds, the accurate estimation of satellite chlorophyll is the key success factor to fully utilize ocean colour satellite systems for fisheries applications. In order to confidently use satellite ocean colour, validation exercises and applicability of ocean colour models need to be conducted to ascertain accuracy and limitations. Therefore this study can make a significant contribution by providing detailed information on the potential and suitability of satellite ocean colour for operational oceanography for Malaysian waters.

The overall aim of this work is to assess the potential use of ocean colour imagery for deriving chlorophyll and CDOM concentrations in east coast of Malaysian waters. We shall do this by making in-situ measurements, and of remote sensing reflectance during different seasons and at different locations. Our specific objectives are.

1. to characterize and assess the variability of bio-optical properties for different monsoon seasons.
2. to assess the suitability of the standard global ocean colour algorithms in providing accurate water colour parameters.
3. to evaluate and improve the algorithms by which the ocean colour can be used to estimate water colour parameters in the study area.
4. to characterize the seasonal and inter-annual variations in chlorophyll and CDOM concentrations using the newly developed algorithms.

This thesis starts with the methodological approach of the research design on which this work is based in chapter 2. In this part, the in-situ method used for retrieval of in-water constituents and absorption properties are presented. In addition, the oceanographic conditions of the study area are also described. In chapter 3, the results of oceanographic conditions and bio-optical properties made during extensive field campaigns in 2009 are presented. The objective in this part of the research is to assess the magnitude of spatial and temporal variability of in-water optical properties for different seasons. For comparison, the results are grouped into three different seasons; southwest monsoon, northeast monsoon and inter-monsoon. In this part, the dependence of optical properties with respect to hydrological parameters and in-water constituents are also presented and compared with results from previous studies. The results in this chapter have been submitted in the International Journal of Remote Sensing. Chapter 4 focuses on the relationships of in-water constituents and optical properties with remote sensing reflectance. First, the MODIS-derived remote sensing reflectances are compared with those measured in-situ. Then, the applicability of the chlorophyll and some of the inherent optical properties algorithms used by MODIS satellite data and algorithm performance is assessed and causes of the variations in performance are discussed. In this part, several empirical algorithms for chlorophyll and absorption properties retrieval are proposed and discussed. Chapter 5 utilizes the algorithms developed in chapter 4 to estimate in-waters constituents and several absorption properties from monthly composite of satellite MODIS data. In this part, the inter-annual variability in water colour is discussed. In chapter 6, the major findings of the research from chapters 3 to 5 are critically discussed and summarized. It provides the conclusions and gives an overview on the prospects, ideas and challenges for future research direction in this field of study.

CHAPTER 1

BACKGROUND

1.1 Introduction to ocean colour remote sensing

The colour of the ocean depends upon the interaction of incident light with the various substances present in the water. The amount and type of substance controls the quantity and colour of the incoming light energy that can penetrate through the water column and scatter out of the water. The two key optical processes involved during the interactions of incident light with substances in the water column are absorption and scattering. Preisendorfer (1961) defines the absorption and scattering coefficients of seawater as inherent optical properties (IOPs) since their magnitude is characterized only by the behaviour of electromagnetic radiation in the medium but not by the intensity or angular distribution of ambient light. In contrast, the part of the incoming light that is returned back toward its source, depends both on the medium (IOPs) and on the geometry of ambient light within the water column. The "remote sensing reflectance, R_{rs}", is classified by Preisendorfer (1961) as apparent optical properties (AOP). Generally, the optically active constituents of the water can be represented by broadly defined substances such as phytoplankton, dissolved organic matter and suspended inorganic sediments. The relative amount of these substances in the water is used to classify the types of water, either as case-1 or case-2 (Morel and Prieur, 1977).

Since the water leaving radiance depends on the medium, there exists a clear relationship between ocean colour and in-water constituents. Investigating the spectral signals associated with the interactions of light with various underwater substances constitutes basic research in oceanic remote sensing. Knowledge of the variability of bio-optical properties of the water constituents and the radiative transfer through the water column and atmosphere as a function of the water constituents enables their derivation through remote sensing. In ocean remote sensing, there are 2 approaches to formulate this derivation from measured R_{rs}, one is empirical, and the other is analytical.

The empirical approach uses strong absorption (principally in the blue bands) and low absorption (in the green) of chlorophyll contained in phytoplankton. This difference in absorption is the basis for the empirical approach in estimating chlorophyll concentration from the early periods of ocean colour remote sensing i.e. Coastal Zone Colour Scanner (Gordon et al., 1983) until the current satellite sensor of MODIS (O'Reilly et al., 2000). Whilst the empirical approach for the retrieval of chlorophyll in case 1-water (open ocean) has proven successful (Gitelson et al., 2007; Darecki and Stramski, 2004; Carder et al., 1999), interpretation of ocean colour data in optically complex case-2 waters (coastal water) is more difficult and has been shown to have poor predictability (Dall'Olmo et al., 2005; Gons, 1999; Schalles, 2006). The analytical approach based on the radiative transfer theory tackles this problem by deriving the magnitude of each IOP component from the spectral observations of ocean colour. The performance of this approach, however, relies on accurate parameterization in the spectral models for absorption coefficients of each constituent present in the water. The analytical approach has evolved considerably in the last 25 years, since the work by Gordon et al., (1988) and Morel (1988). Since then, there have many applications of a semi-analytical algorithm for the retrieval of constituents concentration as well as optical properties of water (e.g., Garver and Siegel, 1997; Carder et al., 1999, 2004; Lee et al., 2002; Chomko et al., 2003). However, significant difficulties remain, mainly because it is not easy to accurately express the change of each optical property of constituent in a wide range of water types.

In general, operational ocean colour algorithms either empirical or semi-analytical, show relatively variable performance depending on the region, season and type of water (e.g., O'Reilly et al., 1998; Darecki and Stramski, 2004; Carder et al., 2004). Since the interpretation of ocean colour data relates the optical properties to a single phytoplankton pigment index (chlorophyll) as indicator of primary production, any changes to the chlorophyll specific absorption coefficients of phytoplankton could result in errors in the chlorophyll estimation from remote sensing observation. As the chlorophyll specific absorption coefficient varies temporally and spatially as a consequence of differences in the composition, cell size and concentration of pigments (Morel and Bricaud, 1986; Sathyendranath et al., 1987; Bricaud et al., 2004), the success of remotely sensed estimates of chlorophyll concentration requires prior knowledge of this absorption property. Empirical and semi-analytical algorithms must be adjusted to account for the specific bio-optical properties of the local environment.

In this study, we seek to understand the spatial variability of the bio-optical properties of east coast Peninsular Malaysia waters over different seasons. While such studies have been relatively well documented in other South China Sea regions (e.g., Tang et al., 2004, Liu et al., 2002) no information regarding bio-optical properties is available in east coast of Peninsular Malaysia waters. Further, the study area is influenced strongly by seasonal atmospheric conditions (the monsoon) and thus, the optical properties of the waters are expected to vary with seasons. If this is the case, we would also expect that the current global chlorophyll algorithms would not work well when applying them to the study area. Therefore, the performance of these algorithms needs to be evaluated and assessed, and alternative or regionally tuned algorithms may need to develop for estimating chlorophyll concentration in east coast of Peninsular Malaysia waters

1.2 Case-1 and Case-2 waters

The optical properties of ocean waters can vary significantly amongst different aquatic environments and is greatly influenced by a variety of physical, biological and chemical processes in the ocean. In optical oceanography and for modeling purposes, water bodies that have similar optical behaviour are often described by similar bio-optical models. The dependence of optical properties on water constituents is generally simplified into case-1 and case-2 waters.

Case-1 waters are those waters whose optical properties are determined primarily by phytoplankton and its related co-varying decay products of biological origins such as detritus and coloured dissolved organic matter (Gordon and Morel, 1983). Several studies (Morel and Ahn, 1990, 1991; Stramski and Kiefer, 1991) have shown that a number of heterotrophic organisms like flagellates, bacteria and viruses that co-exist with phytoplankton can also influence the optical properties of case-1 waters. In these waters, the contribution of other substances is relatively small and can be modeled as a function of phytoplankton concentration (Sathyendranath, 2000). Although it does not always hold as a good assumption, open ocean waters are generally considered as case-1 type. In case-2 waters, other substances which do not always covary with the phytoplankton pigment, significantly contribute to the optical properties of water body. Such substances include coloured dissolved organic matter (CDOM) contained in land runoff and suspended organic particles, are not related to the phytoplankton decay products. In these waters, absorption due to pigments may be a less important factor in determining variations in the optical properties of the water. Case-2 waters are typically coastal or near-shore.

1.3 Marine Optics: Concept and theory

Marine optics is the quantitative study of light propagation through seawater and its interactions with molecules and particles present in water. The geometrical and spectral distributions of this incoming and outgoing light are governed by the radiative transfer equation and depend on the optical properties of water, its constituents, processes at the air-sea interface and incident radiance distribution. Two basic radiometric parameters that are commonly used to describe the spectral distribution of the light field are radiance and irradiance. Further explanations and definitions of these radiometric parameters can be found in Mueller et al (2003), Mobley (1994) and Preisendorfer (1976).

In general, radiance L (μW cm^{-2} sr^{-1}) is defined as the radiant flux per unit solid angle from direction (θ, ϕ), per unit area normal to the direction of the flux.

$$L(\theta, \phi) = \frac{d^2\Phi}{d\varpi dA\cos\theta} \qquad 1.1$$

where $d\varpi$ in steradians is an element of solid angle in the specified direction and θ is the angle between this direction and normal to a specified point on a flat surface. Radiance is thus, a function of both position and direction (Figure 1.1).

Irradiance E (μW cm^{-2}) can be defined as the radiant flux (ϕ) per unit area (A) through any point on a horizontal surface in the hemisphere above the surface (Mueller et al, 2003).

$$E\,(\mu W\,cm^{-1}) = \frac{d\Phi}{dA} \qquad 1.2$$

where $d\Phi$ is the element of radiant flux and dA is the element of area at the surface. Thus, irradiance can be regarded as a function of position on a specified surface (Figure 1.1).

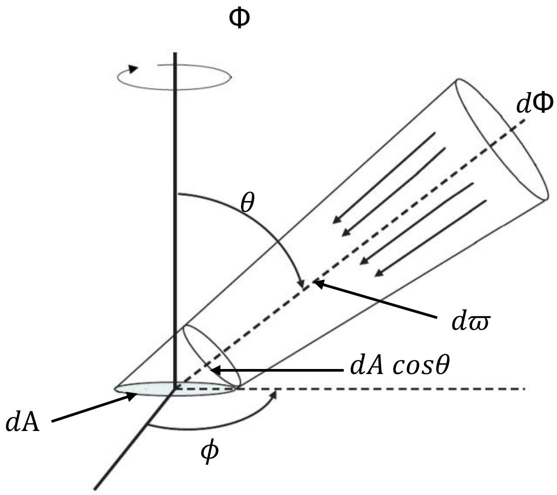

Figure 1.1: The radiance concept

In ocean optics, irradiance can be further divided into a vector and scalar quantity. Vector irradiance describes the total radiant intensity incident on a plane surface (from all directions either above or below it) whilst, scalar irradiance is the total radiant intensity impinging on a spherical surface. Both irradiances can be a measure of either an upward or a downward flux of light. These two measures are the values on the upper (i.e. facing zenith) and lower (i.e. facing nadir) faces (Figure 1.2), respectively, on a horizontal surface. The vector irradiances, downwelling E_d and upwelling E_u components can be defined as an integral of the radiance (L) in a spherical coordinated system by:

$$\mathrm{E_d} = \int_{2\pi} \mathrm{L}(\theta,\varphi)\cos(\theta)\,\mathrm{d}\omega$$

$$\mathrm{E_u} = -\int_{-2\pi} \mathrm{L}(\theta,\varphi)\cos(\theta)\,\mathrm{d}\omega \qquad 1.3$$

where the negative sign before the second integral is used to force E_u to be positive. Similarly, the scalar irradiances, downwelling E_{od} and upwelling E_{ou} components, are described as integral of radiance distribution over the upper or lower hemisphere, respectively.

$$E_{od} = \int_{2\pi} L(\theta, \varphi) d\omega$$

$$E_{ou} = \int_{-2\pi} L(\theta, \varphi) d\omega \qquad 1.4$$

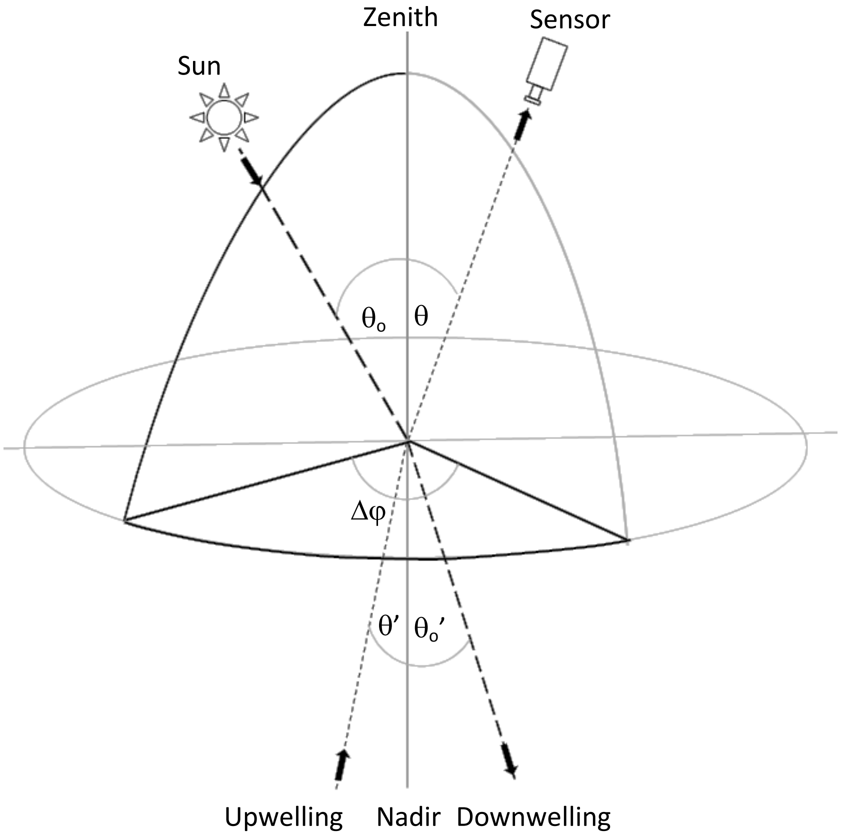

Figure 1.2: Angles used to define the radiation light field.

1.3.1 Apparent Optical Properties (AOPs)

As mentioned earlier, AOPs are the optical properties dependent upon the spatial distribution of the incident radiation and they are commonly used to represent the intrinsic colour of the ocean. Commonly used and measured AOPs in ocean colour studies are reflectance (irradiance and remote sensing reflectance), water leaving radiance and diffuse attenuation coefficient. The irradiance reflectance or spectral hemispherical reflectance $R(z,\lambda)$ is the dimensionless quantity measured at depth z, denoting the ratio of upward and downward irradiance and is given by.

$$R(z,\lambda) = \frac{E_u(z,\lambda)}{E_d(z,\lambda)} \qquad 1.5$$

The $R(z,\lambda)$ value just below the water surface (z=0), $R(0^-,\lambda)$ is determined using the extrapolation of the log-transformed $E_u(0^-,\lambda)$ and $E_d(0^-,\lambda)$ measured at various depths to z=0.

The remote sensing reflectance, $R_{rs}(\lambda)$ in sr^{-1} is defined as the ratio of water leaving radiance to the downward irradiance just above the water surface ($z=0^+$) and is given by:

$$R_{rs}(\lambda) = \frac{L_w(\lambda)}{E_d(0^+,\lambda)} \qquad 1.6$$

where the water leaving radiance $L_w(\lambda)$ in $\mu W\ cm^{-2}\ sr^{-1}\ nm^{-1}$ is the radiance leaving the water and quantified just above the water surface; $E_d(0^+,\lambda)$ in $\mu W\ cm^{-2}\ nm^{-1}$ is the downward irradiance just above the water surface. $L_w(\lambda)$ can be calculated by:

$$L_w(\lambda) = L_u(0^+,\lambda) = L_u(0^-,\lambda) \text{ x } \left(\frac{1-\rho}{{\eta_w}^2}\right) \qquad 1.7$$

where $L_w(0^+,\lambda)$ is the upwelling radiance just above the surface; $L_u(0^-,\lambda)$ is the upwelling radiance just below the surface extrapolated from $L_u(z,\lambda)$ at multiple depths z; ρ is the Fresnel reflectance of the air-sea interface (0.021); η_w is the refractive index of seawater. For η_w equal to 1.345 and the incident angle θ less than 30°, the reflectance is practically constant and the transmittance (1-ρ) is equal to 0.98 (Mobley, 1994). According to Mobley (1994), for angles greater than 30°, the reflectance increases rapidly with ρ approaching 1 when θ for water-incident rays exceeds the critical angle of 48°. In our study, the zenith angle of water leaving radiance is less than 30° (16 to 30° of sun zenith angle) and thus, the transmittance, (1-ρ) has been set to 0.98.

The normalized water leaving radiance which was first introduced by Gordon and Clark (1981) is the variable of most interest in the remote sensing of ocean colour. The normalization process removes the effects of illumination conditions dependent of the sun zenith angle and the atmospheric transmittance (Mueller and Austin, 1995). The normalized water leaving radiance $L_{wn}(\lambda)$ is then given by:

$$L_{wn}(\lambda) = L_w(\lambda) \text{ x } \frac{F_o(\lambda)}{E_d(0^+,\lambda)} = R_{rs}(\lambda) \text{ x } F_o(\lambda) \qquad 1.8$$

where $F_o(\lambda)$ is the mean extraterrestrial solar irradiance. Another parameter that depends on solar zenith angle θ_o is the angular distribution factor of spectral radiance, Q (Austin, 1974; Morel and Gentili, 1996). Its precise determination is of important in ocean colour studies especially when comparing different ocean colour sensors at different times and under different view angles. The Q factor (unit sr) relates upwelled spectral radiance to upwelled spectral irradiance at $z=0^-$ (see Figure 1.2 for the angle terms).

$$Q(\theta_o, \theta', \Delta\varphi) = \frac{E_u(\theta_o)}{L_w(\theta_o, \theta', \Delta\varphi)} \qquad 1.9$$

Considering the optical properties of case I waters and solar and viewing angles typical of those involved in satellite ocean colour observation, Q may vary between 3 and 5 (Morel et al., 1995). However, for most case-2 waters, it may vary between 2.4 and 5.6 (Bukata, 2005).

1.3.2 Inherent Optical Properties (IOPs)

Specifically, the IOPs characterize how a light field propagates through a given point in the medium and quantify the net loss of light by absorption and scattering. The most important IOPs of natural waters are the absorption coefficient a, and the scattering coefficient b. The sum of these two coefficients is the beam attenuation coefficient c, given as.

$$c = a + b \tag{1.10}$$

All these coefficients are measured as fraction of light (either absorbed or scattered) per unit distance in a participating medium and expressed in units of m^{-1}. As schematically illustrated in Figure 1.3, absorption and scattering occur when a narrow collimated monochromatic beam of light with spectral radiant flux, $\Phi_i(\lambda)$, propagates in a volume of water, ΔV, with thickness, Δr. During this process, some incident light is absorbed $[\Phi_a(\lambda)]$, some $\Phi_i(\lambda)$ is scattered out of the direction of the beam at an angle, Ψ, $[\Phi_s(\lambda)]$, and the remaining fraction propagate in the same direction as the beam and is transmitted $[\Phi_t(\lambda)]$ through the volume. For the scattering process, only an elastic scattering is assumed to occur. Theoretical explanations of absorption and scattering can be found in Mobley (1994) and Wozniak and Dera (2007).

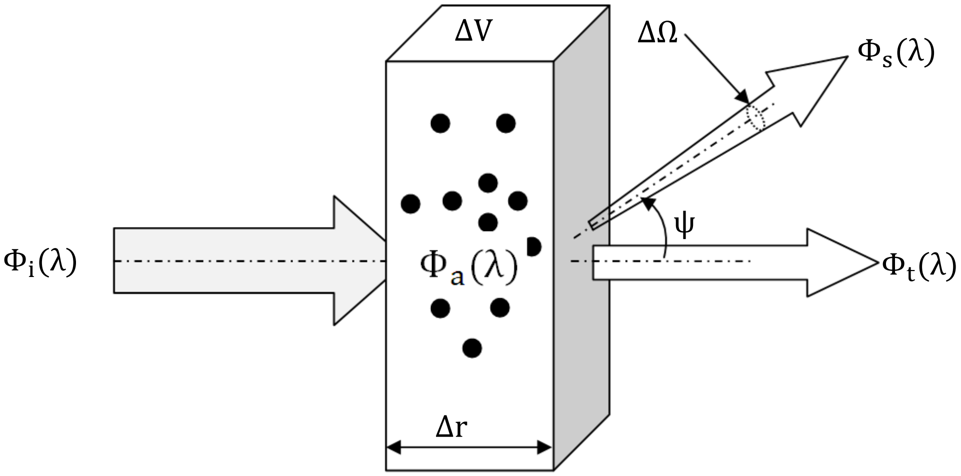

Figure 1.3: Geometry used to define IOPs. After Mobley (1994)

The fraction of incident light that is absorbed per unit distance Δr within the volume is absorption coefficient $a(\lambda)$ and is given by:

$$a(\lambda) = \frac{\Phi_a(\lambda)/\Phi_i(\lambda)}{\Delta r} = \frac{A(\lambda)}{\Delta r} \qquad 1.11$$

The fraction of incident light that is scattered out of the beam is known as scattering coefficient and is given by:

$$b(\lambda) = \frac{\Phi_s(\lambda)/\Phi_i(\lambda)}{\Delta r} = \frac{B(\lambda)}{\Delta r} \qquad 1.12$$

The beam attenuation coefficient is a sum of a(λ) and b(λ) and is calculated as:

$$c(\lambda) = \frac{\Phi_t(\lambda) - \Phi_i(\lambda)}{\Phi_i(\lambda)\Delta r} = \frac{A(\lambda) + B(\lambda)}{\Delta r} \qquad 1.13$$

where $A(\lambda), B(\lambda)$ and $T(\lambda)$ are the spectral absorptance, scatterance and transmittance, respectively. Their standard unit is percent or a factor between 0 and 1.

a) Absorption

The absorption coefficient of natural waters depends on the amount and types of individual particles in the water as well as the wavelength of light incident upon them. Because of the optical independence of the individual particles, absorption of natural water is the sum of the contributions of phytoplankton, non-pigmented particulate or detritus, dissolved organic matter and the pure water itself. The absorption of natural waters or so-called total absorption coefficient, a can be written as:

$$\mathrm{a} = \mathrm{a_w} + \mathrm{a_{ph}} + \mathrm{a_d} + \mathrm{a_g} \qquad 1.14$$

where a_w, a_{ph}, a_d and a_g are denoted to absorption by pure water, phytoplankton, non-pigmented particulate or detritus and CDOM, respectively. Figure 1.4 presents example of the the shapes of absorption spectra of pure water etc. In general, pure water absorbs light very weakly in the blue and green regions of the spectrum, but absorption increases markedly towards both red and UV parts of the spectrum. The most widely used a_w datasets are by Smith and Baker (1981) and Pope and Fry (1997) with the latter absorption values is regarded as one of the most reliable set in the visible wavelengths (Zhao et al., 2002). In this study, we will use the a_w values from Pope and Fry (1997) as their work is more recent.

Phytoplankton pigments which, are the basis of oceanic photosynthesis, are strong absorbers of visible light. The absorption spectrum of phytoplankton typically has two distinct absorption peaks, one near 440 nm and another around 675 nm both of which are produced by chlorophyll-a. Other pigments such as chlorophyll-b, chlorophyll-c and carotenoids usually show some smaller absorption maxima at wavelength between 460 and 650 nm (Kirk, 1994). Detritus and CDOM are strong absorbers in the blue and absorption exponentially decreases with wavelength. Since detritus and CDOM exhibit similar spectral shapes, they are typically modeled together (Roesler, 1998). In coastal waters, CDOM absorption can be significant at all wavelengths and may reduce the light availability to phytoplankton.

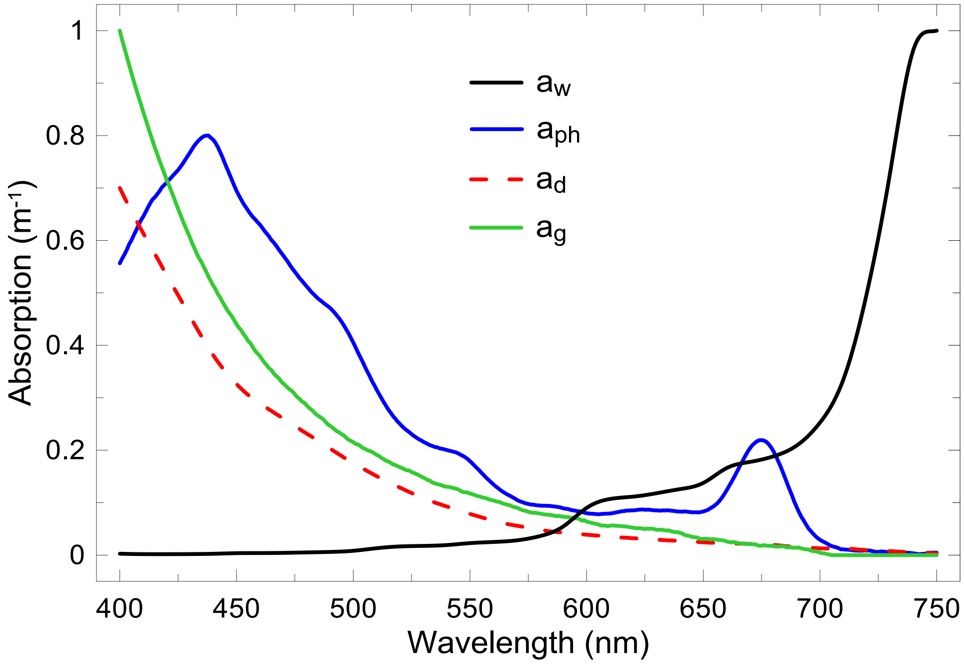

Figure 1.4: Qualitative comparison of the shapes of absorption spectra of pure water (a_w), phytoplankton (a_{ph}), detritus (a_d) and CDOM (a_g).

b) Scattering

The scattering coefficient, b is divided into two parts; forward, b_f and backward scattering, b_b.

$$b = b_f + b_b \qquad 1.15$$

Forward and backscattering coefficients can be derived by the angular ranges $0 \leq \theta \leq \pi$ (0° to 180°) and $\pi/2 \leq \theta \leq \pi$ (90° to 180°) at a given zenith angle θ, respectively. Mathematically, they can be expressed as:

$$b_f = 2\pi \int_{0}^{\frac{\pi}{2}} \beta(\theta)\, sin(\theta)\, d(\theta) \qquad 1.16$$

$$b_b = 2\pi \int_{\frac{\pi}{2}}^{\pi} \beta(\theta)\, sin(\theta)\, d(\theta) \qquad 1.17$$

where β is the volume scattering function that describes the directional dependence of this scattering. The backscattering coefficient is important in remote sensing but it is very difficult to measure. It is often assumed to be constant proportional to total scattering ($b_b \approx 0.019b$) based on a study of Petzold (1972), although it can vary considerably depending on the water type. The backscattering coefficient of natural water can be separated into contributions from pure water, b_{bw} and particles, b_{bp}.

$$b_b = b_{bw} + b_{bp} \qquad 1.18$$

The particle backscattering, b_{bp} can be due to living (phytoplankton) and non-living (mineral) particulates suspended in the water. The scattering by CDOM is neglected in most applications (Pozdnyakov and Grassl, 2003) due to the small size of CDOM molecules relative to the wavelength of visible light and is set to zero. In general, the spectral shape and magnitude of b_{bp} is primarily determined by the concentration of particles, their shape, index of refraction and the particle size distribution. Accurate b_{bp} determinations are importance for the interpretation of remotely sensed signals since the upwelling radiance exiting the ocean is directly proportional to this parameter and inversely proportional to the absorption coefficient.

1.3.3 Relating AOPs and IOPs

Determination of the relationships between AOPs and IOPs is essential for developing quantitative radiative transfer models of spectral irradiance in the ocean (Kirk 1994; Mobley 1994). Radiative transfer models describe the propagation of light within the ocean and thus provide a mathematical solution for linking the known IOPs and spectral radiance distribution to the AOPs of the water column. In ocean colour studies, the conversion of remotely sensed data in terms of water leaving radiance into geophysical data products requires the accurate relationships between these data products and AOPs through in-situ measurements of IOPs.

The most commonly used expression relating irradiance reflectance, R to IOPs was introduced by Gordon et al. (1975).

$$R = f\,\frac{b_b}{a} \quad for\ b_b \ll a \qquad 1.19$$

where f is a dimensionless factor which varies between 0.3 and 0.5, depending on the sun zenith angle (Kirk, 1984; Gordon, 1989) and the inherent optical properties (Morel and Ahn, 1991; Morel and Gentili, 1996). The condition $b_b << a$ usually holds for most oceanic waters where the water itself contributes more to backscattering than the suspended particles. However, this condition may not hold in coastal waters where backscattering by particles are the major contributor to total backscattering. In this case, equation 1.19 is replaced by (Gordon et al., 1975)

$$\mathrm{R} = \mathrm{f}\,\frac{\mathrm{b_b}}{\mathrm{b_b} + \mathrm{a}} \qquad 1.20$$

By combining equations 1.9 and 1.2, Gordon et al., 1988 also show that the remote sensing reflectance, R_{rs} are related to IOPs:

$$\mathrm{R_{rs}} = \frac{\mathrm{L_w}(\theta_0, \theta', \Delta\varphi)}{\mathrm{E_d}(\theta_0)} = \frac{\mathrm{f}(\theta_0)}{\mathrm{Q}(\theta_0, \theta', \Delta\varphi)}\left(\frac{\mathrm{b_b}}{\mathrm{b_b} + \mathrm{a}}\right) \qquad 1.21$$

The ratio f/Q has been shown to less dependent than either f or Q alone and its values range between 0.09 and 0.12 sr^{-1} for homogenous case-1 waters (Morel and Gentili, 1993).

1.3.4 Bio-optical models

Retrievals of in-water constituents from satellite measurements of water leaving radiance has been studied extensively since the launch of the first ocean colour satellite, the coastal zone colour scanner (CZCS) in the late 1970's (O'Reilly et al., 1998). Since then, many studies have focused on developing techniques for estimating in-water constituents especially phytoplankton chlorophyll concentration from ocean colour imagery. In the estimation of chlorophyll and other bio-optical properties, empirical (Clark, 1981, 1994; Gordon and Morel, 1983; Aiken et al., 1995; O'Reilly et al., 1998; Kahru, 1998) and semi-analytical approaches (Gordon et al., 1988; Morel, 1988; Garver and Siegel, 1997; Carder et al., 1999; Lee et al., 2002) have been used extensively over the past decades. Although most of these algorithms are applied globally, it is recognized that there is no universal bio-optical algorithm applicable to all water types and ocean areas. This is due to the inherent variability of many bio-optical constituents that vary with region and season.

a) Band ratio algorithms

The most common empirical ocean colour algorithms are based on assumption that the ratio of the spectral reflectances at two wavelengths is a known function of the chlorophyll concentration. Using the ratio of the reflectance in the blue and green parts of the spectrum, a simple log-linear equation can be used to estimate the phytoplankton pigment concentration. The functional form of the band ratio algorithms is given by:

$$\log_{10}[\mathrm{Chl}] = \sum_{\mathrm{i}=0}^{\mathrm{M}} \mathrm{a_i R^i} \qquad 1.22$$

where R is the $\log_{10}$ ratio of reflectances at specific wavelengths, a is determined empirically from a regression between the radiance ratio and chlorophyll concentration, [Chl] and M varying 1 (first order) to 4 (fourth order). In general, the band ratio algorithms provide a good estimation of chlorophyll concentration in case-1 water, where their efficacy relies on the assumption that other non-pigmented materials (dissolved organic matter and detritus) are highly correlated with chlorophyll. Typically, these algorithms are valid only for data having the same optical properties to those datasets used for the determinations of the coefficients (Sathyendranath, 2000). Therefore, they are particularly sensitive to changes in composition of water constituents that vary accordingly to region and season.

In case-2 water, where radiance at a given wavelength includes contributions by materials other than chlorophyll, the band ratio algorithms are no longer appropriate. In this water, reflectance in the blue spectral range is almost insensitive to changes in chlorophyll due to the strong absorption by dissolved organic matter and detritus (Ruddick et al., 2001). Even though, some attempts have been made for the estimation of chlorophyll in case-2 waters using the absorption wavelength of phytoplankton in the red and near-infrared spectral regions (e.g., Gitelson and Kondratyev 1991; Gitelson 1992; Dekker 1993; Ruddick et al. 2001), the band ratio algorithms do not always work well for this category of waters (Darecki and Stramski, 2004).

The operational band ratio algorithms, SeaWIFS OC4-v6 and MODIS OCM3-v6 that are used in this study, have been developed from the most spatially extensive set of bio-optical measurements of NASA SIMBIOSIS project (Fargion and McClain, 2001) and comprises of some 2,853 sets of measurements, with chlorophyll values between 0.01 and 90 mg m^{-3} (O"Reilly et al., 2000). The OC4 model is a modified cubic polynomial that relates a band ratio to chlorophyll concentration based on whichever reflectance ratio, R_{rs}(443/547), R_{rs}(488/547) or R_{rs}(510/547) is the most dominant (O'Reilly et al., 2000). The MODIS OCM3 (Carder et al., 1999) is a SeaWIFS analogue and takes the same form as the OC4 model. However, as MODIS lacks a 510 nm band used in the OC4 algorithm, it utilizes only the maximum of two band ratios [R_{rs}(443/547) and R_{rs}(488/547)].

b) Semi-analytical algorithms

Semi-analytical algorithms are based on theoretical relationships between reflectance measured by the satellite and inherent optical properties (absorption and scattering coefficients) of the water. The algorithms utilize an analytical approach by relating water reflectance and IOPs through radiative transfer theory and the approximation of R_{rs} as in equation 1.21. The spectral reflectance model is inverted to derive chlorophyll and IOPs (absorption or backscattering coefficients) of other optically active substances (non-pigmented particulate matter and CDOM) that do not covary with chlorophyll. However, several terms used in the radiative transfer model such as backscattering, chlorophyll-a specific absorption coefficient or spectral shapes of detrital absorption are parameterized using empirical relationships (O`Reilly et al, 1998). In that sense, the algorithm is termed as semi-analytic. Because these algorithms separately retrieve chlorophyll and CDOM, they have been proposed for use in case-2 waters.

Although these models and their inversion account for all optically active substances and primarily target case-2 waters, they are more sensitive to errors in water leaving radiance than band ratio algorithms that do not have forward and inverse components (IOCCG, 2000). In coastal waters, where bio-optical properties are complex, the relationship between water reflectance and IOPs behaves as a non-linear function of the concentration of the relevant substance. Any incorrect assumptions or inaccurate parameters will introduce significant errors in the forward model and thus will cause significant variation in the predicted substance concentration. The theoretical approach of the semi-analytical model was first introduced by

Gordon et al (1988) and Morel (1988) for case-1 waters. In their work, the functional dependency of the diffuse attenuation coefficient and chlorophyll concentration was used as a base to invert the reflectance model. Since then, numerous semi-analytical solutions have been proposed for the retrieval of constituent concentrations as well as optical properties of water (Garver and Siegel, 1997; Carder et al, 1999; Lee et al, 2002).

The semi-analytical MODIS algorithm by Carder et al., (1999) was purposely developed to derive chlorophyll concentrations by separating the effects of the major absorption components, phytoplankton pigment and non-pigmented materials. One of the main characteristics of this algorithm is the adjustment of both chlorophyll-specific absorption coefficients and CDOM-detrital absorption coefficients for regional and temporal changes, hence reducing the typical errors of remote estimation of chlorophyll-a concentration in case-2 waters. The success of their algorithm however, depends on the classification of the bio-optical domains that is based on the relationship between sea surface temperature (SST) and nitrate depletion temperature (NDT). The NDT is the surface temperature for a given oceanic location above which the nitrate concentration becomes negligible (Kamykowski, 1987). This is based on the inverse relationship between nutrients (nitrate, phosphate and silicate) and temperature which ultimately affects phytoplankton growth, biomass and species composition. This relationship occurs seasonally in surface water to varying degrees depending on geographic location and can be used to show a place where a major transition in the types of phytoplankton is occurring. In general, a large size class of phytoplankton coincides with a supply of nitrate while a small size class predominates in nitrate-depleted waters (Carder et al., 1999).

The bio-optical domains with different values for the empirical parameters are classified into (1) unpackaged – high ratios of photoprotective pigments to chlorophyll and low self-shading, (2) packaged – low ratio and self-shading and (3) transitional or global average type. In the semi-analytical equations, the model is inverted to solve for two unknown variables, phytoplankton absorption at 675 nm and coloured detrital matter (detritus and CDOM) at 400 nm as a function of ratios of observed remote sensing reflectances. Chlorophyll concentration is then derived from an empirical relationship with $a_{ph}(676)$. However, this semi-analytical model is only valid for oligotrophic waters where chlorophyll concentration does not exceed 2.0 mg m^{-3}. For larger values of chlorophyll concentration, an empirical algorithm of Aiken et al., (1995) is used to derive chlorophyll concentration. Carder et al., (1999) claim that the performance of their semi-analytical algorithm is comparable with the empirical approach for all water types (case-1 and case-2) and the accuracy of the algorithm can be further increased if the data is adjusted into appropriate bio-optical domains. However, they also found that the algorithm tended to overestimate the chlorophyll by a factor of two in upwelling and high-latitude regions.

Lee et al., (2002) developed a multiband quasi-analytical algorithm (QAA) based on the Carder model. As is the case for many other inversion algorithms, the QAA is purposely developed to separate the contribution of phytoplankton and CDOM absorption coefficients from the total absorption coefficient for deriving chlorophyll and CDOM concentrations. However, unlike the conventional semi-analytical algorithm, QAA does not need a priori knowledge of the spectral shape of phytoplankton absorption. One of the advantages of this algorithm is that it is easy to model with relatively simple mathematics and its stepwise derivation concept allows the effect of uncertainties of each variable to be evaluated at each level. Briefly, the QAA employs a series of analytical, semi-analytical and empirical equations to convert R_{rs} to total absorption and backscattering coefficients in two analytical steps. The first step involves a derivation of total absorption and particulate backscattering coefficients at a specific reference wavelength from remote sensing reflectance. Lee et al., (2002) proposed two reference wavelengths, 555 nm for oceanic water (case-1) and 640 nm for high-absorbing coastal waters (case-2). A combination of results at 555 nm and 640 nm is also proposed for both case-1 and case-2 waters. In the second step, phytoplankton and CDOM absorption coefficients are spectrally decomposed from the derived total absorption coefficient by relating them to their spectral ratios at 412 and 443 nm. Therefore, the accuracy of both absorption coefficients depends not only on the accuracy of derived a(λ), but also on their spectral dependencies. The equations of the semi-analytical and QAA can be found in Appendices A and B, respectively.

1.4 Thesis aims and structure

This research is motivated by interest in understanding the marine optical environment in east coast of Peninsular Malaysia. The study is not only important in many aspects of oceanography but also can be used to characterize the ecologically and economically important marine resources at large temporal and spatial scales. In this context, satellite ocean color offers enormous potential for fisheries applications and other environmental problems associated with fisheries such as harmful algal bloom and coastal pollution. Because the satellite is the only biological measurement and fish production and stock depend greatly on production of plankton, there is a large scale relationship either directly or indirectly between the satellite chlorophyll and fish feeding locations. The fishery sector in Malaysia has for decades been playing a significant role in national economy and contributes nearly 1.5% to the national Gross Domestic Product (GDP) (Department of Fisheries Malaysia, 2010). This sector is also a source of employment, foreign exchange and a major supplier (60% - 70%) of animal protein to the Malaysian population. With continued growth in population, intensive exploitation of the coastal resource and under-exploited deep-sea fishing (Mohd Mazlan, 1998), demand for fish in this country is expected to increase beyond its current supply. Under the Third National Agricultural Policy 1998-2010 (NAP3), the government is putting up effort to increase fish production by promoting exploration of offshore marine resources by means of modern technology. The use of satellite ocean colour could facilitate this effort to further explore potential fishing zone in Malaysia Exclusive Economic Zone (EEZ) by reducing search time for locating fish sites and operating costs for fishing vessels, thereby increases catch per unit effort. Although other oceanic conditions such as sea surface temperature (SST), salinity, ocean currents and wind speed are also important to identify the potential fishing grounds, the accurate estimation of satellite chlorophyll is the key success factor to fully utilize ocean colour satellite systems for fisheries applications. In order to confidently use satellite ocean colour, validation exercises and applicability of ocean colour models need to be conducted to ascertain accuracy and limitations. Therefore this study can make a significant contribution by providing detailed information on the potential and suitability of satellite ocean colour for operational oceanography for Malaysian waters.

The overall aim of this work is to assess the potential use of ocean colour imagery for deriving chlorophyll and CDOM concentrations in east coast of Malaysian waters. We shall do this by making in-situ measurements, and of remote sensing reflectance during different seasons and at different locations. Our specific objectives are.

1. to characterize and assess the variability of bio-optical properties for different monsoon seasons.
2. to assess the suitability of the standard global ocean colour algorithms in providing accurate water colour parameters.
3. to evaluate and improve the algorithms by which the ocean colour can be used to estimate water colour parameters in the study area.
4. to characterize the seasonal and inter-annual variations in chlorophyll and CDOM concentrations using the newly developed algorithms.

This thesis starts with the methodological approach of the research design on which this work is based in chapter 2. In this part, the in-situ method used for retrieval of in-water constituents and absorption properties are presented. In addition, the oceanographic conditions of the study area are also described. In chapter 3, the results of oceanographic conditions and bio-optical properties made during extensive field campaigns in 2009 are presented. The objective in this part of the research is to assess the magnitude of spatial and temporal variability of in-water optical properties for different seasons. For comparison, the results are grouped into three different seasons; southwest monsoon, northeast monsoon and inter-monsoon. In this part, the dependence of optical properties with respect to hydrological parameters and in-water constituents are also presented and compared with results from previous studies. The results in this chapter have been submitted in the International Journal of Remote Sensing. Chapter 4 focuses on the relationships of in-water constituents and optical properties with remote sensing reflectance. First, the MODIS-derived remote sensing reflectances are compared with those measured in-situ. Then, the applicability of the chlorophyll and some of the inherent optical properties algorithms used by MODIS satellite data and algorithm performance is assessed and causes of the variations in performance are discussed. In this part, several empirical algorithms for chlorophyll and absorption properties retrieval are proposed and discussed. Chapter 5 utilizes the algorithms developed in chapter 4 to estimate in-waters constituents and several absorption properties from monthly composite of satellite MODIS data. In this part, the inter-annual variability in water colour is discussed. In chapter 6, the major findings of the research from chapters 3 to 5 are critically discussed and summarized. It provides the conclusions and gives an overview on the prospects, ideas and challenges for future research direction in this field of study.

CHAPTER 2

FIELDWORK AND METHODS

2.1 Overview

This chapter describes the study site and the data collection and analysis methods. The study site is a shallow (< 60 m) shelf sea region subject to a Monsoon climate regime. Standard techniques were used to measure radiance and irradiance profiles and concentrations of in-water constituents at 32 stations on 6 cruises in different seasons during 2009. All measurements during the cruises that started in May 2009 were taken by using the University Malaysia Terengganu and Institute of Oceanography's facilities and instrumentation. The main objectives of the research was obtaining comprehensive field data in space and time in order to be able to; i) asses intra seasonal as well as inter seasonal variability in water properties, ii) apply the detailed in-situ and laboratory measurements for interpretation and validating of satellite ocean colour observations, iii) perform detailed reflectance model calculations and applied to the satellite ocean color.

2.2 The study site

The east coast of Peninsular Malaysia is located on the southwestern shelf (Sunda shelf) of the South China Sea (SCS), bordering Thailand in the north and Singapore in the south. The weather regime in this area is directly affected by ocean-atmosphere interaction over the SCS. The region is assumed to be a tropical oceanic system subject to semi-annual reversing winds associated with East Asian monsoon cycle of southwesterly and northeasterly winds. The dry southwest monsoon (SWM) in summer lasts from June to September and the wet northeast monsoon (NEM) in winter lasts from November to March. The northeast monsoon is generally brings heavy rain and stronger wind especially on the East Coast of Peninsular Malaysia. The southwest and northeast monsoon seasons are interrupted by two transition or inter-monsoon periods (April to May and September to October) that are characterized by unpredictable winds speed and direction. Larger quantities of rain may fall during the inter-monsoonal periods due to atmospheric instability and convective activity, especially along the west coast regions.

The east coast is considered the wet belt of Peninsular Malaysia with rainfall on 150 to 200 days of the year (Chua, 1984). The annual rainfall in this area is about 2800 mm and the maximum precipitation usually occurs during the months of November and December. As the heavy rainfall and freshwater discharge from rivers are one of the main characteristics of the NEM season, the water mass especially in the coastal areas is usually characterized by low salinity and temperature. In the offshore waters, however, the surface salinity is higher during NEM season as the strong sea surface winds creates turbulence that causes the mixing of surface low-salinity water with the bottom cold and salty water from the SCS. During this period, the offshore surface salinity increases by 0.5 psu while the temperature decreased by 1 ^{o}C, respectively, compared to the levels observed during the dry, summer months (Saadon and Camerlengo, 1997; Yanagi et al, 2001). Strong riverine discharges during rainfall events especially in the month of December carry large amounts of freshwater and nutrients into coastal areas, significantly affecting the water quality and biophysical processes in the areas. For example, the average discharge from the Terengganu River, one of the largest rivers in the east coast of Peninsular Malaysia, is about 1000 m^3s^{-1} during the NEM season, compared to only 250 m^3 s^{-1} during the SWM season (Mohd-Lokman et al, 1998). The enhancement of vertical mixing during the NEM (Mann and Lazier, 1996) that brings nutrient rich water to the surface is responsible in elevating the primary productivity (Wyrki, 1961; Xie et al., 2003; Tang et al., 2004). During this period, the high phytoplankton community is not only limited to coastal waters but spread out across the offshore regions (Tang et al., 2003).

During the SWM, sea surface water temperature in the offshore east coast of Peninsular Malaysia is higher than during the NEM due to sea surface heating and weak sea surface wind. The water column is well stratified (Yanagi et al, 2001; Lokman et al, 1986) due to the intensification of water exchange between the east coast of Peninsular Malaysia and the SCS, thus reducing the surface salinity. According to Yanagi et al (2001), stratification in this area is most developed in March-May, and then weakens until September-October and vanishes in December-January due to sea surface cooling and strong northeast winds. Weak sea surface winds will also decrease the water surface elevation and causes the mixed layer to shallow. Unlike other monsoon regions such as the Arabian Sea and Indian Ocean, the highly stratified of water column during the SWM is generally characterized by low phytoplankton population (Dey and Singh, 2003; Tang et al., 1998, 1999, 2004) and shows less variation of optical properties (Liu et al., 2002).

Surface currents in the SCS (Figure 2.1) generally follow the topographic configuration of the sea bottom. Although the SCS has very complex bottom topography, the east coast of PM is generally characterized by a gentle slope deepening progressively towards the SCS. Based on the Wyrtki (1961) and Camerlengo and Demmler (1997) circulation models in the SCS, the surface currents are stronger during the NEM when the dominant direction is from the SCS. During the NEM, the mass transport rate along the coast during this period is about 4.0 Sv (Wyrtki, 1961). Due to coastal geometry and geostrophy effects, surface currents from the low-salinity Mekong river enter the Gulf of Thailand along the Vietnam coast. The surface water from the Vietnam coast produce a cyclonic gyre in the Gulf of Thailand before flowing out along the east coast of Peninsular Malaysia towards the Karimata Straits, Indonesia.

Generally, the current velocity along the east coast of Peninsular Malaysia is lower than the surface current flowing along the Vietnamese coast (Wyrtki, 1961; Camerlengo and Demmler, 1997). This is due to Ekman transport that forces the piled-up water mass in the east coast of Peninsular Malaysia to move southward. During the SWM, the current flow is generally weak with a current speed less than 0.5 ms^{-1} (Saadon et al, 1997; Tangang et al, 2007) and a mass transport rate of 3.0 Sv (Wyrtki, 1961). High-salinity water masses from the SCS and Karimata Straits, Indonesia flow northwards along the Peninsula east coast into the Gulf of Thailand, completing a clockwise rotation before eventually reinforcing the flow along the Vietnamese coast in the direction of prevailing winds. The free surface elevation on the east coast is depressed during this period (Azmy et al, 1991).

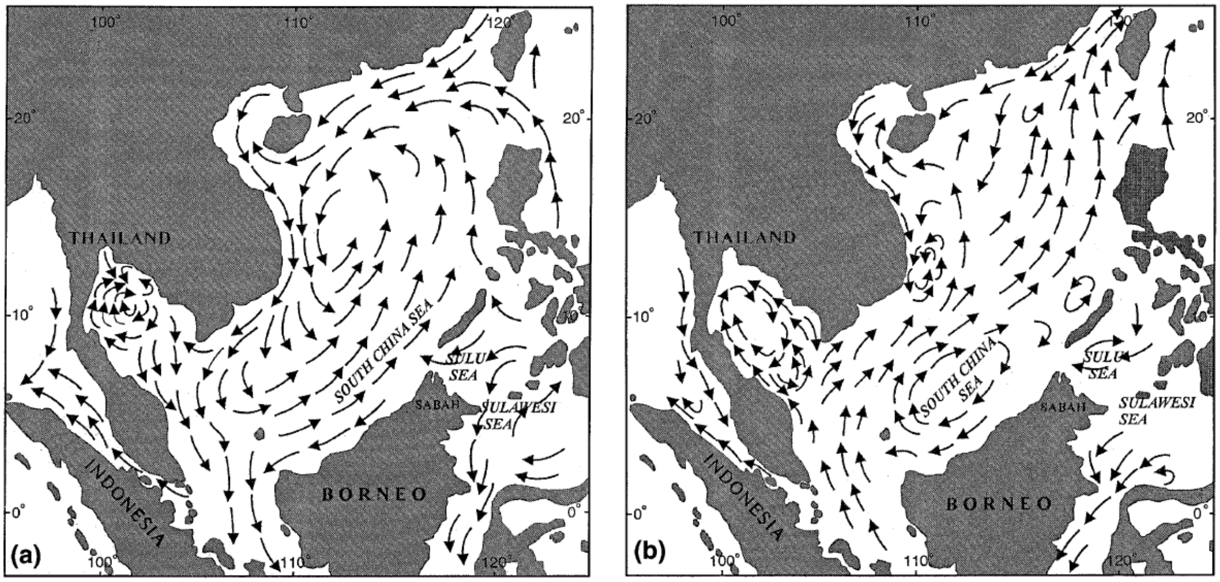

Figure 2.1: The surface currents of the South China Sea during (a) winter and (b) summer. After Morton and Blackmore (2001).

Variations in physical and hydrographic properties, stratification, radiation regime and vertical mixing due to variations in the monsoon regime will result in variability of the bio-optical and biogeochemical characteristics of this area.

2.3 Bio-optical cruises

Figure 2.2 shows the location of all the stations that were visited during six 5-day cruises that were carried-out between May 2009 and November 2009. The sampling dates (Table 2.1) coincide with 3 major monsoon seasons, the southwest monsoon (June to August), northeast monsoon (November) and inter-monsoon (May and October). Although it is difficult to determine the actual timing of each monsoon onset, the monsoon intra-seasonal oscillation is a relatively repeatable large scale phenomenon. The timing of the monsoon onset can vary by two to three weeks and the intensity of rainfall over the South China Sea region strongly varies from year to year (Lau and Yang, 1997; Hoyos and Webster, 2007). The in-situ measurements were performed along inshore-offshore transect that extend from 5.04^o N to 5.97^o N latitudes and 102.76^o E and 103.59^o E longitudes, wide enough to compare to satellite imagery. A total of 32 stations were sampled from a 15-m coastal research boat. Each cruise surveyed 5 transect from depths between 10 m to 60 m. The distance between the sampling stations for each transect varies from 5 km at the coastal stations (the first 3 stations) to 9 km at the seaward stations. All stations were sampled during each cruise except for stations 1-7 in May and October due to weather constraints. In total, 178 in-situ measurements were performed during the course of this study.

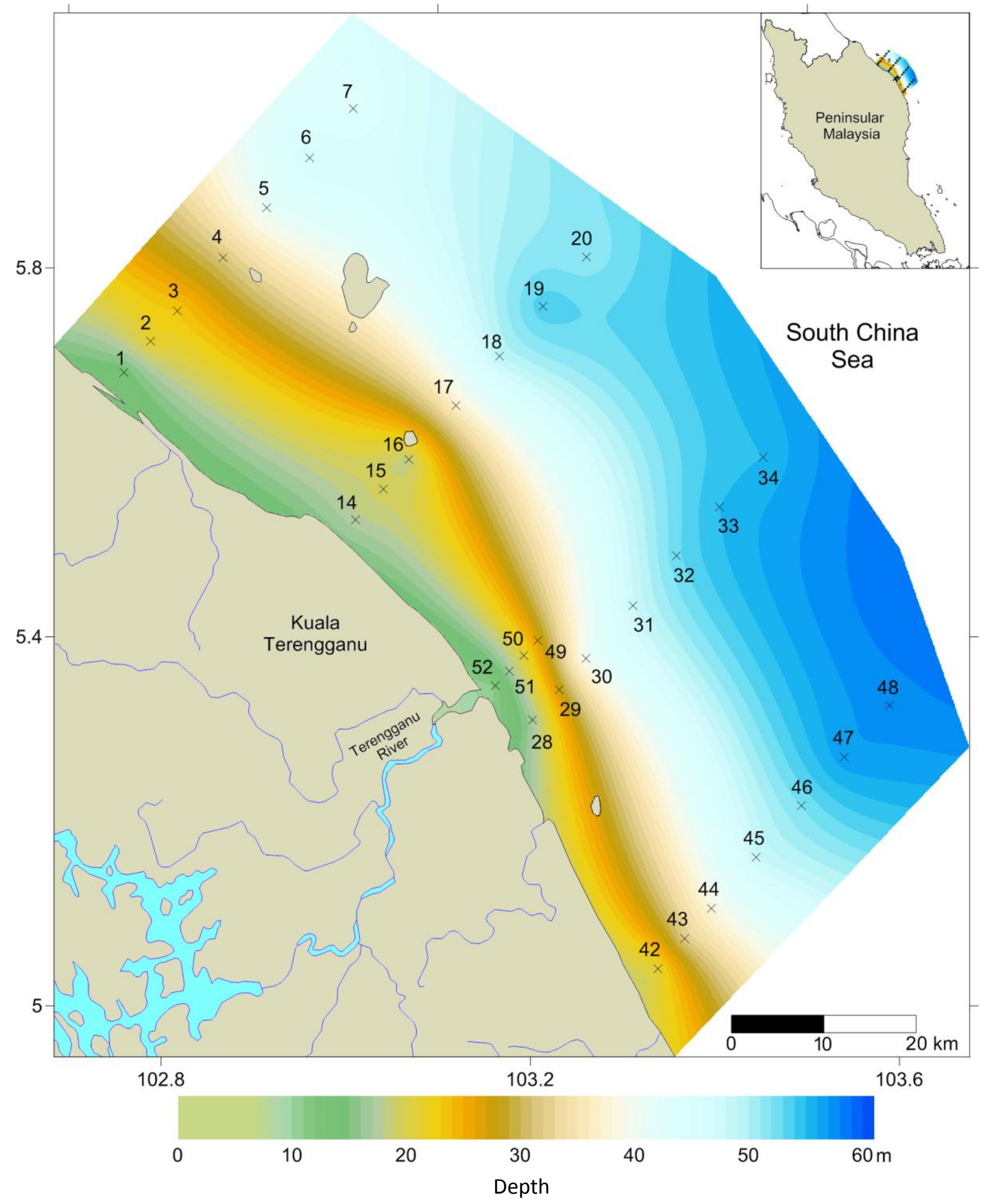

Figure 2.2: Locations of the sampling stations in east coast of Peninsular Malaysia water.

Table 2.1: Dates of cruises

No	Start date	End date	Comments
1	13 May 2009	18 May 2009	Spring inter-monsoon; Relatively clear water; clouds/haze
2	14 June 2009	18 June 2009	SW monsoon; Relatively clear water; clear sky
3	6 July 2009	9 July 2009	SW monsoon; Relatively clear water; clouds/haze
4	11 August 2009	14 August 2009	SW monsoon; Relatively clear water; clouds
5	21 October 2009	24 October 2009	Fall inter-monsoon; Relatively clear water; clouds
6	10 November 2009	12 November 2009	NE monsoon; A week after heavy rain event, clouds

The summary of measurements carried out in the study area is presented in Table 2.2. Except for the May cruise, optical measurements of radiation fields (upwelling radiance and downwelling irradiance) for each station were measured using a Satlantic Hyper Ocean Colour Radiometer sensor (Hyper OCR). During May, the measurements of radiation fields were performed using an ASD Fieldspec UV/VNIR Handheld Spectroradiometer. All water samples were collected from approximately 0.5 m depth using 10L dark bottles for particles and absorption measurements. Vertical profiles of hydrological parameters of temperature and salinity were also determined using CTD and hydrolab instruments. As a complement for the in-water radiation field analysis and to determine how different atmospheric conditions affect the in-situ and satellite reflectances, simultaneous observations of atmospheric characteristics (aerosol optical thickness, direct solar irradiance and sun zenith angle) have been obtained using a Microtop II sunphotometer. Following a recommendation by Werdell et al., (2003), all measurements were carried out within a time window of 3-4 hours (no earlier than 0900 or later than 1500 hours to ensure adequate solar illumination) around the time of a satellite overpass. In this study, data from MODIS Aqua that passes the study area in the afternoon (~1300 hour) were used to compare the in-situ and satellite measurements of remote sensing reflectances and chlorophyll concentrations.

Table 2.2: In-water and above water measurements performed during all bio-optical cruises

In-situ measurements	Wavelength range (nm)	Instrument used
Temperature profiles (^{o}C)	-	YSI multiparameter
Salinity profiles(psu)	-	YSI multiparameter
In water upwelling radiance profiles [L_u]	350 - 800; 136 channels 350 – 1050; 512 channel	Satlantic Hyper OCR ASD Fieldspec Spectroradiometer
In-water downwelling irradiance profiles [E_d]	350 - 800; 136 channels 350 – 1050; 512 channel	Satlantic Hyper OCR ASD Fieldspec Spectroradiometer
Secchi disk depth	-	Secchi disk
Laboratory measurements	Wavelength range (nm)	Instrument used
Total chlorophyll-a [TChl-a] mg m^{-3}	-	Cary spectrophotometer
Suspended particulate matter [SPM] mg l^{-1}	-	Dry oven
Particulate inorganic matter [MSS] mg l^{-1}	-	Muffle furnace
Particulate absorption [$a_p(\lambda)$] m^{-1}	300 – 800	Cary spectrophotometer
Detritus absorption [$a_d((\lambda)$] m^{-1}	300 – 800	Cary spectrophotometer
CDOM absorption [$a_{CDOM}((\lambda)$] m^{-1}	300 – 800	Cary spectrophotometer
Atmospheric observations	Wavelength range (nm)	Instrument used
Aerosol optical thickness [AOT]	440, 500, 675, 870, 936	Microtop II sunphotometer
Sun zenith angle (^{o})	-	Microtop II sunphotometer
Water vapour	440, 500, 675, 870, 936	Microtop II sunphotometer
Direct solar irradiance	440, 500, 675, 870, 936	Microtop II sunphotometer

2.4 Measurements of underwater radiation fields

Measurements of underwater vertical profiles of upwelling radiance, $L_u(z,\lambda)$ and downwelling irradiance, $E_d(z,\lambda)$ were acquired at each location using a Satlantic Hyper OCR and ASD Fieldspec spectroradiometer, from subsurface (0.5 m) to 10 m depth over 3 m intervals. The Satlantic Hyper OCR set combines two in-water hyperspectral radiometers to measure $E_d(z,\lambda)$ and $L_u(z,\lambda)$, connected to a computer interface through a calibrated Y-splice cable. These radiometers operate in a calibrated range from 350 to 800 nm with 136 bands (spectral sampling of 3.3 nm/pixel) and 3 Hz frame rate. The field-of-view (FOV) of in-water $E_d(z,\lambda)$ and $L_u(z,\lambda)$ sensors are 180^{o} and 8.5^{o} respectively, with spectral accuracy of ± 3%. In order to preserve data consistency and reliability and to ensure accuracy, all sensors are calibrated for every 1 or 2 years by the manufacturer. The $E_d(z,\lambda)$ and $L_u(z,\lambda)$ sensors were mounted together on a horizontal T-plane frame (Figure 2.3) with a vertical offset of ±30 cm, which was accounted for when processing the data. For the ASD Fieldspec spectroradiometer, the fore optic of underwater cosine corrected-receptor with 10^{o} FOV was used to collect up and downwelling irradiance. This handheld radiometer has the nominal spectral range of 350 – 1050 nm that uses a fiber optic input that feed directly into the spectrometer.

The sensors were slowly lowered on the sunny side of the boat to a depth of 5 to 6 m and held there for 1-2 minutes to stabilize the instrument against changes in sensitivity and level due to change in ambient temperature and pressure after sitting on deck. In order to avoid inconsistencies relating to the drastic change of light level during measurements, the data were logged for 5 seconds for each depth. Additional information about Secchi disk depth, PAR irradiance profiles, sun elevation, sky conditions, wave height and wind speeds were also recorded for each location (Table 2.2).

Figure 2.3: Satlantic Hyper OCR downwelling (right) and upwelling (left) radiometers are mounted on a horizontal T-plane frame.

HyperOCR data was processed by the Prosoft data analysis package (Satlantic Inc) to Level 2 in which reference and data dark deglitching and correction are applied. Near surface $E_d(z,\lambda)$ and $L_u(z,\lambda)$ were filtered for tilt and data with high tilt angle ($> 5^o$) were manually discarded. High tilt effects on the profile were determined visually by plotting the radiometric data against depth on log axis. $E_d(z,\lambda)$ and $L_u(z,\lambda)$ data that are not log-linear with respect to depth were eliminated from analysis. Since no tilt sensor was attached to the sensor frame, the inclination angle of the sensors was obtained by a direct reading from a clinometer on the wire during each measurement. To estimate the water leaving radiance just-above the sea surface, $L_u(0^-,\lambda)$ was propagated through the interface according to equation 1.7.

Similarly, the above-water downwelling irradiance, $E_d(0^+,\lambda)$ was estimated from $E_d(0^-,\lambda)$ using the transmission procedure as equation 1.7.

$$E_d(0^+,\lambda) = E_d(0^-,\lambda) \text{ x } (1+\alpha) \qquad 2.1$$

$$E_d(0^+,\lambda) = 1.043 \text{ x } E_d(0^-,\lambda) \qquad 2.2$$

where α is the Fresnel reflection albedo for irradiance from sun and sky (~0.043) (Austin, 1974). The calibration and validation of satellite remote sensing data requires field remote sensing reflectance (R_{rs}) measurements concurrently with the collection water samples. The reflectance quantity can either be quantified as the subsurface irradiance reflectance, $R(0^-,\lambda)$ or the remote sensing reflectance, $R_{rs}(\lambda)$. $R(0^-,\lambda)$ can be calculated as:

$$R(0^-,\lambda) = \frac{L_u(0^-,\lambda)}{E_d(0^-,\lambda)} \text{ x } Q \qquad 2.3$$

where Q is the ratio of upwelling irradiance, $E_u(0^-,\lambda)$ to upwelling radiance, $L_u(0^-,\lambda)$. For isotrophic upwelling radiance (for the same direction), Q would have the value π. In fact, the upwelling radiance is not equally distributed and numerical studies have found that Q often has a value close to 5.0 ± 0.1 (Kirk, 1984). However, for the sake of simplicity and for a direct comparison with satellite remote sensing reflectance, $R_{rs}(\lambda)$ was used in the study. Following the recommendations of Mobley (1994), $E_d(0^+,\lambda)$ was used in the denominator for calculating the $R_{rs}(\lambda)$ according to equation 1.6.

2.5 In-water constituents measurements

Concentrations of several in-water constituents were determined from water samples collected from approximately 0.5 m depth. A submersible pump system attached to 1 inch diameter garden hose was used to pump water samples into 10L dark bottles. The samples were stored in the dark for a maximum of 9 hours before filtration for particles and absorption measurements. At each station, vertical profiles of hydrological parameters of temperature and salinity were also determined.

2.5.1 Total Chlorophyll (Chl)

Chlorophyll samples were analysed using the trichromatic method of Jeffrey and Humphrey (1975) and determined spectrophotometrically using a Cary-100 double beam Spectrophotometer. A known volume of water (1 to 5 L depending on particle load) were filtered under low vacuum pressure onto 47 mm Whatman GF/F filters (pore size 0.7 μm). Filters were folded, wrapped in foil squares and subsequently preserved in the dark under low temperature until analysed in the laboratory. In the laboratory, the filters were placed in 10 mL volume of 90 % acetone in a 50 mL pyrex tube and immediately ground for 30 seconds under subdued light using a teflon pestle attached to an Analite high-speed grinder. The liquefied pulp was then added into small polyethylene centrifuge tubes and refrigerated for 24 hours. After 24 hours the liquefied pulp was centrifuged at 3000rpm for 10 minutes and warmed to room temperature prior to spectrophotometric analysis. The chlorophyll absorbances were determined at 750 (background correction), 664, 647 and 630 nm with 1 cm quartz cuvette. Absorbances were referenced against a buffered 90% acetone blank which was inserted after every 4-5 samples.

Total chlorophyll concentration (chlorophyll–a + phaeophytin) was calculated according to equations of Jeffrey and Humphrey (1975).

$$[\mathrm{TChl\ a}] = [11.85 \text{ x } (\mathrm{E}_{664} - \mathrm{E}_{750}) - 1.54 \text{ x } (\mathrm{E}_{647} - \mathrm{E}_{750}) - 0.08 \text{ x } (\mathrm{E}_{630} - \mathrm{E}_{750})] \text{ x } {}^{V_e}\!/_{L \text{ x } V_f} \qquad 2.4$$

where [Chl] are concentrations in mg m^{-3}, E is the optical density at nm wavelength, L is the cuvette pathlength in centimeter, V_e is the extraction volume in millimeter and V_f is the filtered volume in liter.

2.5.2 Suspended particulate matter (SPM)

A sufficient volume of seawater (1 – 5 liter depending on particle load) was filtered through a prepared 0.7 um Whatman GF/F filter. Prior to samples filtration, blank filters were prepared by washing and rinsing the filter with distilled water while under vacuum applied through the filtration assembly. Filters were placed in cleaned aluminum dishes and heated in a muffle furnace at 450 °C for 4 hours. The blank filters were then weighed and stored in labeled airtight bags to avoid the uptake of atmospheric moisture. Particles were collected in triplicate by filtering sufficient volume of seawater under low vacuum. Filters were rinsed with 250 ml of distilled water to remove any trace of salt and the samples were immediately stored cooled until analyzed. Filters were oven-dried at 105 ^{o}C for 4 hours, cooled down to room temperature and weighed on an analytical balance to a 4 decimal places. The concentration of SPM is calculated by the weight difference of filters before and after filtration divided by the filtrate volume. SPM is expressed as mg l^{-1} or equivalently g m^{-3}.

The suspended particulate matter was separated into 2 main fractions; particulate organic matter (POM) and particulate inorganic matter (PIM) by combusting the SPM filters at 450 ^{o}C for 4 hours. The filters were then cooled down to room temperature in a dessicator before weighing. The volatile fraction of SPM is burnt off during the combustion and the weight loss of filters represents the organic fraction of SPM. The concentration of PIM is therefore, calculated by a weight difference of blank filters and combusted filters divided by the filtrate volume.

2.6 Spectrophotometric CDOM absorption

Following a recommendation by NASA Ocean Optic Protocol for SeaWifs validation (Mueller et al, 2003), the amber bottles used to collect sample filtrate were washed with 10% HCl, rinsed with Milli-Q water and oven-dried at 70^{o} for 5 hours. The bottles were then wrapped with aluminum foil and combusted at 450^{o} for 5 hours to remove any potential organic contaminants. A small volume of CDOM (~150 ml) was collected by filtering the samples through 0.2 μm Whatman Nucleopore polycarbonate filters into pre-acid washed and pre-combusted amber glass bottles. The samples were immediately stored cooled in the dark until analysis in order to prevent any potential bleaching effect from the light. Prior to analysis, the samples were allowed to warm to room temperature before being transferred to a 10 cm cylindrical quartz cell. Optical densities of CDOM, $OD_{s`}(\lambda)$ were measured using a Cary-100 dual beam Spectrophotometer throughout 250 to 800 nm at 1 nm intervals. A separate scan, OD_{bs} (λ) with milli-Q water in both the reference and the sample cells was used as a reference. Optical densities at 750 nm (OD_{null}) where absorption by dissolved materials is assumed to be zero was subtracted from each scan ($OD_s = OD_{s'} - OD_{bs} - OD_{null}$).

Measured optical densities (OD_s) were converted into CDOM absorption by multiplying by a $\log_{10}$ transform value (2.303) and dividing by the cell path length (l =0.1 m).

$$a_{CDOM}(\lambda) = 2.303\frac{OD_s}{l} \qquad 2.5$$

The absorption coefficient at 443 nm was selected as a reference wavelength to represent the CDOM concentration. Spectral absorption by CDOM were fitted between 350 to 600 nm to an exponential function by least square techniques using a function of the form:

$$a_g(443) = a_g\,(\lambda_{ref})\,\exp^{-S(\lambda - \lambda_{ref})} \qquad 2.6$$

where (λ_{ref}) is a reference wavelength, $a_g(\lambda_{ref})$ is the measured absorption value at the reference wavelength (443 nm) and the exponent S determines the spectral slope of the absorption spectrum.

2.7 Absorption from filter-pad technique.

Absorption by particles a_p, and by non-algal particles a_d, were determined using the quantitative filter pad technique (Yentsch, 1962; Mitchell, 1990) with the dual beam Cary-100 Spectrophotometer. This technique consists of concentrating and measuring the optical density of particles on glass fiber filters. The advantage of this approach is that it can enhance the particles optical signal and at the same time can allow light scattering effects to be corrected. The optical density is estimated from the transmittance through a reference, $T_r(\lambda)$ and sample filter, $T_s(\lambda)$ filter.

$$\mathrm{OD}(\lambda) = -\log_{10} \frac{T_s(\lambda)}{T_r(\lambda)} \qquad 2.7$$

The attenuation of the incident beam for the homogeneously dispersed sample can be described by the natural logarithm of the ratio of the emergent and incident beam intensities through the sample.

$$K = -l_g^{-1} \log_e \frac{T_s(\lambda)}{T_r(\lambda)} \qquad 2.8$$

where K is the diffuse attenuation coefficient and l_g is the geometric path length of the sample. The attenuation coefficient is related to optical density, OD_f according to:

$$K = \log_{10}(e) \frac{\mathrm{OD}_f(\lambda)}{l_g} \qquad 2.9$$

If scattering losses are minimized and the detector is configured to maximize the collection of forward scattered light, the absorption coefficient can be approximated by the measured attenuation as:

$$a = 2.303 \frac{\mathrm{OD}_f(\lambda)}{l_g} \qquad 2.10$$

where the constant 2.303 converts $\log_{10}$ to $\log_e$. Multiple scattering may occur from the glass fiber filters due to the optical path length amplification. The optical path length amplification factor (β) is defined as a ratio of the optical path length (l_o) to geometrical path length (l_g) in the sample (Butler, 1962) and must be corrected to obtain accurate absorption coefficients. Another factor that may influence the accuracy of the measured absorption is the loss of scattered light by particles. This is indicated by an offset in the red wavelength, OD_{null} where the absorption by particulate material is assumed to be spectrally flat or zero (Roesler, 1998). Considering the above factors, the absorption coefficient of particulate material on the filter pad is then determined according to:

$$a_p(\lambda) = 2.303\,\frac{OD_f(\lambda) - OD_{null}}{l_g\,\beta} \tag{2.11}$$

where OD_{null} used in this study was determined by the mean absorbance in the range 750 to 800 nm, l_g was calculated as the ratio of the volume filtered, V_f to the soiled area, A_f and β is a pathlength correction factor for multiple scattering. In this study, samples of particulate material were concentrated onto 47 mm Whatman glass fiber filters and the radius of soiled area was measured at 21 mm. Therefore, the soiled area, A_f of particulate material on the filter pad is 1.39×10^{-3} m. Sample filters were wetted with 1-2 drops of fresh Milli-Q water and scanned from 300 to 800 nm in 1 nm increments using a wetted blank filter as a reference. A separate scan of wetted blanks filters, OD_{bs} were used a baseline-correction spectrum and subtracted from each scan ($OD_f = OD_{f`} - OD_{bs}$).

Absorption by non-algal particles, $a_d(\lambda)$ was then determined by repeating the same measurements after extracting the pigments with approximately 15 - 20 ml sodium hypochlorite, NaClO for 5 to 10 minutes (Mitchell et al, 2002). The solution was prepared by dissolving 60 g Na_2SO_4 into 1 liter Milli-Q water containing 0.1% of active chlorine. The preferred volume of active chlorine used to bleach pigments has been empirically shown to be approximately 3 times the optical density of the filter at 443 nm, expressed in ml (Mitchell et al, 2002). The samples were rinsed with 50 ml Milli-Q water to draw the NaClO and dissolved pigments under low vacuum. Bleached sample filters were scanned from 300 to 800 nm in 1 nm increments and a complete bleaching of the pigments is indicated by the absence of a 675 nm pigment absorption peak. Therefore, the particulate and detritus absorption could be estimated as:

$$
\begin{aligned}
\mathrm{a_p}(\lambda) \text{ or } \mathrm{a_d}(\lambda) &= 2.303\ \frac{\mathrm{OD_f}(\lambda) - \mathrm{OD_{750}}}{\left({}^{\mathrm{V_f}}/_{\mathrm{A_f}}\right)\beta} \\
&= 2.303 \text{ x } 1.39 \text{ x } 10^{-3}\ \frac{\mathrm{OD_f}(\lambda) - \mathrm{OD_{750}}}{\mathrm{V_f}\,\beta}\ (\mathrm{m^{-1}}) \qquad 2.12
\end{aligned}
$$

Measured absorbances of particles and non-algal particles were corrected for pathlength multiple scattering using the equation of Cleveland and Weidemann (1993):

$$\beta = 0.378\ \mathrm{OD_f} + 0.523\ \mathrm{OD_f^2}\ ;\ \mathrm{OD_f} \leq 0.4 \qquad 2.13$$

where $\mathrm{OD_s}$ and $\mathrm{OD_f}$ are the corrected and measured optical densities of particles. Spectral absorption by non-algal particles, $a_d(\lambda)$ were fitted to an exponential function by least square techniques using a function of the form:

$$\mathrm{a_d}(\lambda) = \mathrm{a_d}\ (\lambda_{\mathrm{ref}})\ \exp^{-S(\lambda - \lambda_{\mathrm{ref}})} \qquad 2.14$$

where (λ_{ref}) is a reference wavelength, $a_d(\lambda_{ref})$ is the measured absorption value at the reference wavelength (443 nm) and the exponent S determines the spectral slope of the absorption spectrum. The non-algal particle absorption data were fitted over 350 to 700 nm but excluding 450 to 550 nm to eliminate artifacts due to iron-oxide absorption. These artifacts are especially apparent at coastal stations with high mineral content (Figure 2.4). The spectral absorption coefficient by phytoplankton $a_{ph}(\lambda)$ was calculated as a difference between particulate and detritus absorption.

$$a_{ph}(\lambda) = a_p(\lambda) - a_d(\lambda) \qquad 2.15$$

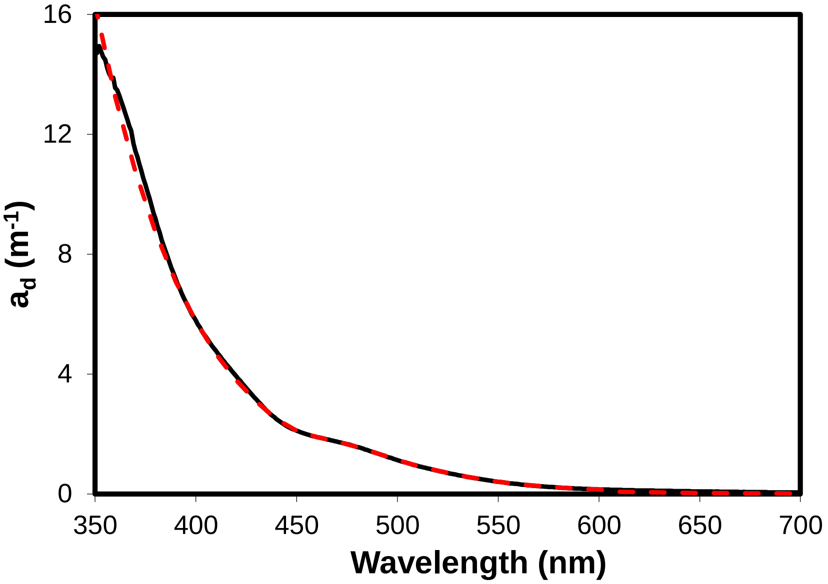

Figure 2.4: Exponential fit into spectral a_d data at station 52 (Nov 12 2009). The solid black line shows the raw data and the red dotted line is the fitted data using λ_{ref} =443 nm. Figure clearly shows a spectral bump between 443 and 550 that might be attributed to the presence of iron-oxide in highly mineral dominated water (Babin et al., 2003). The data of this spectral range was excluded when fitting the curve.

CHAPTER 3

FIELD OBSERVATIONS OF THE BIO-OPTICAL PROPERTIES

3.1 Overview

In this chapter the magnitude of the spatial and temporal variability of the measured bio-optical properties made during the 2009 cruises will be presented. The measurements of bio-optical properties have been grouped into 3 different seasons namely; the southwest monsoon (June to August), northeast monsoon (November) and inter-monsoon (May and October).

3.2 Seasonal variations of surface temperature and salinity

Figure 3.1 shows the seasonal variation in the temperature (^{o}C) and salinity (psu) observed during the measurements in 2009. The surface temperature shows little change although it decreases monotonically throughout the study period with a maximum of 31^{o}C during the spring inter-monsoon season (May) and lowest of 29 ^{o}C during the NEM season (November). This decrease is consistent with seasonal cooling during this period. Water temperatures during the NEM season were almost isothermal with respect to depth, with the subsurface layers especially at near shore stations within 0.5 ^{o}C of the surface layer. The field measurements during this season were performed after a week of exceptionally high rainfall in the East Coast region. The surface salinity demonstrated a wide range of variations increasing from spring inter-monsoon (May) to SWM (July) and then decreasing to the lowest values in August 2009. An increase in salinity was then observed again from fall inter-monsoon month (October) to early NEM month (November). In terms of spatial variation, the salinity gradient (about 10 psu) (not shown) from the coastal towards the offshore water is largest during the NEM (November) season.

Seasonally, the surface salinity ranged from 22 to 33 psu for all stations sampled and thiscould be attributed to the variability in the freshwater discharge as well as water stratification. The T-S diagram shows that the largest range salinity and lowest temperature occurs in November, corresponding to large river discharges emptying into the coastal region and the intrusion of high salinity and colder water masses from the South China Sea. The T-S data for the other seasons shows a larger range in temperature and lower in salinity, corresponding to small freshwater inputs and strong thermal stratification of water column. The scatters of points of low salinity during those seasons were observed at stations close to the river mouth (stations 51 to 52) that is under direct influence of freshwater discharge.

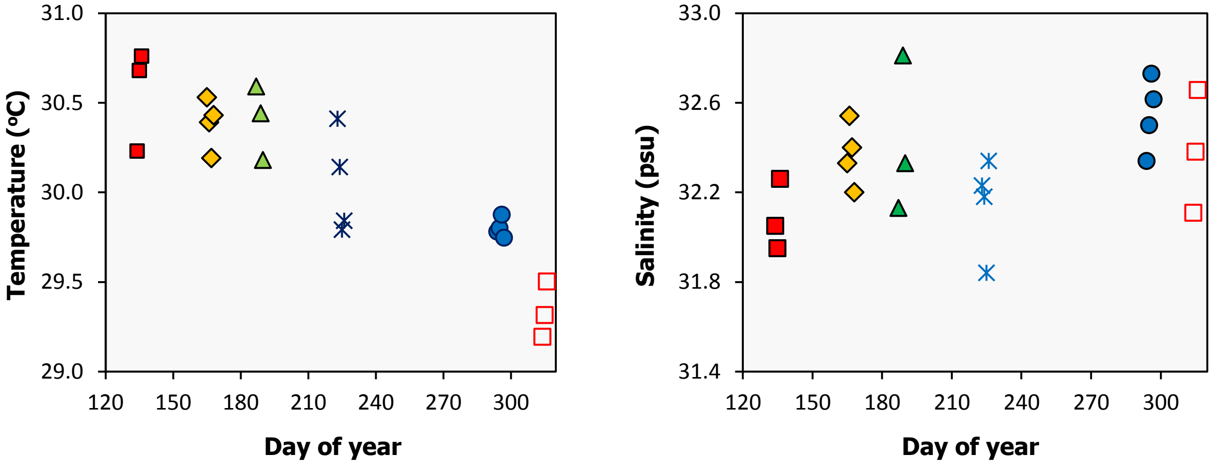

Figure 3.1: Seasonal variation of surface temperature (°C) and surface salinity (psu) as measured in the study area. Only measurements made between 1200 and 1230 hour at offshore stations (St. 7, 20, 34 and 48) are shown. Each survey is represented by a different symbol.

Salinity and temperature cross sections of hydrographic observations by CTD and hydrolab instruments along a transect between stations 28 and 34 throughout the study period is shown in Figure 3.2. In general, the distribution of temperature and salinity in the study area is influenced by monsoonal wind patterns and the introduction of freshwater especially from

Terengganu River during the rainy seasons. The Terengganu River outflow appears as a tongue of low surface salinity and temperature waters that project towards the shelf edge (station 28), flanked on either side by water of higher salinity and temperature (not shown). In general, greater vertical homogeneity in temperature was observed at the shelf edge station (~20 m isobaths) throughout the study period due to water column mixing by tidal stirring. For the offshore stations, the vertical profiles of temperature and salinity showed that stratification began to develop in May (spring inter-monsoon) with a mixed layer depth (MLD) located at about 15 to 20 m. Note that the mixed layer depth used in this study was computed as the depth at which temperature decreased by 1 ^{o}C from the surface temperature (Lamb, 1984; Wagner, 1996). A strong vertical structure of stratification with higher temperature and lower salinity waters overlying a colder and more saline oceanic water body was observed during the SWM season (June to August). The MLD during this season ranged between 5 and 15m. It should be noted that low temperatures at the offshore waters during the Jun to August cruise in Figure 3.2 is caused by diurnal variations in ambient temperatures. During those cruises, all observations were made in the early morning hours from the offshore to inshore stations. Transitional change between stratified and well-mixed conditions was observed in October (fall inter-monsoon) due to strong north winds with poorly defined mixed layer and pycnocline at almost all stations. Strong vertical mixing during the NEM season (November), resulting in vertically homogeneous waters was observed for all stations and the measured salinity and temperature profiles were almost constant with depth. During this season, low surface salinity (<25 psu) and temperature (<29 ^{o}C) were observed to extend until ~30 m isobaths.

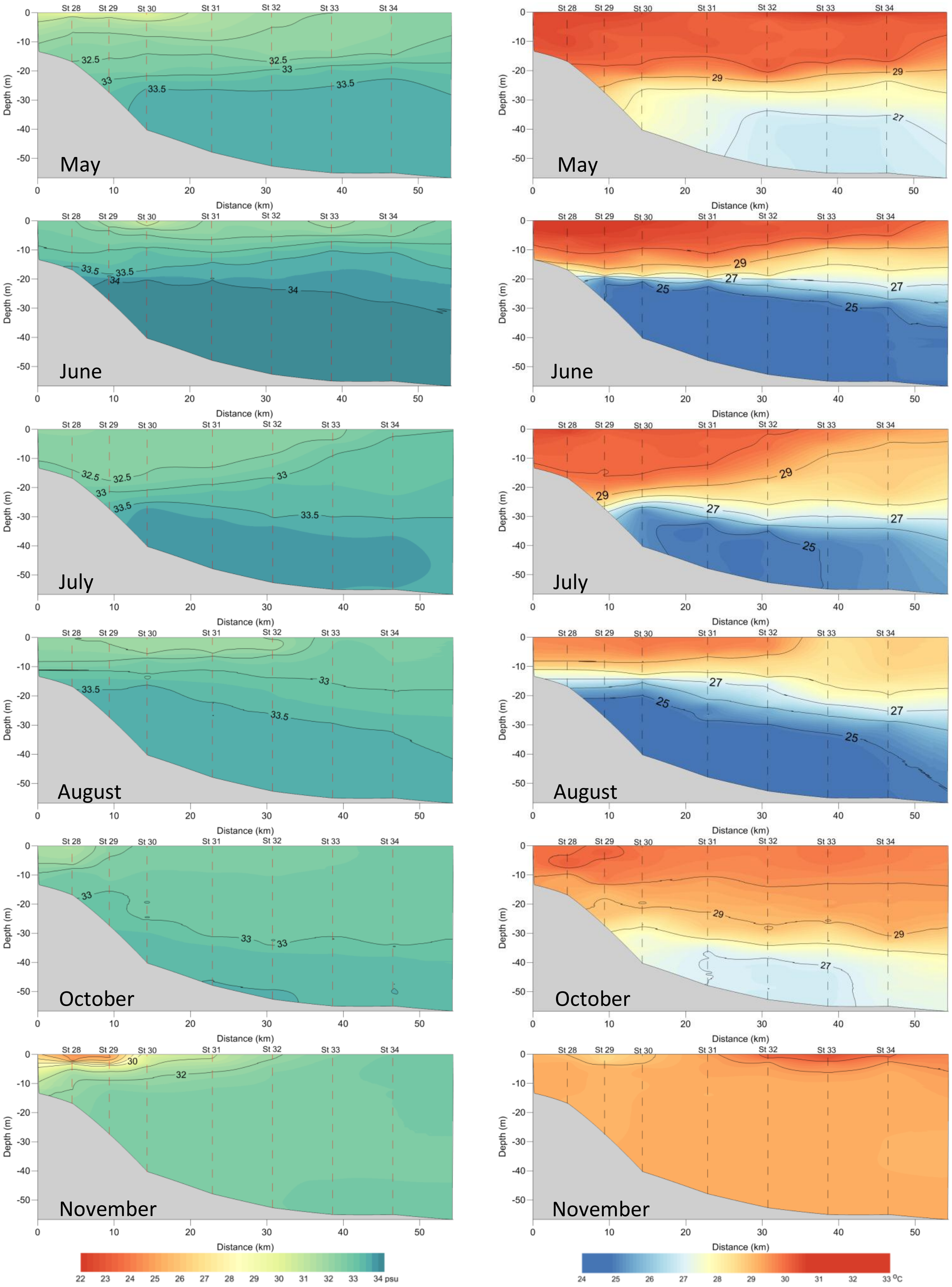

Figure 3.2: Cross-section of salinity (left) and temperature (right) along a transect between stations 28 and 34 for all cruises.

3.3 Variations in ocean-colour constituents

3.3.1 Seasonal variation in chlorophyll concentration

The spatial and temporal distribution of near-surface chlorophyll-a concentration during the six cruises is shown in Figure 3.3 while Table 3.1 summarizes the data range of all in-water constituents measured in this study. With the exception of the May and October cruise, there was a general trend of decreasing concentration with distance from shore. Chlorophyll concentration in the study area showed significant seasonal variations between monsoon periods with a maximum value during the northeast monsoon (NEM) and minimum during the southwest monsoon (SWM) season. Relatively clear waters with low biological activity and low chlorophyll concentration at all stations were observed during the SWM cruises (June to August). During this period there was weak variation in chlorophyll-a distribution with relatively high chlorophyll-a values (± 0.75 mg m^{-3}) found only around the river mouth. At most stations, chlorophyll-a concentration was constant throughout the SWM season and it persisted around 0.40 – 0.45 mg m^{-3}. However, with initiation of the NEM (November) season, there was indication of monsoon impact with the high wind speed enhancing turbulence in water column and large river discharge resulting in a dramatic increase of chlorophyll-a concentration. During this season, high chlorophyll concentration was not only observed at coastal regions but stretching-out into the offshore water. The chlorophyll-a concentration during this period varied from 0.5 mg m^{-3} at the offshore water to 8 mg m^{-3} at the river mouth with an average value of 1.60 mg m^{-3} (SD=1.64). There were some spatial differences found for chlorophyll-a distributions during the inter-monsoon season (May and October). Patchy phytoplankton bloom events which lead to high surface chlorophyll-a concentration (approximately 3 mg m^{-3}) were observed during both months. The patches of elevated chlorophyll-a concentration were mainly located at the offshore stations and the southern part of the study area. The presence of higher chlorophyll values at offshore stations suggest that chlorophyll concentration during this season was not directly influenced by riverine inputs. Due to the occurrence of these phytoplankton blooms, the mean chlorophyll concentration during the inter-monsoon season was sharply increased from 0.4 mg m^{-3} during the SWM to 1.2 mg m^{-3}. It is interesting to note that these phytoplankton blooms have not been reported before in this area during the inter-monsoon season.

Table 3.1: Mean, (minimum, maximum) concentrations of in-water constituents during monsoon and inter-monsoon months. The standard deviation was shown by a * sign. SPM, PIM and MSS samples of July cruise (southwest monsoon) are not shown due to contamination of the distilled water used for rinsing the particle samples.

	Chl-a (mg m^{-3})	CDOM (m^{-1})	SPM (mg l^{-1})	PIM (mg l^{-1})	POM (mg l^{-1})
	Inter-monsoon				
May	1.19 (0.30 - 3.13) 0.79*	0.10 (0.01 - 0.38) 0.10*	1.20 (0.27 – 6.64) 1.70*	0.77 (0.11 – 4.39) 1.12*	0.43 (0.13 – 2.25) 0.60*
Oct	1.14 (0.11 – 2.57) 0.66*	0.06 (0.01 - 0.11) 0.03*	1.01 (0.32 - 4.10) 0.84*	0.60 (0.11 – 3.42) 0.64*	0.44 (0.15 – 2.01) 0.39*
	Southwest monsoon				
June	0.47 (0.20 - 1.13) 0.18*	0.06 (0.03 - 0.18) 0.04*	1.27 (0.29 – 5.83) 1.28*	0.77 (0.09 – 4.95) 0.95*	0.56 (0.08 – 2.07) 0.50*
July	0.43 (0.21 - 1.82) 0.30*	0.01 (0.01 - 0.17) 0.03*	- - -	- - -	- - -
Aug	0.47 (0.25 - 0.98) 0.17*	0.04 (0.01 - 0.13) 0.03*	0.38 (0.18 - 1.80) 0.34*	0.17 (0.07 – 1.27) 0.25*	0.21 (0.10 – 0.53) 0.10*
	Northeast monsoon				
Nov	1.58 (0.46 - 7.74) 1.64*	0.15 (0.01 - 0.43) 0.12*	2.70 (0.20 – 25.80) 5.39*	1.87 (0.11 – 18.80) 3.97*	0.83 (0.09 – 7.00) 1.39*

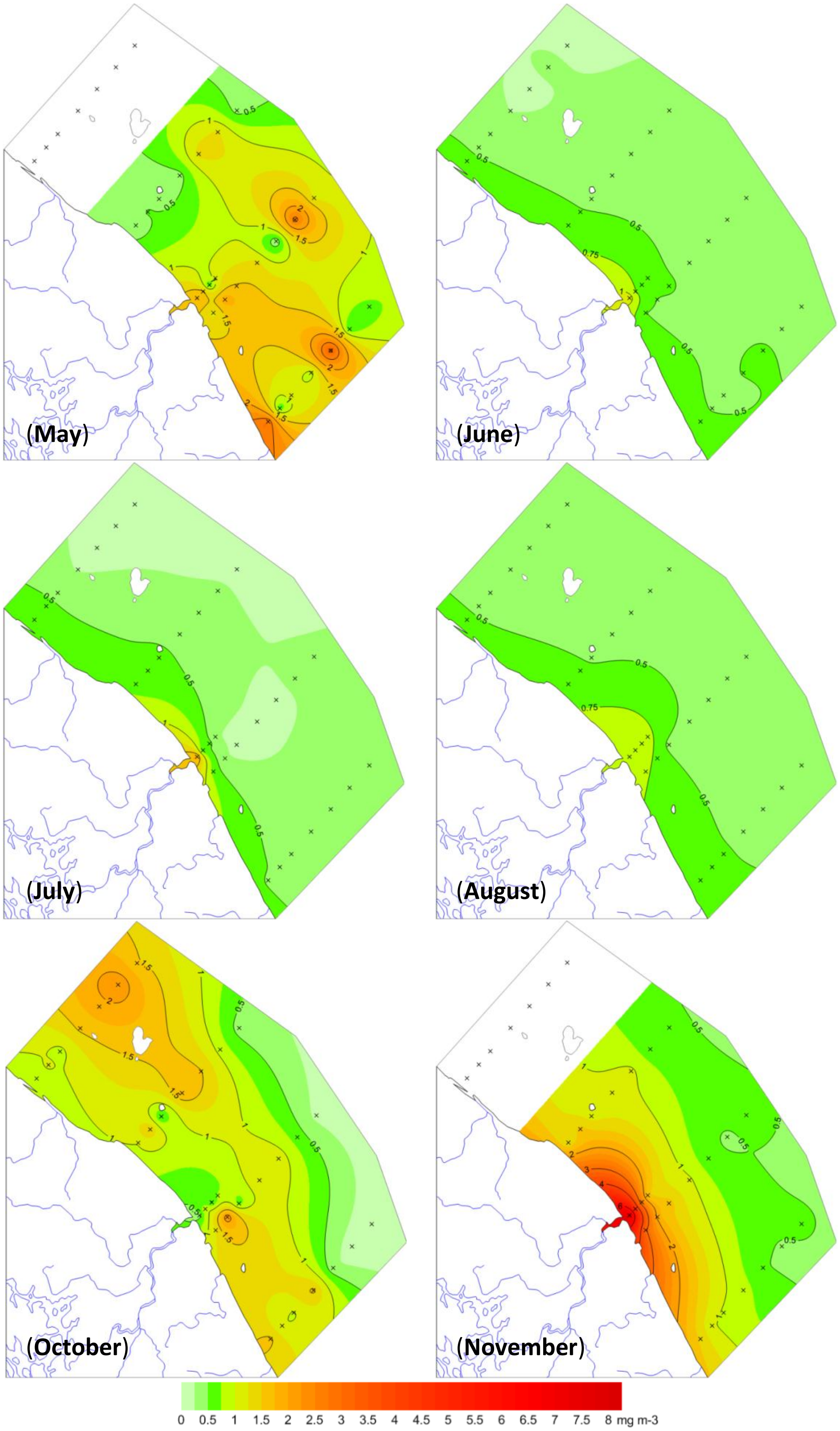

Figure 3.3: Spatial and temporal distribution of near-surface chlorophyll concentration based on in-situ measurements during all cruise periods. No in-situ measurements were performed at stations 1 to 7 during the May and November cruise due to weather constraints. The anomalous chlorophyll maxima at the offshore stations during May and October are due to phytoplankton blooms.

3.3.2 Seasonal variation in suspended particulate matter

Figure 3.4 shows the spatial and temporal distribution of the near surface SPM and PIM concentrations. Samples from the July cruise are not shown due to contamination of the distilled water used for rinsing the particle samples. The SPM concentration in the study area was predominantly inorganic (approximately 60%) and is strongly influenced by seasonal fluctuations in river discharge which varies from daily mean flows of ~300 m^3s^{-1} during the NEM to the SWM minima of ~50 m^3s^{-1} (Mohd-Lokman et al., 1998). Since the contribution of PIM to SPM is nearly constant throughout the study period, the spatial distributions for both PIM and SPM is nearly the same. In general, concentrations of SPM, PIM and POM were more prevalent landward and decreased seaward. All particle concentrations were consistently low and uniform during the SWM season with the mean SPM value less than 1.0 mg l^{-1} (Table 3.1). The concentrations increased slightly during the inter-monsoon period (mean SPM = 1.1 mg l^{-1}) due to increase in river discharge (Figure 3.8) and sediment resuspension by higher wind speeds. Most of the highest concentrations during both seasons were generally found at the stations closest to the river mouth (St 49 – St 52) with SPM concentrations ranged between 0.60 and 2.70 mg l^{-1}. During the NEM season, SPM concentrations were highly variable and there was a very sharp increase in SPM concentrations which reached a maximum of 26 mg l^{-1} (Table 3.1), associated with a significant rain event and extreme wind speeds. The weekly mean discharge of the Terengganu River on the day of data collection was about 2300 m^3s^{-1}, exceeding the recorded mean weekly value for that month. The high levels of SPM (more than 2 mg l^{-1}) were observed to spread beyond 15 km offshore.

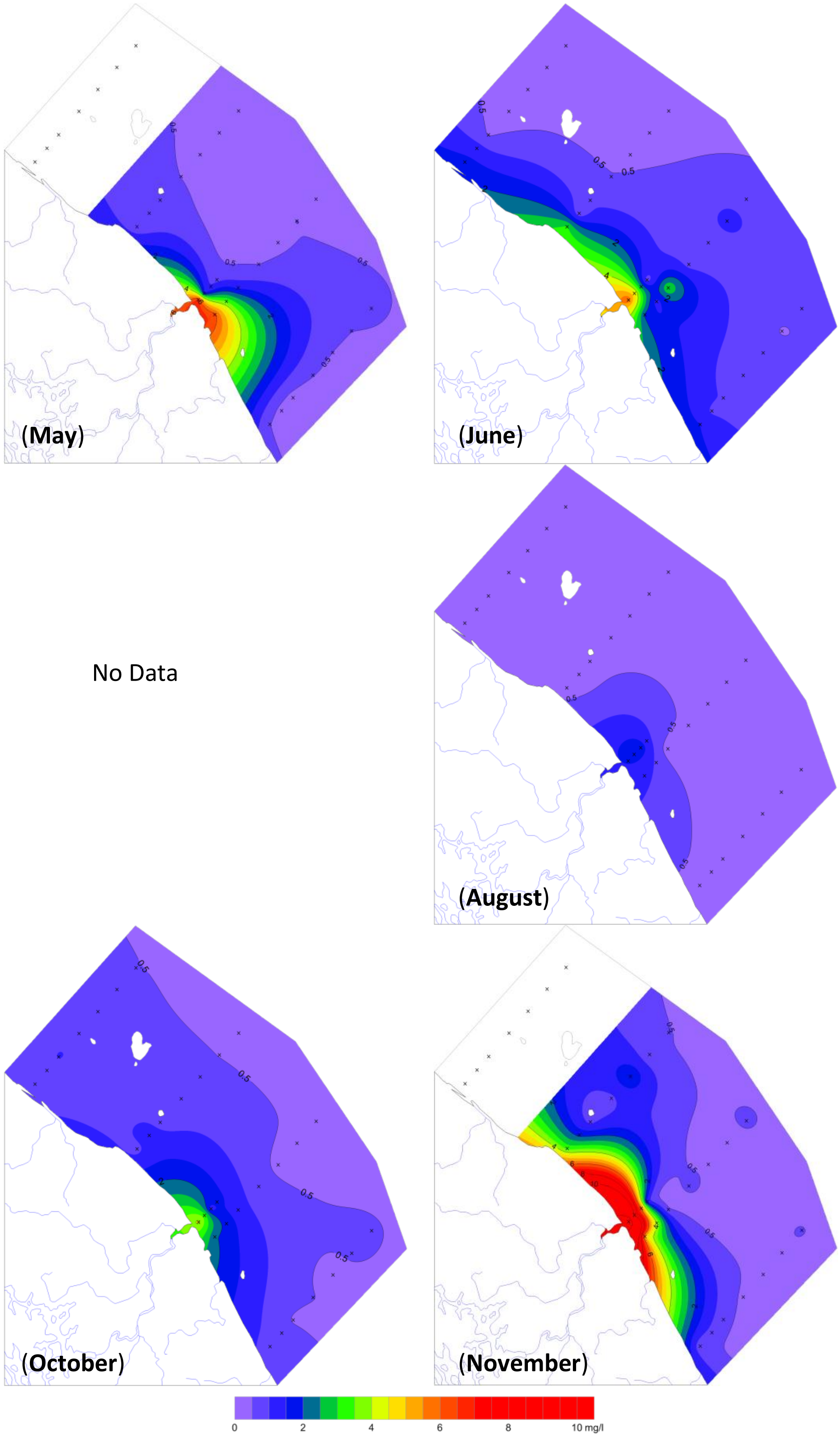

Figure 3.4: Spatial and temporal distribution of near-surface SPM based on in-situ measurements during all cruise periods. No in-situ measurements were performed at stations 1 to 7 during the May and November cruise due to weather constraints.

3.3.3 Seasonal variation in CDOM

The absorption spectrum of CDOM was modeled using the equation 2.6 of Bricaud et al., (1981). The exponential slope, S_g was obtained for each sample and is presented in section 3.5.1. The general spectral curve of CDOM absorption showed an exponential decrease from the maximum values in near ultra-violet wavelength (350 – 400 nm) to zero absorption values, at the red portion of the visible spectrum (700 nm). Since our sampling stations covered both coastal and offshore waters, a large variation of the CDOM absorption spectrum was observed during the cruises which resulted in the large standard deviation shown in Table 3.1.

Absorption spectra and average CDOM absorption coefficients for each sampling period is found in Figure 3.5. Measured individual CDOM absorption, $a_g(443)$ values in the entire dataset ranged from a minimum of 0.01 to a maximum of 0.43 m^{-1}. Relatively higher values of $a_g(443)$ for all study periods were observed along the coastal stations especially stations located very close to the mouth of Terengganu river. Excluding these turbid coastal stations (stations 28, 50 to 52) where $a_g(443)$ was relatively large for all seasons, reduces $a_g(443)$ variability from 0.01 to 0.15 m^{-1}. Surface $a_g(443)$ usually decreased to less than 0.1 m^{-1} and exhibited less variability at stations beyond 40 m isobath. In general, $a_g(443)$ follows the same seasonal pattern as the other water color constituents described before, with the maximum values and minimum variances usually occurred during the NEM season and the minimum absorption values and variance during the SWM season (June – August).

The spatial distributions of $a_g(443)$ for all seasons are shown in Figure 3.6. The spatial and temporal variation in $a_g(443)$ in the study area is largely influenced by freshwater discharge especially from the Terengganu River. As shown in Figure 3.7, the average $a_g(443)$ for all cruises was very well corresponded to a 7-day freshwater discharge from the Terengganu River.

Regression analysis (figure not shown) indicated that mean $a_g(443)$ was highly correlated ($R^2 = 0.99$) with weekly mean river flows, suggesting a strong terrestrial origin of CDOM during the NEM season.

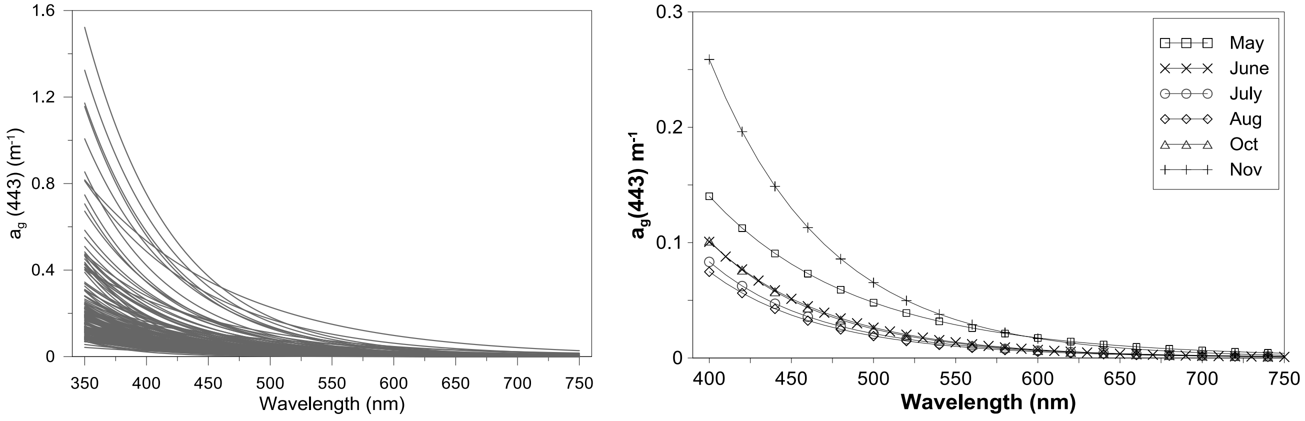

Figure 3.5: CDOM absorption spectra for all seasons (left) and the average spectra for each cruise.

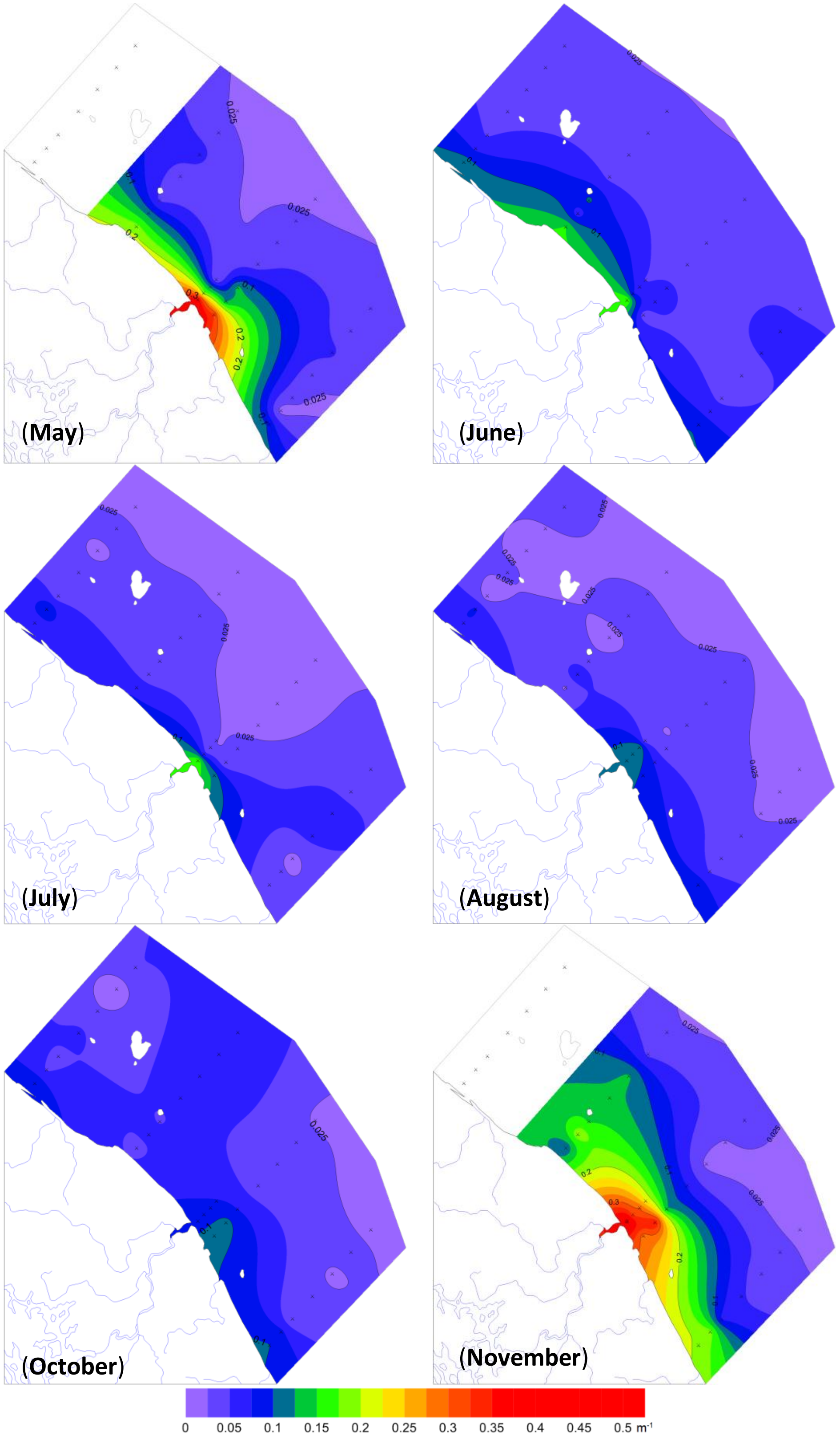

Figure 3.6: Spatial and temporal distribution of near-surface $a_g(443)$ based on in-situ measurements during all cruise periods. No in-situ measurements were performed at stations 1 to 7 during the May and November cruise due to weather constraints.

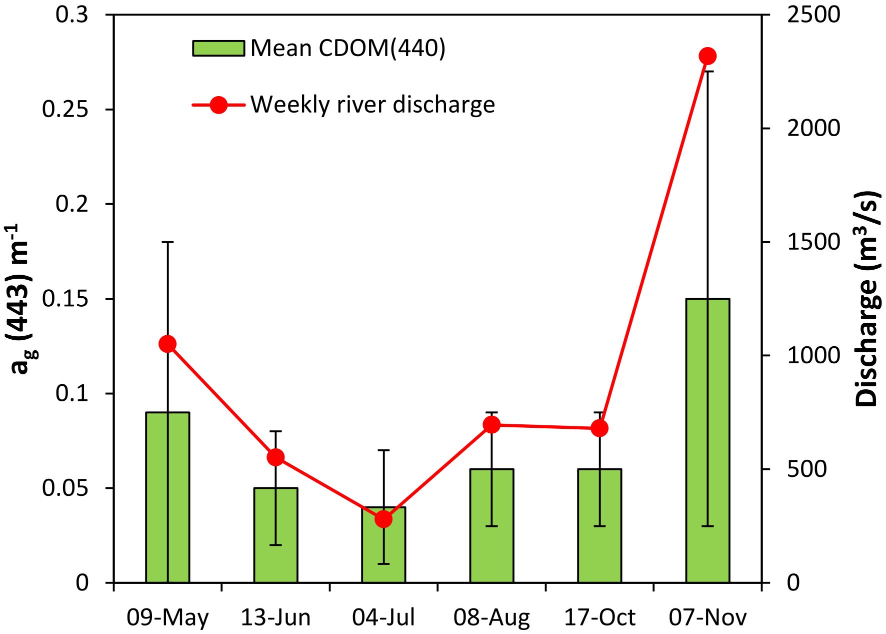

Figure 3.7: Mean and standard deviation of surface $a_g(443)$, and weekly mean freshwater input from the Terengganu River. Source: Department of Irrigation and Drainage (DID) Malaysia.

3.3.4 Coherence of in-water optical constituents

The relationships between CDOM and PIM with chlorophyll concentration for the different seasons are shown in Figure 3.8. Overall, the relationships between CDOM and PIM with chlorophyll for all seasons (not shown) showed a weak correlation. However, when the monsoon (SWM and NEM) and inter-monsoon data were analysed separately, it was found that the CDOM and chlorophyll variables were highly correlated ($p<0.05$; $R^2 = 0.71$) during the SWM and NEM seasons but statistically uncorrelated ($p>0.05$; $R^2 = 0.05$) during the inter-monsoon season. Similarly, the relationship between PIM and chlorophyll is stronger ($p<0.05$; $R^2 = 0.54$) during the SWM and NEM seasons but weak ($p>0.05$; $R^2 = 0.09$) during the inter-monsoon period. The correlation observed between PIM and chlorophyll during the monsoon season (SWM and NEM) was not expected if we consider the negligible proportion of phytoplankton in

PIM. In contrast, a linear regression between CDOM and PIM was significant ($p<0.05$; R^2 = 0.63) for both seasons (monsoon and inter-monsoon).

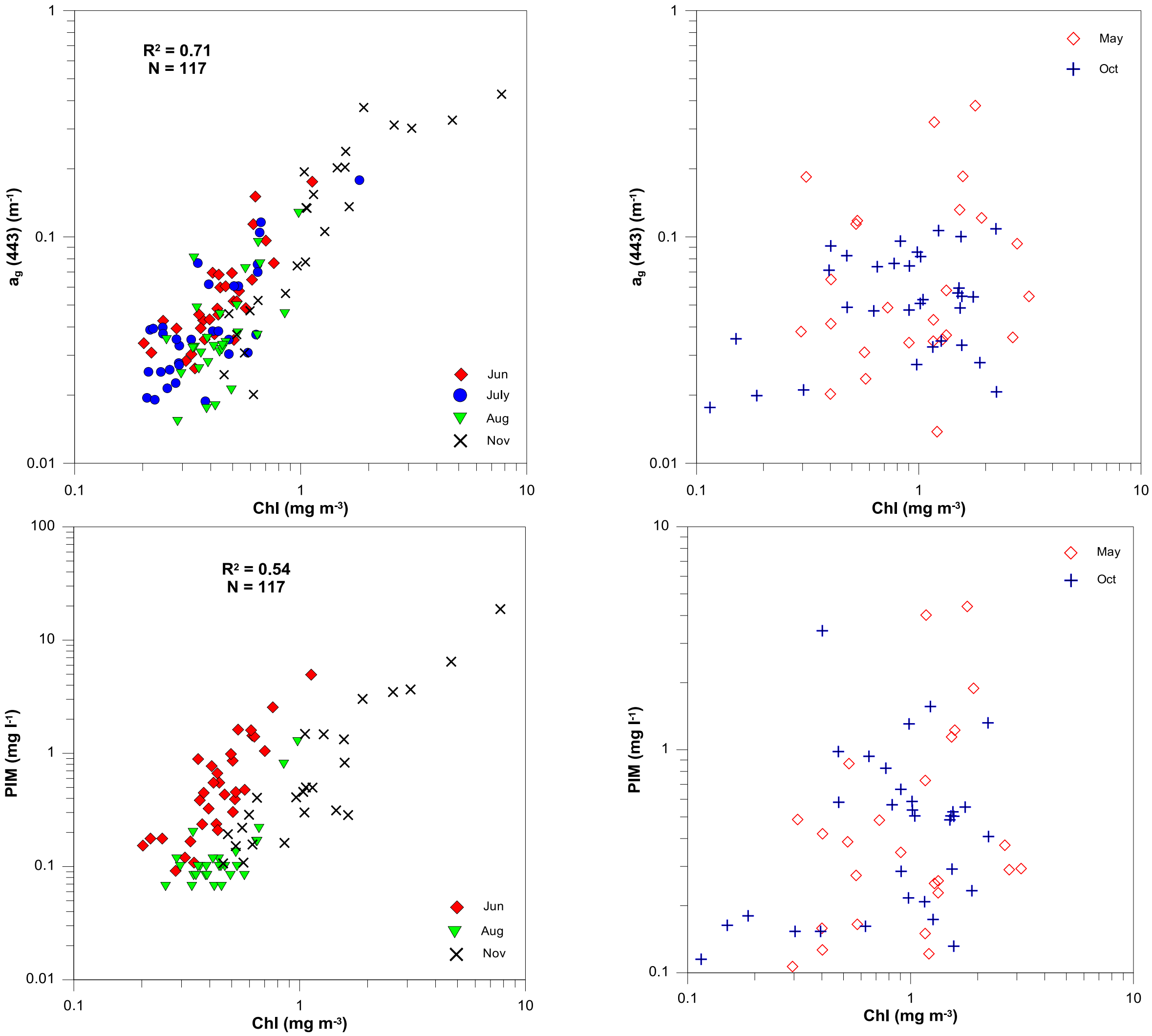

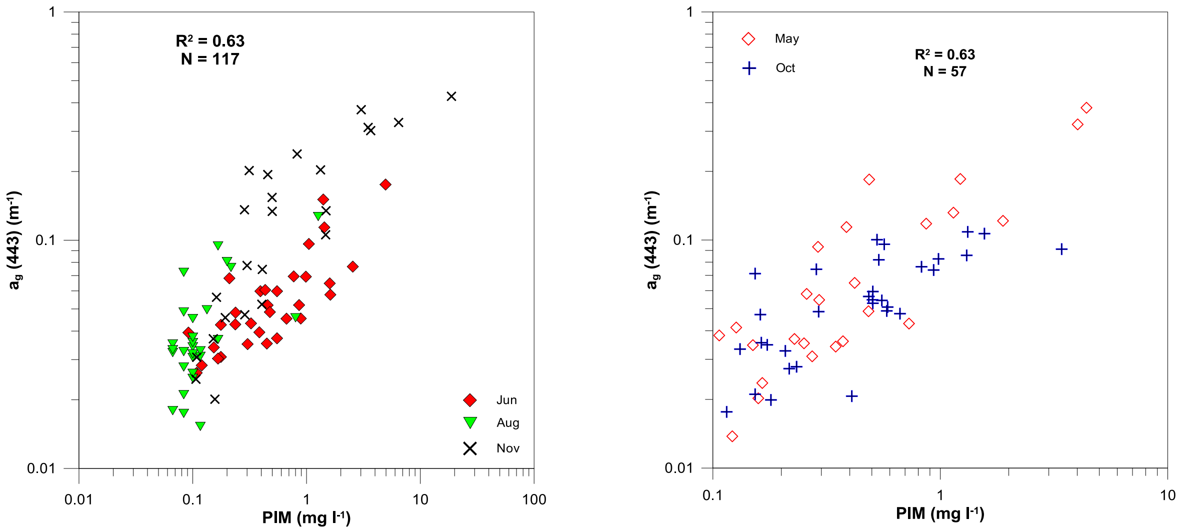

Figure 3.8: Relationships between in-water constituents during (a) SWM and NEM seasons and (b) inter-monsoon season. Note differences in x-axis scaling.

3.4 Variation in Phytoplankton Absorption

The temporal variation in absorption and specific-absorption coefficients of chlorophyll at 443 and 676 measured during the bio-optical cruises are summarized in Table 3.2. Both a_{ph} and a^*_{ph} in the study area were highly variable throughout the season, varied by over an order of magnitude at 676 nm and 443 nm, respectively (Table 3.2 and Figure 3.9). Highest absorption by phytoplankton at 443 and 676 nm was measured during the November cruise, consistent with maximal values of chlorophyll concentration during that season. In general, absorption by phytoplankton decreased during the SWM (June to August) and inter-monsoon (May and October) seasons.

In contrast, the highest values of a^*_{ph} at both 443 and 676 nm were found during the August cruise and the lowest were observed during the May cruise [Figure 3.9 (c)]. During the May cruise, a^*_{ph} (443) was less than 0.01 m^2 mg^{-1} for the chlorophyll range of 0.3-3.1 mg m^{-3}. Differences in the monthly mean of $a^*_{ph}(\lambda)$ were clearly observed in the blue spectral regions, with mean $a^*_{ph}(\lambda)$ during the August and May cruises distinctly separated from the other seasons [Figure 3.9 (d) and (e)]. Most of the phytoplankton absorption spectra in the study area were characterized by the absorption peaks at 443 and 676 nm. Strong absorption in the UV wavelength (around 325 nm) was also observed in some spectra especially during the August cruise (not shown) most probably due to the presence of UV-protective mycosporine-like amino acids (MAAs).

The spectra shape of phytoplankton spectra normalized by the spectral mean of each $a_{ph}(\lambda)$ spectrum (400 – 750 nm) is illustrated in Figure 3.9(a). There was considerable variation around the mean for each cruise, which is attributed to spatial variation in pigment composition. The absorption spectra for all cruises often showed secondary peaks or shoulders around 490 nm and 542 nm. The 490 nm peak may be due to the presence of carotenoid accessory pigments while the 542 nm peak may have been attributable to the presence either by phycoerythrobilin from the cynobacteria assemblages (Sathyendranath et al., 1999) or fucoxanthin, a pigment found primarily in diatoms (Anderson and Barrett, 1986). Both absorption peaks are more pronounced during the November cruise [Figure 3.9(b)]. Despite the high variability observed within cruises, the mean normalized absorption spectra for each cruise do not exhibit significant differences in overall spectral shape.

Table 3.2: Mean, (minimum, maximum) values of a_{ph} and a^*_{ph} at 443 and 676 nm during monsoon and inter-monsoon months. The standard deviation is indicated by a star (*) sign.

	$a_{ph}(443)$ (m^{-1})	$a_{ph}(676)$ (m^{-1})	$a^*_{ph}(443)$ (m^2g^{-1})	$a^*_{ph}(676)$ (m^2g^{-1})
Inter-monsoon				
May	0.022 (0.01-0.043) 0.009*	0.006 (0.002-0.019) 0.004*	0.028 (0.004-0.086) 0.022*	0.007 (0.001-0.023) 0.006*
Oct	0.033 (0.011-0.069) 0.015*	0.008 (0.002-0.022) 0.004*	0.044 (0.009-0.12) 0.030*	0.010 (0.002-0.032) 0.007*
Southwest monsoon				
June	0.021 (0.008-0.092) 0.015*	0.006 (0.003-0.014) 0.002*	0.045 (0.024-0.121) 0.017*	0.013 (0.008-0.018) 0.003*
July	0.020 (0.01-0.085) 0.013*	0.006 (0.003-0.021) 0.003*	0.051 (0.022-0.086) 0.014*	0.016 (0.01-0.027) 0.004*
Aug	0.038 (0.014-0.156) 0.031*	0.007 (0.003-0.017) 0.003*	0.076 (0.04-0.23) 0.041*	0.014 (0.009-0.026) 0.005*
Northeast monsoon				
Nov	0.076 (0.019-0.601) 0.115*	0.017 (0.006-0.07) 0.014*	0.046 (0.024-0.078) 0.014*	0.013 (0.006-0.027) 0.006*

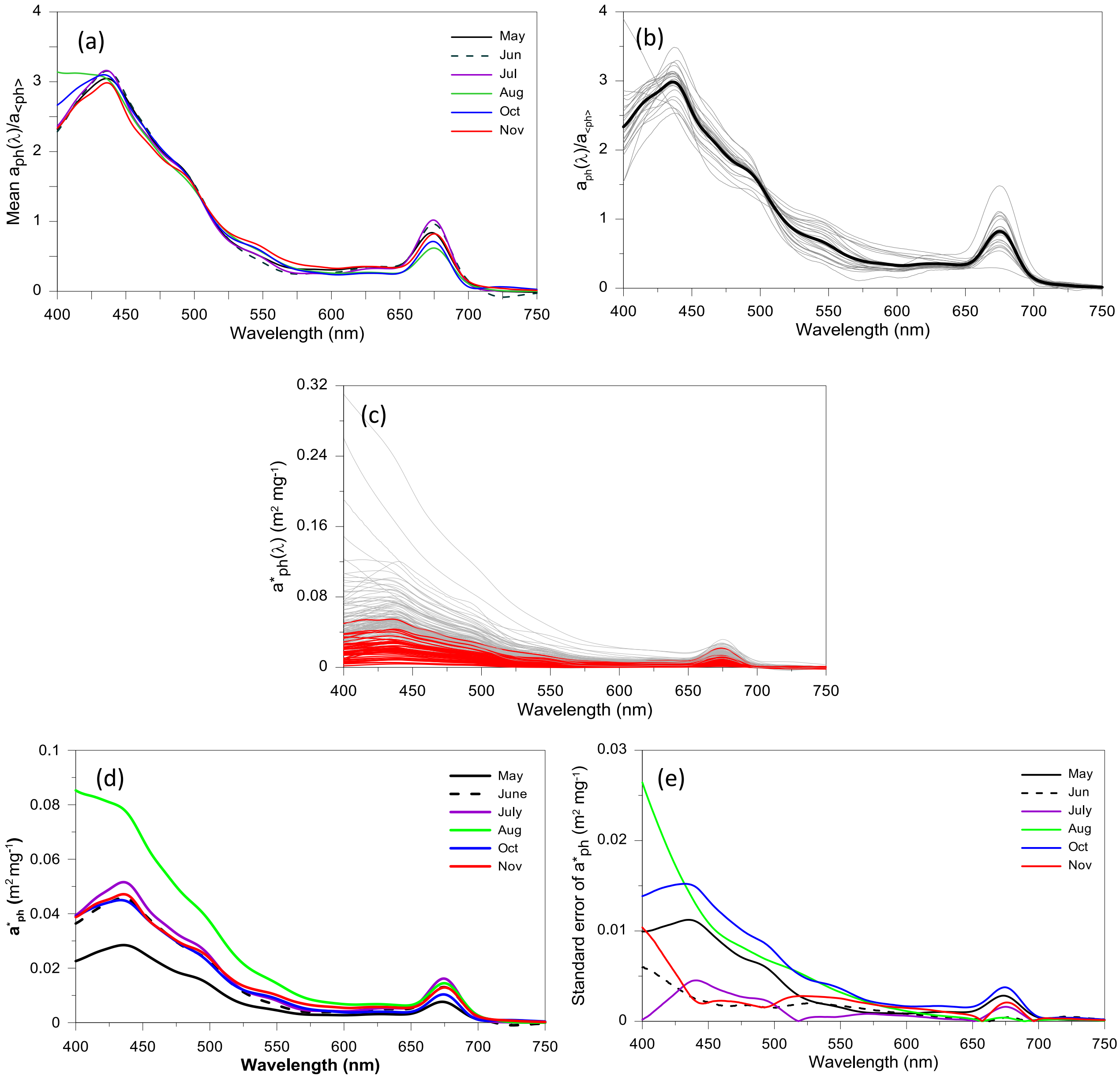

Figure 3.9: Panel (a) Mean normalized phytoplankton absorption spectra measured during all cruises. Panel (b) The individual spectra (grey lines) and the spectra average (solid line) during the NEM cruise. The spectra have been normalized by dividing $a_{ph}(\lambda)$ by the mean a_{ph} over the spectral range 400 – 750 nm. Panel (c) In-situ measured spectra of $a^{*}_{ph}(\lambda)$ during monsoon seasons (grey lines) and inter-monsoon (red lines). Panels (d) and (e) Mean of chlorophyll-specific phytoplankton absorption spectra (in $m^2\ mg^{-1}$) along with standard errors for each cruise.

The relationship between phytoplankton absorption coefficients at 443 and 676 and the chlorophyll concentration are shown in Figures 3.10 and 3.11. The relationship between chlorophyll and phytoplankton absorption is typically defined as a power function (Bricaud et al., 1995, 1998; Prieur and Sathyendranath, 1981):

$$a_{ph}(\lambda) = A(\lambda)[Chl]^{-Eph(\lambda)} \qquad 3.1$$

where A(λ) and $E_{ph}(\lambda)$ are wavelength dependent parameters that can be derived by least square fits of the log-transformed data at 443 and 676 nm. Results showed that there were differences for the fitted coefficients for each season. Therefore, for the sake of simplicity, the monsoon data (SWM and NEM) were separated from the inter-monsoon data. The most significant, positive increase in $a_{ph}(443)$ and $a_{ph}(676)$ with chlorophyll concentration were observed during the SWM and NEM cruises when chlorophyll explains between 84% and 91% of the variability in a_{ph} at 443 and 676 nm, respectively, as indicated by R^2 values. It is apparent from the Figure 3.10a that the $a_{ph}(443)$ and chlorophyll relationship during the August cruise (solid green triangles) had a higher slope compared to the other cruises, suggesting a varying accessory pigments composition among different cruises. Stronger linear relationship between $a_{ph}(676)$ and chlorophyll concentration indicated that the variability of chlorophyll-specific absorption coefficient at 676 nm was small. The results also revealed that there was no relationship ($R^2 < 0$, $p > 0.01$) observed between phytoplankton absorption either at 443 or 676 nm and chlorophyll concentration during the inter-monsoon period [Figure 3.10(b) and (d)]. The variability in the Bricaud et al., (2004) dataset is shown with solid lines. A possible cause of poor relationship between phytoplankton absorption coefficients and chlorophyll concentration during the inter-monsoon season is the package effect. We return to this part later.

The relationships between chlorophyll-specific absorption coefficients at 443 and 676 nm and chlorophyll concentration were also examined separately for the monsoon (SWM and NEM) and inter-monsoon seasons (Figure 3.11). Similar to what was observed by Bricaud et al. (1995), there was tendency of a^*_{ph} to increase with decreasing chlorophyll concentration for some of the measured a_{ph} samples. This has been explained in the past as a package effect that results from the decreased in efficiency of light absorption per unit chlorophyll in larger cells, where chlorophyll is packaged and self-shaded inside the cells. In the present study, the chlorophyll concentration was related in a linear fashion to the a^*_{ph} values at both 443 and 676 nm wavelengths during the inter-monsoon season [Figure 3.11(b) and (d)]. This relationship appears more pronounced at 443 nm with greater coefficient of determination than at 676 nm. Unlike during the inter-monsoon season, the a^*_{ph} at 443 and 676 nm showed no significant relationship with chlorophyll concentration during the SWM and NEM seasons [Figure 3.11(a) and (c)], indicating minimal package effects during this season.

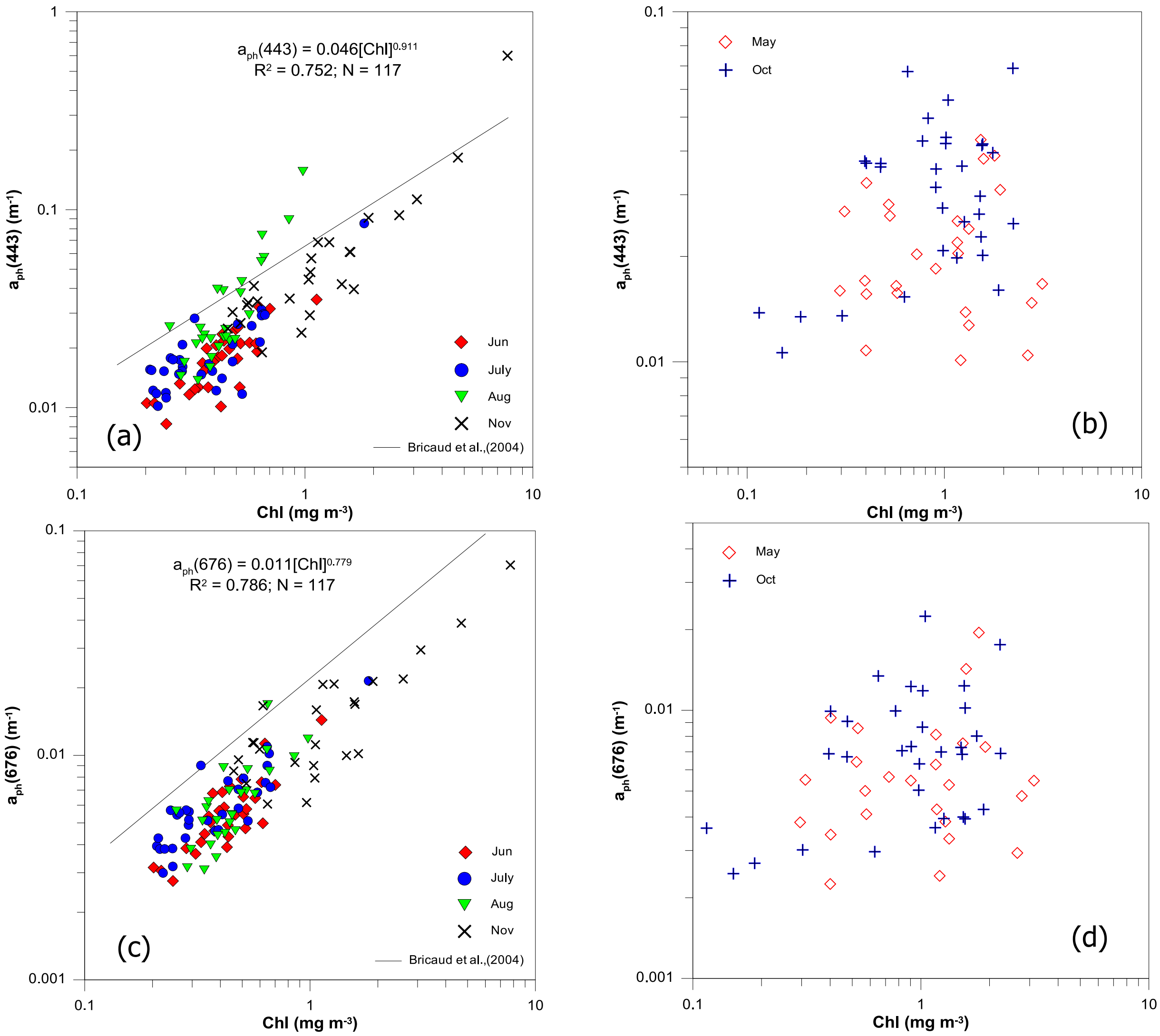

Figure 3.10: Absorption coefficient of phytoplankton at 443 and 676 nm as a function of chlorophyll concentration for (a) the SWM and NEM samples and (b) for the inter-monsoon samples. All relationships were fitted as the power-law function to $y=a[x]^b$. The solid line in panels (a) and (c) shows the trends in the Bricaud et al., (2004).

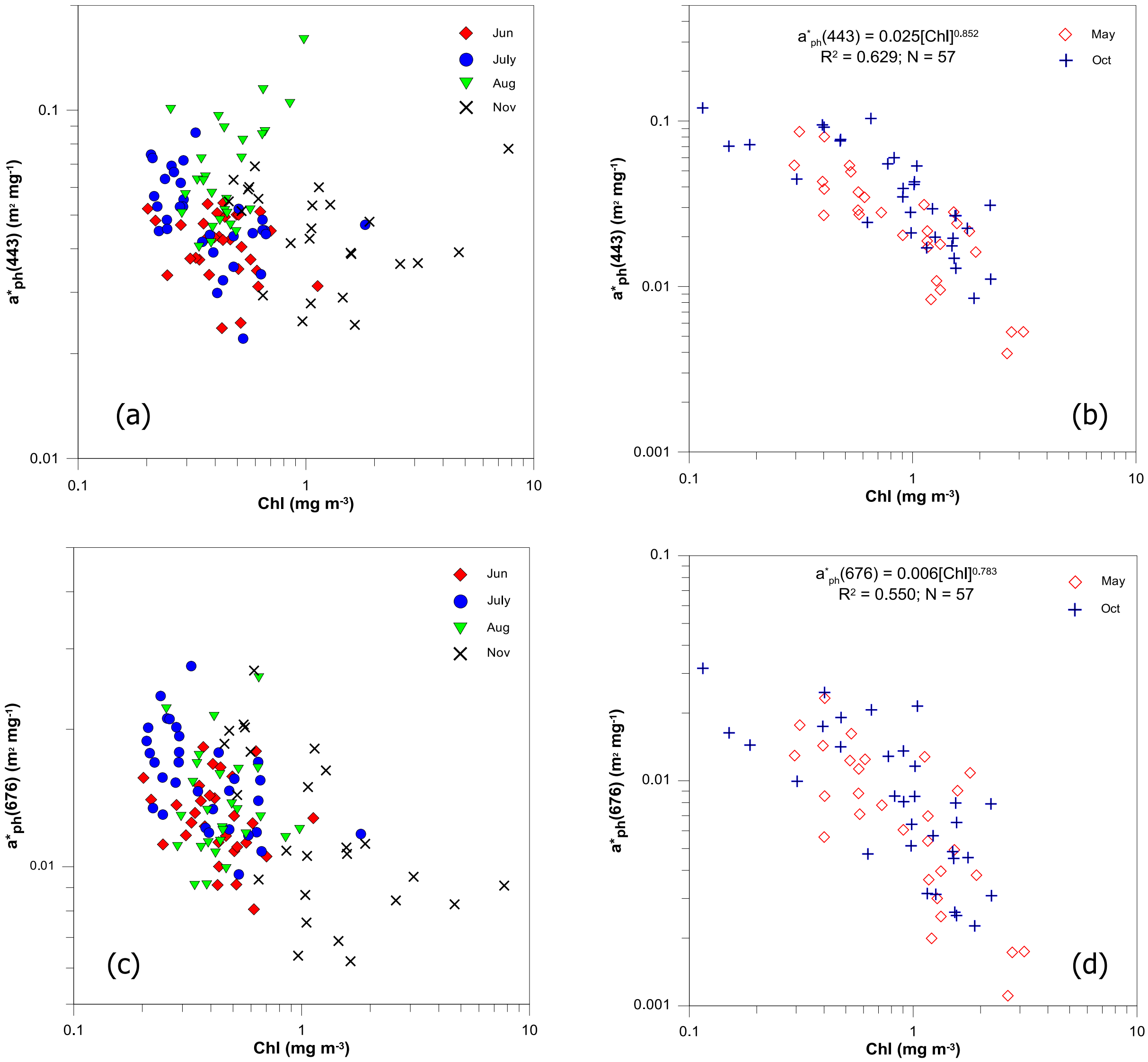

Figure 3.11: Specific-absorption coefficient of phytoplankton at 443 and 676 nm as a function of chlorophyll concentration for the SWM and NEM samples [(a) and (c)] and for the inter-monsoon samples [(b) and (d)]. All relationships were fitted as the power-law function to $y=a[x]^b$.

3.5 Variation in non-pigmented absorption

3.5.1 CDOM spectral slope and its dependence on salinity

Absorption by CDOM is usually parameterized as an exponential function with a single slope parameter, S_g (Bricaud et al., 1981). S_g may indicate the relative proportion of the various sources of chromophores found in the CDOM pool. Figure 3.12 shows the comparison between the measured and fitted $a_g(\lambda)$ values at 350, 380, 400, 412, 490 and 555 nm after applying a least square regression of the log-transformed data in the wavelength regions 300 – 700 nm. The fitted $a_g(\lambda)$ values were well-correlated with the measured a_g values in the wavelength 350 to 490 nm but showed a deviation from a 1:1 line at 555 nm.

Across seasons, S_g ranged from 0.009 to 0.026 nm^{-1} with a maximum and minimum mean value found during the June and November cruise, respectively. The mean value of S_g estimated during each cruise is provided in Table 3.3 and a histogram of values shown in Figure 3.13. Overall, the mean value of S_g estimated for all 174 samples collected during the cruises was 0.016 nm^{-1} with a standard deviation of 0.003 nm^{-1}.

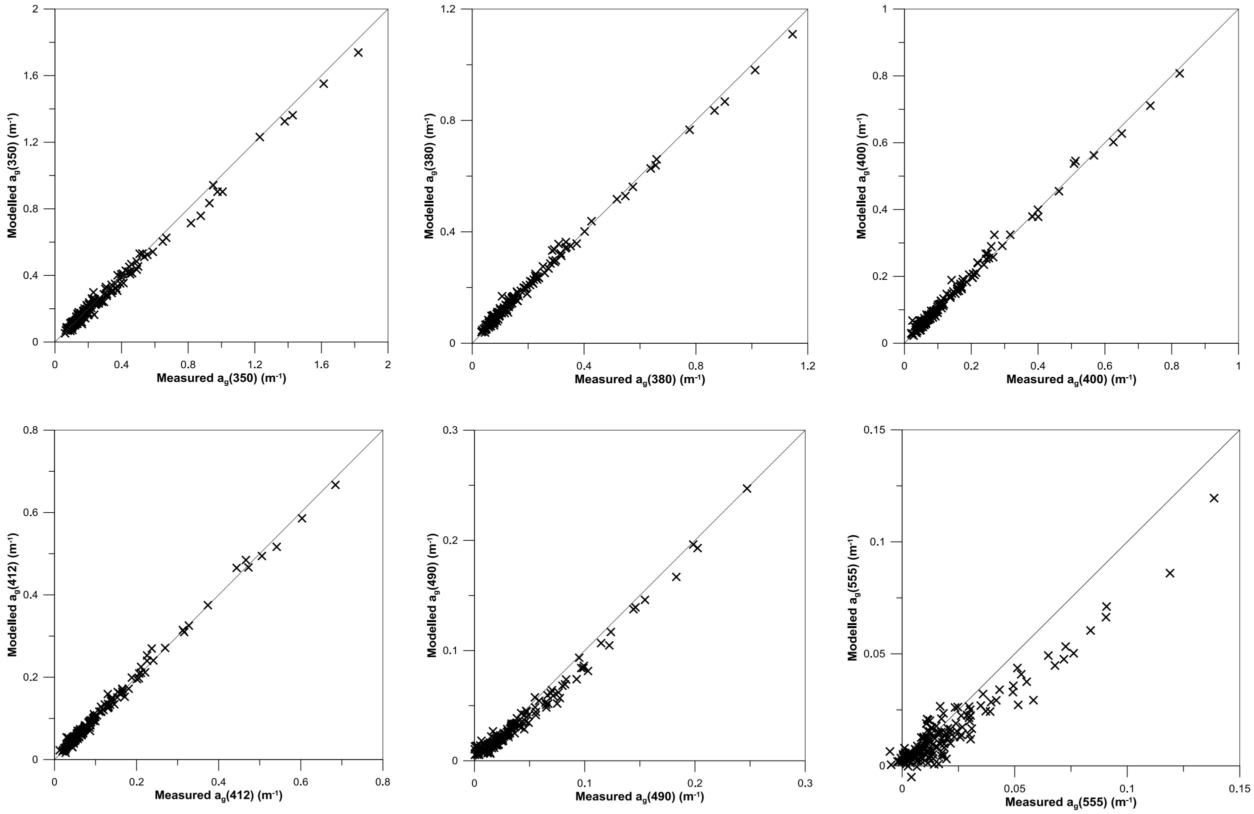

Figure 3.12: Comparison between measured and fitted a_g at the UV (350 and 380 nm) and visible wavelengths (400, 412 and 555 nm).

Table 3.3: Mean, minimum and maximum S_g values measured during all study periods in the study area. Units: nm^{-1}.

	Inter-monsoon		SWM			NEM	All cruises
	May	Oct	June	July	Aug	Nov	
Mean	0.014	0.017	0.015	0.017	0.017	0.013	0.016
Min	0.009	0.014	0.013	0.009	0.012	0.010	0.011
Max	0.019	0.022	0.018	0.025	0.020	0.021	0.021
Stdev	0.003	0.002	0.001	0.004	0.003	0.002	0.003

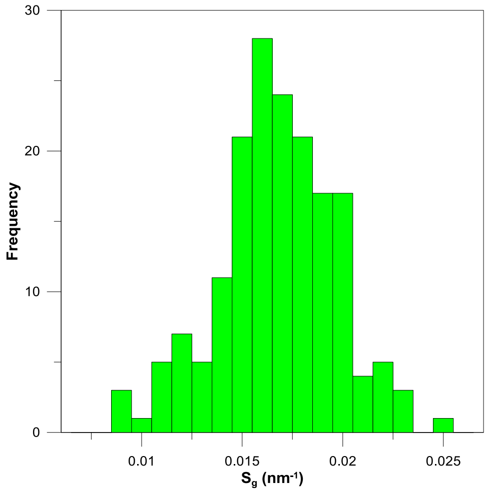

Figure 3.13: Frequency histogram of the S_g measured for all seasons.

Figure 3.14(a) shows the relationship between $a_g(443)$ and salinity for all sampled seasons. In general $a_g(443)$ covaried linearly and inversely with salinity, indicating a strong terrestrial origin of CDOM in the study area. The most conservative CDOM mixing were found in May and November when particularly low salinity waters were found in the inshore regions. High coefficient of determination (R^2 = 0.93) for both months (not shown) is also associated with strong river flows (Figure 3.7) during those sampling periods. For the other sampling seasons, non-conservative CDOM mixing curves (scattered points) were found with coefficients of determination, R^2 ranged from 0.1 to 0.4 (not shown). Plotting S_g against $a_g(443)$ [Figure 3.14(b)] shows that S_g is most variable at low CDOM absorption (i.e low river flow and offshore stations) but tends towards a constant value of about 0.013 nm^{-1} at high absorption.

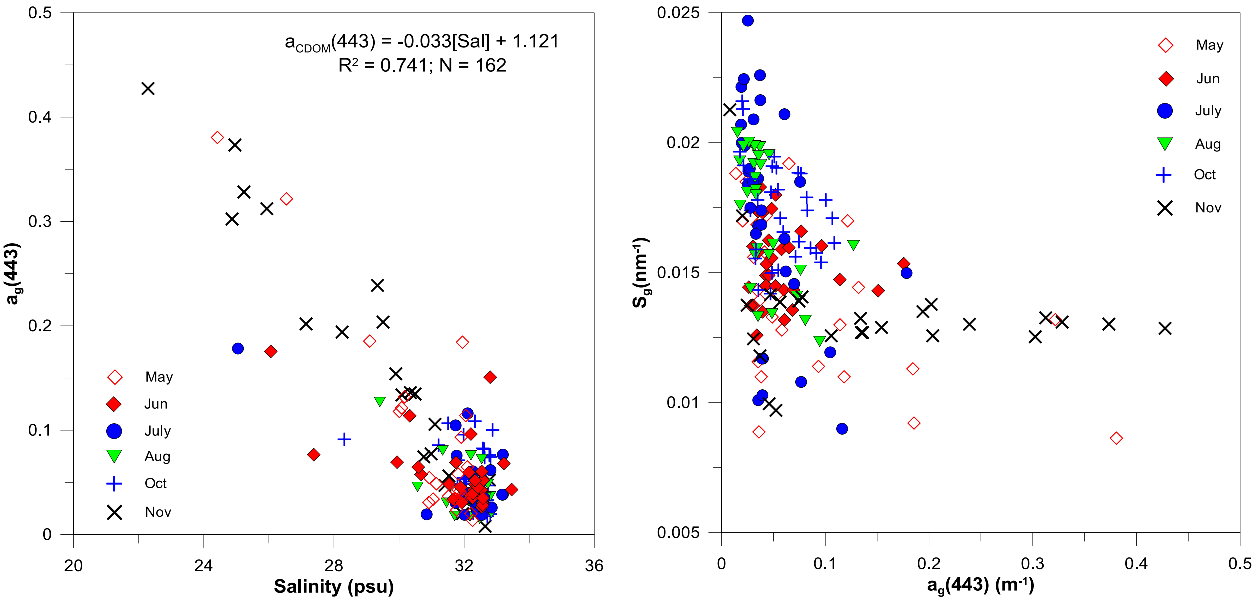

Figure 3.14: (a) Relationship between $a_g(443)$ and salinity for all cruises. (b) Relationship between S_g and $a_g(443)$ for all cruises.

3.5.2 Detritus absorption coefficient

The Quantitative Filter Technique (QFT) of Mitchell (1990) has been used to separate the total absorption coefficient into contributions by the particulate and dissolved fractions. Detrital absorption (a_d) used in this study is described as absorption by both biologically derived non-pigmented and inorganic particles and was calculated from the absorbance of detritus after sodium hypochlorite extraction of pigments.

The absorption spectra and the mean values are shown for each cruise in Figures 3.15(a) and (b). The detritus absorption values for all seasons varied within a broad range with the mean value during the NEM season were about two orders of magnitude higher than in other seasons. An extreme value of $a_d(443)$ (0.235 m^{-1}) was observed during the NEM season at station 52, where a maximum in surface PIM concentration (18 mg l^{-1}) was also observed. Table 3.4 summarizes the statistics of detritus absorption measured at several wavelengths (350, 380, 400, 412 and 443 nm) during the cruises in the study area. In general, the spatial distributions of $a_d(443)$ in the study area were prevalent landward and progressively decreased seaward. The distribution of $a_d(443)$ is also associated with freshwater flows and winds speed with maximum and minimum absorption values were found during the high and low-period of Terengganu river discharge and monsoon wind.

The general spectral absorption curve for detritus is similar to that of CDOM with near zero absorption values in the red region (700 nm) increasing exponentially with decreasing wavelength to maximum values in near UV wavelengths (350 – 400 nm). Due to the similar exponential shape of the absorption curve, detritus absorption was modelled according to the Roesler et al., (1989) exponential function:

$$a_d(\lambda) = a_d \times e^{-S_d(\lambda - 443)} \qquad 3.2$$

where S_d is an exponential slope and a_d is a magnitude of absorption at 443 nm. In this study, the mean spectra value of $a_d(\lambda)$ for wavelength regions 350-650 nm were used to estimate the exponential slope of detritus absorption, S_d. Although the $a_d(\lambda)$ showed the typical negative exponential decrease within the visible region, at some stations (especially near the river mouth) we systematically observed spectra with a bump between 450 – 550 nm [Figure 3.16 (c)]. A similar feature in the absorption spectrum of detritus has been reported by Bowers and Binding (2006) and Babin et al. (2003). According to Babin et al. (2003), these spectral features were most likely attributed to the presence of iron oxide associated with highly mineral-dominated water. Our results revealed that $a_d(\lambda)$ could be accurately estimated from the exponential function ($R^2>0.99$). The S_d values ranged from 0.013 to 0.016 nm^{-1} with maximum values found during the August and November cruises, and minimum values during the July cruise. The statistics of estimated values of S_d are shown in Table 3.5.

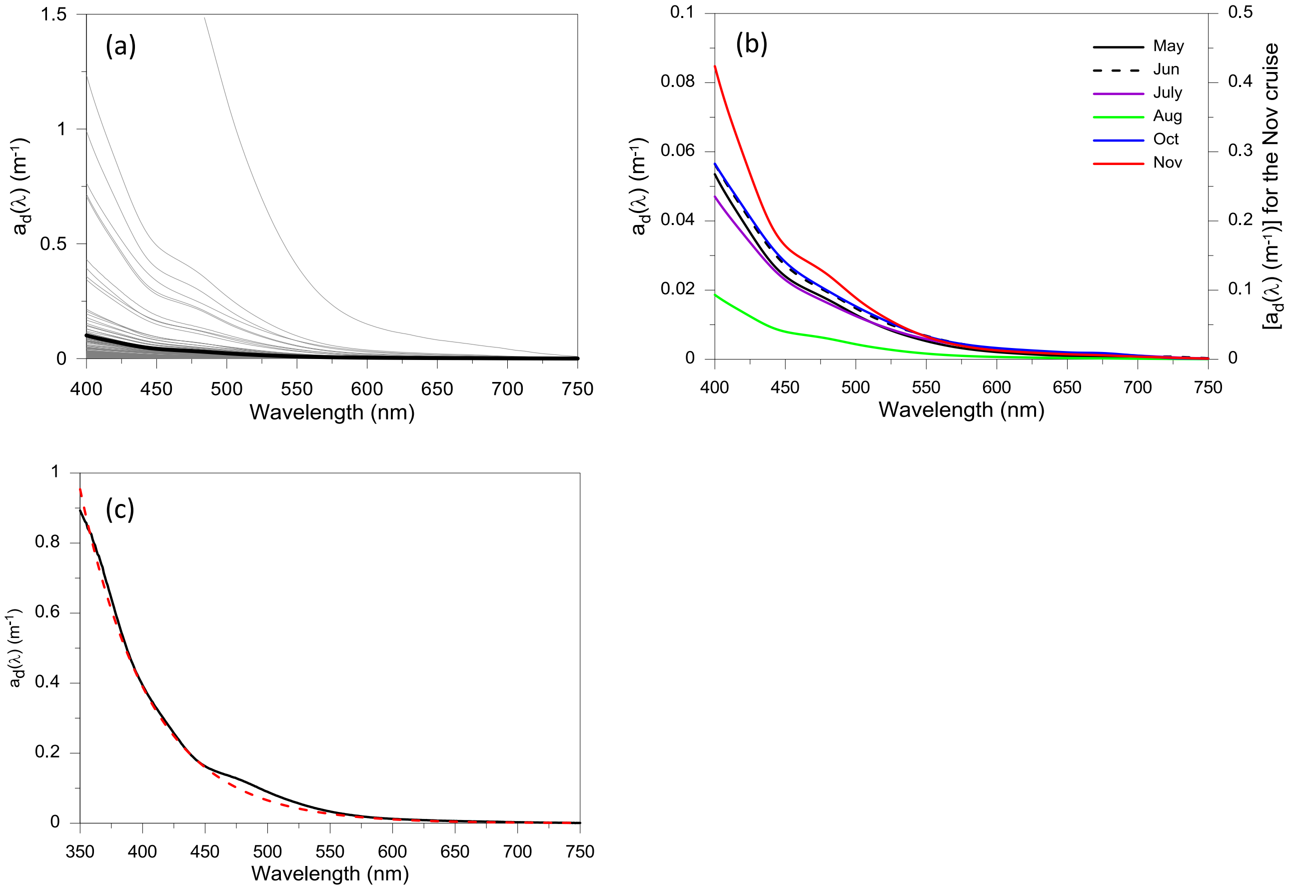

Figure 3.15: (a) Detritus absorption spectra for all cruises. The average spectrum is shown by the solid line. (b) The average detritus absorption spectra for each season. Note that the second Y-axis (right axis) refers to detritus absorption values for the November cruise. (c) Example of a detritus absorption spectrum (solid line) and the corresponding exponential fit (dashed line) at Station 28 on 15th May 2009.

Table 3.4: Mean, (minimum, maximum) values of detritus absorption at 350, 380, 400, 412 and 443 nm during monsoon and inter-monsoon months. The standard deviation was shown by a * sign.

	350 nm	380 nm	400 nm	412 nm	443 nm
Inter-monsoon					
May	0.109 (0.009-0.899) 0.222*	0.074 (0.006-0.582) 0.146*	0.054 (0.004-0.394) 0.100*	0.045 (0.004-0.323) 0.083*	0.027 (0.002-0.181) 0.047*
Oct	0.098 (0.006-0.695) 0.138*	0.073 (0.004-0.489) 0.099*	0.057 (0.004-0.358) 0.073*	0.050 (0.003-0.301) 0.062*	0.032 (0.002-0.183) 0.038*
Southwest monsoon					
June	0.101 (0.008-.872) 0.173*	0.073 (0.005-0.601) 0.120*	0.056 (0.004-0.433) 0.086*	0.048 (0.003-0.359) 0.072*	0.030 (0.002-0.210) 0.042*
July	0.086 (0.013-1.606) 0.284*	0.06 (0.009-1.077) 0.190*	0.046 (0.007-0.765) 0.135*	0.039 (0.006-0.636) 0.112*	0.025 (0.004-0.375) 0.066*
Aug	0.041 (0.005-0.457) 0.095*	0.027 (0.003-0.310) 0.065*	0.018 (0.002-0.215) 0.045*	0.015 (0.001-0.179) 0.037*	0.009 (0.001-0.098) 0.020*
Northeast monsoon					
Nov	1.086 (0.019-15.239) 3.125*	0.67 (0.012-9.166) 1.882*	0.435 (0.008-5.772) 1.187*	0.352 (0.007-4.592) 0.945*	0.187 (0.005-2.356) 0.486*

Table 3.5: Mean values of S_d (in nm^{-1}).

	Inter-monsoon		SWM			NEM	All cruises
	May	Oct	June	July	Aug	Nov	
Mean	0.013	0.012	0.012	0.011	0.016	0.016	0.013
Min	0.010	0.009	0.009	0.008	0.012	0.012	0.008
Max	0.018	0.015	0.016	0.016	0.020	0.021	0.021
Stdev	0.002	0.001	0.002	0.002	0.002	0.002	0.002

The detritus specific absorption coefficient was calculated as:

$$a_d^*(\lambda) = \frac{a_d}{PIM} \qquad 3.3$$

Figure 3.16 shows $a_d(443)$ plotted against PIM on a log-transformed scale and a linear regression forced through the origin. A significant linear relationship between PIM and $a_d(443)$ was observed in the study area with a slope of the regression was about 0.11. The average specific detritus absorption coefficient for all seasons derived from equation 3.3 is shown in Figure 3.17. Table 3.6 shows mean and standard errors of a_d normalized to PIM concentration for selected wavelengths. The mean $a^*_d(443)$ measured separately for each cruise ranged from 0.03 to 0.08 m^2g^{-1}, encompasses the range of $a^*_d(443)$ found in other oceanic waters. Results also indicate that mean $a^*_d(\lambda)$ values increased from May to November.

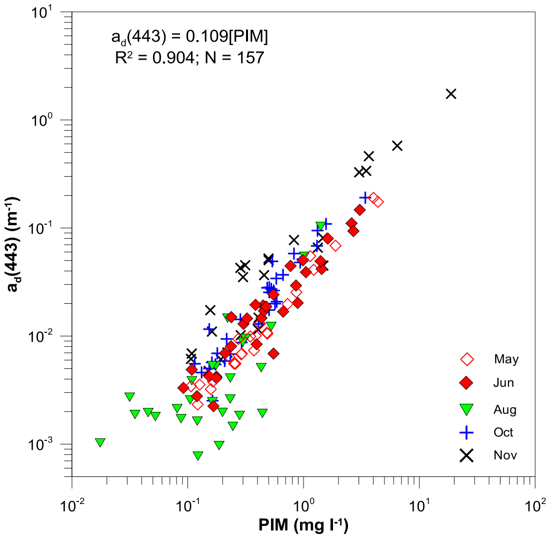

Figure 3.16: Relationship between PIM and $a_d(443)$. Note that the regression fit was forced through the origin.

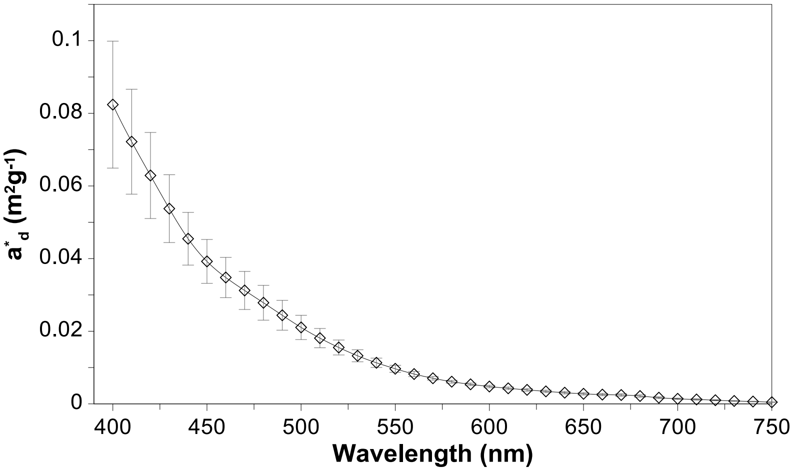

Figure 3.17: Average specific detritus absorption coefficient spectrum for all seasons. Error bars represent one standard error.

Table 3.6: Mean and standard error (std error) of the ratio $a_d(\lambda)$:[PIM] (m^2g^{-1}) for a selection wavelength.

Wavelength (nm)		May	June	Aug	Oct	Nov	All cruise
400	mean	0.051	0.061	0.067	0.080	0.152	0.082
	std error	0.009	0.007	0.023	0.012	0.036	0.017
412	mean	0.044	0.053	0.056	0.070	0.128	0.070
	std error	0.007	0.006	0.019	0.010	0.028	0.014
443	mean	0.029	0.036	0.035	0.048	0.079	0.045
	std error	0.004	0.003	0.010	0.006	0.013	0.007
490	mean	0.015	0.020	0.019	0.025	0.043	0.024
	std error	0.002	0.001	0.006	0.003	0.007	0.004
510	mean	0.011	0.015	0.014	0.020	0.031	0.018
	std error	0.002	0.000	0.004	0.002	0.005	0.003
555	mean	0.005	0.008	0.007	0.010	0.014	0.009
	std error	0.001	0.001	0.001	0.000	0.001	0.001
650	mean	0.001	0.002	0.002	0.004	0.005	0.003
	std error	0.000	0.000	0.000	0.001	0.000	0.000

3.6 Contribution of Absorption Components to Total Absorption

From the measurements of absorption by a_g, a_d and a_{ph}, it was evident that non-pigmented components or coloured detrital matter (a_g and a_d) affect light absorption in the blue region while a_{ph} dominated the red region. The contributions of a_g, a_d and a_{ph} to the total non-water absorption at 443 and 676 nm are shown in ternary plots in Figure 3.18. We found that the a_g was the main absorber at 443 nm throughout the cruise campaigns, contributing on average about 54% of the total absorption budget. The highest contribution of a_g to the total absorption coefficient at 443 nm was observed during May when it makes up nearly 60% of the total non-water absorption. On average, the a_{ph} and a_d coefficients contribution to the total non-water absorption were 28% and 18% respectively. The most striking and unexpected feature was the high $a_{ph}(443)$ contribution during the August cruise with an average of 41%. During this month, contribution by $a_d(443)$ has the lowest percentage of about 6%. Due to the peak in phytoplankton absorption at 676 nm, the $a_{t\text{-}w}$ in this wavelength was significantly dominated by a_{ph} (80 – 90%) with only small fraction (10 – 20%) due to a_d and a_g. The lower value of a_g and a_d in this wavelength was also due to the exponential decrease of those components with increasing wavelength. However, at some stations especially near to river mouth, the percent contribution of CDOM to the total non-water absorption was observed to be as high as 80%.

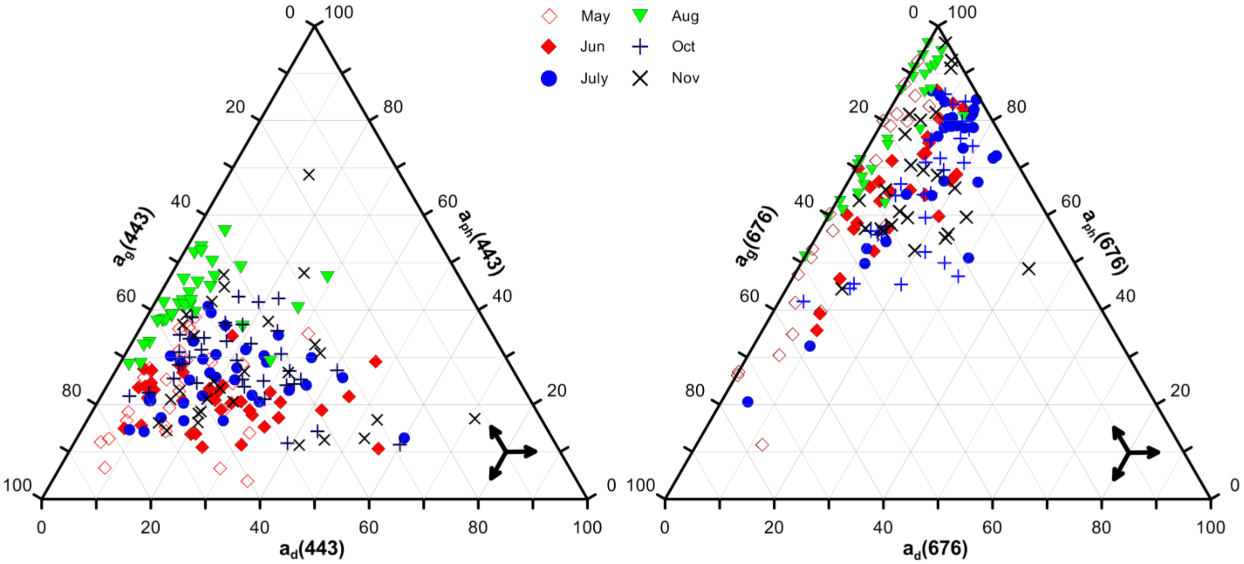

Figure 3.18: Ternary plot illustrating the relative contribution of a_g, a_d and a_{ph} to total non-water absorption at 443nm (left) and 676 nm (right).

3.7 Discussion and conclusion

The results of vertical and horizontal distributions of absorption properties and optical constituents of the surface waters provided a glimpse of optical dynamic in the east coast of Peninsular Malaysia for the first time. For the study period which represented the monsoon and non-monsoon conditions, the optical variability of these waters was a function of assemblage of optical constituents, which in turn was related to oceanographic conditions and the river discharge of the study area. Seasonal differences in oceanographic conditions between the monsoon periods were indicated by deep mixing due to intense wind forcing during the NEM and stratified water column driven by large surface heating during the SWM period. All these physical forcings determined the nutrient availability in the euphotic zone and their impacts are especially obvious in season with shallower mixed-layer depths like the NEM season. These variations produce noticeable differences in optical constituents and absorption coefficients with the highest values occurring in the NEM season, nearly 2 orders of magnitude higher than in other seasons. Spatial variations between seasons was also evident with high measured values stretching-out offshore during large influxes of freshwater discharge in NEM period but limited to a narrow band along the coastal water in other seasons. The observation during the monsoon periods is consistent with previous observations of Tang et al., (2003, 2004) and Liu et al., (2002) in South China Sea waters. While hydrographic characteristics of water stratification and river discharge clearly associated with the spatial distribution of non-pigmented particles (SPM and CDOM) during the inter-monsoon seasons, its influences on chlorophyll concentration at offshore stations is not clear. The phytoplankton blooms in this area during the spring and fall inter-monsoon have not been reported before. In fact, previous studies (eg., Tang et al., 2003, 2004; Liu et al., 2002) reported the oligotrophic nature of the South China Sea waters during the inter-monsoon season. Since the study area is under stratified conditions and large river flows are absent during this period, inter-monsoon blooms imply some other sources of nutrients into the euphotic zone. We speculate that the inter-monsoon blooms are fueled by upwelled nutrients from deeper water through short-lived upwelling (usually persists for only 1 or two weeks) driven by strong offshore winds. This explanation was supported by QuickScat surface winds data. Strong surface winds (>15 m/s) were observed over the offshore waters on 1 May 2009 and 4-7 October 2009, nearly 2 weeks before the field measurement.

A depressed or flattened in the magnitude of $a^*_{ph}(\lambda)$ within the upwelling waters during the inter-monsoon season is consistent with an increase in the pigment packaging effect (Bricaud et al., 1995; Stuart et al, 1998). An inverse relationship between a^*_{ph} (at 443 and 676 nm) and chlorophyll concentration provides a clear evidence that the magnitude of packaging effect is greater during this season than during the monsoon periods. Some of the differences of $a^*_{ph}(\lambda)$ observed in our study area can indeed be related to 2 main factors; changes in phytoplankton cell size and changes in pigment composition. Lower a^*_{ph} and greater pigment packaging effects are generally associated with chlorophyll-rich phytoplankton cells, since light absorption by phytoplankton is scaled to their cross-sectional area and/or self-shaded of the highly packaged cells decrease the light absorption efficiency per unit chlorophyll. Taking into account of these factors, we might expect that large phytoplankton cells dominate during the inter-monsoon and smaller cells during the monsoon seasons. There was some evidence to support this hypothesis in samples from inter-monsoon and monsoon seasons. A notable secondary absorption peak at 542 nm for almost all phytoplankton spectra was observed during the monsoon seasons. It is known that phycoerythrobilin from cynobacteria assemblages (i.e. generally small cells) have an absorption band in this wavelength (Moore et al., 1995). This observation is also supported by the findings of Sathyendranath et al., (1999) who found a similar absorption peak in cynobacteria dominated waters in the Arabian Sea. During the inter-monsoon season, a relative abundance of diatoms in the study area and nearby regions has been reported. For examples, in October (fall inter monsoon), Md-Suffian (unpublished data) observed the abundance of large diatoms (>60μm) off the east coast of Peninsular Malaysia water. Chua (1970) and Tham (1973) observed the consistent blooms of *Hemidiscus sp.*,*Coscinodiscus* and *Chaetoceros spp*. during the inter-monsoon periods in the Singapore Straits. In situations such are those described for the inter-monsoon season, we therefore postulate that remote sensing of chlorophyll that use the blue and green parts of the spectrum might not work well during these periods. As noted by Hoepffner and Sathyendranath (1992), variations in the proportion of the diatoms pigment relative to chlorophyll a can change the blue-green ratio of phytoplankton absorption by a factor of up to 6, and hence could impact water-leaving radiances.

In all season studied, light absorption by seawater at blue wavelengths was constantly dominated by CDOM absorption rather than by phytoplankton pigment which often did not covary with CDOM absorption. If we define Case 1 water as those where $a_{ph}(443)$ represent more than 60% of the total nonwater absorption (IOCCG, 2000), almost all of the data in our study area are classified as Case 2 water. In this case, strong light absorption by non-phytoplankton material (CDOM and detritus) could potentially have significant implications on the estimation of chlorophyll in the blue spectral region, especially when CDOM absorption does not covary with chlorophyll concentration. This is well marked by the situation of the inter-monsoon periods when both pigment packaging effects and non-covarying CDOM were observed. These effects make it difficult for any remote sensing algorithm to provide reliable estimation of chlorophyll concentration. Although the impact of varying absorptions of phytoplankton and CDOM on the blue-green reflectance ratio is difficult to confirm without further modeling analysis, it has been shown that high non-phytoplankton material could alter the absorption coefficients and tend to overestimate chlorophyll estimations from satellite ocean colour observations (e.g. Hu et al., 2000; Gons et al, 2002; Harding et al., 2005). At least for the monsoon periods, the weaker package effect and interference from non-phytoplankton absorptions in the red part of the spectrum might allow us to use the phytoplankton absorption at 676 nm to accurately estimate chlorophyll concentration from ocean colour data.

The slope of CDOM, S_g varied through a wide range and showed a clear seasonal trend with low CDOM concentration (southwest monsoon) often showed much greater range of S_g values than during high CDOM season (northeast monsoon). The large variability of S_g at low CDOM concentration may be due to local production by phytoplankton as well as to photo-bleaching during the summer stratification when CDOM is restricted to a very shallow mixed layer. A relatively constant S_g during the NEM season is probably caused by mixing of water masses with different CDOM sources (marine and freshwater) as suggested by several authors (e.g. Blough et al., 1993; Nelson and Guarda, 1995; Vodacek et al., 1997). This is clearly evident by a significant inverse relationship between salinity and CDOM during this period. The high variability of S_g in the study area could have a significant influence on the performance of ocean colour as it would diverge substantially the magnitudes of a_g and a_{ph} when applying in bio-optical algorithms (Hu et al., 2006).

The absorption by detritus (inorganic particles) contributes the least for the total non-water absorption with spectral dependence of $a_d(\lambda)$ was well represented by an exponential function, similar to that of CDOM spectral shapes. An absorption spectral slope S_d, of 0.013 nm^{-1} is consistent with findings in other regions (e.g. Bowers et al., 1996; Bricaud et al., 1998; Babin et al., 2003). The overall average a^*_d ($a_d(\lambda)$/[PIM]) at 443 nm (0.048 ± 0.09 m^2 g^{-1}) when compared to other studies , is close to those found by Bowers and Binding, [2006](0.05 ± 0.07 m^2 g^{-1}), Binding et al., [2003](0.054± 0.003 m^2 g^{-1})and Babin et al., [2003](0.041 ± 0.02 m^2 g^{-1}).

In summary, the optical properties in our region are strongly associated to seasonal variations. Although our data sets represent the seasonal scenario during the 2009 cruise but they are insufficient to describe the long term variability of optical properties, and more intensive investigation that includes other important biological parameters (phytoplankton size classes and species composition) is required. Nevertheless, our results provide for the first time bio-optical properties in this region. The analysis of seasonal changes in bio-optical properties provided the basis for the required knowledge to develop more realistic algorithms for satellite monitoring of ocean colour in this region.

CHAPTER 4

REMOTE SENSING REFLECTANCE: IN-SITU OBSERVATIONS AND MODELS

4.1 Overview

This chapter describes the various bio-optical models relating in-water constituents (chlorophyll and CDOM) and some inherent optical properties to reflectance measurements. The in-situ data from the Satlantic Hyper OCR underwater sensor is used to develop more accurate local algorithms based on detailed in situ bio-optical characteristics of the study area. The main objective of this section is to assess the applicability of the chlorophyll and some of the inherent optical properties algorithms used by MODIS satellite data and examine alternative algorithms based on the blue-green band ratios. Empirical and semi-analytical chlorophyll algorithms and other absorption algorithms using the blue-green wavelengths are evaluated and discussed. To allow for inclusion of sufficient data, match-up analysis will be using up to ±28 hours satellite data. Overall algorithm performances were assessed by comparing their predicted values (C_{est}) with those measured (C_{mea}) in the laboratory. Systematic and random errors of this comparison were quantified by the mean absolute percentage difference (MAPD) and root mean square error (RMSE), respectively.

$$MAPD = \frac{\sum |(C_{est} - C_{mea})/C_{mea}|}{N} x\, 100 \qquad 4.1$$

$$RMSE = \sqrt{\sum \frac{(C_{est} - C_{mea})^2}{N}} \qquad 4.2$$

4.2 MODIS chlorophyll algorithms

Only MODIS reflectance data (Aqua and Terra) is used in this study to make a comparison with Satlantic HyperOCR data and to help evaluate the developed algorithmic equations. No SeaWiFS clear images are available during the period of study. These daily data with a 1 km resolution were taken from the Ocean Color website (http://oceancolor.gsfc.nasa.gov/). The wavebands and minimum and maximum R_{rs} values in the study area are tabulated in Table 4.1. The most important artifact of MODIS R_{rs} is the negative values found for the red-end wavelengths (645 – 678 nm). These negative values were not only found at coastal stations but also at offshore regions. A reason for such effects could be a failing of the atmospheric correction due to typical aerosol types used by a SEADAS atmospheric corrections schemes (Siegel et al., 2000). In this study, the bands with negative values were discarded from analyses to avoid obvious numerical problems in the tested algorithms.

Table 4.1: MODIS Aqua R_{rs} data range for each band.

Band (nm)	**Min**	**Max**
412	0.002298	0.008776
443	0.002808	0.007132
469	0.003106	0.006680
488	0.003114	0.006686
531	0.002474	0.005510
547	0.001826	0.004990
551	0.001472	0.004520
645	-0.00053	0.000638
667	-0.00044	0.000554
678	-0.00046	0.000522

The standard empirical models of MODIS are listed in Table 4.2. The current operational algorithm for near-surface chlorophyll concentration is version 6 that was updated using MODIS and SeaWifs in-situ bio-optical datasets (NOMAD version 2). This in-situ data spans a wide range of water types from coastal to offshore regions. In this algorithm, X is evaluated as X = R_{rs}(blue)/R_{rs}(green), where the blue and green wavelengths are given in Table 4.2.

Table 4.2: The ocean colour chlorophyll version 6 of MODIS calculated as $Chl = 10^{(a_0 + a_1X + a_2X^2 + a_3X^3 + a_4X^4)}$.

Reference	**Sensor**	**blue**	**green**	**a_0**	**a_1**	**a_2**	**a_3**	**a_4**
OC3Mv6	MODIS	Max[443;488]	547	0.2424	-2.7423	1.8017	0.0015	-1.2280
OC3M-551	MODIS	Max[443;488]	551	0.2424	-2.5828	1.7057	-0.3415	-0.8818
OC2M-551	MODIS	488	551	0.2481	-2.2958	1.4053	-3.1299	0.6478
OC2M-547	MODIS	488	547	0.2500	-2.4752	1.4061	-2.8233	0.5405

source: http://oceancolor.gsfc.nasa.gov/.

4.3 Comparison between in situ and satellite observations

Figure 4.1 shows the comparison between the in-situ and MODIS R_{rs} ratios from the blue and green parts of spectrum for ±4-hours and ±28-hours matching datasets. The time span of ±4-hours is a standard practice for the validation of satellite ocean colour data products (Werdell et al., 2003). For our area, this left a small data to work with so we expanded the comparison to include observations that were within 28-hours of a satellite overpass. We found that in all cases, there is a good agreement between in-situ and MODIS R_{rs} ratios, although the MODIS R_{rs} ratios tend to be slightly higher than the Satlantic values. Overall, the MODIS reflectance ratios were about 15-35% higher than the in-situ measurements. This was not surprising since MODIS data is acquired at the top of atmosphere that is accordingly perturbed by atmospheric contributions as well as sea surface reflectance, especially at the blue regions. The fairly good agreement also indicates that the use of band ratios is less sensitive to possible errors in the atmospheric correction than a single R_{rs} waveband. It is also interesting to note that there was no significant difference observed between ±4-hours and ±28-hours data, suggesting that the water colour has not changed much within 1-2 days of observations. Our results in Figure 4.1

show that band ratios 443/547 and 448/547 nm are better correlated than the other band ratios. These band ratios are currently used in MODIS chlorophyll algorithms.

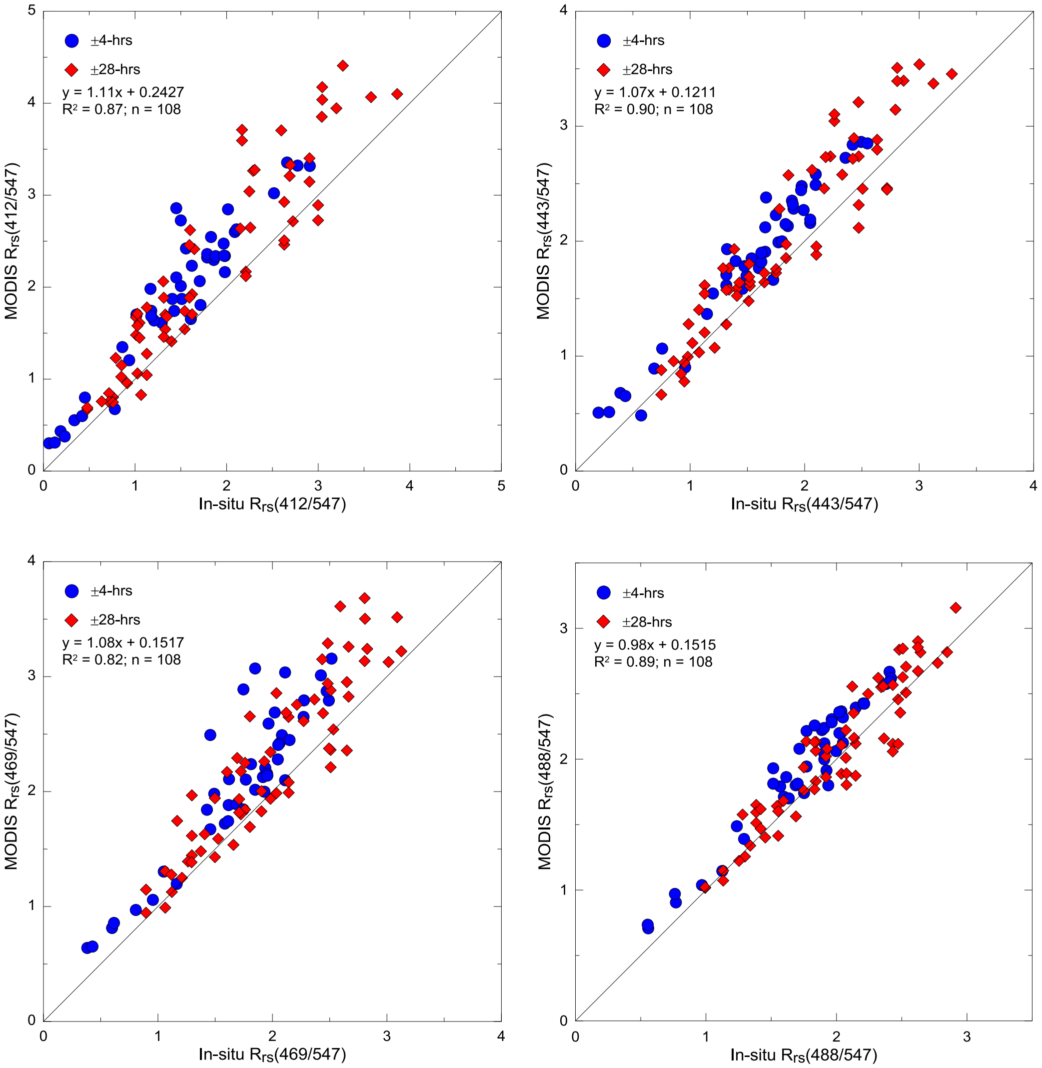

Figure 4.1: Comparison between in-situ and MODIS R_{rs} ratios at 4 nominal wavelengths (412, 443, 469 and 488 nm) for ±4-hours and ±28-hours data acquisition.

Figure 4.2 compares our in-situ determinations of chlorophyll with estimates of chlorophyll obtained from the MODIS algorithm during the monsoon (Jun-August and November) and inter-monsoon (October) seasons. Once again, the time lag between satellite overpass and chlorophyll measurement has been marked as either up to ±4-hours or ±28-hours. The data points clearly show two different cases; a significant underestimation during the inter-monsoon and NEM seasons; and overestimation for relatively high pigment concentration during the SWM season. During the SWM monsoon periods, the MODIS algorithm provides a good estimate at low values but overestimates chlorophyll by nearly 50% when concentration is higher than 0.6 mg m^{-3}. Despite some scatter, the overall MODIS estimation during the SWM season shows a more accurate estimation than in other seasons with lower MAPD (<25%) and RMSE (<0.02 mg m^{-3}) values. The MODIS estimates of chlorophyll are more varied during the inter-monsoon and NEM seasons. During these periods, the algorithm underestimated chlorophyll in offshore waters and overestimated chlorophyll near the coast. The overestimation of chlorophyll is more obvious during the NEM season with a bias as great as 260 mg m^{-3} (St. 42, 12th Nov 2009; data not shown). While overestimation of chlorophyll in optically complex coastal waters during this period can be explained by the presence of high non-pigmented components (CDOM and detritus), a significant underestimation in offshore waters (up to a factor of ~3) was not expected, especially when considering the low pigment package effect and high chlorophyll concentration. As will be shown later in the next section, this variation is probably caused by the algorithm prediction itself. The significant underestimation during the inter-monsoon might be attributed to the high pigment package effect. During the inter-monsoon period, almost all data showed strong negative biases when compared to in-situ chlorophyll measurements.

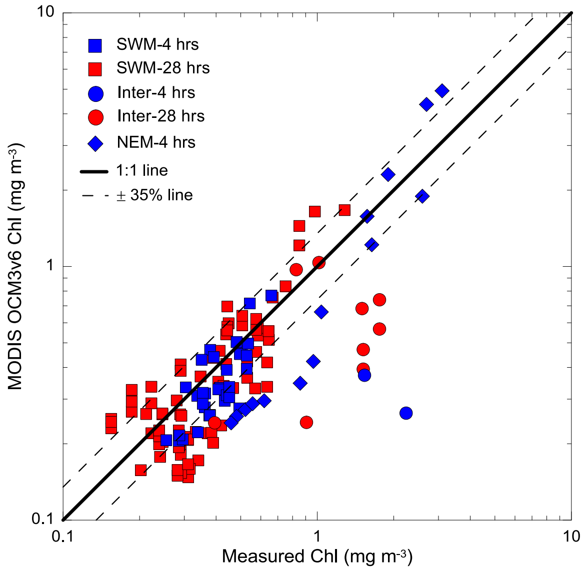

Figure 4.2: Comparison between in-situ chlorophyll measurements and the MODIS OC3Mv6 chlorophyll product. Red and blue points indicate ±4-hrs and ±28-hrs of data points, respectively.

4.4 Evaluation of MODIS chlorophyll algorithms using in-situ Rrs.

The MODIS OC3Mv6 algorithm was applied to Satlantic R_{rs} data in order to evaluate the performance of chlorophyll remote sensing estimates in the study area and to remove the concern about the time lag between R_{rs} and chlorophyll measurements. The comparison of in situ chlorophyll concentration and the corresponding first-order bias (Satlantic OC3Mv6 minus in-situ chlorophyll) of MODIS estimates is shown in Figure 4.3. A significant scatter of data points (Figure 4.3a) was observed with relatively high MAPD (>94%) and RMSE (>1.3 mg m^{-3}) for both seasons. Consistent with Figure 4.2, the MODIS algorithm tends to underestimate chlorophyll for the vast majority of stations characterized either by low or high chlorophyll concentrations in inter-monsoon season and overestimate chlorophyll for chlorophyll > 0.6 mg m^{-3} in monsoon seasons (SWM and NEM). This apparent systematic overestimation and underestimation of OC3Mv6 is clearly illustrated in Figure 4.3b, with the largest positive bias

(~155 mg m^{-3}) is found during the November cruise (station 52), whilst the lowest underestimation (~ -3 mg m^{-3}) occurs in May (station 46).

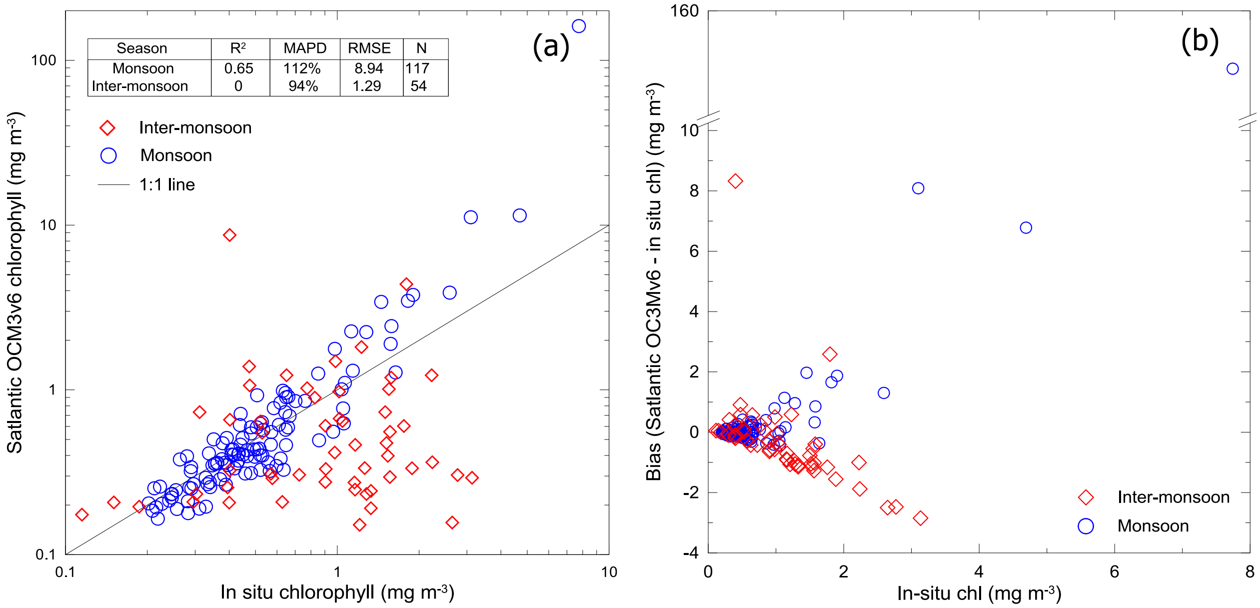

Season	R²	MAPD	RMSE	N
Monsoon	0.65	112%	8.94	117
Inter-monsoon	0	94%	1.29	54

Figure 4.3: (a) Comparison of chlorophyll values estimated by Satlantic OC3Mv6 with measured in-situ chlorophyll. (b) Scatter plots of bias between in-situ chlorophyll and Satlantic Hyper OCR estimation of MODIS standard chlorophyll algorithms. The largest positive bias (~155 mg m^{-3}) was found at station 52 (12/11/2009) during the NEM season.

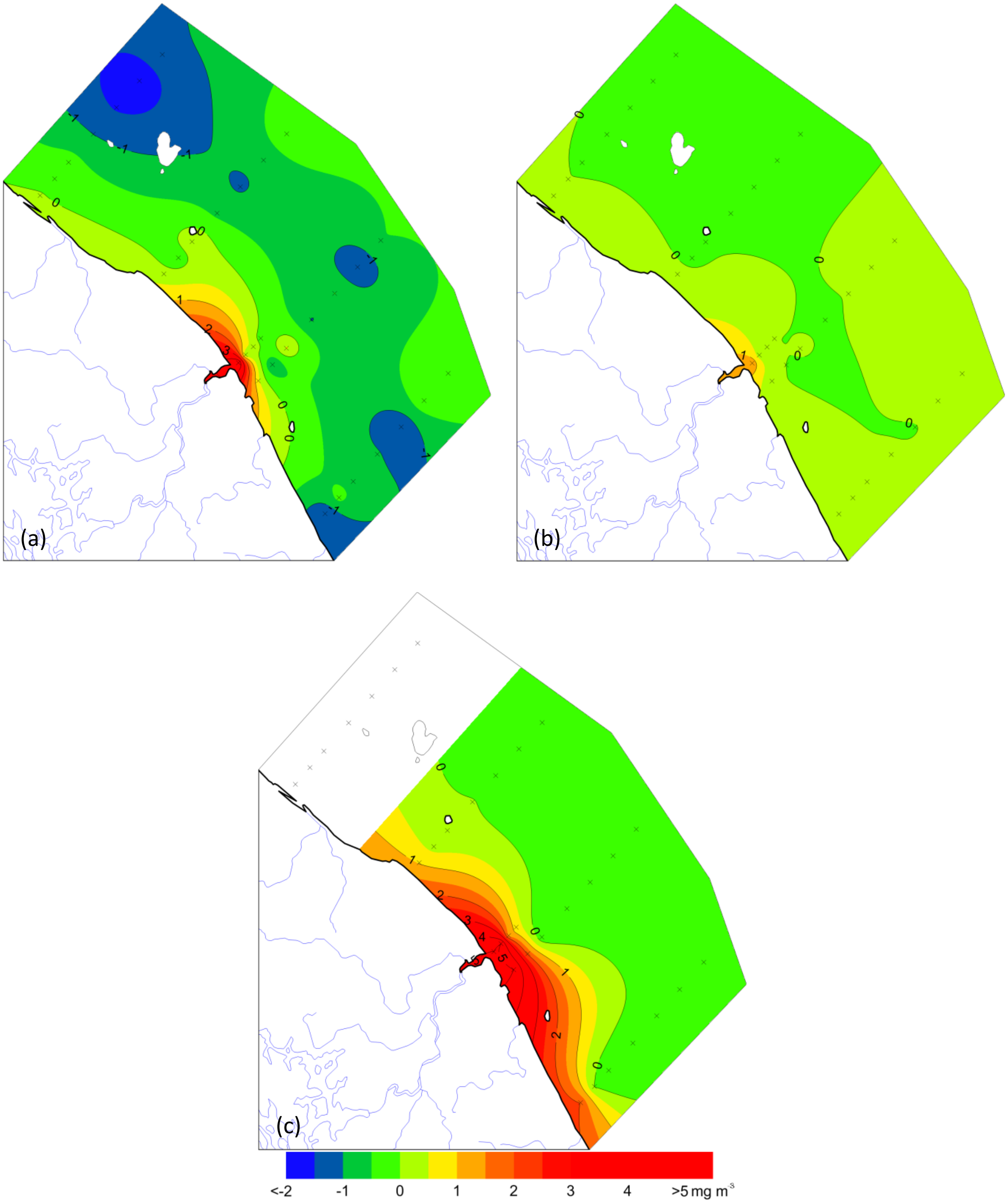

Figure 4.4: The average first-order bias of MODIS estimates chlorophyll concentration during the (a) inter-monsoon, (b) SWM and (c) NEM season.

To provide insight into the seasonal biases of chlorophyll in the investigated waters, the geographic distribution of chlorophyll mismatch for each season was plotted in Figure 4.4. In general, the overestimation of chlorophyll is higher in coastal waters and this effect is particularly evident during the NEM season with overestimation as great as 20-fold in some stations. Given the high covariation of non-pigmented components (CDOM and suspended materials) with chlorophyll concentration (see section 3.34), which represent an ideal remote sensing condition for ocean colour applications, the large overestimation during the NEM season seems to be attributed to the performance of the MODIS algorithm itself. Due to relatively low pigment concentration with co-varying non-pigmented optical constituents, the MODIS estimates of chlorophyll during the SWM season showed less bias for almost all stations. The average chlorophyll difference between in-situ and MODIS estimates during this season is around 0.5 mg m^{-3}. In contrast, the results during the inter-monsoon exhibit a pronounced underestimation especially in offshore waters, consistent with the observed phytoplankton blooms in these waters. The effect of pigment packaging with non-co-varying non-pigmented component appears to have caused underestimates of chlorophyll during this season. This can be explained by a flattening of phytoplankton absorption and a nonlinear relation between chlorophyll concentration and observed absorption. Because absorption is inversely proportional to reflectance, lower absorption especially at the blue and red parts of the spectrum results in greater reflectance signal thus, increase the blue-green reflectance ratios. The result during this period is consistent with findings from a number of studies (e.g. Cota et al., 2003; Stramska et al., 2003; Garcia et al., 2005) and implies that the performance of ocean colour algorithm might change when the species composition changes.

4.5 Regional adaptation of chlorophyll algorithms.

The poor performance of the standard MODIS algorithm (section 4.4) suggests that a local or regional algorithm is needed for east coast Peninsular Malaysia. Although if the data presented above is limited to just one year (2009), they cover the full range of water types and conditions ranging from oligotrophic to eutrophic and from clear to optically thick water. It is therefore possible to use this dataset to develop regional algorithm or to tune the standard ocean colour algorithm especially from the MODIS sensor to improve detection of chlorophyll. Since the data behaves differently in different seasons (as can be seen in Figure 4.3), we performed separate model analyses for inter-monsoon and monsoon seasons. Two sets of retrieval coefficients were derived from regression of both linear and non-linear OCM3 functional models. In this regional parameterization, the entire datasets for both seasons (117 data points for monsoon and 54 for inter-monsoon) were used to determine the best model for estimating chlorophyll concentration.

Our results during the inter-monsoon season indicate that there was statistically no relationship ($p>0.001$; $R^2 = 0.001$; $n=54$) between chlorophyll concentration and Satlantic reflectance ratios (Figure 4.5). With differences in the pigment packaging effect compared to the other seasons, errors in chlorophyll estimates during this season is somewhat expected. In contrast, the reflectance models of chlorophyll concentration during the monsoon season demonstrated relatively good results either using linear or polynomial models. The statistical results of regression between in-situ chlorophyll concentration and Satlantic reflectance ratios are summarized in Table 4.3. It is clear from Table 4.3 that chlorophyll concentration during the monsoon season can be well represented by any combination of the blue-green ratios with all models showed relatively high R^2 values (> 85%) and low RMSE(0.1 mg m^{-3}). It is noteworthy that this result holds for relatively high concentrations of non-pigmented components (CDOM and detritus) in coastal waters especially during the NEM season, the conditions that often make the global algorithms fail. In most cases, global algorithms appear to overestimate the chlorophyll concentration owing to the high contribution of CDOM absorption in the blue part of the spectrum.

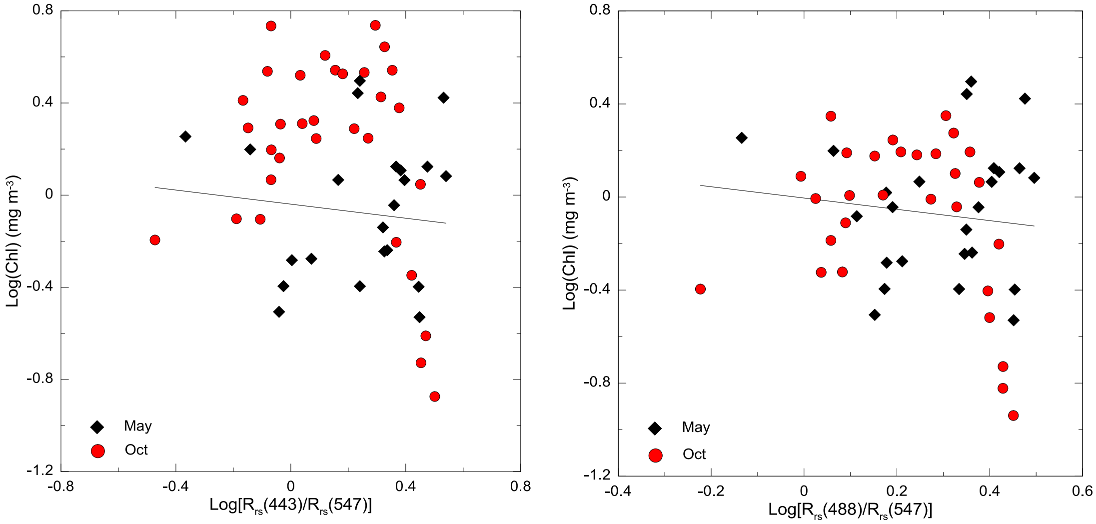

Figure 4.5: Relationships between the spectral band ratio and chlorophyll concentration for the inter-monsoon dataset.

Table 4.3: Regional parameterization of chlorophyll algorithms from the Satlantic reflectance ratios for the monsoon season. A fourth-order polynomial (4-poly) is an algorithm of the form: [Chl = a_0 +a_1X + a_2X^2 + a_3X^3 + a_4X^4] and a linear algorithm has the form: [Chl = a_0 +a_1X], where X is a log reflectance ratio.

Algorithm	Model	a_0	a_1	a_2	a_3	a_4	R^2	RMSE
Adjusted-OCM3v6	4-poly	0.0720	-1.6596	0.3319	0.7290	-0.9472	0.88	0.098
Adjusted-OCM2v6	4-poly	0.0688	-1.6482	0.5210	0.3596	-2.1405	0.87	0.100
Rrs(412/547)	linear	-0.2078	-0.7691				0.87	0.097
Rrs(443/547)	linear	-0.1248	-1.0276				0.89	0.092
Rrs(469/547)	linear	-0.0139	-1.2644				0.88	0.096
Rrs(488/547)	linear	0.0713	-1.5333				0.87	0.099
Rrs(531/547)	linear	0.1968	-6.7090				0.85	0.101
Rrs[Max(412,..,488)/547	linear	0.0578	-1.3852				0.87	0.100
Rrs[(443+488)/547]	linear	0.5329	-1.5333				0.87	0.101

The high performance of our new algorithms was also evident by the validation results shown in Figure 4.6 and Table 4.4. These algorithms present a significant improvement in estimating chlorophyll concentration by reducing nearly 85% of bias in the standard version of MODIS algorithms. Figure 4.6 clearly shows that both MODIS algorithms deviate from observed chlorophyll at both low and high end of chlorophyll concentrations. Given that these new generations of MODIS algorithm are designed to retrieve chlorophyll concentration for both Case 1 and Case 2 waters, the poor performance in our study area was unexpected. One explanation for the discrepancy in MODIS chlorophyll estimates may be related to differences in the magnitude of spectral reflectance ratios (blue-green reflectance) between our dataset and MODIS bio-optical dataset. Most empirical data used to develop the standard global algorithm are collected in ocean waters with smaller contribution of CDOM. In CDOM-dominated environments like our study area, such ratios are significantly reduced compared to the typical ocean waters and these differences made the standard global algorithms tend to overestimate the chlorophyll concentration.

The polynomial model proved the most suitable algorithm with better agreement ($R^2>0.95$) was observed between measured and predicted values compared to other models (Table 4.4). However, we must bear in mind that comparisons shown in Figure 4.6 and Table 4.4 use the same data as the algorithm development. We would expect a different result if independent dataset is used to validate the algorithm.

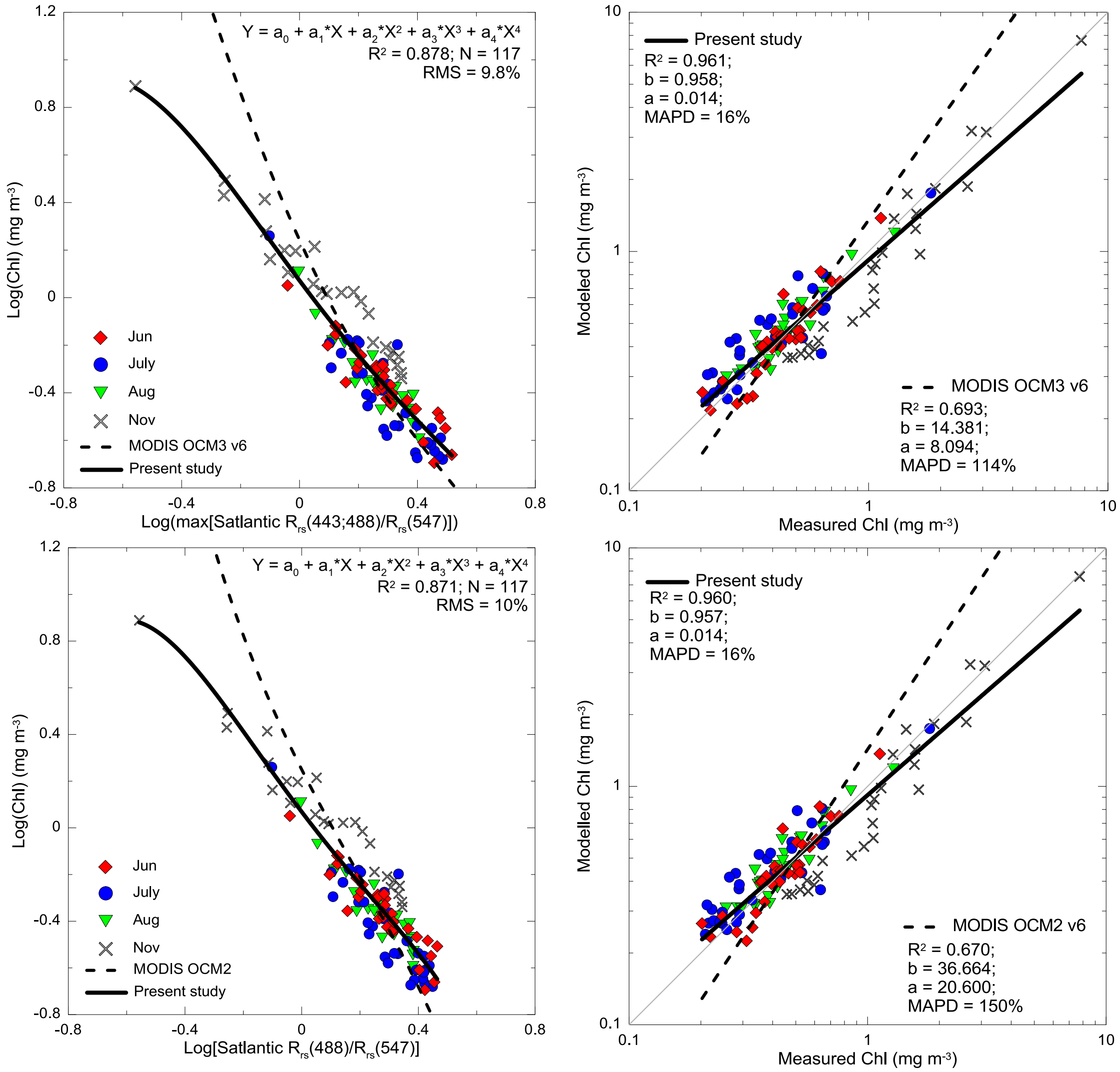

Figure 4.6: Adjusted MODIS OCM3 (upper panel) and OCM2 (lower panel) validation using in-situ spectral reflectance (shown by a solid line) and concurrent chlorophyll measurements. The dashed-lines (left and right panels) are the standard MODIS algorithms and their regression best-fits. Note that the error analyses on the left panels use the same data as the algorithm development.

Table 4.4: Statistical results of the best-fit regression (*y = a + bx*) between measured and chlorophyll estimates. Note that the error analyses use the same data as the algorithm development.

Algorithm	R^2	a	b	MAPD
OCM3v6	0.71	-8.21	15.38	114%
OCM2v6	0.67	20.60	36.66	150%
Adjusted-OCM3v6	0.96	0.01	0.96	16%
Adjusted-OCM2v6	0.96	0.01	0.96	16%
Rrs(412/547)	0.65	-0.22	0.64	23%
Rrs(443/547)	0.94	0.07	0.86	17%
Rrs(469/547)	0.96	0.01	0.96	15%
Rrs(488/547)	0.96	-0.02	1.00	17%
Rrs(531/547)	0.92	-0.13	1.09	22%
Rrs[Max(412,..,488)/547	0.96	0.08	0.83	18%
Rrs[(443+488)/547]	0.96	-0.01	1.00	17%

4.5.1 Satellite match-up analysis.

In order to assess the feasibility of retrieving chlorophyll concentrations with our new algorithms, we performed a validation of the algorithms by comparing satellite estimates with concurrent in-situ chlorophyll observations. All the MODIS matching pairs were obtained during the monsoon season (August 2008 and June to November 2009) that largely represent the offshore waters. Considering the very close distance between observing stations, chlorophyll algorithm was calculated on a pixel by pixel basis. Overall, 108 match-up points ranging from 0.15 to 3.10 mg m^{-3} of chlorophyll concentrations were used for the analysis.

The quality of the satellite reflectance ratios is the key element to the estimation of the chlorophyll concentration and other biophysical products. Any errors in R_{rs} ratios will affect the accuracy of chlorophyll estimation. In our case, we have already seen that satellite reflectance ratios are systematically higher than in-situ measurements (section 4.3). It is then possible to correct the satellite reflectance ratios to match with in-situ measurements (Figure 4.1). The MODIS R_{rs} was corrected by applying the linear equations in Figure 4.1. That is

$$R_I(\lambda) = a_0 + a_1 R_M(\lambda) \qquad 4.3$$

where R_I is the corrected reflectance and R_M is the MODIS reflectance. a_0 and a_1 are based on the linear fits shown in Figure 4.1.

The results of match-up analysis for the different algorithms are summarized in Table 4.5 and Figure 4.7. The performance of the regional algorithms was similar to or better than the standard NASA algorithms (OC3M and OC2M). The small differences in performance between regionally tuned and MODIS algorithms perhaps because of the small range of chlorophyll concentrations were used for match-up analysis. We might expect higher retrieval errors of MODIS algorithms for a wide range of chlorophyll values. Algorithms that involve the reflectance ratios R_{rs}(488/547) and R_{rs}(531/547) perform better than others, contrary to what was observed in the previous analysis using in-situ bio-optical data (Table 4.4). This was mainly due to the residual (that is the scatter about the lines shown in Figure 4.1) between the in-situ and satellite reflectance ratios. Overall, the MODIS algorithms tuned over the study area exhibit the best results and improved significantly the estimation of chlorophyll concentration. These corrected algorithms provide lower MAPD and RMSE and higher R^2 values for both 4-hrs and 28-hrs of the satellite overpass window. It is noteworthy that these corrected algorithms perform well even at higher chlorophyll concentrations. Especially for the adjusted-OCM3v6 algorithm, most of the estimated values are within the NASA ±35% accuracy limit (Figure 4.7). Both the standard MODIS algorithms performed very similarly with MAPD and RMSE values are about twofold higher than that of adjusted algorithms.

Table 4.5: Statistical results of chlorophyll estimation from validation match-ups for different algorithms.

Algorithm	**Model**	**RMSE (mg m^{-3})**		**MAPD (%)**		**R^2**	
		±4-hrs	±28-hrs	±4-hrs	±28-hrs	±4-hrs	±28-hrs
OCM3v6	4-poly	0.378	0.280	33.8	32.1	0.861	0.849
OCM2v6	4-poly	0.335	0.263	33.8	33.6	0.878	0.854
Adjusted-OCM3v6	4-poly	0.157	0.154	16.4	20.0	0.936	0.888
Adjusted-OCM2v6	4-poly	0.161	0.156	16.8	20.2	0.914	0.886
Rrs(412/547)	linear	0.374	0.278	32.1	27.2	0.879	0.884
Rrs(443/547)	linear	0.212	0.172	25.5	23.2	0.776	0.805
Rrs(469/547)	linear	0.428	0.320	32.7	35.7	0.762	0.813
Rrs(488/547)	linear	0.143	0.151	18.2	21.0	0.918	0.876
Rrs(531/547)	linear	0.163	0.149	18.7	21.1	0.927	0.908
Rrs[Max(412,..,488)/547	linear	0.126	0.146	21.4	23.2	0.915	0.861
Rrs[(443+488)/547]	linear	0.221	0.206	24.3	28.8	0.906	0.891

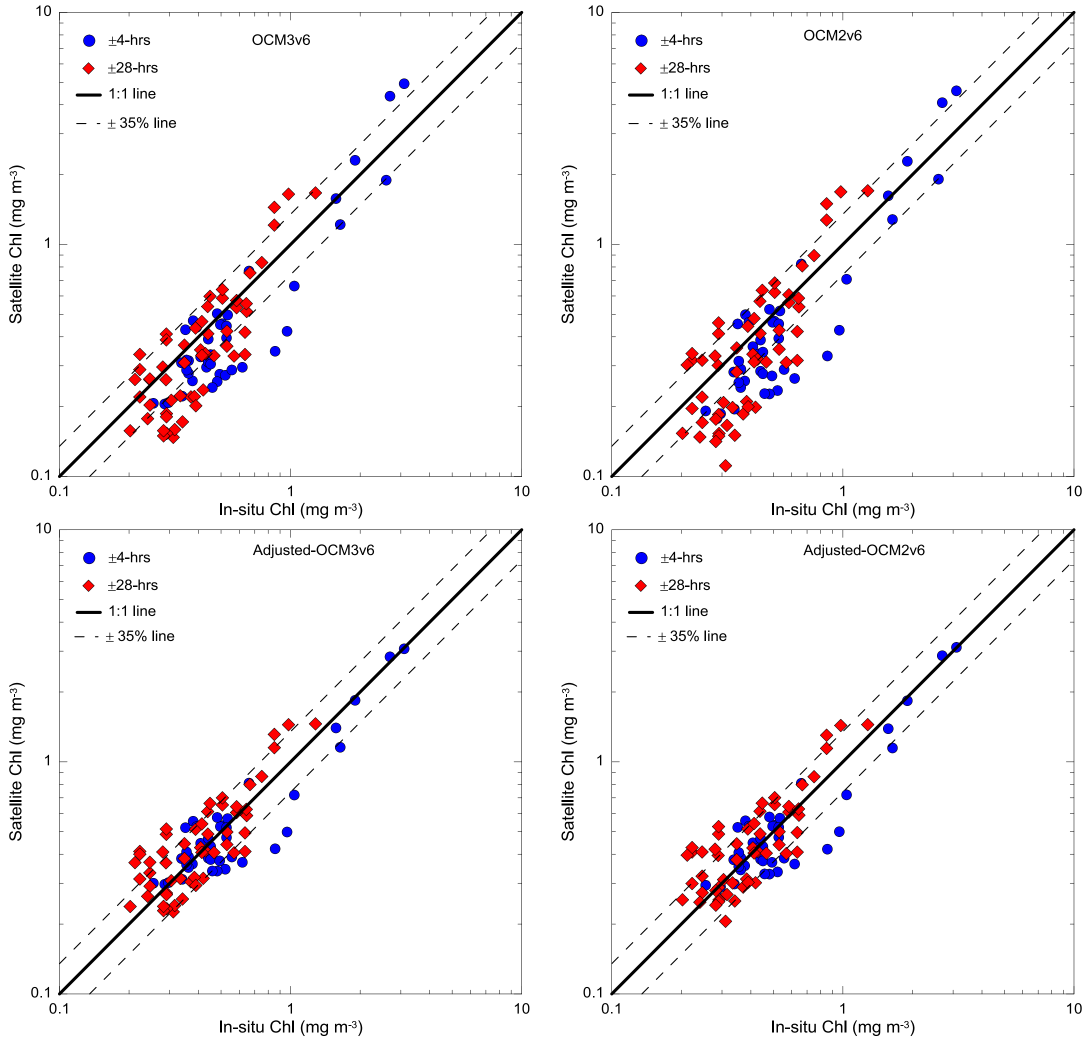

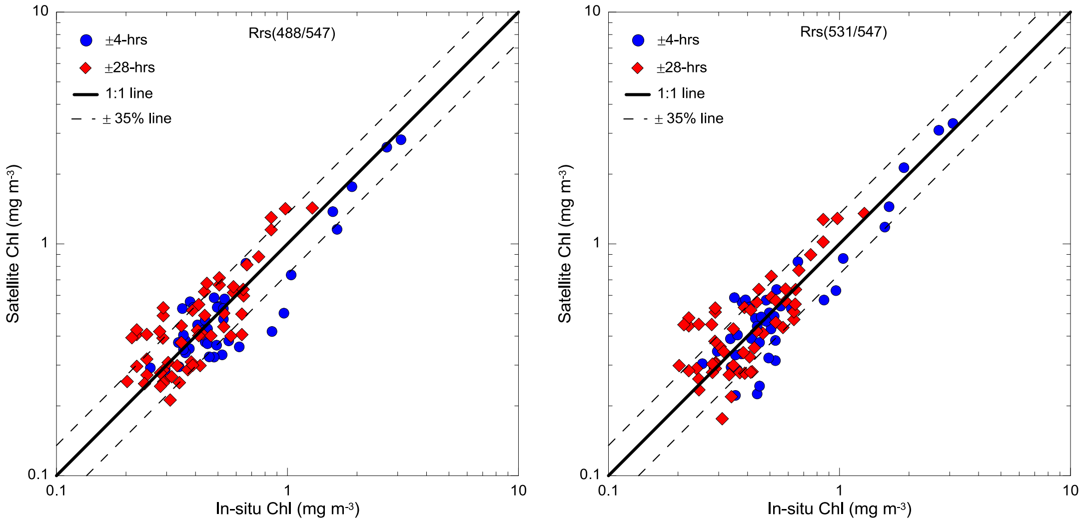

Figure 4.7: Comparisons of MODIS and field observations of chlorophyll for different algorithms and satellite overpass windows. The solid line represents the 1:1 line while dashed lines represent the ±35% bounds of the NASA accuracy requirement. Note that the comparisons were only applied to the monsoon (SWM and NEM) data of 2008 and 2009.

4.6 Semi-analytical model of chlorophyll

An alternative way to derive chlorophyll concentrations and other bio-optical properties components is to use a semi-analytical algorithm. To explore the possibility of using this type of algorithm in our study area, semi-analytical approaches developed by Lee et al. (2002) and Carder et al., (1999) was used to derive $a_{dg}(\lambda)$ and $a_{ph}(\lambda)$ values from in situ measurements of remote sensing reflectance. Chlorophyll concentrations are then determined via a relationship to the inversion estimated of phytoplankton absorption.

4.6.1 Inversion model of Lee et al., (2002)

The QAA consists of two inter-related parts. In the first part, the total absorption coefficients and particle backscattering coefficients are derived with no spectral models involved for the absorption coefficients of each constituent. The derived total absorption coefficient is then decomposed spectrally into phytoplankton absorption and coloured detrital matter absorption coefficients in the second step. Details of the QAA are presented in appendix A.

In this study we derived the total absorption coefficient at a reference wavelength, 555 nm using the following equations.

$$\begin{cases} \chi = log\left(\dfrac{r_{rs}(443) + r_{rs}(490)}{r_{rs}(555) + 5\dfrac{r_{rs}(667)}{r_{rs}(490)}\, r_{rs}(667)}\right) \\ \\ a_t(555) = \ a_w(555) + \ 10^{a_0 + a_1\chi + a_2\chi^2} \end{cases} \qquad 4.4$$

where a_0, a_1 and a_2 are empirically derived coefficients with values of -1.146, -1.366 and -0.469, respectively (Lee et al., 2002) and $r_{rs}(\lambda)$ is calculated according to equation A1 (Appendix A). The derived $a_t(555)$ is then used to derive particle backscattering and total absorption coefficients at other wavelengths using equations 4.5 and 4.6.

$$\begin{cases} b_{bp}(555) = \dfrac{u(555)\, a_t(555)}{1 - u(555)} - \ b_{bw}(555) \\ \\ b_b(\lambda) = \ b_b(555)\left(\dfrac{555}{\lambda}\right)^{Y} \end{cases} \qquad 4.5$$

$$a_t(\lambda) = \frac{[1 - u(\lambda)]b_b(\lambda)}{u(\lambda)} \qquad 4.6$$

where u is a function of the absorption and backscattering coefficients (equation A2) and Y is the wavelength dependence of backscattering (equation A7).

Figure 4.8 compares the measured and estimated values of total absorption coefficients at 412, 443 488 and 555 nm. Overall, the inversion model of QAA shows a poor performance in retrieving $a_t(\lambda)$ in our waters with most of the scattered points occurred at the highest end of $a_t(\lambda)$ values. It can be seen that equation 4.4 underestimates the value of $a_t(555)$ with average error of about 16%. As errors in the derived $a_t(555)$ could further lead to larger errors in retrieved $b_{bp}(555)$ and $a_t(\lambda)$ at other wavelengths, empirical coefficients (a_0 to a_2) in equation 4.4 were empirically tuned to fit the observed data. Although the results show that the new coefficients provide improved $a_t(555)$ estimation (R^2 = 0.91; slope =1.0) over the current formulation (R^2 = 0.8; slope = 0.8), no significant improvements were observed in estimated $a_t(\lambda)$ at 412, 443 and 488 nm. This disagreement seems to be attributed to the measurements errors in b_{bp} calculation and the differences between used and required values of g_0 and g_1. In the QAA model, the spectral slope of the backscattering coefficient, Y is empirically estimated from the ratio of $R_{rs}(443/555)$ (equation A3) and any estimation errors could correspondingly lead the derivations of $b_{bp}(555)$ and $a_t(\lambda)$ to fail. Because no measurements of $b_b(\lambda)$ are available, we could not determine how Y is varied in our waters or whether it is accurately derived from R_{rs} ratio. In the QAA model, the angular dependence of g_0 and g_1 are taken as constants. In fact, these parameters can vary spatially and temporally, depending on particle phase function and scattering properties (Lee et al., 2001). Therefore, these properties can have a strong influence on the retrieval of $b_{bp}(\lambda)$ compared to that of $a(\lambda)$ (Morel and Gentili, 1993; Lee et al., 2002). Due to the fact that all the $a_t(\lambda)$ values derived from the QAA model had low accuracy, a_{ph} and a_{dg} were not derived from the total absorption values.

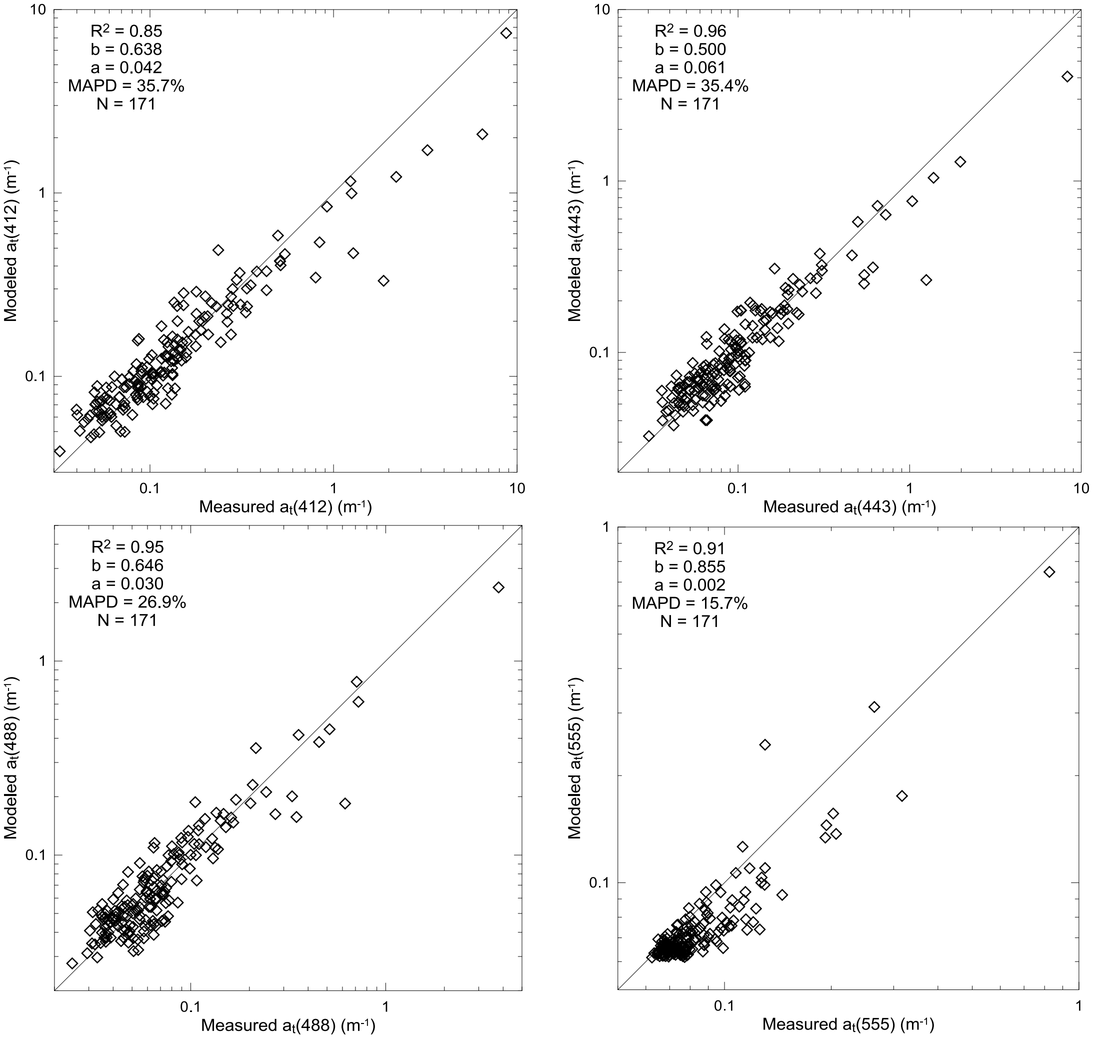

Figure 4.8: Comparisons of QAA-derived and field observations of a_t at 412, 443, 488 and 555 nm. The solid line represents the 1:1 line.

4.6.2 Semi-analytical model of Carder et al., (1999).

In contrast to Lee et al., (2002), the case-2 MODIS semi-analytical algorithm (Carder et al., 1999) is based on the spectral optimization approach which involves the solution of spectral models for absorption and backscattering coefficients for each individual component present in the water. The performance of this algorithm, therefore, relies on accurate spectral models. Details of this algorithm are presented in Appendix B. In the semi-analytical algorithm, the

$a_{ph}(675)$ used to calculate chlorophyll concentration is determined based on two R_{rs} ratio functions:

$$\begin{cases} \dfrac{R_{rs}(412)}{R_{rs}(443)} = \dfrac{b_b(412)}{b_b(443)}\dfrac{a(443)}{a(412)} \\ \dfrac{R_{rs}(443)}{R_{rs}(551)} = \dfrac{b_b(443)}{b_b(551)}\dfrac{a(551)}{a(443)} \end{cases} \qquad 4.7$$

where the backscattering coefficient (b_b) is the sum of the backscattering coefficients of pure water (b_w) and particles (b_{bp}); and the absorption coefficient is the sum of absorption coefficients of pure water (a_w), phytoplankton (a_{ph}), detritus (a_d) and CDOM (a_{CDOM}).

In the semi-analytical algorithm, a_{ph} at 412, 443 and 488 nm is related to $a_{ph}(675)$ by a hyperbolic tangent function (equation B7). Using measured $a_{ph}(\lambda)$ at 412, 443, 551 and 675 nm as inputs, the standard non-linear regression model was applied on equation B7 to obtain the empirical coefficients (a_o to a_3) at each wavelength. In this study, we found that these empirically derived coefficients were less accurate for the phytoplankton absorption at 412 and 443 nm with percentage errors of about 60 and 40%, respectively. As the performance of the semi-analytical algorithm largely depends on the accuracy of the derived $a_{ph}(675)$, this initial result would introduce a large bias in the estimation of chlorophyll concentration. With the consideration of this possible source of error, we derived improved estimations of empirical relationships of $a_{ph}(\lambda)$ using the field data. The coefficients (a_o to a_2) were determined employing a 2nd order polynomial model. This functional model improved the estimation of absorption at both wavelengths by reducing more than 50% in the estimation error. Statistical results of empirically derived parameters of 2nd order polynomial for each $a_{ph}(\lambda)$ are presented in Table 4.6, while Figure 4.9 shows a relationship between $a_{ph}(675)$ and $a_{ph}(443)$.

Table 4.6: Statistical results of 2nd order polynomial ($y = a_0 + a_1x + a_2x^2$) of $a_{ph}(\lambda)$ as a function of $a_{ph}(675)$.

$a_{ph}(\lambda)$	a_0	a_1	a_2	R^2	RMSE (%)
412	0.017	-0.203	157.833	0.97	1.156
443	0.009	1.853	80.004	0.98	0.698
551	0.000	0.592	30.697	0.98	0.225

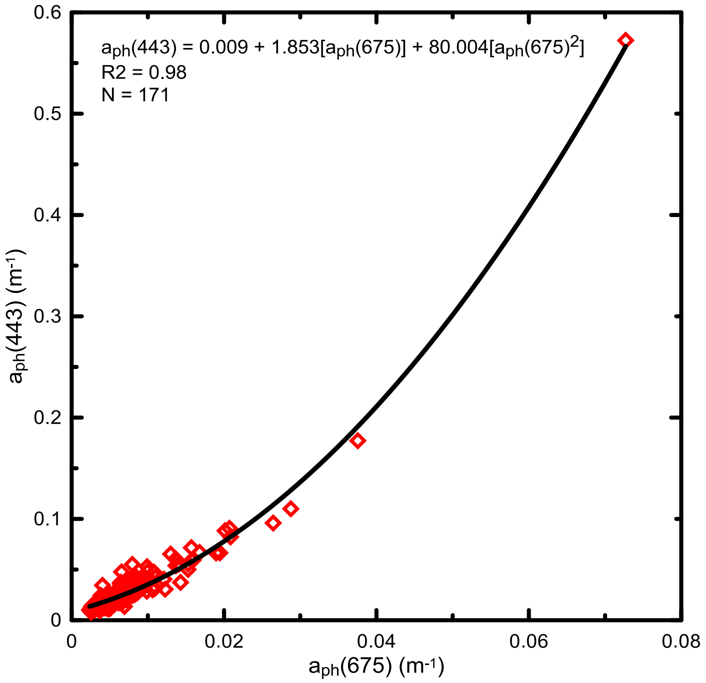

Figure 4.9: Relationship between $a_{ph}(675)$ and $a_{ph}(443)$.

An average value of 0.015 nm^{-1} was used for the spectral slope of coloured detrital matter, S_{dg}. Validation of the observed against derived $a_{dg}(\lambda)$ using this value returned a very significant R^2 value (>0.99) for the blue band of spectrum (412 to 488 nm) but was less well correlated (R^2<0.8) in the green.

Particle backscattering coefficients are modeled following the equation B3 (Gordon and Morel, 1983) with λ_0 is a reference wavelength at 551 nm. $b_{bp}(551)$ is calculated analytically from $R_{rs}(551)$ (equation B4) and the wavelength dependence of backscattering, Y is estimated from the ratio of $R_{rs}(443/488)$ (equation B5). Since there was no available field-measured backscattering data, b_{bp} at 412, 443 and 551 nm were estimated based on the definition of R_{rs}

using equation 1.21. These $b_{bp}(\lambda)$ values were then used to derive Y for each wavelength. If $b_{bp}(\lambda)$ or Y are determined to be negative, they are set to zero.

Comparisons of the derived $b_{bp}(551)$, X and Y parameters with those using the equations of Carder et al.,(2002) are shown in Table 4.7. From this comparison, it is found that our empirical coefficients (Y_0 and Y_1) values were higher than those values used in Carder et al., (1999), perhaps because our derived Y values varied greatly (between 0 and 8) compared to what has been reported by Carder et al., (1999) (between 0 and 3). According to Gordon and Morel (1983), this parameter should be large when the backscattering is mainly caused by small particles and/or water. Figure 4.10 shows statistically derived $b_{bp}(551)$ and Y as a function of observed R_{rs} values. It can be seen that the derived $b_{bp}(551)$ correlates well with $R_{rs}(551)$ (R^2 = 0.86). However, a lack of correlation (R^2 = 0.32) was observed between Y and $R_{rs}(443/488)$ that could lead errors in the derivation of $b_{bp}(\lambda)$ from equation B3.

Table 4.7: Comparisons of the wavelength-dependent parameters between present study and Carder et al. (2002) for the semi-analytical chlorophyll algorithm. X_i and Y_i are empirically derived from equations B4 and B5 (Appendix B)

Parameter	**Present study**	**Carder et al., (2002)**
X_0	-0.0049	-0.00182
X_1	2.119	2.058
Y_0	-3.06	-1.13
Y_1	7.11	2.57

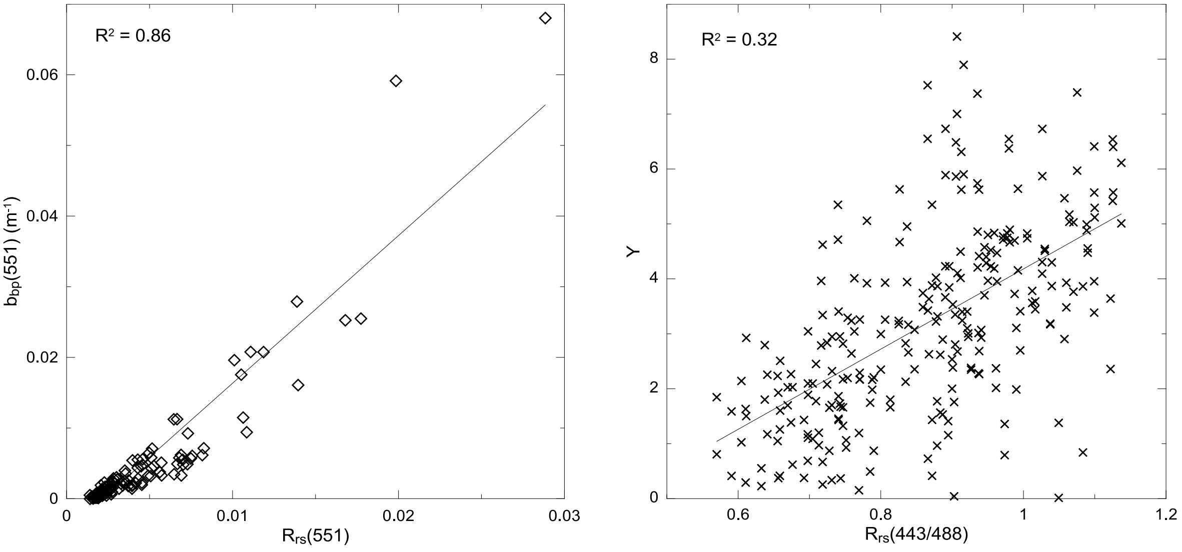

Figure 4.10: $b_{bp}(551)$ versus $R_{rs}(551)$ (left panel) and Y versus $R_{rs}(443/488)$ (right panel).

$a_{ph}(675)$ was calculated using equation B9 after replacing all the absorption and backscattering terms (equations B3 and B8) into equation 4.7. In this study, equation B9 was calculated using the quadratic equation.

$$ax^2 + bx + c = 0 \qquad 4.8$$

where

$$a = F\left(a_{2(551)}\right) - F\left(a_{2(443)}\right) - C\left(a_{2(443)}\right) + C\left(a_{2(412)}\right)$$

$$b = F\left(a_{1(551)}\right) - F\left(a_{1(443)}\right) - C\left(a_{1(443)}\right) + C\left(a_{1(412)}\right)$$

$$c = F(A`) + F\left(a_{0(551)}\right) - F(B`) - F\left(a_{0(443)}\right) - C(D`) - C\left(a_{0(443)}\right) + C(E`) + C\left(a_{0(412)}\right)$$

with $a_{0(\lambda)}$ to $a_{2(\lambda)}$ are empirically derived coefficients of $a_{ph}(\lambda)$ (Table 4.12); A′, B′, C, D′, E′ and F are the known values (other than $a_{ph}(\lambda)$) from equation B9. Absorption by phytoplankton at 675 nm can then be derived.

$$a_{ph}(675) = \frac{-b \pm \sqrt{b^2 - 4ac}}{2a} \qquad 4.9$$

Chlorophyll concentrations were estimated from the derived-$a_{ph}(675)$ according to equation 4.10.

$$[Chl] = P_o[a_{ph}(675)]^{P_1} \qquad 4.10$$

where P_0 and P_1 are empirical coefficients (Carder et al., 2002). Although the study revealed that chlorophyll concentrations correlated well with measured $a_{ph}(675)$ ($R^2 = 0.81$), the results show that the semi-analytical models did not return meaningful values for $a_{ph}(675)$. All predicted $a_{ph}(675)$ values were very small ($\sim 10^{-6}$ m^{-1}) and cannot be used to derive chlorophyll concentration. Similar to what has been observed in the inversion model, the errors in $a_{ph}(675)$ estimation could probably be related to the measurements errors in modeling the spectral shape of particle backscattering

4.7 Absorption algorithm.

Most ocean colour algorithms focus on the retrieval of chlorophyll concentration either using a simple empirical approach or by more complex semi-analytical approaches. Since absorption coefficients are essential for characterizing the marine optical environment and provide a meaningful proxy for estimating chlorophyll concentration from remote sensing reflectance, it would be advantageous to ocean colour observation if these properties can be derived directly from the satellite imagery. In recent years, much effort has been devoted for developing theoretical models for estimating absorption coefficients from underwater light field measurements using forward and inverse models (e.g., Lee et al., 1998; Carder et al., 1999; Loisel et al., 2001; Barnard et al., 1999). In the following sections, we examine the potential for deriving absorption coefficients using observations of remote sensing reflectance in the east coast of Peninsular Malaysia.

4.7.1. Total absorption coefficient algorithm

In this section we examine the relationship between the total absorption coefficient $a_t(\lambda)$ and reflectance ratios. There is a strong linear relationship between $a_t(443)$ and that at other wavelengths (equations 4.11) It is found from in situ measurements that there exist strong linear relationship between total absorption coefficient at 443 nm and other wavelengths.

$$a_t(412) = 1.5472[a_t(443)] - 0.0064\ (R^2 = 0.997; n = 171) \qquad 4.11a$$

$$a_t(469) = 0.7410[a_t(443)] + 0.0024\ (R^2 = 0.999; n = 171) \qquad 4.11b$$

$$a_t(488) = 0.5889[a_t(443)] + 0.0082\ (R^2 = 0.999; n = 171) \qquad 4.11c$$

$$a_t(531) = 0.2785[a_t(443)] + 0.0443\ (R^2 = 0.997; n = 171) \qquad 4.11d$$

$$a_t(547) = 0.2059[a_t(443)] + 0.0567\ (R^2 = 0.994; n = 171) \qquad 4.11e$$

Our results revealed that the spectral relationship for each $a_t(\lambda)$ can be well represented by any combination of the blue-green ratios. Table 4.8 shows that $a_t(\lambda)$ can be related to reflectance ratios $R_{rs}(443)/R_{rs}(547)$ through a second order polynomial. The table shows that the absorption at other wavelengths especially the green part of spectrum, can also be accurately derived using remote sensing techniques. It is clear from Tables 4.8 and 4.9(a) that total absorption at the green wavelength produces a better result than the blue wavelengths with RMSE and MAPD less than 0.07 m^{-1} and 14%, respectively. This is not surprising because most of the total absorption in the green, especially for clear water, come from the water absorption, so the errors might be lower than the blue part of spectrum. With the consideration of the overall performance of the algorithm, we can suggest that variations in the blue-green reflectance ratio in our waters were primarily driven by variations in absorption in this spectral domain.

On the other hand, total absorption coefficients at other wavelengths can also be predicted from $a_t(443)$ by applying the regression results shown in equations 4.4 and Table 4.8. The validation results [Table 4.9(b)] when using this approach produced comparable accuracy levels and consistent with estimates of $a_t(\lambda)$ values derived from R_{rs} band ratio. Figure 4.11 (right panel) shows this comparison with the largest offsets occur at $a_t(412)$ when values less than 0.1 m^{-1}. The large biases observed at this wavelength suggest that dissolved fraction is significant component of the total absorption coefficient.

Table 4.8: Statistical results of 2nd order polynomial ($y = a_0 + a_1x + a_2x^2$) between $a_t(\lambda)$ and R_{rs} band ratio at 443/547.

$a_t(\lambda)$	**a_0**	**a_1**	**a_2**	**R^2**	**RMSE (m^{-1})**
412	0.424	-1.369	-0.672	0.89	0.115
443	0.438	-1.246	-0.813	0.88	0.111
469	0.519	-1.188	-0.940	0.86	0.114
488	0.576	-1.110	-1.011	0.86	0.109
531	0.637	-0.707	-1.053	0.87	0.067
547	0.597	-0.580	-1.044	0.88	0.055

Table 4.9: MAPD and regression results for the in-situ $a_t(\lambda)$. Table A represents validation results of $a_t(\lambda)$ values estimated using R_{rs} ratio and Table B from equations 4.4. *a* and *b* represent the intercept and slope of the best fit line, respectively.

A					**B**				
$a_t(\lambda)$	**R^2**	**a**	**b**	**MAPD (%)**	**$a_t(\lambda)$**	**R^2**	**a**	**b**	**MAPD (%)**
412	0.975	-0.011	1.007	20.1	412	0.972	-0.017	1.049	22.6
443	0.969	-0.011	1.049	20.6	443	-	-	-	-
469	0.968	-0.012	1.085	21.8	469	0.970	-0.008	1.049	21.0
488	0.968	-0.011	1.091	21.5	488	0.969	-0.007	1.049	20.6
531	0.963	0.001	0.979	13.4	531	0.960	-0.005	1.042	14.4
547	0.957	0.005	0.932	11.3	547	0.954	-0.004	1.037	11.9

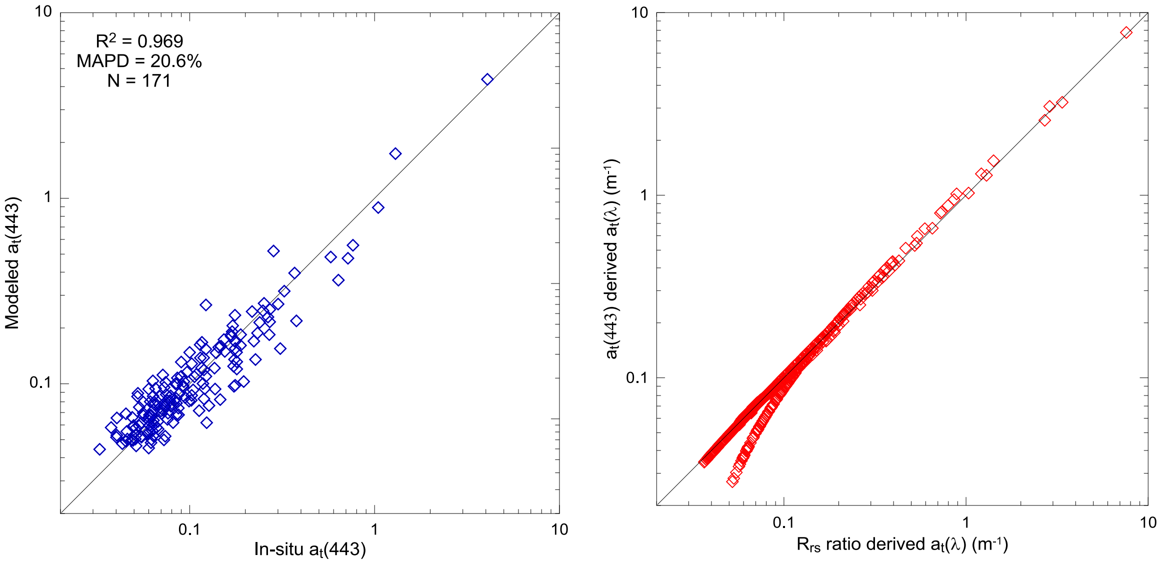

Figure 4.11: Left panel: Estimated $a_t(443)$ using R_{rs} band ratio compared to measured $a_t(443)$. Right panel: Comparison of $a_t(\lambda)$ using R_{rs} band ratio and the $a_t(\lambda)$ estimates using equations 4.11.

4.7.2. Phytoplankton absorption algorithm.

Similar to the total absorption coefficient, a strong spectral relationship exists between $a_{ph}(443)$ and a_{ph} at other wavelengths. The absorption by phytoplankton has been significantly correlated to $a_{ph}(443)$ in a non-linear way, according to Lee et al. (1999).

$$a_{ph}(\lambda) = \{a_0(\lambda) + a_1(\lambda) \ln[a_{ph}(443)]\} \, x \, a_{ph}(443) \qquad 4.12$$

where $a_0(\lambda)$ and $a_1(\lambda)$ are empirical coefficients. This model is designed to allow the $a_{ph}(\lambda)$ shape to change with $a_{ph}(443)$. Statistics from the regressions of this model are presented in Table 4.10 which shows that R^2 values for all wavelengths are greater than 0.90. Figure 4.12 shows the results of using equation 4.12 and in-situ data.

Table 4.10: Statistical results of spectral relationships between $a_{ph}(\lambda)$ and $a_{ph}(443)$ based on equation 4.12.

$a_{ph}(\lambda)$	a_0	a_1	R^2
412	1.575	0.191	0.990
469	0.734	0.000	0.999
488	0.607	-0.002	0.998
531	0.437	0.046	0.986
547	0.391	0.047	0.981
676	0.098	-0.052	0.924

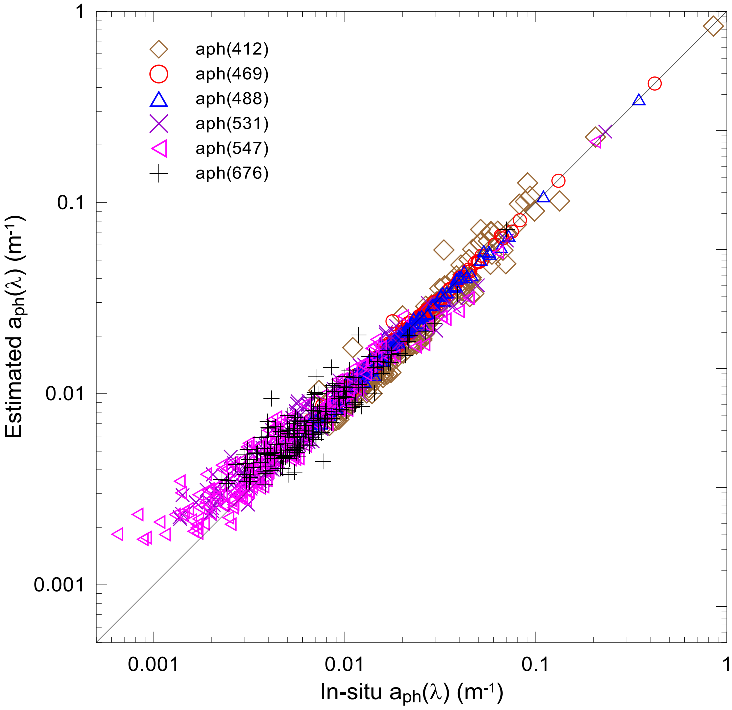

Figure 4.12: Estimated $a_{ph}(\lambda)$compared to measured $a_{ph}(\lambda)$ using equations 4.12.

In a similar approach, we also derive the $a_{ph}(\lambda)$ at selected MODIS wavelengths using a 3rd order polynomial of R_{rs} band ratios. In this study, we found that the R_{rs} band ratio (488/547) was the most suitable for retrieving phytoplankton absorption coefficients. However, the correlation coefficient for phytoplankton absorption is lower than for the total absorption coefficient. This is not surprising since R_{rs} is primarily a function of the total absorption with only a weak dependence on the absorption by the individual component. It can be seen from Table 4.11 that fairly good correlations between $a_{ph}(\lambda)$ and the R_{rs} ratio were achieved with phytoplankton absorption at 443 and 676 nm giving highest R^2 values (~0.80) and lowest RMSE (12%). This is understandable because those bands match absorption maxima in chlorophyll pigments. Figure 4.13 depicts a linear fit between measured and derived a_{ph} from R_{rs} band ratio at 443 and 676 nm. From this figure, it can be seen that R_{rs}-derived a_{ph} at both wavelengths show close agreement and work well over a wide range of conditions for the investigated waters. Both wavelengths yielded similar MAPD accuracy levels.

Table 4.11: Statistical results of 3rd order polynomial ($y = a_0 + a_1x + a_2x^2 + a_3x^3$) between $a_{ph}(\lambda)$ and R_{rs} band ratio 488/547.

$a_{ph}(\lambda)$	**a_0**	**a_1**	**a_2**	**a_3**	**R^2**	**RMSE (%)**
412	-1.326	-1.174	0.474	-2.288	0.61	19.6
443	-1.275	-1.435	0.393	-0.616	0.80	12.3
469	-1.437	-1.268	0.382	-1.064	0.69	15.4
488	-1.514	-1.306	0.387	-0.936	0.70	15.1
531	-1.820	-1.683	0.204	-1.162	0.70	20.2
547	-1.897	-1.920	0.294	-0.287	0.68	21.6
676	-1.326	-1.174	0.474	-2.288	0.77	19.6

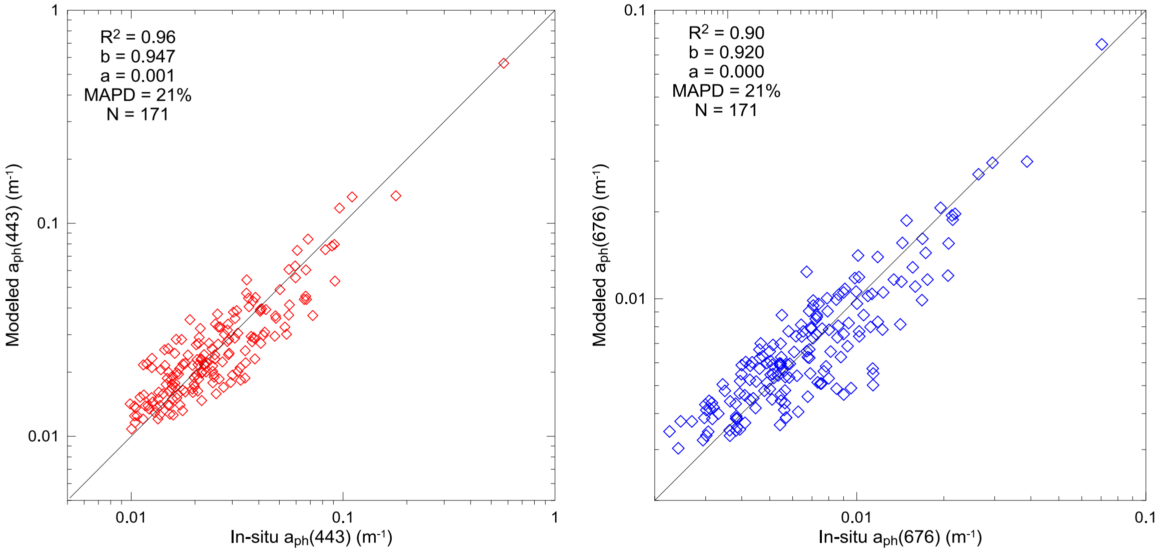

Figure 4.13: Comparisons of model-derived and field observations of $a_{ph}(443)$ (left panel) and $a_{ph}(676)$ (right panel). The solid line represents the 1:1 line.

There are two procedures for determining $a_{ph}(\lambda)$. One is to use remote sensing reflectance to give $a_{ph}(443)$. We have already shown (Table 4.11) that there is a good relationship between $a_{ph}(443)$ and $R_{rs}(488/547)$. a_{ph} at other wavelengths can then be determined from the spectral shape of a_{ph} (Table 4.10). The other procedure is to derive a_{ph} at each wavelength independently from remote sensing reflectance. Table 4.12 compares these two procedures. The left side of this table shows the results of $a_{ph}(\lambda)$ values derived from $R_{rs}(488/547)$ and those determined using the estimated $a_{ph}(443)$ based on the regression results shown in Table 4.10. It can be seen that estimation of $a_{ph}(\lambda)$ for 412, 469, 488, 531 and 547 nm were significantly improved when deriving from $a_{ph}(443)$ with average errors (MAPD) dropped by nearly 8% and regression slopes approaching one.

Table 4.12: MAPD and regression results for the in-situ $a_{ph}(\lambda)$. Table A represents validation results of $a_{ph}(\lambda)$ values estimated using R_{rs} ratio and Table B from equation 4.5. *a* and *b* represent the intercept and slope of the best fit line, respectively.

A					**B**				
$a_{ph}(\lambda)$	**R^2**	**a**	**b**	**MAPD (%)**	**$a_{ph}(\lambda)$**	**R^2**	**a**	**b**	**MAPD (%)**
412	0.901	0.003	0.783	35.8	412	0.947	-0.001	0.957	28.0
443	0.958	0.001	0.947	21.0	443	-	-	-	-
469	0.898	0.003	0.803	28.7	469	0.941	0.001	0.960	20.8
488	0.902	-0.001	1.104	28.0	488	0.941	0.001	0.962	20.3
531	0.930	0.000	0.951	32.3	531	0.940	0.001	0.968	24.8
547	0.940	0.000	0.935	32.5	547	0.937	0.001	0.966	26.6
676	0.895	0.000	0.920	20.8	676	-	-	-	-

4.7.3. Coloured detrital matter absorption algorithms

In general, absorption by detritus follows the same spectral shape as CDOM absorption in the visible wavelengths (Bukata et al., 1983) with relatively smaller spectral slopes (Roesler et al., 1989), so it is difficult to separate them especially in high turbidity coastal water. Therefore, the majority of ocean colour algorithms combine the effect of CDOM and detritus absorption into a single term, a_{dg}, so-called coloured detrital matter.

Table 4.13 shows the results of all models in estimating $a_d(\lambda)$, $a_g(\lambda)$ and $a_{dg}(\lambda)$ based on field reflectance measurements. We found that all models can be well correlated using a 2nd order polynomial function but with different combination of R_{rs} band ratio. Although the correlation was not high, our data show that $a_d(\lambda)$ can be best estimated using a two band ratio, $R_{rs}(488/547)$ and $R_{rs}(531/547)$. Whilst the best models for $a_g(\lambda)$ and $a_{dg}(\lambda)$ involve the reflectance ratios $R_{rs}(412/547)$ and $R_{rs}(443/547)$, respectively. It can be seen that results for absorption at all three wavelengths (380, 400 and 412 nm) show close agreement and provided relatively higher R^2 and smaller RMSE values than the wavelength at 443 nm. This implies that the UV and short blue wavelengths are relatively more important for estimating the non-algal products compared with 443 nm. Considering all absorption models, a_g and a_{dg} provided better results than the a_d model. The reduced correlation for $a_d(\lambda)$ might be due to the relatively lower proportion of this component to the total light absorption compared to absorption by CDOM (refer to chapter 3).

Figure 4.14 and Table 4.14 compare the results of all non-pigmented absorption derived from the model and those from in-situ measurements at 380, 400, 412 and 443 nm, respectively. The R_{rs}-derived a_{dg} for the first three wavelengths fit the in-situ data quite well with R^2 = 0.96, a slope of almost unity and average difference of less than 25% for a_{dg} in the range of 0.02 to 10.5 m^{-1}. These results demonstrate that a_{dg} can be accurately derived from the empirical approach of remote sensing technique even for this wide range of a_{dg} values. For a_g, the empirical model systematically underestimated for most wavelengths, though good correlation of determination (R^2 = 0.90) and low MAPD (~20%) were achieved between R_{rs}-derived and in-situ datasets. In contrast, R_{rs}-derived a_d was overestimated for all wavelengths although they are well correlated (R^2=0.97) with in-situ measurements.

Table 4.13: Statistical results of 2^{rd} order polynomial (one band ratio:$y = a_0 + a_1x + a_2x^2$; two band ratio: $y = a_0 + a_1x + a_2x^2 + b_1y + b_2y^2$) between $a_d(\lambda)$, $a_g(\lambda)$ and $_{adg}(\lambda)$ and R_{rs} band ratio.

a(λ)	**Band ratio**	**a_0**	**a_1**	**a_2**	**b_1**	**b_2**	**R^2**	**RMSE (%)**
$a_d(380)$	488/547 & 531/547	-0.667	-2.214	3.013	-3.653	-55.825	0.81	26.5
$a_d(400)$		-0.763	-1.772	2.473	-5.270	-49.569	0.79	27.6
$a_d(412)$		-0.820	-1.607	2.237	-5.877	-46.794	0.78	28.1
$a_d(443)$		-1.036	-1.408	1.969	-6.315	-42.051	0.76	28.7
$a_g(380)$	412/547	-0.832	-0.971	0.304			0.86	11.1
$a_g(400)$		-0.957	-0.971	0.274			0.84	12.0
$a_g(412)$		-1.034	-0.952	0.286			0.82	12.5
$a_g(443)$		-1.260	-0.924	0.423			0.68	17.7
$a_{dg}(380)$	443/547	-0.578	-1.487	0.342			0.86	14.6
$a_{dg}(400)$		-0.700	-1.469	0.259			0.85	15.0
$a_{dg}(412)$		-0.774	-1.443	0.266			0.85	15.0
$a_{dg}(443)$		-0.994	-1.386	0.324			0.77	18.3

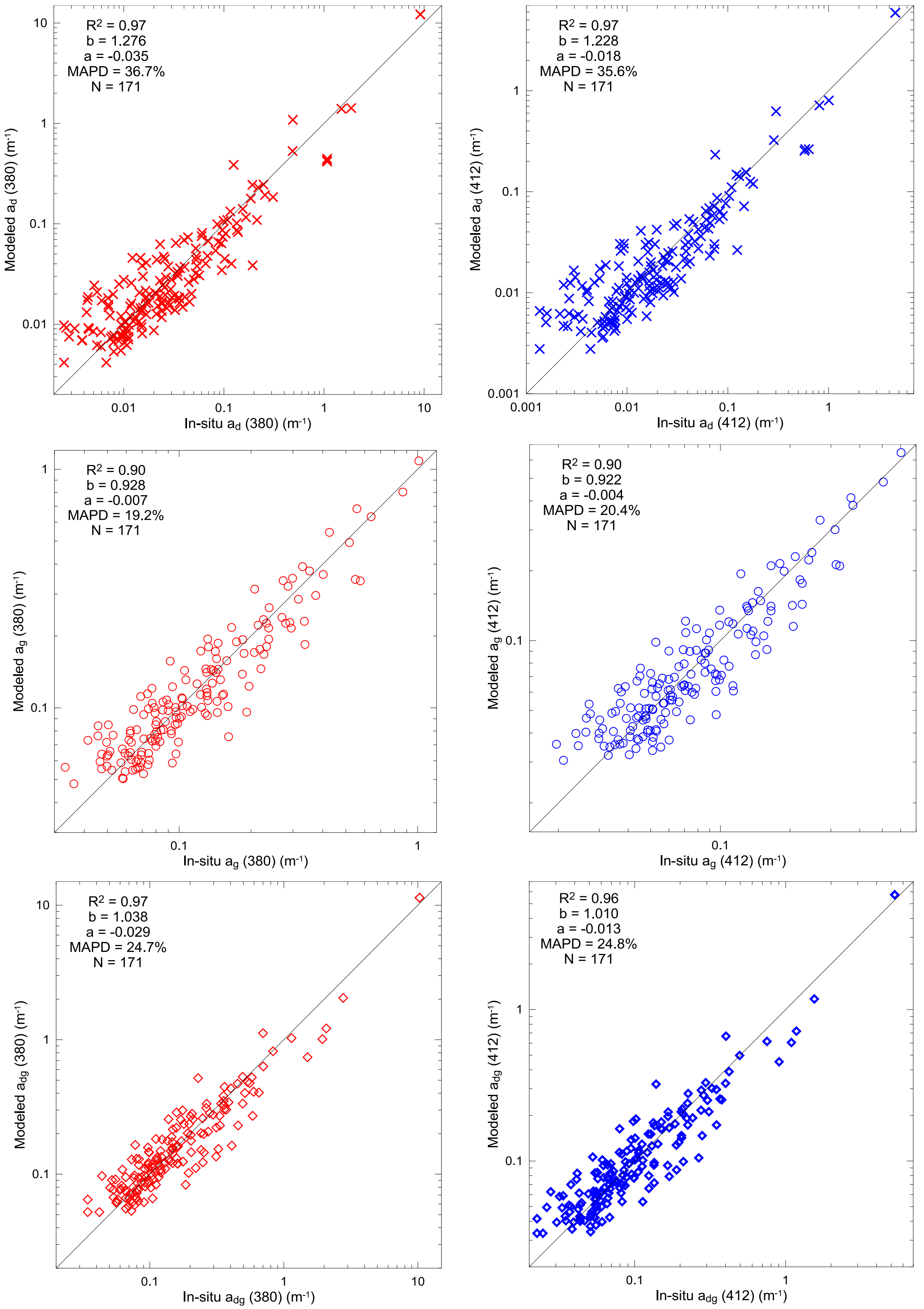

Figure 4.14: Comparisons of model-derived and field observations of a_d, a_g and a_{dg} at 380 nm (left panel) and 412 nm (right panel). The solid line represents the 1:1 line.

Table 4.14: MAPD and regression results of band ratio algorithms for $a_d(\lambda)$, $a_g(\lambda)$ and $_{adg}(\lambda)$. *a* and *b* represent the intercept and slope of the best fit line, respectively.

$a(\lambda)$	**R^2**	**a**	**b**	**MAPD (%)**
$a_d(380)$	0.97	-0.035	1.276	36.7
$a_d(400)$	0.97	-0.023	1.243	35.8
$a_d(412)$	0.97	-0.018	1.228	35.6
$a_d(443)$	0.96	-0.011	1.243	36.4
$a_g(380)$	0.90	0.007	0.928	19.2
$a_g(400)$	0.90	0.005	0.926	20.1
$a_g(412)$	0.90	0.004	0.922	20.4
$a_g(443)$	0.83	0.003	0.897	28.1
$a_{dg}(380)$	0.97	-0.029	1.038	24.7
$a_{dg}(400)$	0.96	-0.015	1.001	24.3
$a_{dg}(412)$	0.96	-0.013	1.010	24.8
$a_{dg}(443)$	0.94	-0.019	1.110	30.9

4.8 Discussion and conclusion

In east coast Peninsular Malaysia water, the standard global MODIS chlorophyll algorithm performance varies significantly between different seasons. The algorithm tended to systematically underestimate chlorophyll concentration during the SWM and overestimate during the NEM season. In contrast, the bias of MODIS-derived chlorophyll varied non-systematically during the inter-monsoon season. These systematic biases of chlorophyll in waters with low and high chlorophyll values are consistent with previous observations in the other ocean regions (e.g. Darecki and Stramski, 2004; Kudela and Chavez, 2004; Garcia et al, 2005). The systematic errors of standard global MODIS algorithms can be explained in terms of the variations in the bio-optical properties. These differences, especially in the phytoplankton and CDOM absorption properties could affect the spectral values of R_{rs} and hence the remote sensing of phytoplankton pigments. Consistent with a systematic variation of $a_{ph}(443)$ (see Chapter 3) from the global average data of Bricaud et al., (1995), the systematic shifts in the fitted regression line of chlorophyll-reflectance ratios suggest that there were major differences in phytoplankton pigment composition between our waters compared with other ocean regions. As clearly indicated in Figure 4.6, reflectance ratios measured in this study are generally lower per unit chlorophyll for chlorophyll values >1.0 mg m^{-3} compared to the standard MODIS-OCM3 reflectance ratios. This difference is likely to be from the elevated CDOM-chlorophyll absorption ratios observed in the study area. Especially during the NEM season, CDOM-chlorophyll absorption ratios in the study area can exceed those observed for many case 1 waters. Since CDOM and phytoplankton absorb the blue light strongly, blue-green absorption ratios increase and result in decreases in blue-green reflectance ratios. This effect is likely to return greater chlorophyll values for a given blue-green ratio during the NEM season. During the SWM season, lower than normal CDOM:chlorophyll ratios may account for the underestimation of chlorophyll concentration for chlorophyll values <0.4 mg m^{-3} during the SWM season.

The underestimation by the MODIS algorithm during the inter-monsoon season is likely attributed to pigment packaging effects and non-covarying CDOM that result in a reduced absorption coefficient and an increase in remote sensing reflectance. Although these results are in conformance with some published studies (e.g., Mitchell, 1992; Sathyendranath et al, 2001; Stramska et al., 2003), an underestimation of chlorophyll concentration during this season occurred in a non-systematic way, with a lack of a relationship (R^2=0.001) between chlorophyll and R_{rs} values. It is difficult to explain the possible cause of this uncertainties as the lack of field data prevented us from determining whether the phytoplankton communities (species and size) or other factor such as scattering properties play a major role.

In this study, we showed that our derived-empirical algorithms significantly improved the accuracy errors of chlorophyll estimation for the monsoon seasons from 150% to less than 25%. These error margins are below the accuracy goal for satellite retrieved chlorophyll estimates. It is interesting to note that our new algorithms work well even in coastal waters affected by very high concentrations of CDOM and suspended particles. This was specially apparent during the NEM season when CDOM largely overwhelmed the influence of the phytoplankton pigment. This excellent performance is likely to be compounded by three factors; 1) the covarying impact of CDOM absorption coefficient; 2) relatively constant contribution of CDOM to the total nonwater absorption; and, 3) the least contribution of detritus absorption coefficient in the study area during the monsoon season. On a regional basis, the empirical algorithm based on linear and 4th-order polynomial functions developed from the band ratios R_{rs}(488/547) and R_{rs}(531/547) are proposed for the remote estimation of chlorophyll concentration. The advantage of using these band ratios for estimating chlorophyll concentration is that the interference due to CDOM absorption is lower (O`Reilly et al., 2000).

Although inversion models using semi-analytical algorithms offer an improvement over empirical algorithms in determining biogeochemical quantities in many waters (Lee et al., 2002; Hoge et al., 1999; Maritorena et al., 2002; Carder et al., 1999), our findings suggest that they may not be a feasible alternative for the determination of chlorophyll concentration and absorption properties in our study area. In conformance with other studies (Garcia et al., 2006; Chang and Gould, 2006; Zhu et al., 2011), we found that both the QAA inversion model and the semi-analytical algorithm perform poorly and exclude the possibility of estimating the chlorophyll concentration and absorption coefficients from these models. Both models showed many outliers or very low values of $a_t(\lambda)$ and $a_{ph}(676)$ when in-situ reflectances were used. The complete failure of these algorithms can be related to shortcomings of modeling the spectral shape of particle backscattering and phytoplankton absorption. As indicated in Figure 4.10, there was a lack of correlation between the wavelength dependence of backscattering, Y and the band ratio R_{rs}(443/488) that lead to significant errors in the prediction of the particulate backscattering coefficient. As this step is of first order importance in the derivation of absorption properties, any errors in backscattering calculation could conceivably lead to larger errors in retrieving each absorption property. In this case, further work is required to establish a relationship between band ratios and backscattering coefficients. It also appears that the assumptions of the QAA model and MODIS semi-analytical algorithm do not hold in waters with high concentration of CDOM and large variations in both magnitude and spectral shape of phytoplankton absorption. For waters with strong interference by CDOM absorption such as those in our area, the remote sensing reflectance in the blue wavelengths (412 and 443 nm) can be very small which could prevent the algorithm from performing properly. The low performance of this algorithm in coastal water was also reported by Qin et al., (2007) who found that the accuracy of the QAA algorithm degrades rapidly with increasing CDOM and detritus concentrations.

Another important finding from this study was that each absorption coefficient can be retrieved empirically within reasonable certainty over a wide range of absorption values. The algorithms perform better than the inversion model and semi-analytical algorithm with MAPD errors between 20% and 35%. Fitting the measured data to both spectral models found no spatial or temporal variations in the model parameters, suggesting a significant potential of this simple algorithm technique to be operationally applied to satellite ocean colour data in our waters. These findings are consistent with those of other studies in different ocean regions (Stramska et al., 2003; Blondeau-Patissier et al., 2004; Pan et al., 2008). In this study, band ratios $R_{rs}(443/547)$ and $R_{rs}(488/547)$ are proposed to estimate $a_t(443)$ and $a_{ph}(443$ and $676)$, respectively. It is also interesting to note that $a_t(443)$ and $a_{ph}(443)$ can also be used to derive estimates $a_t(\lambda)$ and $a_{ph}(\lambda)$ at other wavelengths with a good accuracy. The results indicate that it is more accurate to estimate the coloured detrital matter (a_{dg}) and CDOM absorption coefficients than the detritus absorption coefficient from reflectance data. This is likely due to the broad range of CDOM absorption coefficient compared to absorption by detritus in our waters. In this study we also found that it is more accurate to estimate CDOM absorption at wavelengths shorter than 443 nm using band ratio $R_{rs}(412/547)$.

CHAPTER 5

SEASONAL AND INTER-ANNUAL VARIABILITY OF MODIS-DERIVED OCEAN COLOUR

5.1 Overview

This chapter presents the results concerning the seasonal and inter-annual variability of the surface ocean colour field in the South China Sea and nearby areas. The objective of this chapter is to derive the spatial and temporal variations of chlorophyll and CDOM concentrations using our new empirical models from a 5-year satellite derived dataset (2006 – 2011). The relationship between ocean colour variables and the ocean dynamics (SST and wind speed) are also examined.

5.2 Data coverage

The area selected in this study covers most of the western part of the South China Sea (SCS) and Gulf of Thailand (GoT) from 1.5 ^{o}N to 13 ^{o}N, and from 99 ^{o}E to 109 ^{o}E (Figure 5.1). Physical and dynamical features of this marginal sea have been briefly summarized in chapter 2. A more detailed description can be found in several reviews (e.g., Wyrtki, 1961; Shaw and Chao, 1994; Liu et al., 2002). In this study, monthly composites of reflectance data were used, as weekly averages generally suffered from insufficient coverage of the studied area due to cloud cover. These monthly binned data with a 4 km resolution over the years between 2006 and 2011 were taken from the Ocean Color website (http://oceancolor.gsfc.nasa.gov/) that is operated by the NASA Ocean Biology Processing Group. These reflectance data are those from MODIS Terra and Aqua (412, 443, 488, 547 and 667 nm) that overpass the study area at around 1030 and 1430 local time, respectively. Reflectance data that represent three different seasons; SWM (June to September), NEM (November to March) and inter-monsoon (April to

May; October) were analysed using the ITTVIS ENVI software (ITT Corporation, 2008). To display spatial distribution of chlorophyll and CDOM, we applied our derived-empirical models (adjusted-OCM3v6 and CDOM algorithms from tables 4.3 and 4.10, respectively) to the MODIS images over the entire studied region.

This large area coverage will allow us to determine how environmental conditions in these regions regulate the phytoplankton biomass and CDOM in the study area. This study however, will only describe the seasonal pattern of water colour in the SCS and GoT waters. All other areas (i.e. Straits of Malacca) are excluded as they are subject to different environmental conditions from those of the eastern coast of Peninsular Malaysia. As the satellite images cover a large area, the following points must be kept in mind when interpreting results of this study. First, the sampling extent was spatially limited within the central part of the east coast region of Peninsular Malaysia; the empirical algorithms used to determine chlorophyll and CDOM concentrations may not be valid in other areas. Second, as shown previously (chapter 4), our chlorophyll algorithm is applicable only during the monsoon periods (SWM and NEM seasons) and did not work during the inter-monsoon season.

To describe the environmental conditions in the study area, we also analysed the monthly sea surface temperature (SST) and sea surface wind conditions for each season. For the SST data, only night-time images (11 µm band) were used in order to avoid the diurnal warming effect on the surface layer during the daylight hours, particularly in regions with low wind speeds. These images were taken from the MODIS Aqua L3 data (better coverage than the Terra). The monthly average wind vector data of QuikScat and WindSat were acquired from the Remote Sensing Systems website (http://www.ssmi.com/). These surface wind data are provided by the NASA Ocean Vector Winds Science Team (NASA, 2001).

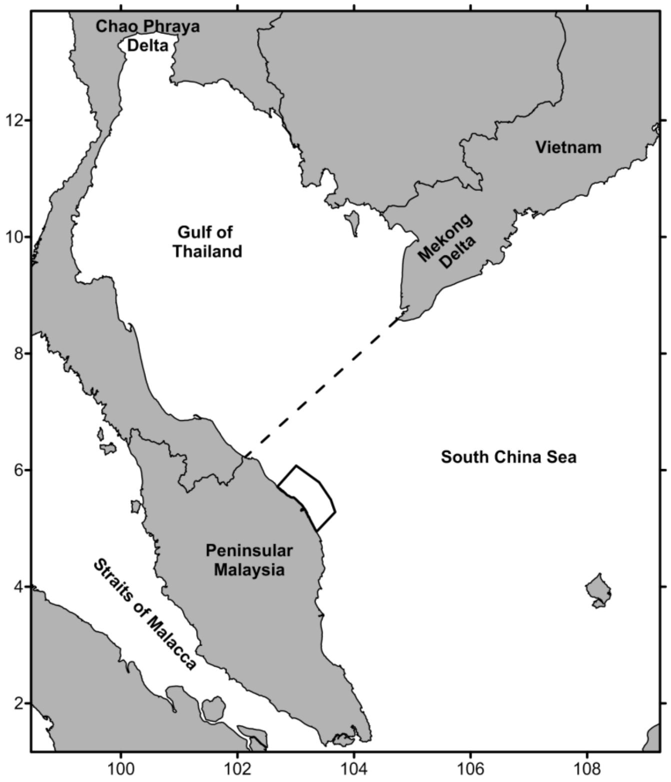

Figure 5.1: Geography and map of the western part of South China Sea. The small box shows the sampling area. The latitude (N) and longitude (E) coordinates are in degrees.

5.3 Seasonal variability of chlorophyll and CDOM distributions

The monthly mean images of surface chlorophyll and CDOM concentration derived from MODIS satellite data for a study period of 2006 to 2011 are displayed in Figures 5.3 and 5.5 (areas in white had no valid data due to persistent cloud cover).

5.3.1 Seasonal variability of chlorophyll

Monthly mean chlorophyll from 2006 to 2011 (Figures 5.2 and 5.3) clearly showed seasonal variability with high concentration observed during the NEM (November-February) and SWM (July-August) seasons, and low during spring (April-May) and fall inter-monsoon (October) periods. Analysis of monthly mean chlorophyll for 2006-2011 (Figure 5.2) reveals that the peaks of chlorophyll differ between regions. The winter (NEM) bloom in the SCS occurred in January whereas it peaks in December and November in GoT and the study area, respectively. For the secondary summer bloom, the highest value in the SCS was recorded in July and August but took place in June and August in the GoT and the study area, respectively.

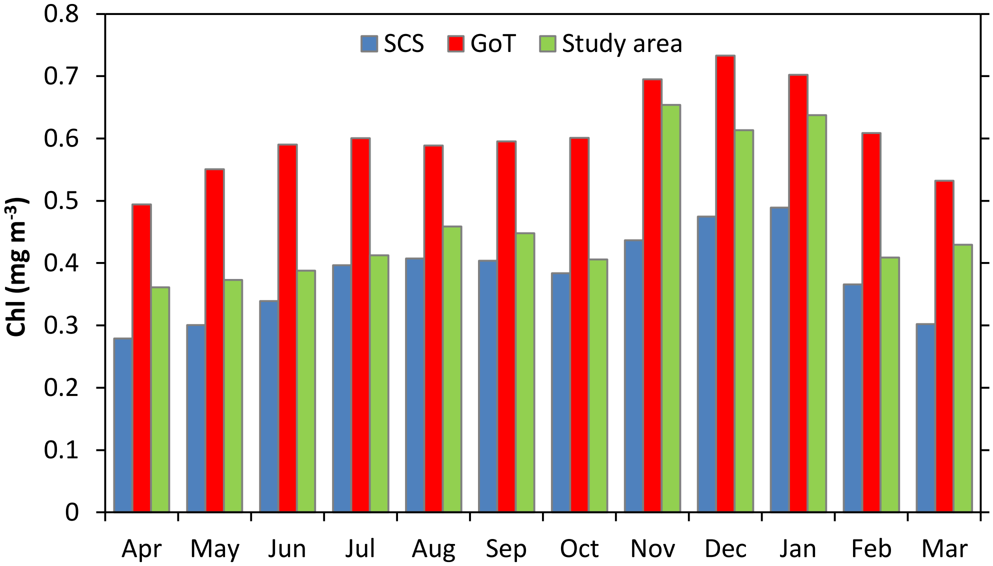

Figure 5.2: Time series of the mean monthly MODIS chlorophyll concentrations from April 2006 to March 2011 in the SCS, GoT and the study area. Error bars are omitted for clarity; in each case, the SD for each point was more than 20% of the mean.

During the spring inter-monsoon (April-May), chlorophyll concentrations were relatively low (0.1 – 0.3 mg m^{-3}) over the most of the SCS and GoT regions (Figure 5.3). During this season, high chlorophyll concentrations (> 1 mg m^{-3}) were confined in a narrow band along the coast and river mouth. April is a transition month between the winter and summer, with river flows at their lowest annual level (Chao et al., 1996). During this month, chlorophyll concentrations were at the lowest level throughout the study period. Following the onset of stratification and an increase in a river flow in May, chlorophyll increases in concentration (> 1.5 mg m^{-3}) along the lower GoT (Chao Phraya river delta) and Vietnamese coast (Mekong delta). However, chlorophyll concentrations in offshore waters, remained low (0.1 -0.2 mg m^{-3}) and is almost identical to that seen in April. On the other hand, chlorophyll concentrations along the east coast of Peninsular Malaysia did not change much and remained persistently low (~0.3 mg m^{-3}) throughout the spring season.

As the SWM strengthens in the summer, chlorophyll concentrations in this region is highly spatially variable and showed marked changes when compared to the previous season. In June, the monthly composite image clearly shows an increase in chlorophyll concentrations, particularly in the Mekong delta, lower GoT and the southern tip of Peninsular Malaysia. A large plume was apparent in the Mekong delta that spread the phytoplankton far offshore into the nearby SCS and GoT. In the central regions of the GoT and offshore waters of the SCS, pigment levels remained persistently low (0.15 – 0.25 mg m^{-3}). The most remarkably feature in this season is the elevated chlorophyll concentrations (~0.4 mg m^{-3}), with an arc-like shape that extended from the coastal water of Peninsular Malaysia into the southern tip of Mekong delta. This cross-shelf transport may be driven by strong cross-shelf winds that bring nutrient-rich coastal waters offshore. The occurrence of this feature however, was annually variable from June to July, depending on the strength of the wind.

In July, a region of increased chlorophyll (0.4 – 0.5 mg m^{-3}) from the Chao Phraya and Mekong delta spreads into the entire GoT and extends southward into the South China Sea region. The arc of elevated chlorophyll off the east coast of Peninsular Malaysia was still present, although the concentrations were relatively low (<0.5 mg m^{-3}). Again, the phytoplankton plume of the Mekong delta extended further offshore and moved northeast in the direction of prevailing wind. The persistent bloom of phytoplankton along the coastal area of Vietnam may be attributed to nutrient provided by river runoff as well as upwelling forcing. In contrast to the east coast of Peninsular Malaysia, this area experiences heavy rain fall and strong southwesterly winds that usually peak in July (Chao et al., 1996). Upwelling in this area has been widely reported to occur between June and October (e.g. Tang et al., 2003; 2004). Due to the impact of water circulation, there is a northeastward offshore movement of chlorophyll off the Vietnamese coast. This offshore jet is known as the Summer Southeast Vietnam Offshore Current (Fang et al., 2002, 2006) that contributes to the high chlorophyll in this region. The bloom (>1.5 mg m^{-3}) along the Vietnamese coast and lower GoT continued until August with the spatial pattern of chlorophyll distribution relatively similar to July. Meanwhile, a cross-shelf pattern of elevated chlorophyll off the east coast of Peninsular Malaysia is still maintained. As summer enters its final phase in September, surface chlorophyll starts to decline progressively, although higher chlorophyll concentration (>1.5 mg m^{-3}) was observed continuously along the coastal waters of Vietnam and the lower GoT. In response to a weak wind forcing in this month, a band of elevated chlorophyll moved inshore and the cross-shelf chlorophyll off the east coast of Peninsular Malaysia was no longer present.

During the fall inter-monsoon (October), the pigment concentration in the GoT and SCS continually decreased with chlorophyll fronts (~0.5 mg m^{-3}) moved further inshore However, the bloom along the Mekong delta and the lower GoT did not lose its magnitude but was more pronounced than during the previous month. This can be seen by the widespread distribution of chlorophyll rich waters (>1.0 mg m^{-3}) downwind of the southern coast of Vietnam. Chlorophyll concentrations along the east coast of Peninsular Malaysia and offshore waters of SCS were low and varied from 0.15 to 0.4 mg m^{-3}.

During the NEM season, chlorophyll concentration increased dramatically with high chlorophyll values spread out over a large part of the GoT and SCS waters. Chlorophyll concentration starts to increase at the beginning of the NEM season in November and typically peaks in December or January. In November, chlorophyll concentration in the GoT and most parts of the SCS increased to more than 0.30 mg m^{-3} and the high chlorophyll area along the coast in the region moved further offshore. During this month, an obvious phytoplankton bloom (>1.5 mg m^{-3}) in a band barely 30 km wide was present along the east coast of Peninsular Malaysia. The phytoplankton blooms in this area at this time are likely associated more with the sudden onset of high-intensity rainfall, which resulted in a very high river discharge. As the wind events further strengthen and become more frequent in December and January, and concurrent with the lowest SST, high surface chlorophyll (>0.30 mg m^{-3}) spreads out over a wider area. This remarkable increase in phytoplankton biomass can be seen in the December and January images with a broad band of high chlorophyll concentration (>2 mg m^{-3}) appearing along the coastal region. It can also be seen that plumes of phytoplankton from the Mekong delta extended further southward, stretching across the GoT and merged with the chlorophyll-rich waters (~0.5 mg m^{-3}) from the northern region of Peninsular Malaysia. In contrast, the concentration of surface chlorophyll along the east of Peninsular Malaysia declined significantly (0.3-0.8 mg m^{-3}) during December-January and high chlorophyll concentrations were only confined to a very narrow band (approximately <10 km). The last 2 months of the NEM season (February to March) showed a gradual decrease in phytoplankton biomass with the offshore chlorophyll concentrations dropped from 0.3 mg m^{-3} in January to only 0.1 mg m^{-3} in March.

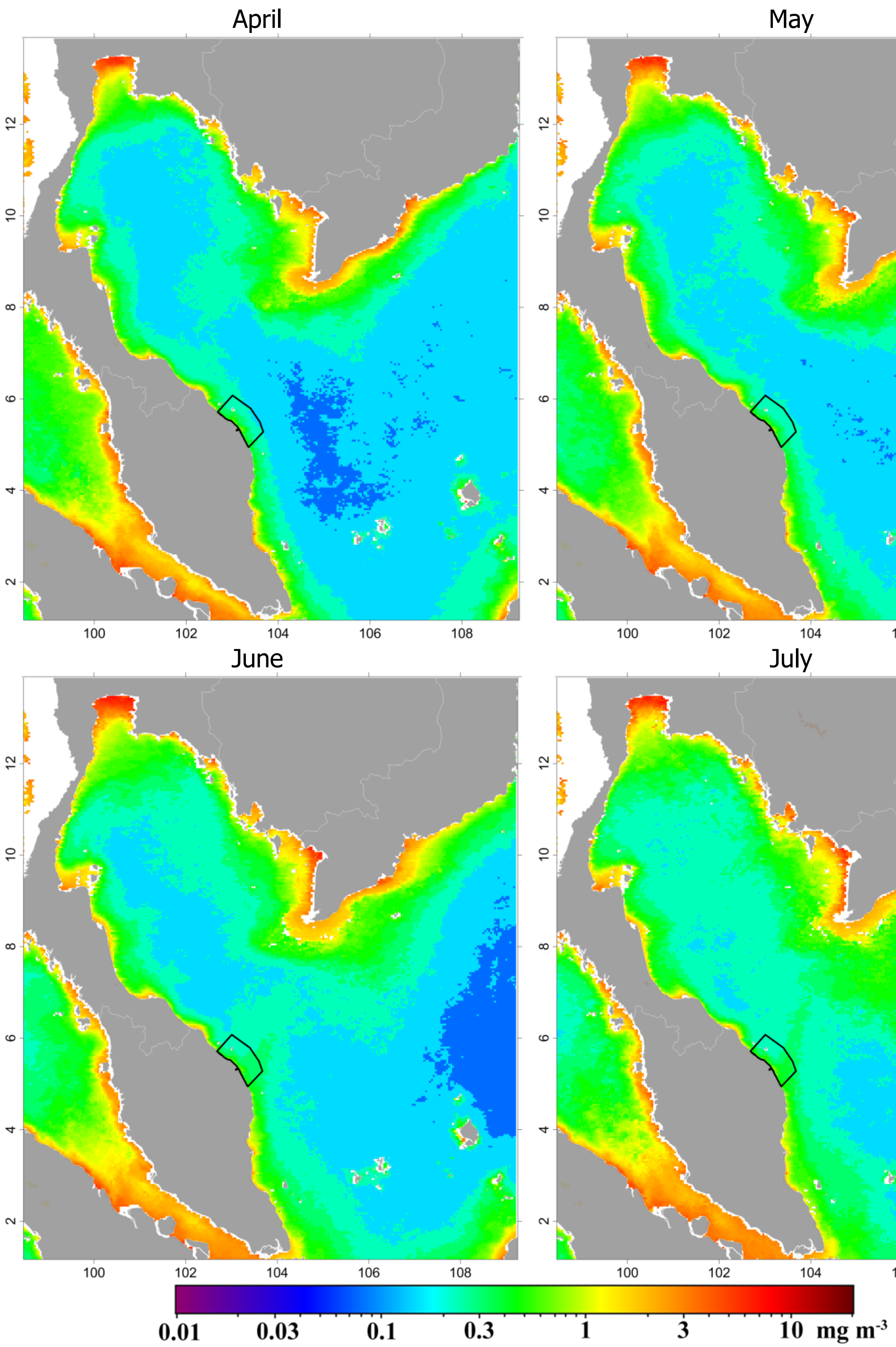
April
May
June
July
12
10
8
6
4
2
100
102
104
106
108
0.01
0.03
0.1
0.3
1
3
10 mg m^{-3}

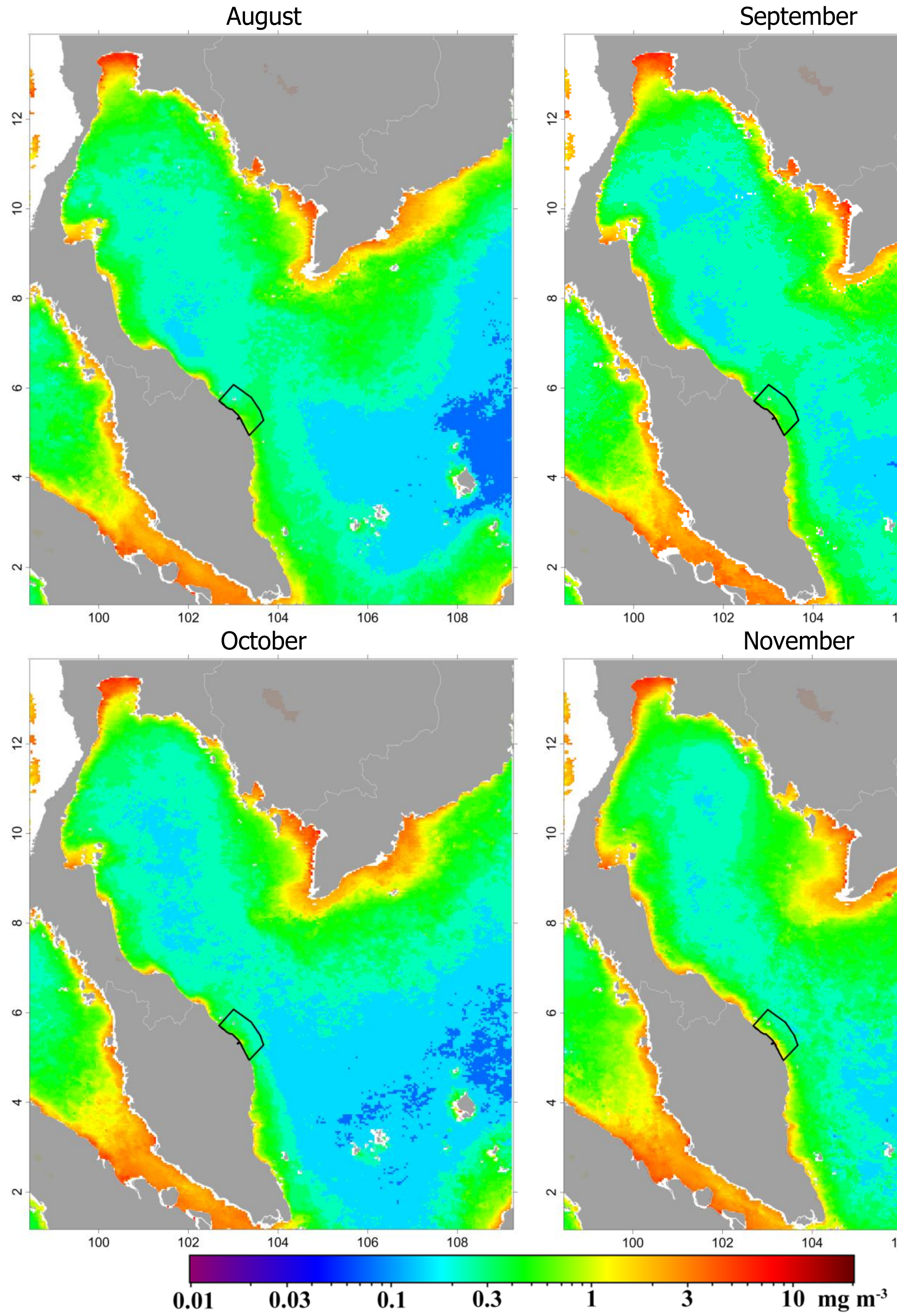
August
September
October
November
2
4
6
8
10
12
100
102
104
106
108
0.01
0.03
0.1
0.3
1
3
10 mg m^{-3}

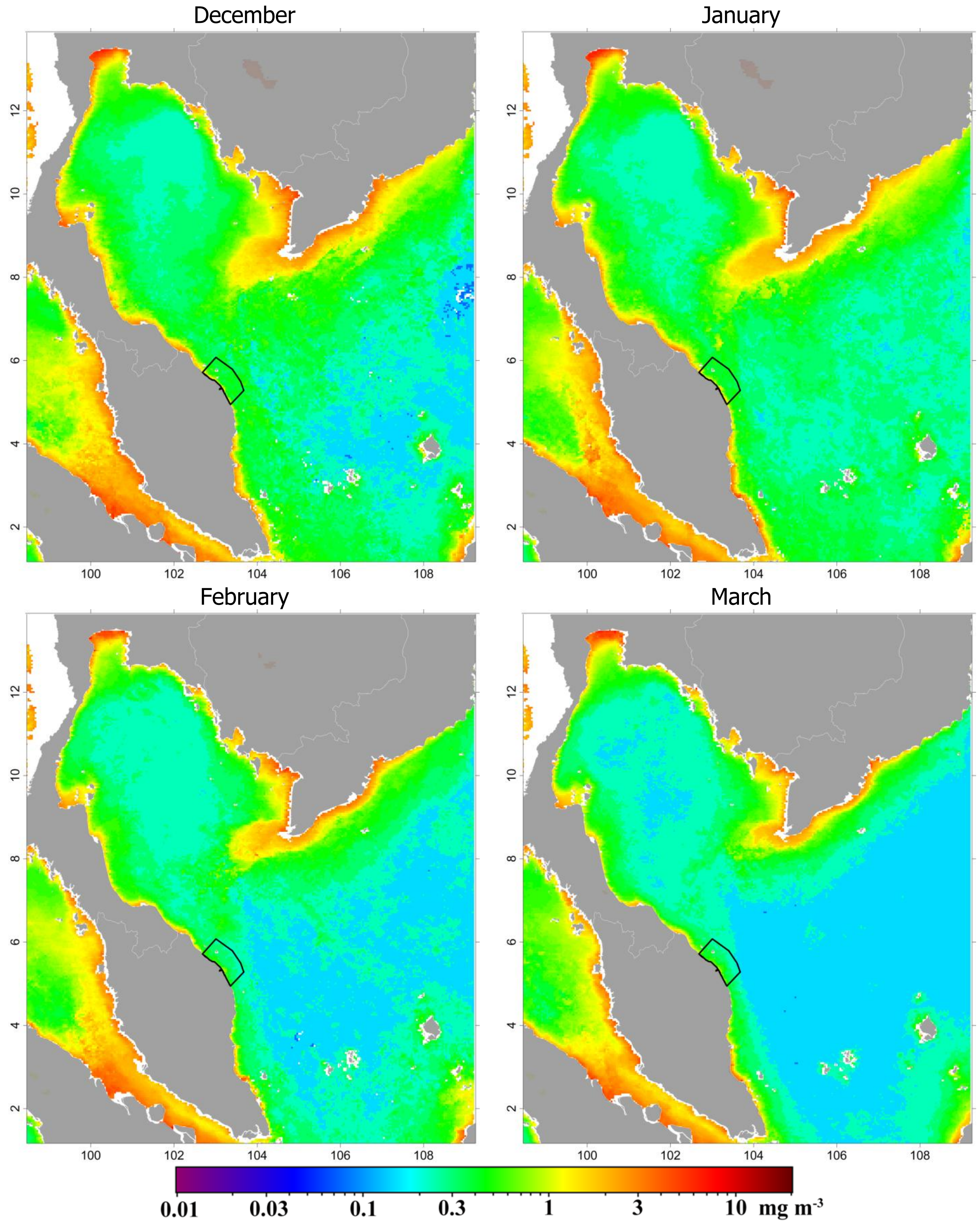

Figure 5.3: Map of the mean monthly MODIS chlorophyll concentrations of the average from April 2006 to March 2011

However, chlorophyll concentrations remained high through this period in the Mekong delta and the lower GoT (Chao Phraya delta) with chlorophyll values of about 2 mg m^{-3}. Along the coastal water of Peninsular Malaysia, chlorophyll concentrations show a sharp decrease from January to March and fall to around 0.35 mg m^{-3} during the last stage of NEM season.

5.3.2 Seasonal variability of CDOM

The monthly maps of CDOM concentrations derived from MODIS data from 2006 to 2011 are displayed in Figure 5.5. As expected, the spatio-temporal variations of CDOM concentrations resemble those of the chlorophyll concentration. In general, there is a marked seasonal cycle, with a general trend toward high and low values in winter and springtime, respectively. For most of the years, CDOM patterns consistent with the monsoon seasonal cycle of winds that reaches its peak during the NEM season and progressively weak towards the SWM season. In contrast to the chlorophyll pattern, the highest values of CDOM (Figure 5.4) for all regions took place in January. Figure 5.4 also suggests a secondary summer peak of CDOM appeared in June in the GoT and in July in the SCS and the study area.

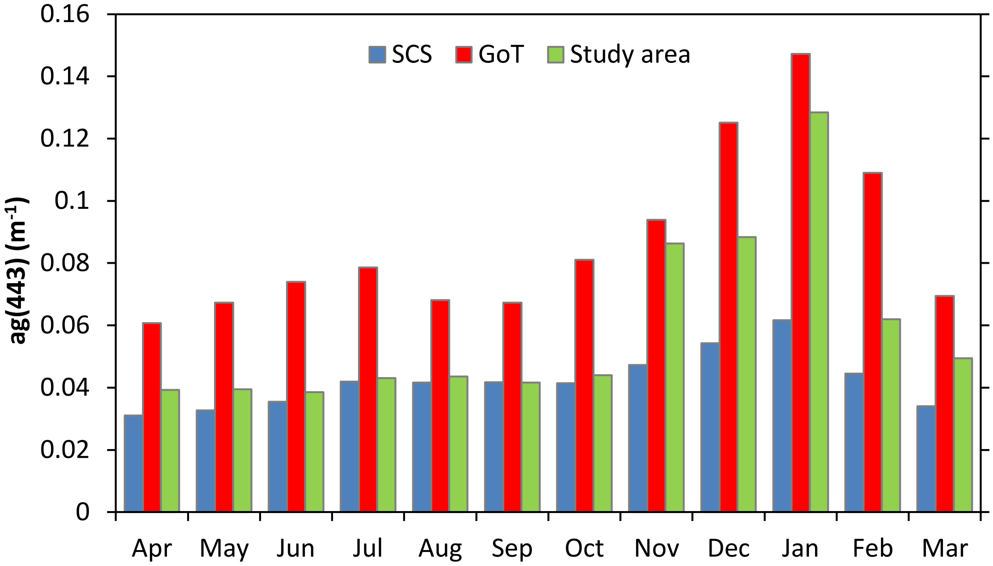

Figure 5.4: Time series of the mean monthly MODIS CDOM concentrations of the average from April 2006 to March 2011 in the SCS, GoT and the study area. Error bars are omitted for clarity; in each case, the SD for each point was more than 20% of the mean.

The spring months are characterized by low CDOM concentrations (<0.02 m^{-1}) over most of the studied regions. During this season, high CDOM values were confined to a narrow strip along the coast and river mouth (Figure 5.5). Without surprise, the majority of high CDOM concentrations (>0.2 m^{-1}) were consistently displayed in the lower GoT and Mekong delta through the season. Along the east coast of Peninsular Malaysia, CDOM concentrations remained low (0.03-0.04 m^{-1}) for both months. The spatio-temporal variations in CDOM concentrations changed drastically as the season progressed from spring to summer. In the lower GoT and Mekong delta, CDOM concentrations remained persistently high and reached 0.6 m^{-1} in July. The plumes from both areas spread into the upper GoT and nearby SCS. This can be clearly seen in the July image with high CDOM concentrations (yellow colour) stretched in a downwind direction off the southern coast of Vietnam. In a similar way to the phytoplankton biomass, strong Ekman pumping and high river discharge from the Mekong river have direct impacts on the distribution of CDOM (Tang et al., 2004).

The CDOM distribution during this season coincides with the upwelling and the offshore current in location, shape, and season (Ma et al., 2011). In offshore waters, CDOM concentrations were between 0.02 and 0.03 m^{-1} with sporadic patches of higher concentrations (0.035 m-1) found in offshore waters of SCS. Along the east coast of Peninsular Malaysia, CDOM levels were persistently low (0.03 -0.05 m^{-1}) for most of the SWM period. Similar to the spatial pattern of chlorophyll, an arc-like feature of high CDOM concentrations (0.03-0.04 m^{-1}) was also observed in June and July for each year of study. Such similar seasonal pattern may indicate that CDOM is locally produced as a byproduct of algal degradation.

During the fall inter-monsoon, offshore waters of the study area are characterized by low concentration of CDOM (~0.02 m^{-1}). While CDOM levels declined significantly in most areas in the GoT, elevated CDOM values were observed in the Mekong delta. In this area, rich CDOM waters (>0.1 m^{-1}) were not only confined along the coast but spread far into the nearby SCS, probably due to high river discharge off the Mekong river mouth. CDOM concentrations along the east coast of Peninsular Malaysia remained consistently low (<0.05 m^{-1}) through the fall period. There was a large increase in CDOM concentration over the entire region during the NEM season. During this season, the CDOM spatial pattern showed a steady increase from November to January and decreased progressively towards the end of NEM period (March). From November to January, a band of high CDOM water appeared from almost any point along the coast. This increase could be seen clearly in the Mekong delta where a plume of high CDOM waters (>0.2 m^{-1}) spread out into a wider area, and extended to the middle of the GoT basin. This leads to a dramatic increase of CDOM concentration in the GoT, from 0.02 m^{-1} in November to 0.035 m^{-1} in January. However the general pattern of CDOM distribution in the SCS was not so obvious and increased only slightly from November (0.02 m^{-1}) to January (0.025 m^{-1}). As the NEM season progressed, the effects of reduced winds and rainfall intensity subsequently reduced the river flow and CDOM concentrations in coastal water. Bands of high CDOM concentration clearly show an onshore movement from February to March. During this period (February-March), the Mekong river plume was observed to gradually retreat laterally toward the river mouth. There was a noticeable drop in CDOM concentrations at the middle of GoT from 0.03 m^{-1} in February to less than 0.02 m^{-1} in March.

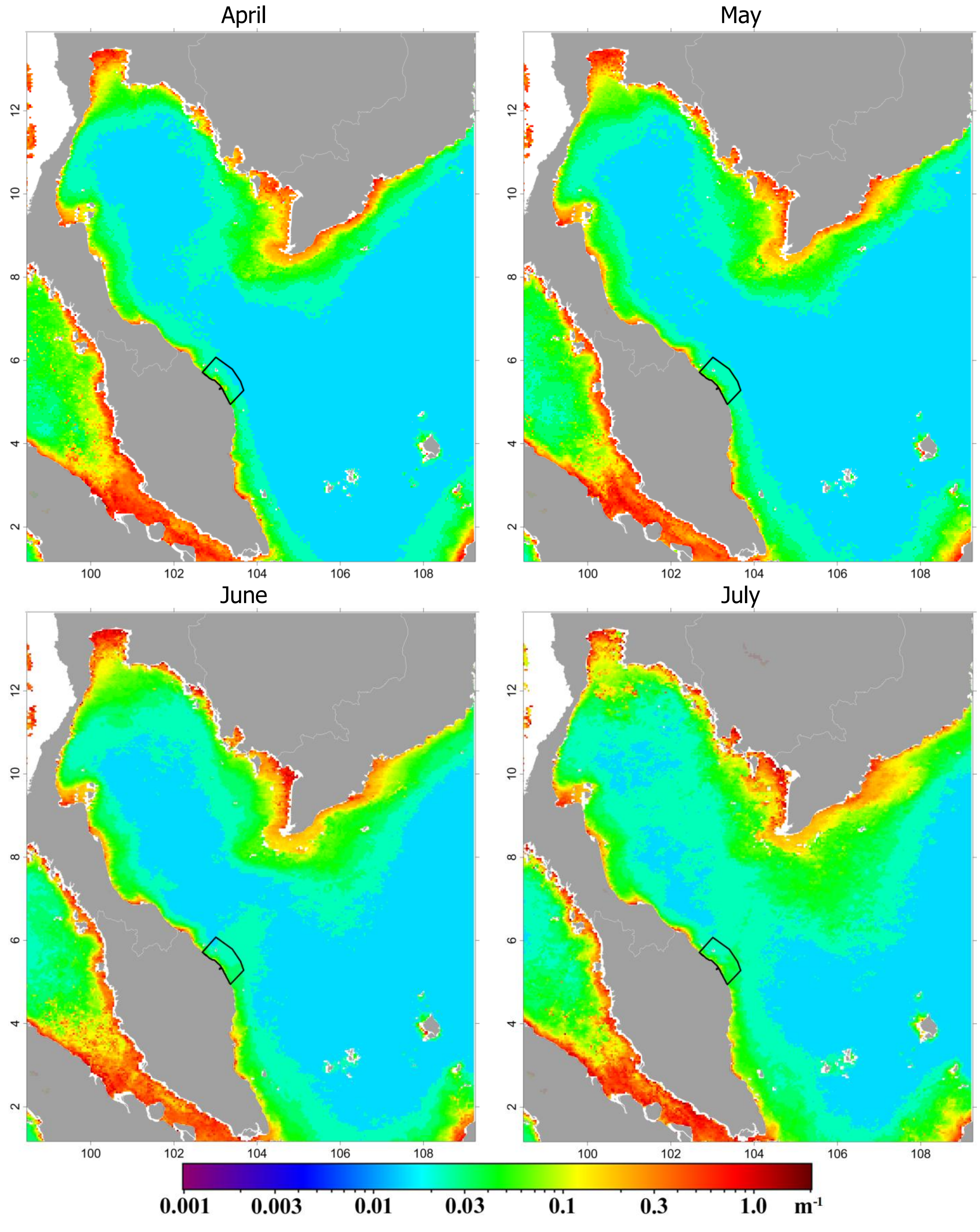
April
May
June
July
12
10
8
6
4
2
100
102
104
106
108
0.001
0.003
0.01
0.03
0.1
0.3
1.0
m⁻¹

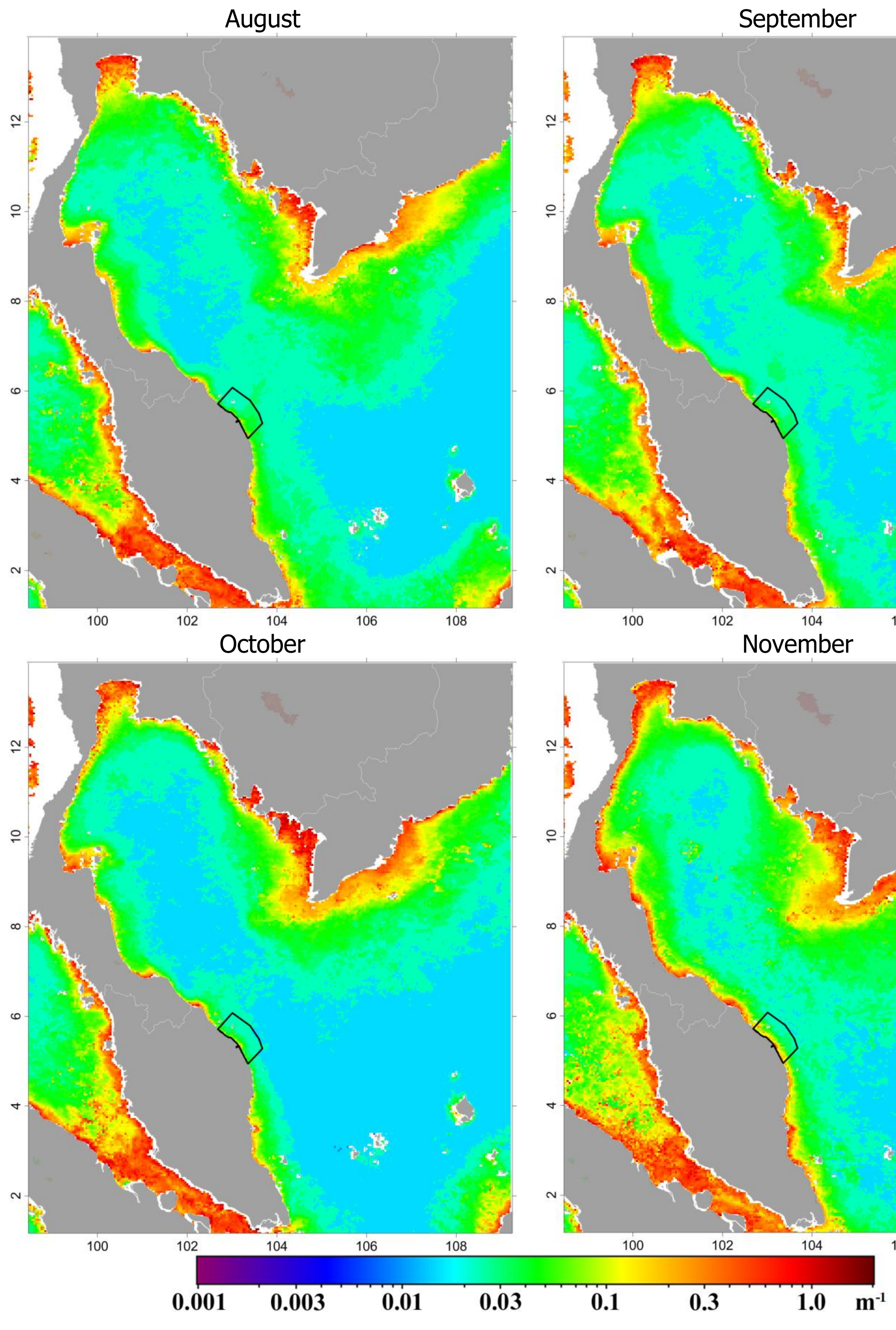
August
September
October
November
12
10
8
6
4
2
100
102
104
106
108
0.001
0.003
0.01
0.03
0.1
0.3
1.0
m⁻¹

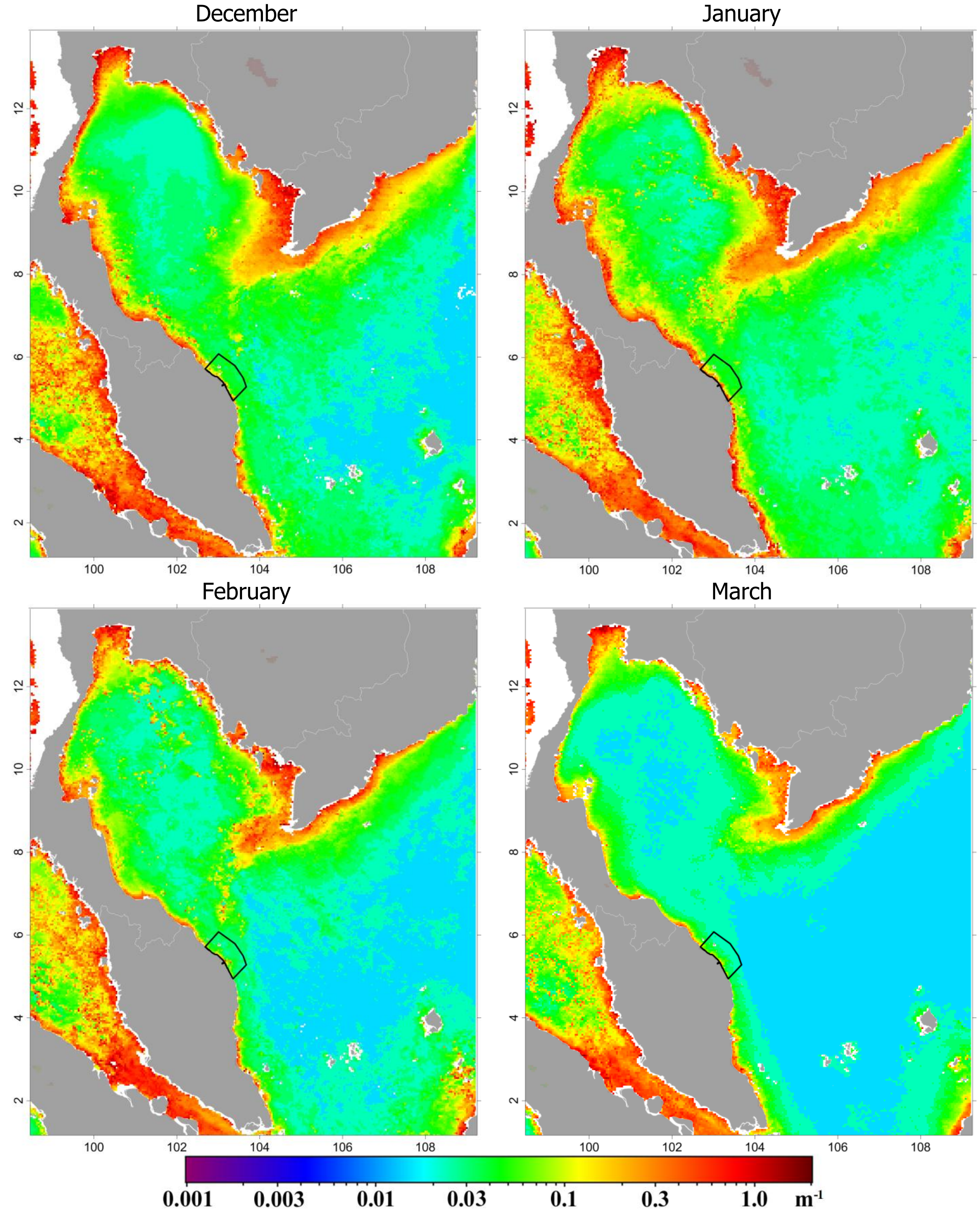

Figure 5.5: Map of the mean monthly CDOM (443 nm) concentrations of the average from April 2006 to March 2011.

5.4 Inter-annual variability of chlorophyll and CDOM concentrations.

Time series of monthly chlorophyll concentrations derived from MODIS satellite imagery over the study area are shown in Figure 5.6. The dataset presented in Figures 5.6 and 5.7 also allows us to visualize the differences in the temporal variability of surface chlorophyll and CDOM concentrations between the SCS and GoT from April 2006 to March 2011. These data are affected by the fact that some images were subject to cloud cover or missing values. The location of cloud cover pixels is variable from image to image and most of the missing values in this region usually occurred during the inter-monsoon and the NEM seasons. The satellite-derived time series (Figures 5.6 and 5.7) reveal a marked inter-annual fluctuation of chlorophyll and CDOM for both regions. Compared to 2006 and 2009, the chlorophyll and CDOM maxima are nearly double in 2007, 2008 and 2010.

In general, the annual cycle of chlorophyll shows the typical pattern of a well-defined winter phytoplankton bloom combined with a short spring period of very low chlorophyll levels. Both regions show an indication of the bloom peak in November-January and chlorophyll minima in April or May. Except in the 2010/2011 season, there appears to be a similar seasonal pattern of winter maxima in the SCS and GoT, although the timing of the peak varies between regions. In the 2010/2011 season, the chlorophyll peaks as early as November in the GoT but is delayed by two months (January) in the SCS. Analysis of chlorophyll concentration time series within the SCS and GoT reveals that between 2006 and 2008, chlorophyll maxima occurred in December of each year. However, the winter peaks are shifted forwards to January in 2008/2009, whereas in 2009/2010 a winter bloom occurred at the beginning of the NEM in November. The monthly climatology of chlorophyll also suggests a smaller, secondary summer bloom for both regions, and the timing of the bloom varies from year to year and between regions. For both regions, the summer bloom usually extended from July and September with a short disruption in chlorophyll concentration between July and September. The highest overall summer chlorophyll concentration in the SCS was found in 2006 while the lowest overall concentrations were found in 2009 and 2010. In the GoT, the highest and lowest overall values were observed in 2010 and 2009, respectively.

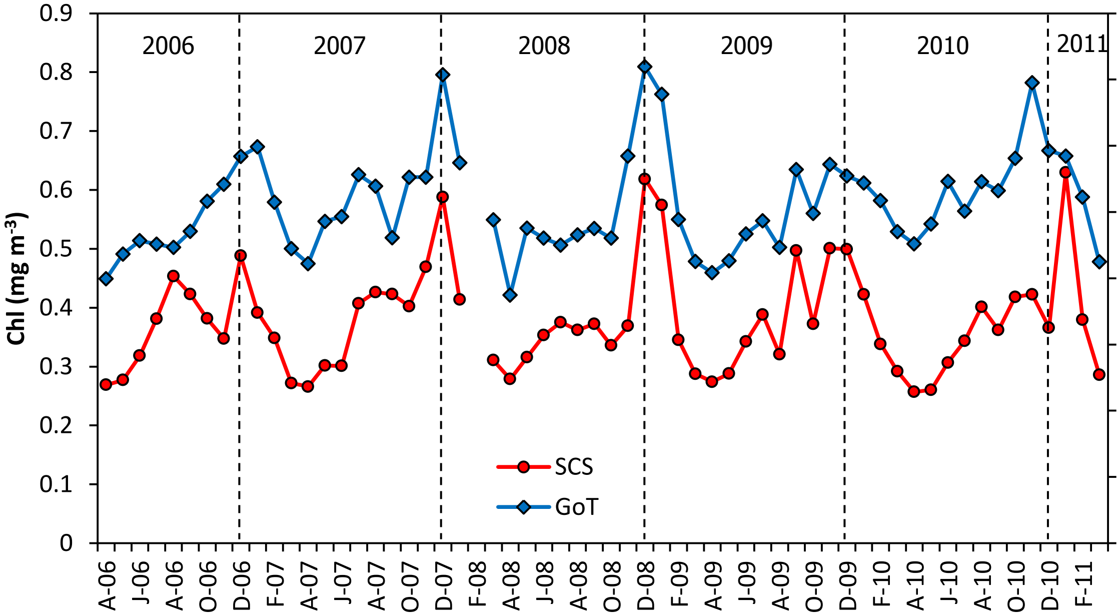

Figure 5.6: Time series of monthly average chlorophyll concentrations in the SCS (red lines) and GoT (blue lines) from April 2006 to March 2011.

The SCS region presents two peaks of CDOM maxima, one during the NEM (December or January) and another smaller one during the SWM (July or August) season (Figure 5.7). A time-series of the mean monthly CDOM in this region also shows a marked reduction in surface concentration during 2009-2010. The cause for the decrease in surface CDOM concentration is re-visited in the Discussion. Annual CDOM cycles with one dominant December-February peak are evident in the GoT water. Similar to the SCS, the inter-annual variability showed a decreased in concentration for the period of 2009-2010.

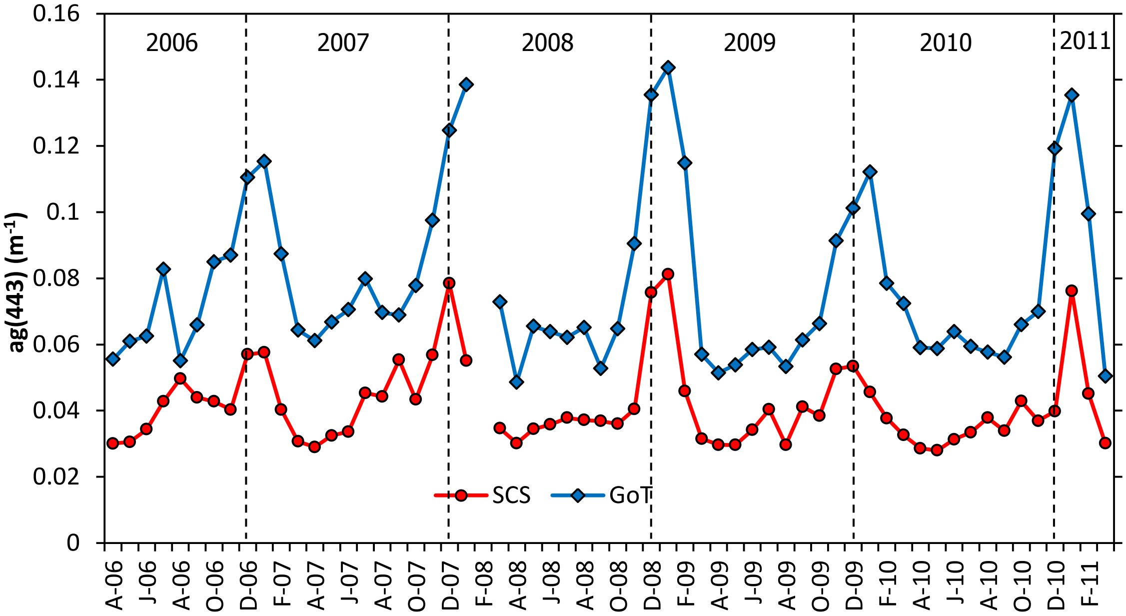

Figure 5.7: Time series of monthly average CDOM concentrations in the SCS (red lines) and GoT (blue lines) from April 2006 to March 2011.

5.4.1 Seasonal chlorophyll and CDOM anomalies

The seasonal MODIS chlorophyll and CDOM anomaly images (Figure 5.8), derived by subtracting the climatological mean (average of 2006-2011) provide additional insight into the temporal variability and their spatial location within the SCS and GoT. As expected, most of the strongest anomalies (positive or negative) were particularly pronounced along the Vietnamese coast and the lower GoT. The overall seasonal pattern of CDOM anomalies along the coastal regions followed that of chlorophyll, especially during the period of low concentrations in spring and fall. During high concentrations of CDOM in the SWM and NEM seasons, it appears there are some distinctive patterns of anomalies especially in offshore regions.

In 2006 strongest positive anomalies occurred during the fall inter-monsoon in the Mekong delta while negative anomalies were prevalent during the spring and NEM season along most of the coast. Small patches of high chlorophyll and CDOM concentrations relative to the overall seasonal average for 2006-2011 were also observed during the SWM and NEM seasons along the upwelling areas off the Vietnamese coast. A large patch of positive CDOM anomaly was observed in the lower GoT during the SWM 2006. This localized high concentration of CDOM patch however, did not show similar spatially coherent pattern with chlorophyll, probably caused by sediment resuspension from the strong mixing event during the SWM. In 2007, chlorophyll and CDOM anomalies increased in magnitude and spatial extent along most of the coast. Stronger anomalies were observed inshore and offshore during the fall and NEM seasons although there were several scattered patches of negative anomalies in the southernmost tip off the Mekong delta. The offshore anomalies during these times would suggest they are extension of the nutrient rich and turbid inputs from the Mekong and lower GoT river plumes. During SWM and fall of 2008, negative anomalies were found over most of the coast in the study area, while fewer anomalies occurred during the spring and NEM along the southern Vietnamese and northern Malaysian coasts. During the NEM, CDOM anomalies along the southern Vietnamese coast are much higher in magnitude and spatial extent, indicating there is a large regional rise of CDOM than the chlorophyll. The increase of CDOM during this season is most likely contributed by the high terrestrial inputs from the Mekong river as the coastal upwelling are no longer present.

A period of strong negative anomalies is evident during fall inter-monsoon in 2009. Chlorophyll concentrations along the coast during this time decreased by almost 0.5 mg m^{-3} compared to the overall seasonal average for 2006-2011. However, an extensive positive event took place as the season progressed from spring to fall. The most obvious feature can be seen during the fall inter-monsoon off Vietnamese coast, with chlorophyll and CDOM anomalies as high as +1.50 mg m^{-3} and 0.15 m^{-1}, respectively. Fall inter-monsoon was also a period of upwelling favorable winds along the Vietnamese coast which resulted in the northeastward offshore current flow and this may explain the positive anomalies observed offshore (Tang et al., 2006). The chlorophyll anomaly becomes weaker and even slightly negative offshore during the NEM season. While much of the areas show significant negative anomalies, there were increased anomalies along the east coast of Peninsular Malaysia during this season. Lastly, 2010-2011 appears to be characterized by strong positive anomalies inshore and offshore during the fall inter-monsoon. During the NEM season however, the anomaly signals show a contrast result between chlorophyll and CDOM over most of the study area. As can be seen in Figure 5.9, positive chlorophyll anomalies are dominant along the coast while surface CDOM shows significant negative anomalies over most parts of the study area. Especially at the Mekong river, the magnitude of CDOM anomaly decreased down to -1.0 m^{-1}.

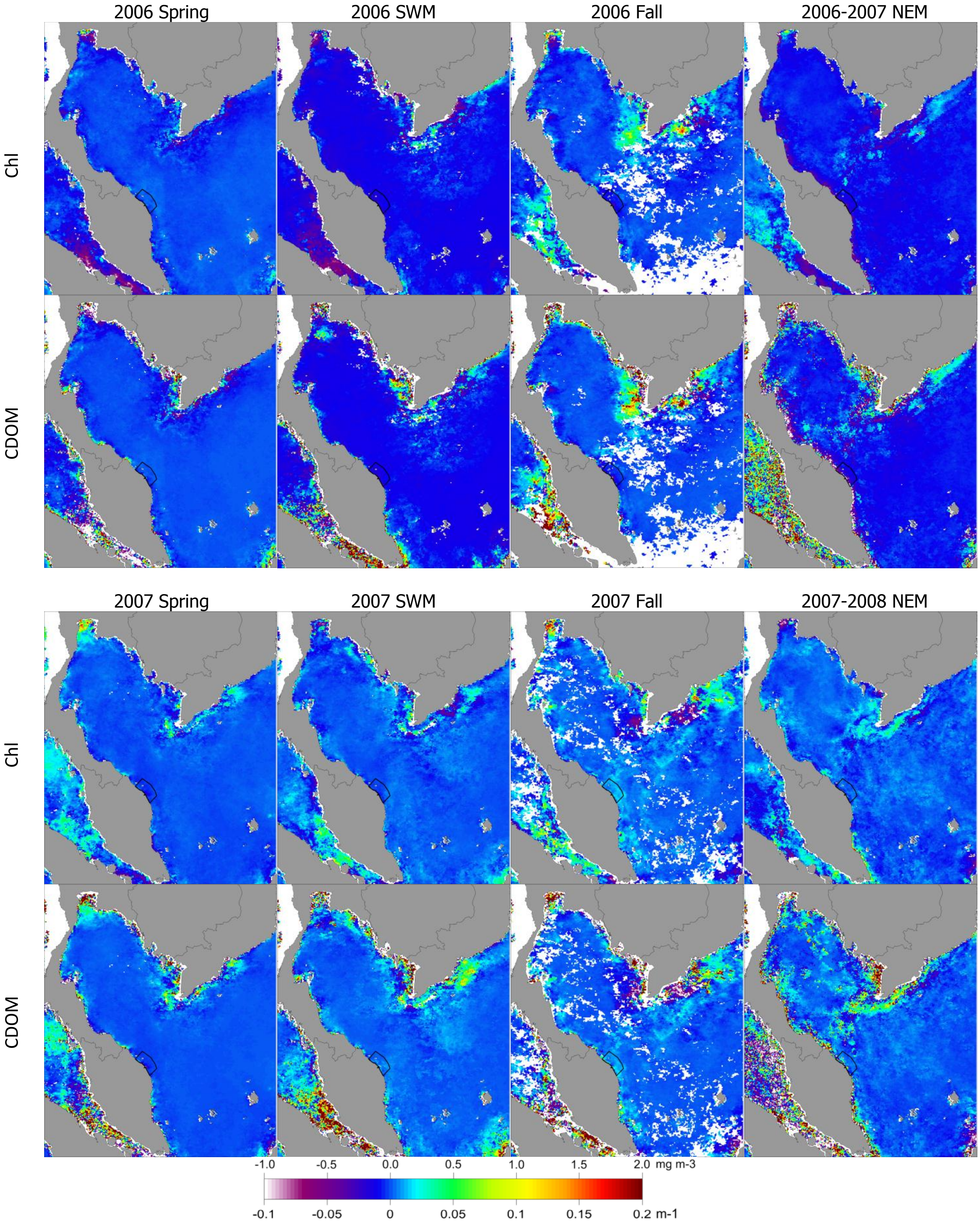
2006 Spring
2006 SWM
2006 Fall
2006-2007 NEM
Chl
CDOM
2007 Spring
2007 SWM
2007 Fall
2007-2008 NEM
Chl
CDOM
-1.0
-0.5
0.0
0.5
1.0
1.5
2.0 mg m-3
-0.1
-0.05
0
0.05
0.1
0.15
0.2 m-1

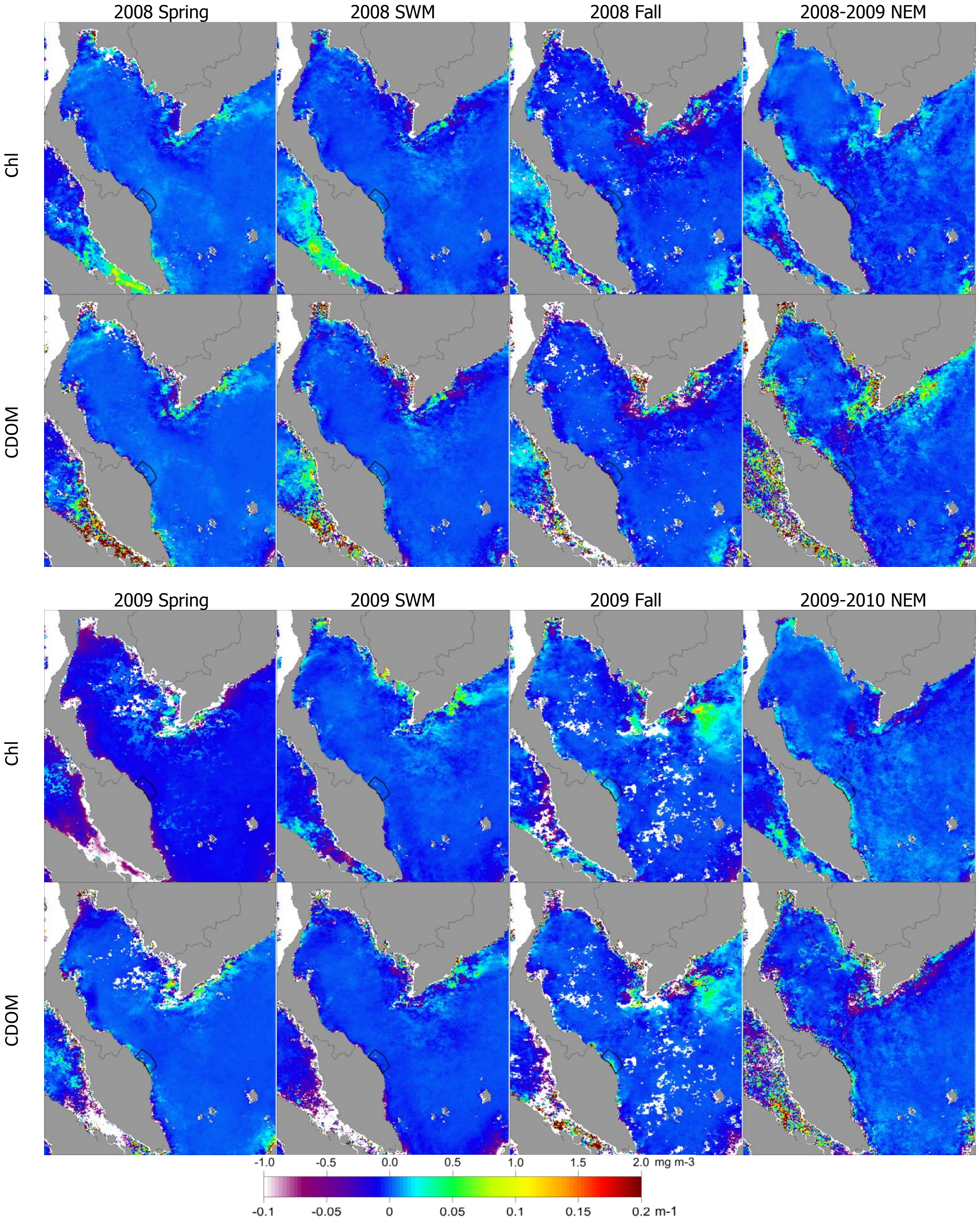
2008 Spring
2008 SWM
2008 Fall
2008-2009 NEM
Chl
CDOM
2009 Spring
2009 SWM
2009 Fall
2009-2010 NEM
Chl
CDOM
-1.0
-0.5
0.0
0.5
1.0
1.5
2.0 mg m-3
-0.1
-0.05
0
0.05
0.1
0.15
0.2 m-1

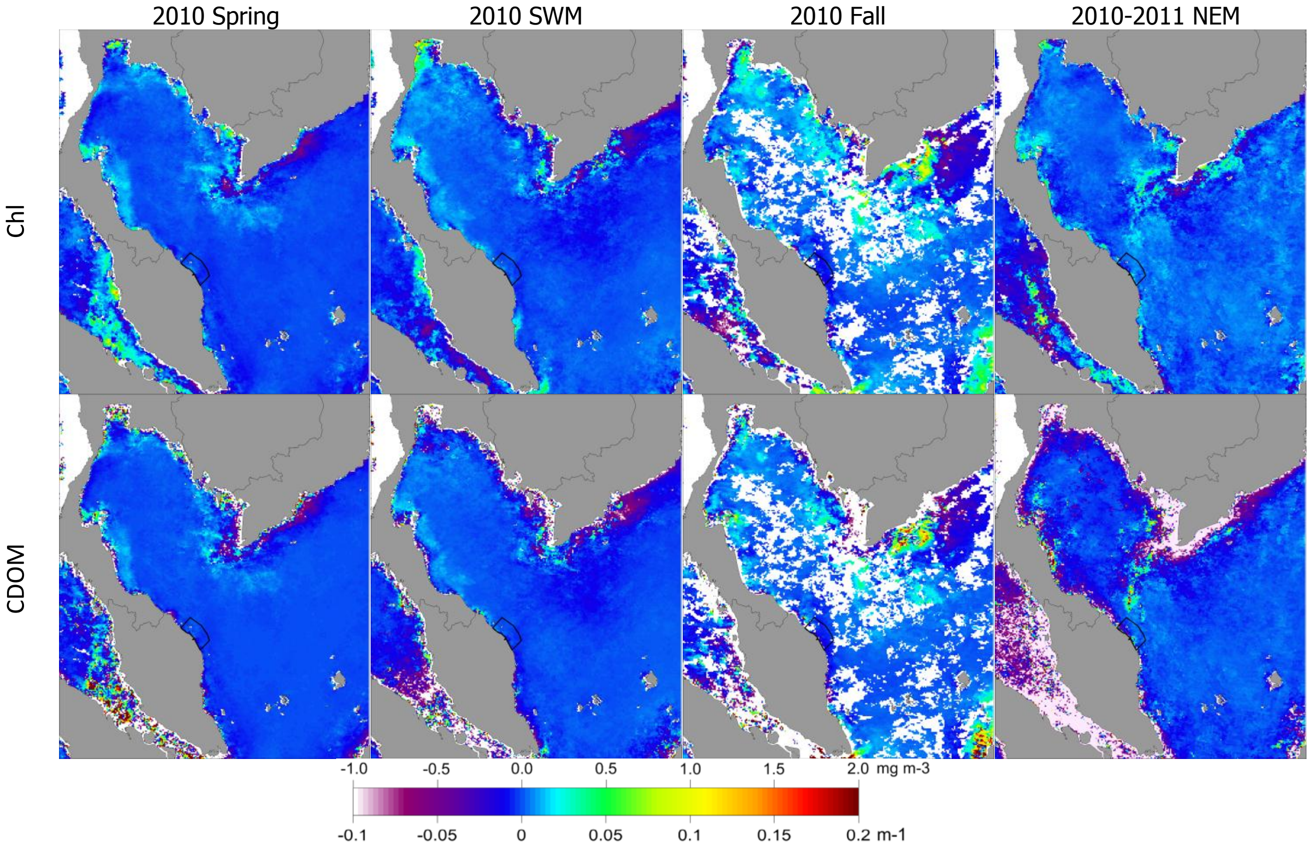

Figure 5.8: 2006-2011 MODIS chlorophyll (mg m^{-3}) and CDOM (m^{-1}) anomaly images.

5.5 Winds and sea surface temperature

Monthly average of wind vector (speed and direction) and SST for different monsoon seasons are shown in Figure 5.9. Wind speed and directions show a clear seasonal reversal in this region with the southwesterly winds in summer and northeasterly winds in winter. During the inter-monsoon months (April and October), the wind speed was generally weak (~5 m/s) with variability in direction in some areas. In a region of weak winds, large sea surface heating results in relative uniform SSTs (30-32 ^{o}C) for this season. For areas characterized by higher winds speed regimes (e.g. Gulf of Thailand and Vietnamese coast in October), monthly SSTs tend to be slightly lower (~29 ^{o}C). In June (SWM), the strong southwesterly winds (~8 m/s) appear in the Gulf of Thailand and along the Vietnamese coast, while other areas reside in relatively weak winds. Off the east coast of Peninsular Malaysia however, wind speed remained low throughout the season (June to September) due to the blocking effect of the mainland. Water stratification is well developed during this season, which results in relative uniform surface temperatures over the entire region. During this season, along shore winds were observed at coastal water of the east coast of Peninsular Malaysia as well as off the Vietnamese coast, providing the most favourable conditions for upwelling. Because the wind speed and current flow are much weaker in the east coast of Peninsular Malaysia (Camerlengo and Demmler, 1997), the occurrence of coastal upwelling is more obvious along the Vietnamese coast. The sea surface cooling off the Vietnamese coast can be seen on the SST image of June 2009 (blue colour) when the surface temperature is about 26 ^{o}C. The occurrence of upwelling events in this area has been widely documented in the literature (e.g. Wyrtki, 1961; Kuo et al., 2000; Ho et al., 2000; Dippner et al., 2007). Although it is not so obvious from the SST image in Figure 5.9, a slight decrease in SST (to about 28.5 ^{o}C) was also observed in the east coast of Peninsular Malaysia, coinciding roughly with the wind direction along the coast. However, the presence of a wind-driven upwelling has not been reported before in this area.

The dominant direction of southwesterly winds changes to northeast direction in November and winds increase in speed to a peak of > 10 m/s in December. This strong northeasterly winds blow directly towards the east coast of Peninsular Malaysia, bringing heavy rainfall and often causing floods in the region. The most prominent feature in SST variation during this season is the intrusion of a large body of relatively cold water (24-26 ^{o}C) from the Pacific Ocean into the SCS and this is clearly displayed in Figure 5.9. During this season, the surface temperature decreases to its lowest value around 27 ^{o}C and this is distributed evenly over the whole region.

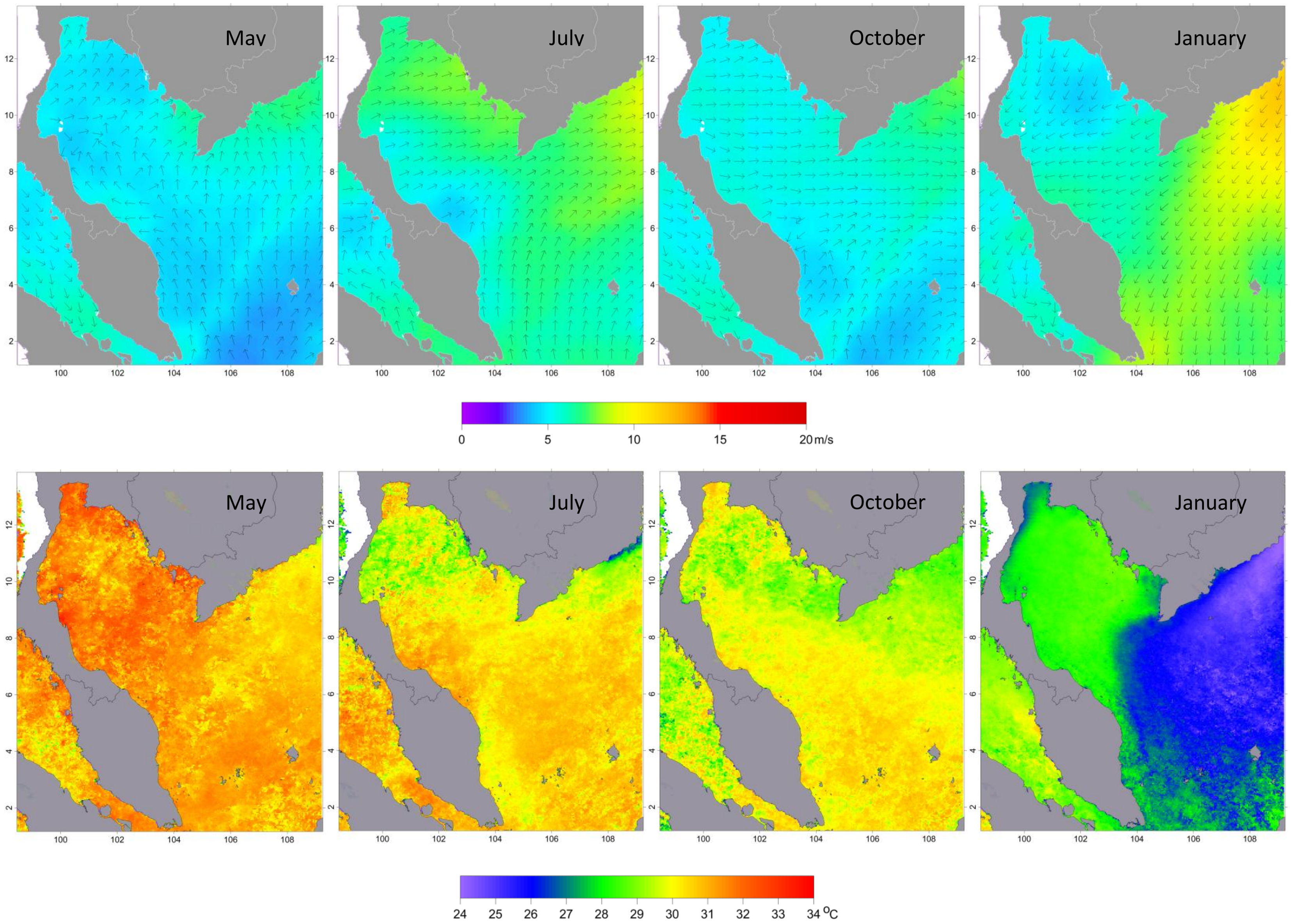

Figure 5.9: Monthly average d wind images derived from QuikScat and WindSat (upper panel) along with monthly averaged MODIS Aqua SST (lower panel) for 2006 to 2010

Because of the strong NEM and sea surface cooling, vertical mixing is well-developed and plays an important role for the winter phytoplankton blooms by bringing nutrients up to the surface.

5.5.1 Seasonal periodicity and inter-annual variations of SST and wind speed

In order to discern inter-annual variations of SST and wind speed, we analysed the variables as time series. The correlation analysis between chlorophyll and CDOM and SST and wind speed were also performed to examine their relationships. Although this simple linear correlation does not provide a complete description of the variability, general trends can certainly be revealed. Figure 5.10 represents the temporal series of SST and wind speed superimposed on the spatially averaged monthly chlorophyll and CDOM for the whole study area from 2006 until 2011. As terrestrial processes especially from river discharge have dominant control on the variation of surface chlorophyll and CDOM in coastal regions, we limit our analyses to the offshore region (~ 50 km from the coastlines).

Consistent negative correlations were found between chlorophyll-SST and CDOM-SST, while positive correlations were found between chlorophyll-wind speed and CDOM-wind speed. Although these correlations were in general not particularly strong, the positive and negative relationships between these two variables are consistent with the idea that phytoplankton growth and biomass are limited by the upward flux of nutrients. Stronger winds may cause increased evaporation, increased nutrient flux (through vertical mixing) and increased spreading of cold coastal waters, resulting in colder SST. This fact is supported by the negative correlation between SST and wind speed in Figure 5.10, which suggests that high wind speeds are related to low SST in the study region. Superimposed on the seasonal pattern of wind speed, SST maxima show an apparent time lag in the order of one month. Time series of SST-chlorophyll and SST-CDOM provide clear evidence of the SST influence on the variations of chlorophyll and

CDOM in the study area. Peaks of chlorophyll and CDOM coincided well with low SST and vice versa, suggesting that SST is one of the major driving mechanisms for enhanced chlorophyll concentration in this region. The trends retrieved for the wind speed show two distinctive peaks, one during the SWM and another peak during the NEM season. The trend observed for the chlorophyll-wind speed and CDOM-wind speed are slightly more complex, with different trends between winter and summer periods. During winter, there is a strong coherence between the patterns of wind speed and both chlorophyll and CDOM, with high concentrations correspond with strong wind speeds. This can be attributed to the nutrient-rich condition due to enhanced ocean mixing that brings cold nutrient-laden waters to the surface. Chlorophyll and CDOM concentrations however, did not significantly increase during the peak of wind speed in summer (SWM season). The reason for that can be the high SST which led to an increase in the vertical stratification of the surface layer, limiting the subsurface high nutrient water to the surface.

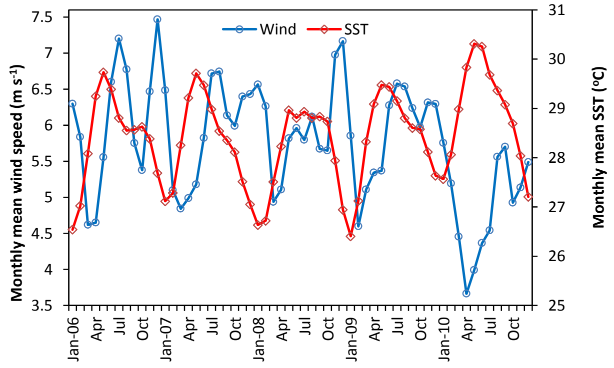
Wind
SST
Monthly mean wind speed (m s-1)
Monthly mean SST (ºC)
7.5
7
6.5
6
5.5
5
4.5
4
3.5
31
30
29
28
27
26
25
Jan-06
Apr
Jul
Oct
Jan-07
Apr
Jul
Oct
Jan-08
Apr
Jul
Oct
Jan-09
Apr
Jul
Oct
Jan-10
Apr
Jul
Oct

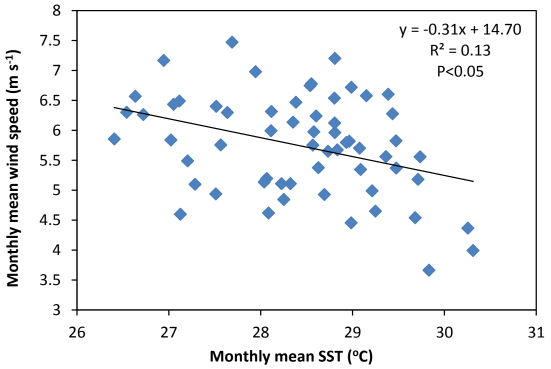
y = -0.31x + 14.70
R² = 0.13
P<0.05
Monthly mean wind speed (m s-1)
Monthly mean SST (ºC)
8
7.5
7
6.5
6
5.5
5
4.5
4
3.5
3
26
27
28
29
30
31

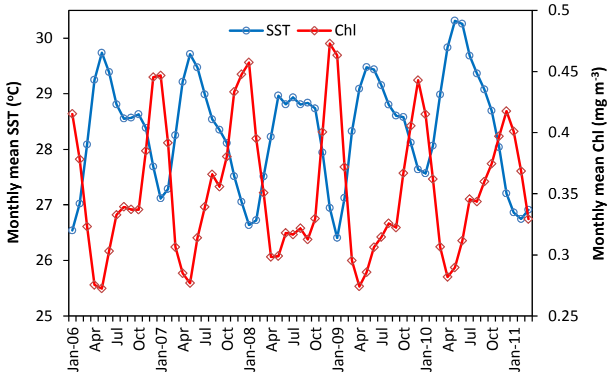
SST
Chl
Monthly mean SST (ºC)
Monthly mean Chl (mg m-3)
30
29
28
27
26
25
0.5
0.45
0.4
0.35
0.3
0.25
Jan-06
Apr
Jul
Oct
Jan-07
Apr
Jul
Oct
Jan-08
Apr
Jul
Oct
Jan-09
Apr
Jul
Oct
Jan-10
Apr
Jul
Oct
Jan-11

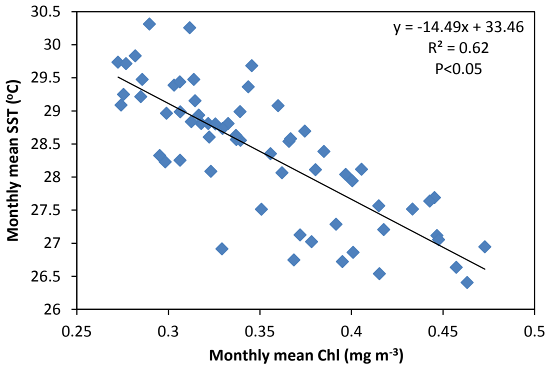
y = -14.49x + 33.46
R² = 0.62
P<0.05
Monthly mean SST (ºC)
Monthly mean Chl (mg m-3)
30.5
30
29.5
29
28.5
28
27.5
27
26.5
26
0.25
0.3
0.35
0.4
0.45
0.5

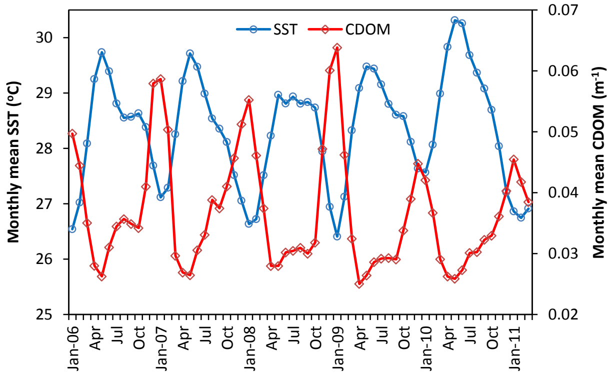
SST
CDOM
Monthly mean SST (ºC)
Monthly mean CDOM (m-1)
30
29
28
27
26
25
0.07
0.06
0.05
0.04
0.03
0.02
Jan-06
Apr
Jul
Oct
Jan-07
Apr
Jul
Oct
Jan-08
Apr
Jul
Oct
Jan-09
Apr
Jul
Oct
Jan-10
Apr
Jul
Oct
Jan-11

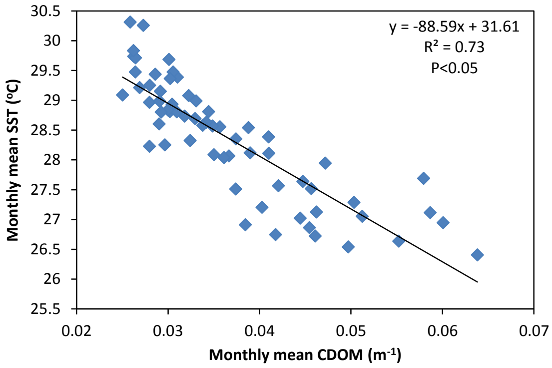
y = -88.59x + 31.61
R² = 0.73
P<0.05
Monthly mean SST (ºC)
Monthly mean CDOM (m-1)
30.5
30
29.5
29
28.5
28
27.5
27
26.5
26
25.5
0.02
0.03
0.04
0.05
0.06
0.07

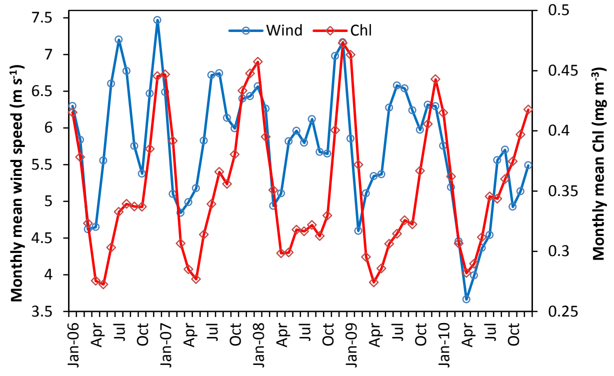
Wind
Chl
Monthly mean wind speed (m s-1)
Monthly mean Chl (mg m-3)
7.5
7
6.5
6
5.5
5
4.5
4
3.5
0.5
0.45
0.4
0.35
0.3
0.25
Jan-06
Apr
Jul
Oct
Jan-07
Apr
Jul
Oct
Jan-08
Apr
Jul
Oct
Jan-09
Apr
Jul
Oct
Jan-10
Apr
Jul
Oct

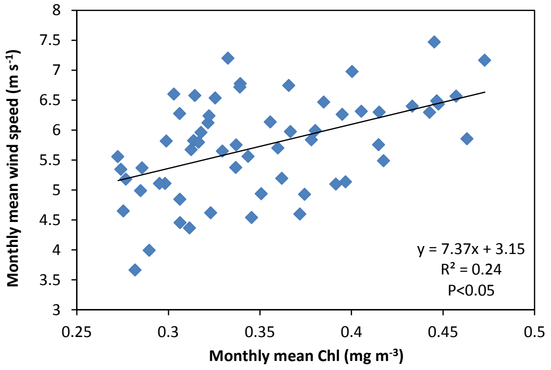
y = 7.37x + 3.15
R² = 0.24
P<0.05
Monthly mean wind speed (m s-1)
Monthly mean Chl (mg m-3)
8
7.5
7
6.5
6
5.5
5
4.5
4
3.5
3
0.25
0.3
0.35
0.4
0.45
0.5

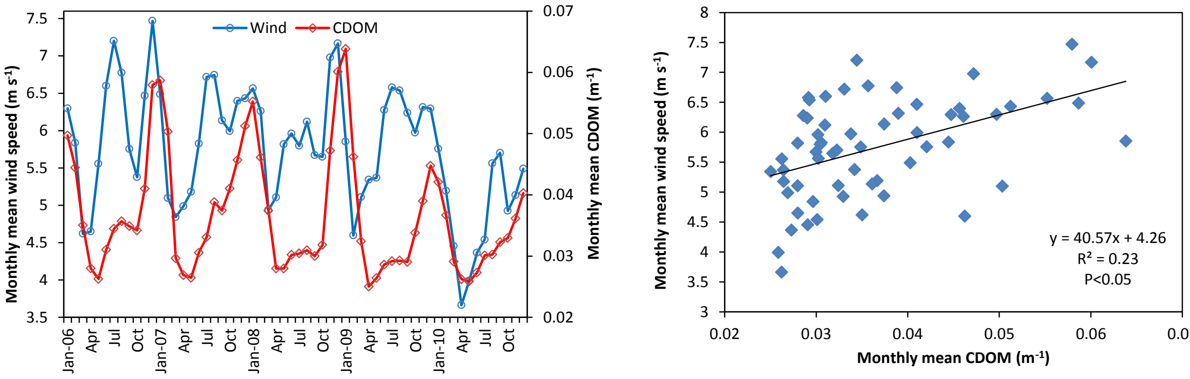

Figure 5.10: Monthly mean time series of SST and wind speed superimposed on the chlorophyll and CDOM (left panels) along with scatter plots between each variable (right panels)

5.6 Discussion and conclusion

In the present study we investigate the seasonal and inter-annual variations of surface chlorophyll and CDOM in the GoT and SCS and analyzed its relationship with SST and wind speed. Analysis of MODIS data reveals a strong seasonality of chlorophyll concentration in the study area. The seasonal and inter-annual analysis of 5 years of MODIS data clearly reveals a seasonal signal with the GoT region presenting higher fluctuations along the year while the nearby SCS, on the contrary, is characterized by low primary production. Region-wide phytoplankton blooms typically occurred during the NEM season (November – January). During other seasons there appeared to be well-defined spatial patterns in the phytoplankton biomass, which suggest that there are distinctive bio-geographical provinces within the South China Sea water. For example, chlorophyll concentrations along the east coast of Peninsular Malaysia are typically low during the summer (SWM and inter monsoon seasons) with chlorophyll values rarely exceeded 0.5 mg m^{-3}. In comparison, the GoT and Vietnamese shore regions had numerous blooms, resulting in high chlorophyll concentrations (> 1 mg m^{-3}) throughout the summer season. Summer production was greatest in these regions where the seasonality of chlorophyll concentration was virtually absent. The bio-geographical differences between those regions can be explained by the lack of major freshwater discharge along the east coast of Peninsular Malaysia. Added to this factor, the Peninsular Malaysia is generally influenced by low southwesterly wind forcing due to a northeastward deflection by the land. The patterns in chlorophyll distribution observed in this study are qualitatively consistent with previous investigations of the SCS and GoT using satellite data (Tang et al., 2003; 2006). However, no investigations have been made on the seasonality in CDOM concentration in the study area before. The present study is the first to document the seasonal and inter-annual variations of CDOM and the extent to which they influence the water colour distribution in this region.

Similar to chlorophyll concentration, the analysis of MODIS data reveals the strong seasonality of CDOM concentrations in the study area, with high concentrations were observed during the strong NEM season and low during the other seasons. Obviously, the distribution of CDOM bears a strong resemblance to the pattern displayed by the corresponding distribution of chlorophyll concentration. Indeed, the offshore extension and structure of both parameters are closely related. Time series of concentration anomalies provide some further evidence of a spatially and seasonally coherent of both water quality parameters occur in this region. The similarity between the patterns of chlorophyll and CDOM distribution indicates a strong association between the phytoplankton biomass and the CDOM production. This would also suggest that the spatial variation of chlorophyll and CDOM in the study area is largely influenced by river discharge. This is also consistent with the results of in-situ data where both parameters showed a strong correlation between each other.

The results show that patterns of chlorophyll and CDOM distribution in the study area are primarily controlled by monsoonal winds and the impact from terrestrial hydrological processes. Changes in circulation and oceanic process associated with this shelf water vary on a synoptic (monthly) and seasonal scale (Liu et al., 2002). This seasonal wind modifies climate, and influences water current speed and direction of water above the pycnocline (~40 m depth) and the surface currents in the nearby South China Sea (Stansfield and Garrett, 1997; Snidvongs and Sojisuporn, 1999). In winter (NEM season), sea surface cooling and intense vertical mixing may play an important role for the high chlorophyll and CDOM concentrations in offshore waters. In the coastal area however, the influx of terrestrial nutrients through river discharge and coastal processes are dominant mechanisms of phytoplankton and CDOM productions. In summer, those processes are reverse. Owing to intense solar radiation and weak winds, shallow mixed layer depth limits the vertical transport and entrainment of nutrients into the surface ocean, resulting in low chlorophyll and CDOM concentrations in most parts of the study area. However this is not a case in the summer upwelling region, Southeast of Vietnam where vertical mixing and stratification are not so important compared with Ekman pumping. In this region, upwelling and associated advection play important roles in the distribution of chlorophyll and CDOM throughout the whole summer. The influence of seasonal solar radiation and the wind forcing on chlorophyll and CDOM concentrations especially in offshore waters is evident by a significant negative correlation with SST and positive correlation with wind speed. However, although SST showed higher correlation than the wind, it is not the direct factor controlling chlorophyll and CDOM distributions. In tropic monsoon regions, wind (in form of wind stress rather than wind speed) is the principle mechanism governing upwelling and vertical mixing into the upper ocean (Mudgal et al., 2009; Pradhan et al., 2006) by which nutrients are entrained into surface layers.

Another important result is the existence of inter-annual fluctuations in both chlorophyll and CDOM during the study period. Both parameters presented a significant decreasing trend (negative anomaly) in 2006 and 2009, and an increasing trend (positive anomaly) in 2007, 2008 and 2010. This inter-annual variation is likely related to the El-Nino Southern Oscillation

(ENSO) events of El-Nino (warm phase) and La Nina (cold phase) (http://www.cpc.ncep.noaa.gov). The Nino 3.4 index is calculated from the monthly or seasonal fluctuation in the SST anomaly over the Pacific Ocean (5 °S - 5 °N; 170 °W - 120 °W). Figure 5.11 demonstrates that these cold and warm phase events have strong impacts on surface chlorophyll and CDOM in this region. The curve of monthly mean chlorophyll and CDOM correlate well with the Nino 3.4 Index in 2006, 2007, 2009 and 2010. Surface chlorophyll and CDOM in 2006 and 2009 correspond strongly with a strong Nino 3.4 index. On the opposite side, negative Nino 3.4 indices (cold phases) in 2007-2008 and 2010 correspond with high chlorophyll and CDOM concentrations. The effect of El-Nino event on the inter-annual variation of CDOM in the SCS has been reported by Ma et al., (2011). They found the abnormal low surface CDOM during summer and winter of 1997/1998 El-Nino year are caused by weaker upwelling due to anomalously weak winds.

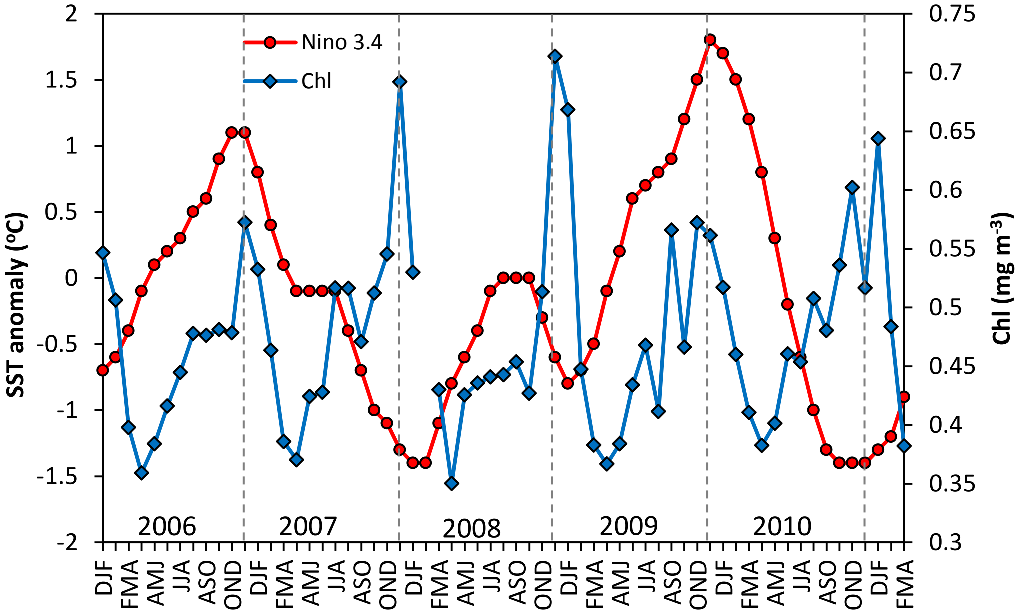

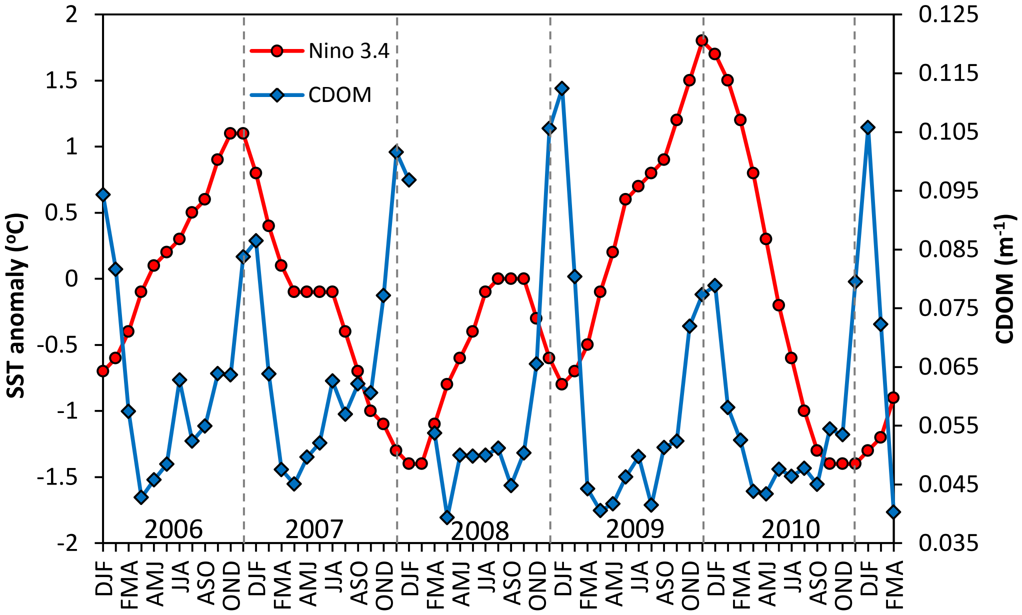

Figure 5.11: Monthly mean chlorophyll (upper panel) and CDOM (lower panel) with Nino 3.4 indices.

The analysis of the seasonal and inter-annual variability has largely been restricted by the presence of clouds in MODIS image. Monthly estimates of surface chlorophyll and CDOM with a spatial resolution of 4 km were used as a compromise but they provide only rough information in highly dynamic regions like the SCS. Even with monthly resolution, the spatial coverage was largely incomplete and this precluded detail analysis of spatial and temporal dynamic of ocean colour in this region. For the future studies, the used of combined ocean colour data (e.g. MODIS, SeaWifs, OCM) should be envisaged as it would improve the coverage and provide more information on ocean ecosystem. Due to the absence of a complete validation data, the values of chlorophyll and CDOM outside the sampling area cannot be ascertained and therefore must be considered with caution. Nevertheless, this work gives improved insight on the interpretation of ocean colour data not seen before.

CHAPTER 6

DISCUSSION AND CONCLUSIONS

6.1 Introduction

This study was motivated by the absence of information about the bio-optical properties of Malaysian waters, despite the fact that these parameters are the key factors influencing the accuracy of derived water constituents from remote sensing ocean colour data. The primary questions arising then are; how do bio-optical properties vary seasonally and is there any influence of seasonal changes on ocean colour estimation from remote sensing algorithms? To address the above issues, two research strategies were carried-out in east coast of Peninsular Malaysia waters from May to November 2009. The first study focused on the characterization of bio-optical constituents and their effects on optical properties during different seasons and on quantifying the contribution of each water constituent to the total absorption. It is important to determine the influence of seasonal and regional variations on optical properties and to identify the spectral domain where each constituent is dominant. The second study investigated the suitability of the MODIS global algorithms for quantitative and qualitative retrieval of chlorophyll and CDOM in the study area, and examined alternatives algorithms that are best-suited to the local optical conditions.

The proposed algorithms were then applied to the MODIS monthly composite images from a 5-year MODIS dataset to estimate chlorophyll and CDOM concentrations in the study region. Seasonal and spatial variations of surface ocean colours were studied in detail in order to identify possible long term changes in phytoplankton biomass and water colour concentrations.

6.2 Seasonal variability of optical properties

The analysis of in-situ water constituents and optical properties described in chapter 3 clearly reveals a seasonal signal, with the winter (NEM) season presenting higher values of both concentration and absorption, as well as wider spatial extent with elevated concentrations levels. The summer (SWM and inter-monsoon seasons) on the contrary is characterized by low levels of constituent concentrations and absorption coefficients. The timing, magnitude and spatial extent of these bio-optical properties in the study area were highly responsive to hydrographic conditions (wind forcing, temperature and freshwater input). The winter phytoplankton bloom is triggered by deep winter mixing and strong river discharge that provide the euphotic zone with an abundant supply of nutrients. This was evident by the increasing concentrations of all constituents and significant inverse relationship between CDOM and salinity during the NEM season. On the other hand, the oligotrophic nature of surface waters during summer is associated with a strong thermal stratification and lack of a significant freshwater input. Although it is generally perceived that strong summer stratification and a shallow mixed layer do not allow for nutrient enrichment of surface water to occur, the mechanism of phytoplankton blooms in offshore water during spring and fall inter-monsoon is not clear. It is during these seasons that a pigment package effect was observed. Contrary to the general trend found in other seasons that, a_{ph} at a specific wavelength (e.g. 443 and 676 nm) is well correlated with chlorophyll concentration, in the inter-monsoon season this is not so. The package effect (Kirk, 1994) describes the decreased absorption of pigments in cells compared to the absorption potential of the same amount of pigment in solution (Duysens, 1956; Kirk, 1976, 1994; Morel and Bricaud, 1981). It is well known that packaging of pigments is strongly related to cell size and the intra-cellular concentration of pigments (Bricaud and Morel, 1986; Sathyendranath et al., 1987) since light absorption by phytoplankton is scaled to their cross-sectional area and/or self-shaded of the highly packaged cells decrease the light absorption efficiency per unit chlorophyll. Based on previous studies (e.g. Sathyendranath et al., 1999; Nelson et al., 1993; Tham, 1973; Chua, 1970) in nearby regions and elsewhere, it is biologically plausible that this interesting result is largely due to the presence in the inter-monsoon of large chlorophyll-rich diatoms. The lower package effect during the monsoon season is expected to be dominated by smaller phytoplankton species. Packaging of pigments during the inter-monsoon season could have significant implications for interpretation of ocean colour imagery for the region. This effect has been shown to influence upwelling radiance (Carder et al., 1991) and diffuse attenuation coefficients (Mitchel and Holme-Hansen, 1991) thus, affecting the relationship between ocean colour signal and chlorophyll concentration. We have also shown that the characteristics of phytoplankton absorption per unit chlorophyll during the monsoon season depart from the global trend reported by Bricaud et al., (2004). This indicates that variations in phytoplankton spectral absorption coefficients can occur not only from the same geographic area but also from seasonally within the same area.

Another important result of this study is the dominant influence of non-pigmented material on light absorption in the blue spectral region (>70% of the total absorption budget). In this spectral region, the relative contribution of phytoplankton absorption to the total nonwater absorption is less than 30%. The high contribution of substances other than phytoplankton to the total absorption of blue light in the study area makes it difficult for a global algorithm to perform well. The findings of this study also indicate that CDOM and detritus absorption coefficients covaried strongly with chlorophyll concentration during the monsoon periods (NEM and SWM). However, they did not exhibit the same pattern during the inter-monsoon season. At least for the monsoon period, the coherence between non-pigmented substances and chlorophyll concentration has provided a great advantage to using the blue band (443 nm) to estimate chlorophyll concentration from ocean colour data, although both components could take competing roles in the retrieval process.

6.3 Bio-optical model for east coast Malaysia water.

In chapter 4, we showed that there is a strong variability of the standard MODIS algorithm performance between different monsoon seasons. MODIS-derived chlorophyll appeared to be susceptible to systematic errors both at lower (<0.6 mg m^{-3}) and higher (>1.0 mg m^{-3}) chlorophyll values during the monsoon season. The bias of MODIS chlorophyll products however, varied unsystematically during the inter-monsoon season. This indicates that the global MODIS algorithm works less successfully over a wide range of bio-optical and environmental conditions such as those in our area. The failure of the MODIS algorithm during the monsoon season is most likely due to a phytoplankton community with optical properties different from the average community on which OC4v6 is based, similarly to what have been reported in many studies (e.g. Volpe et al., 2007; Stramska et al., 2006; Sathyendranath et al., 2001). As has been noted, the phytoplankton absorption coefficient in the study area showed a different slope when plotted against chlorophyll than that reported by Bricaud et al., (2004), implying that the performance of this algorithm changes according to regional in-situ conditions. In the inter-monsoon period, both strong non-covarying CDOM and a pigment package effect are likely the cause of MODIS algorithm failure. Under these circumstances, the observed reflectance spectra (either shape or magnitude) may not be well represented by the reflectance model, indicating an inadequate solution of bio-optical models in retrieving chlorophyll concentration during this season.

The empirical findings indicate there were 2 different scenarios in the chlorophyll retrieval errors; 1) a systematic error during the monsoon period and 2) non-systematic (unpredictable) error during the inter-monsoon season. In the former scenario, a fine-tuning of existing algorithms with regional parameters could be a key point to further improve the accuracy of remotely–derived chlorophyll concentration. In the latter, utilization of the red part of the spectrum using inversion or a semi-analytical model can be used to estimate the chlorophyll concentration by taking advantage of the fact that phytoplankton has a distinct signature at 676 nm. In addition, the red absorption peak is less affected by pigment packaging (by virtue of its smaller magnitude than the blue). Satlantic HyperOCR and water samples were used to provide a regional update of bio-optical parameters to establish a relationship between water constituents and optical properties.

The application of a regionally tuned algorithm for the monsoon season demonstrates the significantly improved performance with retrieval error (MAPD) less than 17%, within the accuracy requirements for the ocean colour research. Furthermore, it could also be shown that the algorithm performs well either in very optically thick water during NEM or clear water in SWM season. These findings suggest that the adapted regional algorithm during this season is applicable to a wide range of conditions and shows robustness in the face of strong monsoon influences. The use of band ratio $R_{rs}(488/547)$ to retrieve chlorophyll concentration in the proposed algorithm can also minimise the interference from the CDOM absorption that absorbs light strongly in the blue part of the spectrum. However, it is important to underline that the algorithm proposed in this study has to be considered very preliminary because the in-situ chlorophyll dataset used to validate the algorithm is not independent from the one used to generate it. Furthermore, due to limited spatial coverage of the study area and the range in chlorophyll concentration (<10 mg m^{-3}), it is not even certain that a proposed chlorophyll algorithm will be applicable for the whole waters of Peninsular Malaysia. A larger dataset of bio-optical in-situ measurement is obviously necessary.

Further indicators of the potential applicability of the empirical algorithm in the study area are shown by a great algorithm performance in estimating the absorption coefficients. The important finding is that CDOM and phytoplankton absorptions can be well retrieved using different combinations of blue-green band ratios. In this study, band ratios $R_{rs}(412/547)$ and $R_{rs}(488/547)$ are proposed to estimate $a_g(412)$ and $a_{ph}(443$ and $676)$, respectively. Considering the strong influence of CDOM on the reflectance signal, the findings could be used to distinguish the optical signatures of chlorophyll from CDOM, allowing the accurate estimation of both constituents from the satellite data. These results are very promising taking into account that only a few band ratio algorithms specially designed to estimate CDOM absorption coefficient have been published until now (e.g. Kahru and Mitchell, 2001; D`Sa and Miller, 2003; Kowalczuk et al., 2005, 2010; Mannino et al., 2008). In contrast to our finding, most of the published band ratio algorithms for the retrieval of CDOM coefficient use reflectance values at the phytoplankton peak wavelength of 443 nm or longer. The use of different reflectance values in our band ratio algorithms for CDOM and phytoplankton absorption retrieval is obviously an advantage as both coefficients do not compete for the photons of the same wavelength. This could also improve the sensitivity of empirical algorithms for retrieving CDOM absorption and chlorophyll concentrations.

The failure of band ratio algorithms during the inter-monsoon periods, although expected, raises an interesting question about the extent of the packaging effect on the reflectance signal in the study area. Although the package effect phenomenon appears to be largely responsible for the algorithm failure, it is believe that other factors may in part contribute to the algorithm failing completely. One possible factor is the strong absorption of CDOM that would cause further reduction in the light absorption and decrease significantly the water leaving radiance in the blue bands. Future efforts will be directed towards investigating the probable cause of this phenomena and linkages between phytoplankton community structure and the package effect.

In this study, we have also shown that the use of semi-analytical algorithms does not improve significantly the accuracy of chlorophyll and other absorption components (a_{ph} and CDOM). The statistical accuracy calculated for both models returned unrealistic values of $a_{ph}(676)$ and cannot be used to derive chlorophyll concentration. This failure may be due by several factors such as uncertainties in the spectral shape of IOPs (absorption and backscattering) and uncertainties in the relationship between the reflectance and IOP. As both models depend greatly to first order on the spectral shape and magnitude of IOP and owing to the lack of backscattering data, the exact cause of the complete failure of the analytical algorithms cannot be ascertained without further studies. This emphasises the need of in-situ backscattering coefficient data to allow a better description of its optical properties in the study area thus, obtaining a more accurate estimates of chlorophyll concentration from the semi-analytical algorithm.

6.4 Inter-annual variation of chlorophyll and CDOM.

The new empirical algorithms derived from large datasets representing the optical conditions during the monsoon season were applied to the satellite data over the SCS and GoT. The seasonal and inter-annual analysis of five years of MODIS data (2006-2011), shown in chapter 5 revealed a strong seasonal cycle that responds to climatological conditions and seasonal differences in physical forcing. The spring inter-monsoon (April-May) was associated with the post bloom stages of phytoplankton and the clearest waters, driven by a decrease in terrestrial inputs and depleted nutrients. The emergence of plankton-rich waters and increased CDOM concentrations during the SWM season (July-August) could be reflected to increased river discharge that provides nutrient-rich water as well as wind-induced coastal upwelling (along the Vietnamese coast) and cross-shelf transport of chlorophyll rich water. The high levels of phytoplankton biomass and CDOM concentrations during the NEM season were attributed to particularly high increases in nutrient supply to surface layers following the intense water column mixing, large river discharge and sea surface cooling.

The significant correlation between the physical variables (wind speed and SST) and chlorophyll and CDOM demonstrates the important role of seasonal physical forcing on the biogeochemical processes in the study region. Strong wind speeds (wind stress) trigger strong upper ocean responses, producing upwelling favourable conditions, evaporative cooling and local SST minima. However, wind speed and SST were not the only factors influencing chlorophyll production in this region. Other mechanisms such as river flows, surface current and the availability of nutrients can also contribute to the chlorophyll enrichment especially in coastal water. All of these factors explain the differences in variations of water colour between east coast of Peninsular Malaysia and other areas in the study region. Compared to the Mekong and GoT waters, chlorophyll and CDOM concentrations in the east coast of Peninsular Malaysia are typically low except during the first half of the NEM season.

Based on MODIS time series analysis of 5 years, we have shown the present of inter-annual fluctuations in both chlorophyll and CDOM in the region. As shown by positive and negative anomalies, the most extreme fluctuations were particularly conspicuous along the Vietnamese and GoT coasts. The findings also suggest that there were considerable inter-annual variability for both parameters with minimal production in 2006 and 2009 and maximum production during 2007, 2008 and 2010. This long-term variability appears to be overshadowed by inter-annual climate variability associated with the El Nino-Southern Oscillation (ENSO) event. Regional impact of warm El Nino episodes is evident by a significant reduced in winter maxima during 2006/2007 and 2009/2010. Meanwhile, the profound enhance of winter maxima during 2007/2008, 2008/2009 and 2010/2011 were coincidence with the strong cold La Nina episodes. These findings suggest that the inter-annual climate variability of ENSO episodes can have a major influence on biological oceanographic conditions in the study region.

6.5 Conclusions

This work made the attempt to assess the potential use of satellite ocean colour imagery for deriving water colour parameters in east coast of Malaysian waters. The general importance of investigations in satellite sensor applications in this area lies further in the assessment of the bio-optical properties of the water column. This study provides direct and indirect evidence of the bio-optical nature of the east coast of Malaysian water and how they vary under varying environmental conditions. These highly variable of optical properties have undoubtedly limited the applicability of global algorithms to accurately quantify water constituents in the study area. Notwithstanding, regional adapted algorithms specifically for the monsoon season have been proposed and they have shown to be more robust and significantly better than the global algorithms. The limited applicability of these algorithms during non-monsoon season needs further investigation. Returning to the objectives posed at the beginning of this study, we may highlight a list of important points obtained with this research.

1. The data obtained by extensive in-situ measurements and analysis of water samples demonstrated a large variability in water constituents and its optical characteristics. The findings of this study has shown that local oceanographic conditions responding to changing monsoon conditions has significant impact on the surface optical properties and physiological properties of phytoplankton in the study area.

2. This study has revealed that both empirical and analytical algorithms failed to provide reasonable results on several occasions. These differences are likely attributed to environmental bio-optical characteristics of the study area, which ask for further investigations. The results of this study suggest that both algorithms require more regional tuning and new parameterizations based on expanded in-situ measurements of backscattering and absorption properties.
3. This study has shown that the regionally-tuned algorithm can provide more accurate chlorophyll retrievals in a wide range of water types, on the condition that the chlorophyll concentration co-varies with CDOM and the spectral shape of IOP (e.g. phytoplankton absorption) does not change with varying environmental conditions. The results of this study also show that each absorption property can also be well estimated using different combinations of the blue-green band ratios.
4. The seasonal and inter-annual variations in chlorophyll and CDOM concentrations revealed a strong seasonal cycle, related to climatically driven cycles of monsoon and seasonal differences in physical forcing (wind speed and SST). It was also shown that the annual cycle for both chlorophyll and CDOM concentrations is often overshadowed by inter-annual variability of ENSO episodes.

6.6 Future work

The results presented in this study even if encouraging, are far from conclusive. There are several issues that require further investigation. Three in particular are worthy of note:

1. One of the limitations of the bio-optical studies and the application of a semi-analytical algorithm in the study area is the lack of backscattering data. As this parameter is an

important IOP and it is also a basic parameter of bio-optical models, it is necessary to measure the backscattering coefficient in order to improve our remote sensing algorithms as well as to increase our understanding of the optics of our waters. This can be done using the backscattering sensor (e.g. HydroScat-6P) that measures backscattering coefficient at six different wavelengths.

2. Another important issue that needs to be addressed is the influence of the pigment package effect on the performance of bio-optical algorithms. Although, there is no ideal solution to this problem has been established until now, the use of the less affected band at the secondary chlorophyll absorption peak (676 nm) would minimise errors in chlorophyll estimation from the remote sensing algorithms.
3. In this study we presented a limited spatial coverage and time-series of in-situ measurements of optical properties. A major improvement would be to conduct an extended period of time (at least a year) of in-situ measurements and cover large areas. Such a time series and large spatial coverage would enable spatial and temporal changes in the optical properties to be studied in detail.

APPENDIX

A: Quasi Analytical Algorithm (QAA_v5) (Lee et al., 2009).

Part 1: Part 1 derives the total absorption coefficient and backscattering coefficient. The equations are as follows.

$$r_{rs}(\lambda) = \frac{R_{rs}(\lambda)}{0.52 + 1.7\, R_{rs}(\lambda)} \qquad A1$$

$$\begin{cases} r_{rs}(\lambda) = [g_0 + g_1 u(\lambda)]u(\lambda) \\ u = \dfrac{b_b}{a + b_b} \end{cases} \qquad A2$$

$$u(\lambda) = \frac{-g_0 + \sqrt{(g_0) + 4g_1 r_{rs}(\lambda)}}{2g_1}\ ; g_0 = 0.089, g_1 = 0.125 \qquad A3$$

$$\begin{cases} b_b(\lambda) = \dfrac{u(\lambda)a(\lambda)}{1 - u(\lambda)} \\ a(\lambda) = \dfrac{[1 - u(\lambda)]b_b(\lambda)}{u(\lambda)} \end{cases} \qquad A4$$

$$\begin{cases} a(\lambda_0) = a_w(\lambda_0) + 10^{-1.146-1.366\chi-0.469\chi^2} \\ \chi = log\left[\dfrac{r_{rs}(443) + r_{rs}(490)}{r_{rs}(\lambda_0) + 5\dfrac{r_{rs}(667)}{r_{rs}(490)}\, r_{rs}(667)}\right] \end{cases} ; \lambda_0 = 550; 555, 560\, nm \qquad A5$$

$$b_{bp}(\lambda) = b_{bp}(\lambda_0)\left[\frac{\lambda_0}{\lambda}\right]^Y \quad ; \lambda_0 = 550; 555, 560\, nm \qquad A6$$

$$Y = 2.0\left\{1 - 1.2\exp\left[-0.9\frac{r_{rs}(443)}{r_{rs}(\lambda_0)}\right]\right\} \quad ; \lambda_0 = 550; 555, 560\, nm \qquad A7$$

Part 2: Part 2 decomposes the total absorption coefficient into absorption coefficients of phytoplankton and coloured detrital matter.

$$\begin{cases} a_{dg}(443) = \dfrac{[a(411) - \alpha\, a(443)] - [a_w(411) - \alpha\, a_w(443)]}{\beta - \alpha} \\ \\ a_{ph}(\lambda) = a(\lambda) - a_w(\lambda) - a_{dg}(443)e^{-S(\lambda - 443)} \end{cases} \qquad A8$$

$$\begin{cases} \alpha = \dfrac{a_{ph}(411)}{a_{ph}(443)} \\ \\ \alpha = 0.74 + \dfrac{0.2}{0.8 + \dfrac{r_{rs}(443)}{r_{rs}(\lambda_0)}} \end{cases} \quad ; \lambda_0 = 550; 555, 560\, nm \qquad A9$$

$$\begin{cases} \beta = \dfrac{a_{dg}(411)}{a_{dg}(411)} \\ \beta = e^{S(443-411)} \\ S = 0.015 + \dfrac{0.002}{0.6 + \dfrac{r_{rs}(443)}{r_{rs}(\lambda_0)}} \end{cases} \quad ; \lambda_0 = 550; 555, 560\, nm \qquad A10$$

B: MODIS semi-analytical algorithm (Carder et al., 1999).

The semi-analytical MODIS algorithm of Carder et al., (1999) is based as on two R_{rs} ratio functions:

$$\begin{cases} \dfrac{R_{rs}(412)}{R_{rs}(443)} = \dfrac{b_b(412)}{b_b(443)}\dfrac{a(443)}{a(412)} \\ \dfrac{R_{rs}(443)}{R_{rs}(551)} = \dfrac{b_b(443)}{b_b(551)}\dfrac{a(551)}{a(443)} \end{cases} \qquad B1$$

The backscattering terms are defined as:

$$b_b(\lambda) = b_w(\lambda) + b_{bp}(\lambda) \qquad B2$$

$$b_{bp}(\lambda) = X\left[\frac{\lambda_0}{\lambda}\right]^Y \quad ; X = b_{bp}(551) \qquad B3$$

$$X = X_0 + X_1 R_{rs}(551) \qquad B4$$

$$Y = Y_0 + Y_1 \frac{R_{rs}(443)}{R_{rs}(488)} \qquad B5$$

The absorptions terms are defined as:

$$a(\lambda) = a_w(\lambda) + a_{ph}(\lambda) + a_{dg}(\lambda) \qquad B6$$

$$a_{ph}(\lambda) = a_o(\lambda)\exp[a_1(\lambda)\tanh[a_2(\lambda)\ln(\frac{a_{ph}(675)}{a_3(\lambda)})]]a_{ph}(675) \qquad B7$$

where $a_0(\lambda)$ to $a_3(\lambda)$ are derived empirically for each wavelength of 412, 443 and 551 nm.

$$a_{dg}(\lambda) = a_{dg}(400)exp^{-S(\lambda-400)} \qquad B8$$

Replacing all the absorption and backscattering terms (equations B3, B7 and B8) into equation B1 returns 2 unknown equations with two unknowns variables, $a_{ph}(675)$ and $a_{dg}(400)$. Given R_{rs}

values are known, these functions can be solved algebraically to provide values for $a_{ph}(675)$ and $a_{dg}(400)$. $a_{ph}(675)$ is then calculated by inverting one of the equations and substituting into the other equation.

$$\frac{(A-B)}{C} = \frac{(D-E)}{F} \qquad B9$$

where:

$$A = R_{rs}(551)(b_w(443) + X(\frac{551^{Y}}{443})(a_w(547) + \left[\, a_{ph}(551)\right])$$

$$B = R_{rs}(443)(b_w(551) + X)(a_w(443) + \left[\, a_{ph}(443)\right])$$

$$C = R_{rs}(443)(b_w(551) + X)exp(-43S) - R_{rs}(551)(b_w(443)X(\frac{551^{Y}}{443}))\exp(-151S)$$

$$D = R_{rs}(443)(b_w(412) + X(\frac{551^{Y}}{412}))(a_w(443) + \left[\, a_{ph}(443)\right])$$

$$E = R_{rs}(412)(b_w(443) + X(\frac{551^{Y}}{443}))(a_w(412) + \left[\, a_{ph}(412)\right])$$

$$F = R_{rs}(412)\left(b_w(443) + X(\frac{551^{Y}}{443})\right)exp(-12S) - R_{rs}(443)(b_w(412)X(\frac{551^{Y}}{412}))\exp(-43S)$$

For $a_{ph}(675)$ lower than 0.03 m^{-1}, the semi-analytical algorithm employed for the calculation of chlorophyll-a concentration is:

$$[Chl] = P_o[a_{ph}(675)]^{P_1} \qquad B10$$

where P_0 and P_1 are empirically coefficients. Otherwise, the following empirical algorithm is used by default (Aiken et al., 1995).

$$\begin{cases} [Chl] \quad = \quad 10^{c_0 + c_1\log(X) + c_2[\log(X)]^2 + c_3[\log(X)]^3} \\ X = \dfrac{R_{rs}(488)}{R_{rs}(551)} \end{cases} \qquad B11$$

where c_0 to c_3 are empirically derived coefficients

REFERENCES

Aiken, J., Moore G.F., Trees C.C., Hooker S.B., Clark D.K., The SeaWiFS CZCS-Type Pigment Algorithm. SeaWiFS Technical Report Series, NASA Technical Memorandum 104566, Vol. 29. Goddard Space Flight Center, Maryland 1995.

Anderson, J.M. and Barrett, J. 1986. Light-harvesting pigment-protein complexes of algae. In: Staehelin, L.A. and Arntzen, C.J. (eds.) Photosynthesis III. Encl Plant Phys Vol. 19, Springer-Verlag, Berlin, p 269-285.

Austin. R.W. 1974. Inherent spectral radiance signatures of the ocean surface. In: Ocean Color Analysis (La Jolla, CA: Scripps Institute of Oceanography), p 195.

Azmy, A. R., Y. Isoda and T. Yanagi. 1991 . Sea Level Variations due to Wind around West Malaysia. Memoirs of the Faculty of Engineering. Ehime University, XII: 148-161.

Babin, M., Stramski, D., Ferrari, G.M., Claustre, H., Bricaud, A., Obolensky, G., and Hoepffner, N. 2003. Variations in the light absorption coefficients of phytoplankton, non-algal particles, and dissolved organic matter in coastal waters around Europe. Journal of Geophysical Research, 108(C7), 3211, doi:10.1029/2001JC000882.

Barnard, A.H., Zaneveld, J.R.V. and Pegau, W.S. 1999. In situ determination of the remotely sensed reflectance and the absorption coefficient: closure and inversion, Applied Optics 38(24):5108–5117.

Binding, C.E., Bowers, D.G. and Mitchelson-Jacob, E.G. 2003. Estimating suspended sediment concentrations from ocean colour measurements in moderately turbid waters; the impact of variable particle scattering properties. Remote Sensing of Environment, 94(3):373-383.

Blondeau-Patissier, D., Tilstone, G.H., Martinez-Vicente, V. and Moore, G F. 2004. Comparison of bio-physical marine products from SeaWiFS, MODIS and a bio-optical model with in situ measurements from Northern European waters. Journal of Optic A: Pure and Applied Optic 6:875–889.

Blough, N. V., Zafiriou, O. C., and Bonilla, J. 1993. Optical absorption spectra of waters from the Orinoco River outflow: terrestrial input of coloured organic matter to the Caribbean. Journal of Geophysical Research 98, 2271–2278.

Bowers, D.G. and Binding, C.E. 2006. The optical properties of mineral suspended particles. A review and synthesis. Estuarine, Coastal and Shelf Science 67: 219-230.

Bowers, D.G. and Mitchelson-Jacob, E.G. 1996. Inherent Optical Properties of the Irish Sea Determined from Underwater Irradiance Measurements. Estuarine, Coastal and Shelf Science 43: 433–447.

Bricaud, A., Claustre, H., Ras, J. and Oubelkheir, K. 2004. Natural variability of phytoplankton absorption in oceanic waters: influence of the size structure of algal populations. Journal of Geophysical Research, 109, C11010, doi:10.1029/2004JC002419.

Bricaud, A., and Morel, A. 1986. Light attenuation and scattering by phytoplankton cells: A theoretical modeling, Applied Optics, 25(4): 571-580.

Bricaud, A., Morel, A., Babin, M., Allali, K. and Claustre, H. 1998. Variations of light absorption by suspended particles with the chlorophyll a concentration in oceanic (Case 1) waters : analysis and implications for bio-optical models. Journal of Geophysical Research, 103, 31,033-31,044.

Bricaud, A., Morel, A. and Prieur, L. 1981. Absorption by dissolved organic matter of the sea (yellow substance) in the UV and visible domains. Limnology and Oceanography, 26: 45–53.

Bukata., R.P. 2005. Satellite Monitoring of Inland and Coastal Water Quality: Retrospection, Introspection, Future Directions. Taylor & Francis/CRC Press, 263 pp., solicited monograph by Taylor & Francis, UK.

Bukata, R.P., Bruton, J.E. and Jerome, J.H. 1983. Use of chromaticity in remote measurements of water quality. Remote Sensing of Environment, 13(2): 161-177.

Butler, L.W. 1962. Absorption of light by turbid materials. Journal of the Optical Society of America, 52:292-299.

Carder, K.L., Cattrall, C. and Chen, F.R. 2002. MODIS Clear Water Epsilons Algorithm Theoretical Basis Document: ATBD21, Version 6, June 2002. 71p

Carder, K.L., Chen, F.R., Cannizzaro, J.W., Campbell, J.W., Mitchell, B.G. 2004. Performance of the MODIS semi-analytical ocean color algorithm for chlorophyll-a. Advances in Space Research. 33:1152-1159.

Carder, K.L., Chen, F.R., Lee, Z.P., Hawes, S.K. and Kamykowski, D. 1999. Semianalytic Moderate-Resolution Imaging Spectrometer algorithms for chlorophyll-a and absorption with bio-optical domains based on nitrate-depletion temperatures. Journal of Geophysical Research, 104:5403–5421.

Carder, K.L., Hawes, S.K., Baker, K.A., Smith, R.C., Stewart, R.G. and Mitchell, B.G. 1991. Reflectance model for quantifying chlorophyll a in the presence of productivity degradation products, Journal of Geophysical Research, 96:599-611.

Camerlengo, A., and Demmler, M. I. 1997, Wind-driven circulation of Peninsular Malaysia’s eastern continental shelf. Scientia Marina, 61: 203–211.

Chang, G.C. and Gould Jr., R.W. 2006. Comparisons of optical properties of the coastal ocean derived from satellite ocean color and in situ measurements. Optics Express 10149, Vol. 14, No. 22.

Chao, S.Y., Shaw, P.T. and Wu, S.Y., 1996. El Nino modulation of the South China Sea circulation. Progress in Oceanography, 38:51–93.

Chomko, R.M., Gordon, H.R., Maritorena, S. and Siegel, D.A. 2003. Simultaneous determination of oceanic and atmospheric parameters for ocean color imagery by spectral optimization: a validation. Remote Sensing of the Environment, 84:208-220.

Chua, T.E. 1970. Notes on the abundance of the diatom Hemidiscus hardmannianus (Grev.-Mann) in the Singapore Straits. Hydrobiologia, 36(1):61-64.

Chua, T.E. 1984. Physical environments of the East Coast of Peninsular Malaysia. p. 1–10. In Coastal Resources of East Coast Peninsular Malaysia—An Assessment in Relation to Potential Oil Spills, eds. by T.E., Chua and J. K. Charles, 306 pp., Penerbit Universiti Sains Malaysia, Pulau Pinang.

Cleveland, J.S. and Weidermann, A.D. 1993. Quantifying absorption by aquatic particles: A multiple scattering correction for glass-fiber filters. Limnology and Oceanography, 38, 1321-1327.

Cota, G. F., Wang, J. and Comiso, J. C. 2004. Transformation of global satellite chlorophyll retrievals with a regionally tuned algorithm, Remote Sensing of Environment, 90, 373– 377.

Dall'Olmo, G., Gitelson, A. A., Rundquist, D. C., Leavitt, B., Barrow, T. and Holz, J. C. 2005. Assessing the potential of SeaWiFS and MODIS for estimating chlorophyll concentration in turbid productive waters using red and near-infrared bands. Remote Sensing of Environment, 96:176−187.

Darecki, M. and Stramski, D. 2004. An evaluation of MODIS and SeaWiFS bio-optical algorithms in the Baltic Sea. Remote Sensing of Environment, 89(3):326-350.

Dekker, A.G. 1993. Detection of optical water quality parameters for eutrophic waters by high resolution remote sensing. Ph.D. thesis, Free University, Amsterdam, 222p.

Department of Fisheries Malaysia. 2010. Annual Fisheries Statistic 2010, Volume 1, 45p.

Dey, S. and Singh, R.P. 2003. Comparison of chlorophyll distributions in the northeastern Arabian Sea and southern Bay of Bengal using IRS-P4 Ocean Color Monitor Data. Remote Sensing of Environment, 85, 424–428.

Dippner, J.W., Nguyen K.V., Hein, H., Ohde, T. and Loick, N. 2007. Monsoon-induced upwelling off the Vietnamese coast. Ocean Dynamics, 57: 46–62.

D'Sa, E. J., Miller, R. L. 2003. Bio-optical properties in waters influenced by the Mississippi River during low flow conditions, Remote Sensing of Environment, 84 (4):538–549.

Duysens, L. N. M. 1956. The flattening of the absorption spectrum of suspensions, as compared to that of solutions. Biochimica et Biophysica Acta, 19, 1–12.

Fang, W., Fang, G., Shi, P., Huang, Q. and Xei, Q. 2002. Seasonal structures of upper layer circulation in the southern South China Sea from in situ observation. Journal of Geophysical Research, 107(C11):3202–3212.

Fargion, G. S. and McClain, C.R. 2002. SIMBIOS Project 2001 Annual Report. NASA Technical Memo. 2002-210005, NASA Goddard Space Flight Center, Greenbelt, Maryland, 184 pp.

Garcia, C.A.E., Garcia, V.M.T. and McClain, C.R. 2005. Evaluation of SeaWiFS chlorophyll algorithms in the Southwestern Atlantic and Southern Oceans. Remote Sensing of Environment, 95: 125-137.

Garcia C.A.E, Garcia V.M.T, McClain, C.R. 2006. Empirical and semi-analytical chlorophyll algorithms in the southwestern Atlantic coastal region (25–40°S and 60–45°W). International Journal of Remote Sensing, 27(8): 1539–1562.

Garver, S.A. and Siegel, D.A. 1997. Inherent optical property inversion of ocean color spectra and its biogeochemical interpretation 1. Time series from the Sargasso Sea. Journal of Geophysical Research-Oceans, 102:18607-18625.

Gitelson, A.A. 1992. The peak near 700 nm on reflectance spectra of algae and water: relationships of its magnitude and position with chlorophyll concentration. International Journal of Remote Sensing, 13(17): 3367–3373.

Gitelson, A.A. and Kondratyev, K. Y. 1991. Optical models of mesotrophic and eutrophic water bodies. International Journal of Remote Sensing, 12(3): 373–385.

Gitelson, A.A., Schalles, J.F. and Hladik, C.M. 2007. Remote chlorophyll-a retrieval in turbid, productive estuaries: Chesapeake Bay case study. Remote Sensing of Environment, 109(4):464-472.

Gons, H.J. 1999. Optical teledetection of chlorophyll a in turbid inland waters. Environmental Science and Technology, 33:1127−1132.

Gons, H.J., Rijkeboer, M. and Ruddick, K. G. 2002. A chlorophyll-retrieval algorithm for satellite imagery (Medium Resolution Imaging Spectrometer) of inland and coastal waters. Journal of Plankton Research, 24, 947–951.

Gordon, H.R., Brown, O. B., Evans, R.H., Brown, J.W., Smith, R.C., Baker, K.S. and Clark, D.K. 1988. A Semianalytic Radiance Model of Ocean Color. Journal of Geophysical Research, 93(D9):10909–10924.

Gordon, H.R., Brown, O.B. and Jacobs, M.M. 1975. Computed relationships between the inherent and apparent optical properties of a flat, homogenous ocean. Applied Optics, 14: 417–427.

Gordon, H.R. and Clark, D.K. 1981. Clear water radiances for atmospheric correction of Coastal Zone Color Scanner imagery. Applied Optics, 20: 4175–4180.

Gordon, HR., Clark, D.K., Brown, J.W., Brown, O.B., Evans, R.H. and Broenkow, W.W. 1983. Phytoplankton pigment concentrations in the middle Atlantic bight: Comparison of ship determinations and Coastal Zone Color Scanner measurements. Applied Optics, 22: 20-36.

Gordon, H.R. and Morel, A.Y. 1983. Remote Assessment of Ocean Color for Interpretation of Satellite Visible Imagery: A Review. Springer-Verlag, New York, 114 pp.

Harding Jr., L.W., Magnuson, A., Mallonee, M.E., 2005. Bio-optical and remote sensing observations in Chesapeake Bay. Estuarine, Coastal and Shelf Science 62, 75-94.

Ho, C.R., Zheng, Q., Soong, Y.S., Kuo, N.J. and Ho, J.H. 2000. Seasonal variability of sea surface height in the South China Sea observed with TOPE/POSEIDON altimeter data. Journal of Geophysical Research, 105 (C6):13,981–13,990.

Hoepfner, N. and Sathyendranath, S. 1992. Bio-optical characteristics of coastal waters: Absorption spectra of phytoplankton and pigment distribution in the western North Atlantic. Limnology and Oceanography, 37(8):1660-1679.

Hoge, F. E., Wright, C. W., Lyon, P. E., Swift, R. N. and Yungel, J. 1999. Satellite retrival of the absorption coefficient of phytoplankton phycoerythrin pigment: Theory and feasibility status. MODIS ATBD doc. 27.

Hoyos, C. D. and Webster, P. J. 2007. The Role of Intraseasonal Variability in the Nature of Asian Monsoon Precipitation. Journal of Climate, 20 (17), 4402-4424.

Hu, C., Lee, Z., Muller-Karger, E., Carder, L. and Walsh, J.J. 2006. Ocean color reveals phase shift between marine plants and yellow substance, IEEE Geoscience and Remote Sensing Letters, 3, 262–266.

Hu, J., Kawamura, H., Hong, H. and Qi, Y. 2000. A review on the currents in the South China Sea: Seasonal circulation, South China Sea Warm Current and Kuroshio intrusion. Journal of Oceanography, 56:607–624.

IOCCG. 2000. Remote sensing of ocean colour in coastal, and optically-complex, waters, in Reports of the International Ocean-Colour Coordinating Group, no. 3, edited by S. Sathyendranath, pp. 140, Dartmouth.

Jeffrey, S.W and Humphrey, G.F. 1975. New spectrophotometric equations for determining chlorophylls a, b, c in higher plants, algae and natural phytoplankton. Biochemie und Physiologie der Pflanzen, 167:191-194.

Kahru, M., Mitchell, B.G. 2001. Seasonal and non-seasonal variability of satellite derived chlorophyll and colored dissolved organic matter concentration in the California Current, Journal of Geophysical Research, 106 (C2), 2517–2529.

Kamykowski, D. 1987. A preliminary biophysical model of the relationship between temperature and plant nutrients in the upper ocean. Deep-Sea Research, 34, 1067-1079.

Kirk, J. T. O. 1976. A theoretical analysis of the contribution of algal cells to the attenuation of light within natural waters. III. Cylindrical and spheroidal cells. New Phytologist, 77:341–358.

Kirk, J.T.O. 1984. Dependence of relationship between inherent and apparent optical properties of water on solar altitude. Limnology and Oceanography 29(2): 350-356

Kirk, J.T.O. 1994, Light and Photosynthesis in Aquatic Ecosystems, Cambridge University Press, London-New York, p. 509.

Kowalczuk, P., Darecki, M., Zablocka, M. and Gorecka, I. 2010. Validation of empirical and semi-analytical remote sensing algorithms for estimating absorption by coloured dissolved organic matter in the Baltic Sea from SeaWIFS and MODIS imagery, Oceanologia, 52(2):171-196.

Kowalczuk, P., Darecki, M., Olszewski, J., Kaczmarek, S., 2005. Empirical relationships between Coloured Dissolved Organic Matter (CDOM) absorption and apparent optical properties in Baltic Sea waters, International Journal of Remote Sensing, 26(2):345–370.

Kudela, R.M. and Chavez. F.P. 2004. The impact of coastal runoff on ocean color during an El Niño year in central California. Deep-Sea Research Part II, 51(10-11): 1173-1185.

Kuo, N.J., Zheng, Q.N. and Ho, C.R. 2000. Satellite observation of upwelling along the Western Coast of the South China Sea. Remote Sensing of Environment, 74:465–470.

Lamb, P.J. 1984. On the mixed-layer climatology of the North and Tropical Atlantic. Tellus, 36A, 292-305.

Lau, K.-M., and yang, S. 1997. Climatology and interannual variability of the Southeast Asian Summer Monsoon. Advances in Atmospheric Sciences, 14, 141-162.

Lee, Z. P., Carder, K. L., and Arnone, R. 2002. Deriving inherent optical properties from water color: A multi-band quasi-analytical algorithm for optically deep waters. Applied Optics, 41, 5755– 5772.

Lee, Z. P., Carder, K. L., Chen, R. F., and Peacock, T. G. 2001. Properties of the water column and bottom derived from AVIRIS data. Journal of Geophysical Research, 106, 11639– 11652.

Lee, Z. P., Carder, K. L., Mobley, C. D., Steward, R. G., and Patch, J. S. 1999. Hyperspectral remote sensing for shallow waters: 2. Deriving bottom depths and water properties by optimization. Applied Optics, 38, 3831– 3843.

Lee, Z.P., Carder, K.L., Steward, R.G., Peacock, T.G., Davis, C.O. and Patch, J.S. 1998. An empirical algorithm for light absorption by ocean water based on color. Journal of Geophysical Research, 103, 27,967-27,978.

Liu, K.K., Chao, S.Y., Shaw, P.T., Gong, G.C., Chen, C.-C. and Tang, T.Y. 2002. Monsoon-forced chlorophyll distribution and primary production in the South China Sea: observations and a numerical study. Deep-Sea Research I, 49: 1387–1412.

Loisel, H., Stramski, D., Mitchell, B.G., Fell, F., Fournier-Sicre, V., Lemasle, B. and Babin, M. 2001. Comparison of the ocean inherent optical properties obtained from measurements and inverse modeling. Applied Optics 40(15): 2384-2397.

Lokman, H., Yacoob ,R. and Shazili, N.A.M. 1986. Some Measurements of Temperature and Salinity on a Portion of the South China Sea. In: A.K. Mohsin, M.I. Mohamed and M.A. Ambak (eds.) Ekspedisi Matahari '85: A Study of the Offshore Waters of the Malaysian EEZ. Faculty of Fisheries and Marine Science, UPM. Occasional Publication No.3, pp. 49-79.

Ma, J., Zhan, H. and Du, Y. 2011. Seasonal and interannual variability of surface CDOM in the South China Sea associated with El Niño. Journal of Marine Systems, 85, 86–95.

Mann, H.K. and Lazier, J.R.N. 1996. Dynamics of marine ecosystems : biological-physical interactions in the oceans. 2nd edition. Cambridge: Blackwell Science, XII, 394p.

Mannino, A., Russ, M.E., Hooker, S.B., 2008. Algorithm development and validation for satellite-derived distributions of DOC and CDOM in the U.S. Middle Atlantic Bight, Journal of Geophysical Research, 113, C07051, doi:10.1029/2007JC004493.

Maritorena, S., Siegel, D.A. and Peterson, A.R. 2002. Optimization of a semi-analytical ocean color model for global-scale applications. Applied Optics, 41: 2705–2714.

Md-Suffian, I. 2007. Phytoplankton abundance in east coast Peninsular Malaysia waters. Unpublished raw data.

Mitchell, B.G., 1990. Algorithms for determining the absorption coefficient of aquatic particulates using the quantitative filter technique. In: Ocean Optics, 10, Proc. SPIE 1302, pp. 137-148.

Mitchell, B.G. 1992. Predictive bio-optical relationships for polar oceans and marginal ice zones. Journal of Marine Systems, 3, 91–105.

Mitchell, B.G. and Holm-Hansen, O. 1991. Bio-optical properties of Antarctic Peninsula waters. Differentiation from temperate ocean models. Deep Sea Research, 38:1009–1028.

Mitchell, B.G., Kahru, M., Wieland, J. and Stramska, M. 2002. Determination of spectral absorption coefficients of particles, dissolved material and phytoplankton for discrete water samples. In: Mueller, J.L., Fargion, G.S. and McClain, C.R. (Eds.), Ocean Optics Protocols for

Satellite Ocean Color Sensor Validation, Revision 4: Volume IV. NASA/TM-2003-211621/Rev4-Vol.IV.

Mobley, C.D. 1994. Light and water: radiative transfer in natural waters, Academic Press, San Diego. p. 592.

Mohd-Lokman, H., Rosnan, Ejria, S., Shazili, N. A. M. and Kassim, K. K. Y. 1998. Deducing sediment transport direction and the relative importance of rivers on a tropical microtidal beach using the "McLaren model". Environmental Geology, 34(2-3): 128-134.

Mohd Mazlan, J. 1998. Malaysian Fisheries Policy Beyond 2000. In: Fisheries and the Environment: Beyond 2000. Japar Sidik, B., F.M. Yusoff, M.S. Mohd Zaki and T. Petr (eds.), p.15–20. Universiti Putra Malaysia, Serdang, Malaysia.

Moore, L.R., Goericke, R. and Chisholm, S.W. 1995. Comparative physiology of Synechococcus and Prochlorococcus: influence of light and temperature on growth, pigments, fluorescence and absorptive properties. Marine Ecology Progress Series, 116:259-275.

Morel, A. 1988. Optical modeling of the upper ocean in relation to its biogenous matter content (case 1 water). Journal of Geophysical Research, 93, 10,749-10,768.

Morel, A., and Ahn, Y.-H. 1990. Optical efficiency factors of free-living marine bacteria: Influence of bacterioplankton upon the optical properties and particulate organic carbon in oceanic waters, Journal of Marine Research, 48, 145-175.

Morel, A., and Ahn, Y.-H. 1991. Optics of heterotrophic nanoflagellates and ciliates: A tentative assessment of their scattering role in oceanic waters compared to those of bacterial and algal cells. Journal of Marine Research, 49, 177-202.

Morel, A. and Bricaud, A. 1981. Theoretical results concerning light absorption in a discrete medium, and application to specific absorption of phytoplankton, Deep-Sea Research, 28:1375-1393.

Morel, A. and Bricaud, A. 1986. Inherent optical properties of algal cells, including picoplankton. Theoretical and experimental results. Canadian Bulletin of Fisheries and Aquatic Science, 214, 521-559.

Morel, A., Gentili, B., 1993. Diffuse reflectance of oceanic waters. II. Bidirectional aspects. Applied Optics, 32, 6864-6879.

Morel, A., Gentili, B., 1996. Diffuse reflectance of oceanic waters. 3. Implication of bidirectionality for the remote-sensing problem. Applied Optics, 35, 4850-4862.

Morel, A. and Prieur, L. 1977. Analysis of variations in ocean color, Limnology and Oceanography, 22, 709-722.

Morel, A., Voss, K.J. and Gentili, B. 1995. Bidirectional reflectance of oceanic waters: A comparison of modeled and measured upward radiance fields, Journal of Geophysical Research, 100, 13,143-13,150.

Morton, B. and Blackmore, G. 2002. South China Sea. Marine Pollution Bulletin, 12:1236-1263.

Mudgal, R., Dash, M.K. and Pandey, P.C. 2009. Seasonal and Inter-annual Variability of Chlorophyll–a in the Arabian Sea from SeaWiFS Data. e-Journal Earth Science India, 2, 21- 32.

Mueller et al., 2003. In J.L., Mueller, G.S., Fargion and C.R., McClain (eds.) Ocean Optics Protocols For Satellite Ocean Color Sensor Validation, Revision 4, Volume I-VI.

Mueller, J.L. and Austin, R.W. 1995. Ocean Optics Protocols for SeaWiFS Validation, Revision 1. NASA Tech. Memo. 104566, Vol. 25, S.B. Hooker, E.R. Firestone and J.G. Acker, Eds., NASA Goddard Space Flight Center, Greenbelt, Maryland, 67 pp.

Nelson, J. R., and Guarda, S. 1995. Particulate and dissolved spectral absorption on the continental shelf of the southeastern United States. Journal of Geophysical Research, 100(C5), 8715– 8732, 1995.

Nelson, N.B., Prezelin, B.B. and Bidigare., R.R. 1993. Phytoplankton light absorption and the package effect in California coastal waters. Marine Ecology Progress Series, 94:217-227.

NOAA National Climate Service, Climate Prediction Center: http://www.cpc.ncep.noaa.gov/

Ocean Color Web: http://oceancolor.gsfc.nasa.gov/

O'Reilly, J., Maritorena, S., Mitchell, B. G., Siegel, D., Carder, K. L., Garver, S., Kahru, M. and McClain, C. 1998. Ocean color chlorophyll algorithms for SeaWiFS. Journal of Geophysical Research, 103,24937– 24953.

O'Reilly, J. E. and 24 co-authors. 2000. Ocean color chlorophyll-a algorithms for SeaWiFS, OC2 and OC4, In: SeaWiFS Postlaunch Calibration and Validation Analyses: Part 3, SeaWiFS Postlaunch Tech. Rep. Ser., vol. 11, version 4, edited by S. B. Hooker and E. R. Firestone, pp. 9– 23, NASA Goddard Space Flight Cent., Greenbelt, Md.

Pan, X., Mannino, A., Russ, M. E. and Hooker, S. B. 2008. Remote sensing of the absorption coefficients and chlorophyll a concentration in the United States southern Middle Atlantic Bight from SeaWiFS and MODIS-Aqua, Journal of Geophysical Research, 113, C11022, doi:10.1029/2008JC004852.

Petzold, T.J. 1972. Volume scattering functions for selected ocean waters. SIO Reference 72–78, Technical Report, Scripps Institution of Oceanography, Visibility Laboratory, San Diego, California.

Pope, R. and Fry, E.S. 1997. Absorption spectrum (380 - 700 nm) of pure waters: II. Integrating cavity measurements. Applied Optics, 36:8710-8723.

Pozdnyakov, D. and Grassl, H. 2003. Colour of inland and coastal waters - a methodology for its interpretation. Springer Verlag Berlin/Heidelberg/New York, Praxis Publishing Ltd. Chichester.

Pradhan, Y., Lavender, S.J., Hardman-Mountford, N.J. and Aiken, J. 2006. Seasonal and inter-annual variability of chlorophyll-a concentration in the Mauritanian upwelling: Observation of an anomalous event during 1998–1999. Deep-Sea Research II, 53, 1548–1559.

Preisendorfer, R.W. 1961. Applications of radiation transfer theory to light measurements in the sea. Union de Geologie et Geophysique Internationale (I.U.G.G) Monographie, 10:11-30.

Preisendorfer, R. W. 1976. Hydrologic optics. Pacific Marine Environment Lab/NOAA.

Prieur, L. and Sathyendranath, S. 1981. An optical classification of coastal and oceanic waters based on the specific spectral absorption curves of phytoplankton pigments, dissolved organic matter, and other particulate materials. Limnology and Oceanography, 26(4): 671-689.

Qin, Y., Brando, V., Dekker, A. and Blondeau-Patissier, D. 2007. Validity of SeaDAS water constituents retrieval algorithms in Australian tropical coastal waters, Geophysical Research Letters, 34, L21, 603, doi:10.1029/2007GL030, 599.

Remote Sensing System: http://www.ssmi.com/

Roesler, C.S. 1998. Theoretical and experimental approaches to improve the accuracy of particulate absorption coefficients derived from the quantitative filter technique. Limnology and Oceanography 43(7): 1649-1660.

Roesler, C.S., Perry, M.J. and Carder, K.L. 1989. Modeling in situ phytoplankton absorption from total absorption spectra in productive inland marine waters. Limnology and Oceanography, 34:1510-1523, 1989.

Ruddick, K.G., Gons, H.J., Rijkeboer, M., Tilstone, G., 2001. Optical remote sensing of chlorophyll a in case 2 waters by use of an adaptive two-band algorithm with optimal error properties. Applied Optics 40 (21), 3575-3585.

Saadon, M.N. and Camerlengo, A.L. 1997. Response of the ocean mixed layer, off the east coast of Peninsular Malaysia, during the north-east and south-west monsoons. Geoacta, 22:134-143.

Saadon, M.N., Camerlengo, A.L. and Wan-Hazli, W-K. 1997. Coastal Current in the Northern Region of the East Coast of Peninsular Malaysia. Sains Malaysiana, 26(2): 5-14.

Sathyendranath, S. 2000. Remote Sensing of Ocean Colour in Coastal and Other Optically-Complex, Water. Reports of the International Ocean-Colour Coordinating Group, IOCCG Report Number 3. p.140.

Sathyendranath, S., Cota, G., Stuart, V., Maass, H. and Platt, T. 2001. Remote sensing of phytoplankton pigments: a comparison of empirical and theoretical approaches. International Journal of Remote Sensing, 22 (2&3): 249–273.

Sathyendranath, S., Lazzara, L. and Prieur, L. 1987. Variations in the Spectral Values of Specific Absorption of Phytoplankton. Limnology and Oceanography, Vol. 32, No. 2, pp. 403-415.

Sathyendranath, S., Stuart, V., Irwin, B.D., Maass, H., Svidge, G., Gilpin, L. and Platt, T. 1999. Seasonal variations in bio-optical properties of phytoplankton in the Arabian Sea. Deep-Sea Research II 46: 633-653.

Schalles, J.F. 2006. Optical remote sensing techniques to estimate phytoplankton chlorophyll a concentrations in coastal waters in varying suspended matter and CDOM concentrations. In: L.L Richardson and E.F LeDrew (eds). Remote Sensing of Aquatic Coastal Ecosystem Processes: Science and Management Application. Springer, Netherlands. p. 325.

Shaw, P.-T. and Chao, S.-Y. 1994. Surface circulation in the South China Sea. Deep-Sea Research I, 41:1663–1683.

Smith, R.C., Baker, K.S., 1981. Optical properties of the clearest natural waters (200-800 nm). Applied Optics 20, 177-184.

Snidvongs, A., Sojisuporn, P. 1999. Numerical simulations of the current in the Gulf of Thailand under different monsoon regimes. In: Proceedings of The First Technical Seminar on Marine Fishery Resources Survey in the South China Sea (Samutprakan, Thailand) pp. 54–72.

Stansfield, K. and Garrett, C. 1997. Implications of the salt and heat budgets of the Gulf of Thailand. Journal of Marine Research, 55, 935-963.

Stramska, M., Stramski, D., Hapter, R., Kaczmarek, S. and Ston, J. 2003. Bio-optical relationships and ocean color algorithms for the north polar region of the Atlantic. Journal of Geophysical Research, 108, No. C5, 1-16.

Stramska, M., Stramski, D., Kaczmarek, S., Allison, D.B. and Schwarz, J. 2006. Seasonal and regional differentiation of bio-optical properties within the north polar Atlantic. Journal of Geophysical Research, 111(C8):1-16.

Stramski, D. and Kiefer, D. A. 1991. Light scattering by microorganisms in the open ocean. Progress in Oceanography, 28:343–383.

Stuart, V., Sathyendranath, S., Platt, T., Maass, H. and Irwin, B.D. 1998. Pigments and species composition of natural phytoplankton populations: effect on the absorption spectra. Journal of Plankton Research, 20: 187 – 217.

Tang, D.L., Kawamura, H., Lee, M. A. and Dien, T. V. 2003. Seasonal and spatial distribution of chlorophyll a concentrations and water conditions in the Gulf of Tonkin, South China Sea. Remote Sensing of Environment, 85: 476–483.

Tang, D.L., Kawamura, H., Shi, P., Takahashi, W., Guan, L., Shimada, T., Sakaida, F. and Isoguchi, O. 2006. Seasonal phytoplankton blooms associated with monsoonal influences and coastal environments in the sea areas either side of the Indochina Peninsula, Journal of Geophysical Research, 111, G01010, doi:10.1029/2005JG000050.

Tang D.L., Ni, I-H. Kester, D. E. and Müller-Karger, F. E. 1999. Remote sensing observations of winter phytoplankton blooms southwest of the Luzon Strait in the South China Sea. Marine Ecology Progress Series, 191: 43–51.

Tang, D.L., Ni, I-H. Müller-Karger, F. E. and Liu, Z. J. 1998. Analysis of annual and spatial patterns of CZCS-derived pigment concentration on the continental shelf of China. Continental Shelf Research, 18:1493–1515.

Tang, D.L., Ni, I.-H., Müller-Karger, F.E. and Oh, I.S. 2004. Monthly variation of pigment concentrations and seasonal winds in China’s marginal seas. Hydrobiologia, 511: 1–15.

Tangang, F.T., Mohd-Syamil, M.Y. and Juneng, L. 2007. Current Circulation Pattern in Waters Around Pulau Tinggi, Johor. Sains Malaysiana, 36(2): 165-173.

Tham, A.K. 1973. Seasonal distribution of the plankton in Singapore straits. MBAI Special Publication dedicated to Dr.N K Panikkar (1). pp. 60-73.

Vodacek, A., Blough, N.V., DeGrandpre, M.D., Peltzer. E.T. and Nelson, R.K. 1997. Seasonal Variation of CDOM and DOC in the Middle Atlantic Bight: Terrestrial Inputs and Photo-oxidation. Limnology and Oceanography, 42(4): 674-686.

Volpe, G., Santoleri, R., Vellucci, V., Ribera d'Alcalà, M., Marullo, S. and D'Ortenzio, F. 2007. The colour of the Mediterranean Sea: global versus regional bio-optical algorithms evaluation and implication for satellite chlorophyll estimates. Remote Sensing of Environment, 107, 625-638.

Wagner, R.G. 1996. Decadal scale trends in mechanisms controlling meridional SST gradients in the tropical Atlantic. Journal of Geophysical Research, 101 (C7), 16,683-16,694, doi:10.1029/96JC01214.

Werdell, P.J., Bailey, S., Fargion, G., Pietras, C., Knobelspiesse, K., Feldman, G. and McClain, C. 2003. Unique Data Repository Facilitates Ocean Color Satellite Validation. Eos, Vol. 84(38):377-392.

Wozniak, B. and Dera, J. 2007. Light Absorption in Sea Water. In: L.A., Mysak and K., Hamilton (eds.). Atmospheric and Oceanographic Sciences Library. Volume 33 Springer Science Business Media. New York. 453 p.

Wyrtki, K. (1961): Physical oceanography of the Southeast Asian waters. NAGA Report Vol. 2, Scientific Results of Marine Investigation of the South China Sea and the Gulf of Thailand, Scripps Institution of Oceanography, La Jolla, California, 195 pp.

Xie, S-P., Xie, Q., Wang, D. and Timothy, L.W. 2003. Summer upwelling in the South China Sea and its role in regional climate variations. Journal of Geophysical Research, 108, (C8), 3261, doi:10.1029/2003JC001867.

Yanagi, T., Sachoemar, S.I., Takao, T. and Fujiwara, S. 2001. Seasonal variation of stratification in the Gulf of Thailand. Journal of Oceanography, 57:461-470.

Yentch, C. S. 1962. Measurement of visible light absorption by particulate matter in the ocean. Limnology and Oceanography, 7:207-217.

Zhao, X.Z., Lu, Z. and Fry, E.S. 2002. Absorption spectrum (300-700) of pure water using an integrating cavity absorption meter. Proceeding Ocean Optics Meeting, Santa Fe, NM.

Zhu, W., Yu, Q., Tian, Y. Q., Chen, R. F. and Gardner, G. B. 2011. Estimation of chromophoric dissolved organic matter in the Mississippi and Atchafalaya river plume regions using above-surface hyperspectral remote sensing, Journal of Geophysical Research 116, C02011, doi:10.1029/2010JC006523.